THE SIMULATION OF SINGLE PHASE, COMPRESSIBLE FLUID FLOW IN FRACTURED PETROLEUM RESERVOIRS USING FINITE ELEMENTS

by

Shane Kenneth Francis Hattingh

Thesis Presented for the Degree of

DOCTOR OF PHILOSOPHY

in the Department of Mathematics and Applied Mathematics

UNIVERSITY OF CAPE TOWN

January 2002

ABSTRACT

THE SIMULATION OF SINGLE PHASE, COMPRESSIBLE FLUID FLOW IN FRACTURED PETROLEUM RESERVOIRS USING FINITE ELEMENTS

Shane K. F. Hattingh

The petroleum industry relies on numerical simulation to manage production of naturally occurring oil and gas from porous and permeable underground reservoirs. Where these rock formations contain networks of fractures, the need to deal with two different but linked systems increases the complexity of the modelling process. This is exacerbated when the reservoir fluid is a compressible gas, as the governing equations are highly nonlinear, and when the rock matrix is characterised by a low permeability, as this magnifies the physical differences between the two systems.

In this thesis, commonly used equations governing the flow of fluids are reviewed, from first principles where appropriate. The assumptions that are made in the process are critically assessed and their limitations are discussed. The equations deal with flow through a porous and permeable medium, a single fracture, a network of fractures, and with the coupling of the fracture network and blocks of matrix material.

A finite element program has been developed to model the flow of highly compressible gas through a fractured reservoir. The finite element method offers benefits over finite difference methods, which include the ability to model complex domains efficiently and achieve higher order accuracy. The approach described in this thesis is unique in several respects. Firstly, the use of finite elements to model fully compressible flow through both the fracture network and the matrix blocks has not been described in the literature. Secondly, the use of multiple finite elements to model each matrix block eliminates the need for the conventional dual porosity transfer function, and permits accurate modelling of transient effects occurring in the matrix blocks. Thirdly, a new approach for dealing with variable geometric shapes of the matrix blocks has been developed.

The simulator is verified via comparison with analytical solutions for a range of simple problems, and it is then utilised to gain new understanding into the performance of fractured reservoirs. Matrix block geometry is shown to be an important parameter requiring accurate representation, for both transient and pseudo-steady state flow regimes. It is shown that where transient effects do occur, neglecting to capture them in the model can result in large errors. A system is presented whereby fractured reservoirs can be classified into eight distinct types according to the response of the reservoir as determined by the values of the two most important properties, matrix permeability and fracture density. Modelling approaches appropriate to each type are presented.

Finally, a case study is presented of a commercial gas field producing from a low permeability fractured carbonate via two wells. A history match involving both long term field production and a reservoir performance test of a single well is successfully accomplished due to the flexible meshing capability of the finite element method and the transient modelling capabilities of the algorithms.

DECLARATION

I, Shane Kenneth Francis Hattingh, hereby declare that this thesis is essentially my own work and that no part of it has been submitted for a degree to any other university.

S K F Hattingh

January 2002

ACKNOWLEDGEMENTS

I wish to express my gratitude to the following:

My supervisor and mentor, Professor Daya Reddy, for his guidance, enormous patience and remarkable ability to make the journey of learning a joyous one.

The oil company that granted permission for me to use their reservoir as a case study and provided me with the information that I needed.

The National Research Foundation for their financial assistance.

Lizette Jordaan, for typing the computer code.

My company's technical director, Adrian Nel, whose understanding and continued support allowed me to complete this work.

My mother and father, Alfreda and Kenneth, for their encouragement, understanding and endless patience.

All those who have had to share my living space over the years, for their patience.

My spaniels, Nutkin and Lucy, for the endless hours of intimate companionship shared in my study.

Lastly, I wish to thank my wife and companion, Sandra, for her enormous and varied support without which this work could not have happened, for the continued interest and enthusiasm that she has displayed in my research over the years, and for the many instances of sound advice offered.

I wish to pay a special tribute to Laurie Dake, who taught me much of what I know of reservoir engineering, and whose lingering words continue to be a source of inspiration in my career.

CONTENTS

CHAPTER 1

INTRODUCTION

1.1 Background

Petroleum occurs in a natural state under pressure in underground rock formations in which it has accumulated over geologic time. Where these rock formations are porous and permeable, the natural resource may be exploited through wells drilled into the reservoirs. Petroleum reservoirs may be complex in nature, with physical properties that exhibit high degrees of anisotropy and heterogeneity. Petroleum ranges in character from heavy, highly viscous, slightly compressible crude oil to low density, low viscosity, highly compressible gas. During the exploitation process, the equilibrium state of the reservoir is disturbed by the reduction of fluid pressure in the producing well bores and by the re-introduction of various fluids via injection wells. This disturbance in equilibrium causes the reservoir fluids to move though the reservoir according to complex flow patterns that are dictated by both the governing physical laws and the reservoir and fluid properties.

Petroleum reservoirs often contain fractures that alter the manner in which fluid is transported through the reservoir, and the way that the reservoir responds to disturbances in the pressure field. Fractures provide conduits along which fluids can flow with relative ease. The porous and permeable rock matrix becomes fragmented when these fractures are interconnected to form networks. In such reservoirs, the fracture networks provide the pathways for bulk transport of fluids across the reservoir, while the matrix blocks provide the storage space for the fluids. This concept is often referred to as the 'dual porosity' model.

The presence of fracture networks adds considerable complexity to the process of modelling fluid flow, as the reservoir comprises two coupled systems with different characteristics. This is particularly true when the reservoir contains compressible gas and when the matrix material has a low value for permeability, resulting in the need to model nonlinear effects and transient behaviour. Understanding and predicting the behaviour of such a reservoir is further complicated when the blocks of rock matrix vary in shape and size.

Numerical simulation is an important tool used in the petroleum industry throughout the life of a reservoir for managing the exploitation of these natural resources. There is a continual drive to maximise the profits from producing reservoirs, and in recent years the industry's ability to improve definition of subsurface geology has increased greatly due to advances in seismic technology. These two factors have respectively lead to a need for, and the ability to achieve, a higher level of precision in the dynamic modelling of reservoirs. In this study, a numerical simulator has been developed based on the finite element method. This approach permits the achievement of higher order approximations and improvements in domain description, when compared with commonly used finite difference methods.

The dual porosity problem is usually solved numerically by constructing two overlapping simulation grids (Aziz and Settari, 1979), representing the matrix and fracture networks respectively, which are linked via the transfer function. In this thesis a new approach is developed in which finite element methods are utilised to reproduce the flow of highly compressible fluid to and from matrix blocks for any prevailing flow regime, including that of transient behaviour. This is achieved by first transforming each representative matrix block to one dimension. This one-dimensional representation is then modelled with a sequence comprising any number and type of one-dimensional finite elements. The fracture network in turn is represented by a two-dimensional mesh in which the nonlinear governing equations for fully compressible fluid are solved with a finite element method.

1.2 Objectives and motivation

The primary objective of the research undertaken in preparation of this thesis has been to study the behaviour of highly compressible fluid flow in fractured reservoirs and to develop a suitable numerical modelling process in the context of the finite element method.

Expulsion of gas from matrix blocks into fractures can occur under conditions that are transient in nature, the effects of which may continue for long periods, particularly when the rock matrix material has low permeability. This may have an important influence on the accuracy of production forecasts, if not fully accounted for. This work was motivated by the desire to determine the conditions under which it is important to include such transient behaviour in the modelling process, and to determine the consequences of not doing so. This lead to the objective of developing a modelling procedure that could be applied to a wide spectrum of practical reservoir engineering problems. Reservoir variables that have been explicitly dealt with in this study include the size, geometric shape and physical properties of the blocks of matrix material, and the physical properties of the fracture network.

The finite element method has several characteristics that are attractive for the modelling of petroleum reservoirs. In particular, the inherent flexibility with which the domain can be subdivided, or meshed, allows greater definition of the reservoir in the vicinity of wells, where knowledge of the physical domain is greatest, and where the most rapid dynamic changes occur. The finite element method is therefore very suitable for modelling the fracture network. In addition, as shown in later chapters of this thesis, matrix blocks can be reduced to one-dimensional representations to which the finite element method can be conveniently applied. Finally, the ability of the finite element method to accommodate a large variety of element types in a common model, such as the use of one dimensional elements to model an explicit fracture in a two dimensional continuum of porous medium, has provided a strong motivation to develop a numerical simulator based on the finite element method.

1.3 Layout of thesis

Subsequent chapters of this thesis deal respectively with the governing equations, the finite element formulation, numerical results, a case study, and conclusions.

In the first part of Chapter 2, the general equations governing flow of multi-component, multi-phase fluids through a multi-dimensional porous and permeable reservoir are derived and discussed. The limitations of the empirical laws are investigated. The specific problem of single phase gas flow in a reservoir that may be anisotropic and heterogeneous is given special attention. The compressibility of gas results in governing equations that are nonlinear and therefore particularly challenging to solve. The different forms of the governing equations currently in use in the industry are discussed, and the implications of making simplifying assumptions to facilitate solution of the equations are investigated.

In the second part of Chapter 2, the equations governing flow of gas through fractures are discussed, beginning with flow through a single fracture and ending with a set of equations governing the flow through the fractured reservoir as a whole. The study of flow through a single fracture approximated by a smooth walled slit is important, as it is this process that served as the basis for expressions commonly used in industry to describe the permeability of the fracture continuum. The limitations of these expressions are discussed in some detail via an analysis of the influences of friction, turbulence, fluid type, and through a literature survey. It is shown that the estimation of a fracture network permeability from the theoretical analysis of individual fractures can lead to greatly varying results.

This is followed by a statement of the equations governing flow through a fracture network continuum by drawing an analogy between the porous and permeable rock on a small scale and the fracture network continuum on a large scale. The final section of Chapter 2 is a discussion in the form of a literature survey on the combined model of the fracture network and imbedded blocks of porous and permeable matrix. Special attention is given to the transfer function linking the two systems. The different analytical transfer functions that have been developed for both pseudo-steady state and transient flow conditions, and their limitations, are discussed. Alternative methods to the analytical transfer function are cited. This discussion leads to the conclusion that analytical transfer functions are either impractical or inaccurate for full field simulation of systems that contain highly compressible fluids, or which are dominated by transient effects.

Chapter 3 commences with a literature survey on the use of finite elements for solving fluid flow problems in porous and in fractured media in general. This is followed by the development of the finite element algorithms implemented in the simulation program. The two-dimensional primary mesh representing the fracture network is coupled to a large number of individual one-dimensional secondary meshes, each representing a group of matrix blocks. During a time step, nonlinear equations are solved iteratively within each of the coupled systems. The set of algorithms developed for this purpose represents an innovative use of the finite element method, and the manner in which this has been accomplished is expounded upon in the second part of Chapter 3. These algorithms have been implemented in a computer program developed specifically for this purpose during the course of this research. Chapter 3 concludes with a description of the computer program.

Numerical results of the implementation of the modelling concepts developed in Chapters 2 and 3 are presented in Chapter 4. In the first part, model results are presented with the aim of verifying the numerical simulator. For this purpose, a single porosity approach is used and a number of models constructed for which analytical solution techniques are possible. The latter include material balance, steady state linear flow calculations, and the analytical solution to the radial diffusivity equation for both transient and pseudo-steady state behaviour. Additionally, numerical results are verified through a process of successive refinement of the model in time and space.

In the second part of Chapter 4, the results of a detailed investigation into the performance of individual matrix blocks are discussed. The aim has been to identify and verify the limitations of the modelling concept, the algorithms and the computer code discussed in Chapter 3. Numerical results are compared to the results of analytical calculations where possible, and to results obtained from finely meshed two-dimensional simulations. The question of transience is given special attention, as the ability to accurately replicate transient effects occurring in matrix blocks during the full field simulation of highly compressible fluid is a new development. Particular attention is also given to matrix block geometry as the correct population of the finite element mesh allows information of the two-dimensional geometry to be captured in the one-dimensional model. This provides a new, practical way to incorporate matrix geometry into a full field simulation model.

In the final section of Chapter 4 the numerical results of the modelling of a simple, fractured reservoir are discussed. The aim is to demonstrate that the two systems describing the fractures and matrix block can be coupled successfully. The effects of varying matrix permeability and matrix block size, shape and orientation on the full field simulation results, are investigated. The variety of problems addressed during the course of the work reported in Chapter 4 has lead to an improved understanding of the performance of a fractured reservoir. These observations are summarised in the final section of Chapter 4 in the form of a classification of fractured reservoirs according to recommended modelling approaches.

A case study of a naturally fractured, low permeability carbonate reservoir is presented in Chapter 5. This has involved assimilating existing geological descriptions and information into a full field simulation model in a format suitable for analysis using the techniques and computer software reported on in previous chapters. The aim of this work has been to demonstrate the practicality of the simulation methods and to gain new insight into the behaviour of the reservoir. In addition to the dual porosity aspects, the practicality of using a highly refined mesh to explicitly model the well bore in a full field simulator is evaluated. The simulation model has been history matched against production and pressure data spanning one year of the reservoir's life. Additionally, a reservoir evaluation well test has been replicated using the simulator. The chapter is concluded with a list of observations about the reservoir made during the history matching process.

In the final chapter, conclusions are drawn on the work and results presented in this thesis. Some recommendations for future work are also made.

CHAPTER 2

THE GOVERNING EQUATIONS

This chapter is divided into two parts, dealing with nonfractured and fractured reservoirs respectively. Section 2.1 begins with a statement of a general set of conservation equations describing the flow of fluids through a porous, but not fractured, medium. This is accompanied by a discussion of the components of the equations and the underlying assumptions, followed by a derivation of the equations themselves. The simplifying assumptions for the specific problem dealt with in this thesis are discussed. In Section 2.2, the reservoir model is extended to include fractures. This begins with a discussion on the physics governing the flow of fluids through individual, discrete fractures, and of various simplifying assumptions. The interaction between an individual fracture and porous matrix material is considered, and is followed by the development of a continuum theory. The equations that are eventually taken forward for implementation in the finite element program are summarised.

2.1 Fluid flow through a porous medium

2.1.1 General equations for multi-dimensional, multi-phase flow

In his historical review paper, de Boer (1992) described the efforts of pioneers of the theory of flow of fluid through porous media, initiated in the late eighteenth century by Reinhard Woltman, and the subsequent development of the subject to the present day. De Boer reported important contributions made during the nineteenth century by Adolf Fick, Henri Darcy and Joseph Stefan. In the twentieth century, the theory was further refined by Paul Fillunger, Karl von Terzaghi and Maurice Biot.

Reinhard Woltman, who was the harbour director in Hamburg, introduced the concept of volume fraction in his work on mud (Woltman, 1794), which ultimately led to the concept of porosity. In 1856 Henri Darcy published a detailed account of the work which he had carried out in his position as engineer responsible for the water works of the French town of Dijon. He had conducted numerous experiments with sand filters from which he deduced an empirical relation that is widely used today in many aspects of reservoir engineering. Paul Fillunger (1883 to 1937), first professor at the Technological Gewerbemuseum in Vienna, pioneered the porous media theory of liquid saturated porous solids, and developed theories dealing with capillary forces (Fillunger, 1934). He also investigated the friction forces involved with the flow of liquid through a porous medium. Karl von Terzaghi (1883 to 1963), professor at the Technische Hochschule of Vienna, was the first author to treat a deformable porous solid with an inviscid fluid, namely water saturated clay. He published a book (von Terzaghi, 1925) on the settlement of clays, which is regarded as the first comprehensive text on soil mechanics.

Muskat (1949) applied the science of fluid flow through porous media to the petroleum industry, and developed an understanding of the mechanisms that drive oil and gas reservoirs. Biot (1941, 1955) studied the effects of consolidation of porous media. He expanded on the work of von Terzaghi to include viscoelastic anisotropic porous solids. His work culminated in two important papers (1956a and b) which summarised the pool of knowledge available at that time. Subsequently, Bedford and Drumhellen (1983) produced a review paper dealing with all findings up to 1983.

The study of fluid flow through porous media has been augmented by a large number of researchers who over the years have contributed to the theory currently in use. This work has lead to a general set of equations which govern the flow of multi-component, multi-phase fluids through a multi-dimensional porous medium. This set of equations is given by

$$\sum_{p=1}^{n_p}\nabla\cdot\left(\rho_p y_{c,p}\frac{kk_{rp}}{\mu_p}\left(\nabla P_p+\rho_p g\nabla D\right)\right)=\sum_{p=1}^{n_p}\left(\frac{\partial}{\partial t}\left(\phi\rho_p y_{c,p}S_p\right)\right)+q_c\text{, for } c=1 \text{ to } n_c, \qquad (2.1)$$

in which p is the phase index, n_p is the number of phases, c is the component index, n_c is the number of components, $y_{c,p}$ is the fraction of component c in phase p, ρ_p is the density of phase p, $\boldsymbol{k}$ is the permeability tensor, k_{rp} is the relative permeability to phase p, μ_p is the viscosity of phase p, P_p is the pressure of phase p, g is gravitational acceleration, D is the height above some datum, ϕ is the porosity, S_p is the saturation of phase p, and q_c is a source (positive) or sink (negative) term. The (n_c) equations (2.1), which include both viscous and gravity forces, contain ($n_c n_p+2n_p$) unknowns. To equations (2.1) must be added the following constraints:

- Phase constraint: $\sum_{c=1}^{n_c} y_{c,p}=1$ n_p equations (2.2)
- Saturation constraint: $\sum_{p=1}^{n_p} S_p=1$ 1 equation (2.3)
- Capillary pressure: (n_p-1) equations (2.4)
- Phase equilibrium relationships: $(n_c(n_p-1))$ equations (2.5)

Equations (2.2) to (2.5) represent ($n_c n_p+2n_p$) equations with ($n_c n_p+2n_p$) unknowns.

2.1.2 Discussion of terms

Components and phases. The term 'phase' is used to distinguish the physical states of water, oil and gas as they occur in the reservoir. Components are the constituents of these phases, for example methane, ethane, water, etc. The component methane may, for example, be present in all three of the physical phases. The component water occurs predominantly in the water phase, but may also occur in, for example, the gas phase. As the pressure and temperature of the reservoir change, so components can move from one phase to another. Conservation of mass pertains to the components while Darcy's law governs the movement of the physical phases, and by implication, all the components held within that phase at the time. An equation of state (EOS) is needed to describe thermodynamic equilibrium and to ascertain what proportion of each component occurs within each of the phases in the reservoir under the prevailing local conditions.

Porosity, saturation and compressibility. Porosity is defined by expression (2.6) as the ratio of the total volume of pore space, to the bulk volume of rock. It is a property of the reservoir rock and can vary in value across the reservoir. There is generally some relationship between porosity and permeability that depends on the type of rock from which the reservoir is formed. Porosity is indirectly a function of time via its pressure dependence. The saturation of a phase is defined simply as that fraction of the pore volume that is occupied by the phase. Fractional porosity ϕ, and saturation S_p of phase p, are given by

$$\phi = \frac{V_\phi}{V_b}, \text{ and } S_p = \frac{V_p}{V_\phi}, \text{ with } V_b = V_r + V_\phi, \text{ and } V_\phi = \sum_{p=1}^{n_p} V_p, \tag{2.6}$$

in which V_b is the bulk, or total volume, V_r is the volume occupied by the rock skeleton, V_ϕ is the volume occupied by the pore space, and V_p is the volume occupied by phase p. From this definition, it follows that

$$\sum_{p=1}^{n_p} S_p = 1. \tag{2.7}$$

Compressibility of a non-porous material is defined (Zimmerman, 1991) by

$$c = -\frac{1}{V}\frac{\partial V}{\partial P}, \tag{2.8}$$

in which V is the volume of the body and P is the hydrostatic pressure exerted on its outer surface. A porous reservoir experiences pressure exerted by the saturating fluid, P_{fl}, and by the mass of rock overlying the reservoir, the overburden, or confining pressure, P_c. A changes in either pressure affects the bulk volume V_b, and the pore volume V_ϕ. Four compressibilities can consequently be defined (Zimmerman *et. al.*, 1986),

$$c_{b,c} = -\frac{1}{V_b}\frac{\partial V_b}{\partial P_{fc}}, \quad c_{b.fl} = -\frac{1}{V_b}\frac{\partial V_b}{\partial P_{fl}}, \quad c_{\phi,c} = -\frac{1}{V_\phi}\frac{\partial V_\phi}{\partial P_c} \text{ and } c_{\phi.fl} = -\frac{1}{V_\phi}\frac{\partial V_\phi}{\partial P_{fl}} \tag{2.9}$$

in which $c_{b.c}$ and $c_{b,fl}$ are the compressibilities of the bulk reservoir volume with respect to changes in confining and fluid pressures respectively, and $c_{\phi.c}$ and $c_{\phi,fl}$ are likewise the compressibilities of the pore volume with respect to changes in the confining and fluid pressures respectively. Of these, the compressibility term that is by far the most significant for the purposes of modelling fluid flow in reservoirs, is that which deals with change in the pore volume as fluid pressure is altered, i.e. $c_{\phi.fl}$. Henceforth in this thesis, $c_{\phi.fl}$ will be referred to simply as the rock compressibility, c_r, and the fluid pressure will be referred to simply as the pressure P.

The rock compressibility can also be written in the form

$$c_r = -\frac{1}{V_\phi}\frac{\partial V_\phi}{\partial P} = +\frac{1}{\phi}\frac{\partial \phi}{\partial P}, \tag{2.10}$$

so that

$$\phi = \phi_0 \, exp\big(c_r(P - P_0)\big). \tag{2.11}$$

Fluid compressibility c_{fl} is defined in a similar way to the general equation (2.8); that is,

$$c_{fl} = -\frac{1}{V}\frac{\partial V}{\partial P} = +\frac{1}{\rho}\frac{\partial \rho}{\partial P}. \tag{2.12}$$

It follows that

$$\rho = \rho_0 \, exp\left(c_{fl}\left(P - P_0\right)\right), \text{ or} \tag{2.13a}$$

$$P = P_0 + \frac{1}{c_{fl}} ln\left(\frac{\rho}{\rho_0}\right), \tag{2.13b}$$

where P_0 and ρ_0 are the pressure and density at some datum.

As a general rule, the compressibility of gas may be 10 to 100 times greater than the rock compressibility and consequently has a far greater effect on the performance of a reservoir.

Absolute and relative permeability. The absolute permeability (k) is considered to be a property of the reservoir rock and is believed to be largely independent of the type of fluid present in the reservoir. In the natural reservoir environment, permeability may be very heterogeneous, far more so than porosity, and may span several orders of magnitude in value in a single reservoir. Permeability may be strongly anisotropic and direction dependent, in which case it is represented by a second-order tensor. Permeability as defined by Darcy is adequate for describing flow of a single-phase fluid through a porous medium. When more than one phase is present, however, competition for occupancy of the pore spaces ensues. For a given potential gradient, the velocity of a particular phase in the presence of other phases is less than what it would be if that phase alone had occupied the pore spaces. This has led to the concept of phase relative permeability, denoted k_{rp} , which is a function of the saturation of the phase and ranges in value between 0 and 1.

Pressure, capillary pressure and gravity. Hydrocarbon reservoirs are normally in a state of thermodynamic and hydrostatic equilibrium prior to the commencement of production. The fluids are naturally segregated according to chemical potential, density and surface tension. The vertical pressure gradient within any phase is then a function of the density of the phase at reservoir conditions. At any point in the reservoir the saturation values of the phases are controlled by their relative densities and by capillary pressure effects. Capillary pressure curves, usually derived in the laboratory, reduce the number of unknowns in equations (2.1) as they offer a relationship between phase saturation and elevation in the reservoir.

Source and sink terms. The source and sink terms relate to injection and production respectively. While petroleum is being extracted via production wells, water and gas may be injected into the reservoir as a means of maintaining the pressure, sweeping the reservoir fluids towards the producing wells or disposing of unwanted fluids.

Phase equilibrium relationships. These expressions range in complexity from a simple relationship between pressure and the gas-oil ratio to sophisticated thermodynamic equations.

2.1.3 Background to the general equations

The governing equation for single-phase compressible flow is derived by combining an equation of continuity with an equation of motion and including an expression for compressibility. The equation of motion is Darcy's law which is empirical in nature, and for which different formulations are possible. In particular, alternatives to the definition of potential in Darcy's law are discussed in this section. The general equations (2.1) are obtained by extending the single-phase equation to multiple phases and dimensions.

The equation of continuity: mass balance. The mass balance equation is given by

$$-\nabla \cdot (\rho \boldsymbol{u}) = \frac{\partial}{\partial t}(\rho \phi) + q . \tag{2.14}$$

The equation of motion: Darcy's Law. Darcy formulated an empirical law relating potential gradient to fluid velocity by performing experiments on gravel packs for the purpose of sizing filters for purification of water. Subsequently, various other workers have extended Darcy's experiments by considering different types of fluids, different porous media and different orientations of the experimental apparatus with respect to the gravitational field. These experiments ultimately led to the equation relating the velocity of the fluid to the potential gradient, in the form (Schreidegger, 1957, Collins, 1961, Dake, 1978)

$$\boldsymbol{u} = -\frac{\boldsymbol{k}\rho}{\mu} \nabla \Phi , \tag{2.15}$$

where Φ is the fluid potential. The constant of proportionality incorporates effects of the type of fluid being used (ρ and μ) and the nature of the porous medium ($\boldsymbol{k}$). This potential has dimensions of potential energy per unit mass. The potential of a fluid (compressible or incompressible) moving under the influences of a pressure gradient and gravity has been accepted by the petroleum industry (Schreidegger, 1957, Collins, 1961, Dake, 1978) as

$$\Phi = \int \frac{dP}{\rho} + gD . \tag{2.16}$$

By incorporating this expression for fluid velocity potential into Darcy's law (2.15), we get

$$\boldsymbol{u} = -\frac{\boldsymbol{k}\rho}{\mu} \nabla \left(\int \frac{dP}{\rho} + gD \right) . \tag{2.17}$$

Because density is either independent of pressure (in the case of an incompressible fluid), or is a single-valued function of the pressure (in the case of a compressible fluid),

$$\nabla \int \frac{\partial P}{\rho} = \frac{1}{\rho} \nabla P . \tag{2.18}$$

By inserting expression (2.18) into (2.17), we obtain

$$\boldsymbol{u} = -\frac{\boldsymbol{k}}{\mu} (\nabla P + \rho g \nabla D) . \tag{2.19}$$

Darcy's empirical law has been accepted in the form presented above for both compressible and incompressible fluid flow through years of use in the industry.

The governing equations. If the equation of motion (2.19) is combined with the mass balance equation (2.14), this leads to the equation

$$\nabla \cdot \left(\frac{\rho k}{\mu} (\nabla P + \rho g \nabla D) \right) = \frac{\partial}{\partial t}(\rho \phi) + q \, . \tag{2.20}$$

The first term on the righthand side of equation (2.20) can be rewritten as

$$\begin{aligned} \frac{\partial}{\partial t}(\rho\phi) &= \phi \frac{\partial \rho}{\partial t} + \rho \frac{\partial \phi}{\partial t} \\ &= \phi \left(\frac{\partial \rho}{\partial P} \frac{\partial P}{\partial t} \right) + \rho \left(\frac{\partial \phi}{\partial P} \frac{\partial P}{\partial t} \right) \\ &= \left(\phi \rho c_{fl} + \rho \phi c_r \right) \frac{\partial P}{\partial t} \\ &= \rho \phi c_t \frac{\partial P}{\partial t} \, , \end{aligned} \tag{2.21}$$

where c_t is the total compressibility, defined by

$$c_t = c_{fl} + c_r \, . \tag{2.22}$$

Equation (2.20) can therefore be written as

$$\nabla \cdot \left(\frac{\rho k_m}{\mu} (\nabla P + \rho g \nabla D) \right) = \rho \phi_m \left(c_{fl} + c_m \right) \frac{\partial P}{\partial t} + q \, , \tag{2.23}$$

where the subscript m has been included to emphasise that the properties relate to the rock matrix (as opposed to the fracture network). Equation (2.23) fully describes isothermal flow of single-phase fluid through a porous and permeable formation under the influences of a pressure gradient and gravity.

Discussion of the fluid potential in Darcy's Law. Although Darcy's law in the form described by equations (2.15) to (2.19) is widely accepted, there is an alternative definition of the potential that leads to a governing equation that differs from (2.23) when the fluid is compressible. Scheidegger (1957, p60) discussed the difficulty of defining Darcy's law and the corresponding 'velocity potential', for a heterogeneous reservoir when the empirical equations were based on laboratory experiments. He cited the work done by Gardner, Collier and Farr (1934) in which the conventional form of Darcy's law (2.15) was questioned. Due to the difficulty in performing experiments on non-homogeneous media in the laboratory, they argued that an equation of the form

$$\mathbf{u} = -\rho \nabla \left(\frac{k \Phi}{\mu} \right) , \tag{2.24}$$

may be more appropriate. An implicit assumption in Darcy's potential (2.16) is that the process is isothermal, justified by the large heat capacity of the reservoir rock. In the extreme case where no exchange of energy takes place between the rock skeleton and the fluid, the potential takes on the form

$$\Phi_c = \frac{P}{\rho} + gD \, . \tag{2.25}$$

The use of expression (2.25) introduces an additional term, $c_{fl} P$, into the governing equation (2.23) which then becomes

$$\nabla\cdot\left(\frac{\rho k}{\mu}\left(\left(1+c_{fl}P\right)\nabla P+\rho g\nabla D\right)\right)=\phi\rho c_t\frac{\partial P}{\partial t}+q\,. \qquad (2.26)$$

For real gas, the value of this term may be in the order of 0.3, which is significant. (The term has a value of 1 for ideal gas.) For water and oil, the term takes on values in the order of 0.01 and 0.05 respectively and can safely be ignored.

Multiple phases and components. Consider the case in which multiple phases that contain multiple components flow through the porous medium. Mass balance applies to components, and for component c, the mass balance equation (2.14) becomes

$$-\nabla\cdot\left(\rho_c\boldsymbol{u}_c\right)=\frac{\partial}{\partial t}\left(\rho_c\phi_c\right)+q_c\,. \qquad (2.27)$$

The first term in brackets on the lefthand side of this expression can be written as

$$\rho_c\boldsymbol{u}_c=\sum_{p=1}^{n_p}y_{c,p}\rho_p\boldsymbol{u}_p\,. \qquad (2.28)$$

Likewise, the first term in brackets on the righthand side of equation (2.31), can be written as

$$\rho_c\phi_c=\sum_{p=1}^{n_p}\rho_p y_{c,p}\phi_p=\sum_{p=1}^{n_p}\rho_p y_{c,p}\phi S_p\,. \qquad (2.29)$$

Darcy's equation (2.15) applies to physical phases, and therefore, for phase, p, becomes

$$\boldsymbol{u}_p=\frac{-kk_{rp}}{\mu_p}\left(\nabla P_p+\rho_p g\nabla D\right). \qquad (2.30)$$

Pressure, density and viscosity are all phase properties, indicated with the subscript p. In addition, permeability is here no longer a property of the medium alone and the effective permeability is the product of the absolute ($\boldsymbol{k}$) and the relative permeability (k_{rp}). By combining equations (2.27) to (2.30), the required set of equations (2.1), is obtained.

2.1.4 Simplifying assumptions

Three special cases of simplified versions of equations (2.1) dealing with single-phase, two-phase immiscible and two-phase miscible flow respectively, are described. Mention of multi-phase flow is made here as many of the issues surrounding dual porosity modelling described later in this thesis have come from the study of multi-phase flow.

Single-phase, single component. If a single fluid phase flows through the medium, equations (2.1) simplify to the equation (2.20) derived in the previous section. If gravity is ignored, and if it is assumed that the reservoir is homogenous, isotropic and incompressible, that the fluid viscosity remains constant and if the source-sink term is ignored, then equation (2.20) becomes

$$\nabla\rho\cdot\nabla P+\rho\nabla^2 P=\frac{\phi\mu}{k}\frac{\partial\rho}{\partial t}\,. \qquad (2.31)$$

If the definition of fluid compressibility (2.12) is incorporated into (2.31) and the terms are rearranged, then (Bai and Roegiers, 1994)

$$c(\nabla P)^2 + \nabla^2 P = \frac{\phi \mu c}{k}\frac{\partial P}{\partial t}. \tag{2.32}$$

From Darcy's law (2.19) without the gravity term, it follows that

$$\nabla P = -\frac{\mu}{k}\boldsymbol{u}. \tag{2.33}$$

By substituting this expression for one of the terms in the nonlinear part of equation (2.32) and re-arranging, we get

$$\left(\frac{k}{\phi c \mu}\right)\nabla^2 P - \left(\frac{1}{\phi}\right)\boldsymbol{u}\cdot\nabla P = \frac{\partial P}{\partial t}. \tag{2.34}$$

This is the convection–diffusion equation with the first term on the lefthand side representing diffusion and the second term represents convection. The Peclet number Pe is defined by

$$Pe = \frac{c\mu}{k}. \tag{2.35}$$

For a value of Pe less than 1, diffusion dominates and the equation is parabolic in nature. For a value of Pe greater than 1, convective transport dominates and the equation is hyperbolic. Petroleum exhibits a negative correlation between compressibility and viscosity, so that the permeability is the dominant factor controlling the value of Pe. The latter can vary between 0.001 and 1000 so that both transport modes are common in petroleum reservoirs.

The nonlinear term, $(\nabla P)^2$ in equation (2.34) is very often ignored, which amounts to ignoring the convective transport component. This is often justified by the assumption of a 'low compressibility' fluid, implemented by taking the density out of the divergence operand in equation (2.20). Much of the work done on fractured reservoirs, particularly of an analytical nature, ignores the nonlinear terms. Difficulties in explaining the behaviour of fluid flow through fractured reservoirs may in part be attributable to this omission. Fractured reservoirs are often characterised by matrix rock with very low permeability, which plays a dominant role in determining the degree of nonlinearity of the problem.

Finally, for the flow of an incompressible fluid, equation (2.34) simplifies to Laplace's equation,

$$\nabla^2 P = 0. \tag{2.36}$$

Two-phase immiscible displacement. The immiscibility constraint dictates that the components and phases are identical and the phase equilibrium relationships become

$$y_{c,p} = 1 \text{ for } c = p \text{ and } y_{c,p} = 0 \text{ for } c \neq p. \tag{2.37}$$

Equations governing the flow of co-existing oil (subscript o) and water (subscript w) are

$$\nabla\cdot\left(\rho_{o,w}\frac{kk_{ro,rw}}{\mu_{o,w}}\left(\nabla P_{o,w} + \rho_{o,w} g \nabla D\right)\right) = \frac{\partial}{\partial t}\left(\phi \rho_{o,w} S_{o,w}\right) + q_{o,w}, \tag{2.38}$$

in which P_o, P_w, S_o and S_w are unknowns. Additional equations required to solve for these unknowns are

- Saturation constraint: $S_w + S_o = 1$ (2.39)
- Capillary pressure equation: $P_c = P_o - P_w$ (2.40)

Gravity and capillary pressure are important physical processes in this type of problem.

Two-phase miscible displacement. During the miscible displacement of one fluid phase by another, the exchange of components between phases can take place. The capillary pressure term is often ignored as the surface tension between the two miscible phases is generally small. The simplified case of two phases (gas and oil as they occur in the reservoir) with two components (gas and oil as they occur at surface) is considered here. Equations (2.1) then become

$$\nabla \cdot \left(\rho_o y_{o,o} \frac{kk_{ro}}{\mu_o} \left(\nabla P_o + \rho_o g \nabla D \right) \right) + \nabla \cdot \left(\rho_g y_{o,g} \frac{kk_{rg}}{\mu_g} \left(\nabla P_g + \rho_g g \nabla D \right) \right)$$
$$= \frac{\partial}{\partial t} \left(\phi_o \rho_o y_{o,o} S_o \right) + \frac{\partial}{\partial t} \left(\phi_g \rho_g y_{o,g} S_g \right) + q_o \qquad (2.41)$$

for the oil component, and

$$\nabla \cdot \left(\rho_o y_{g,o} \frac{kk_{ro}}{\mu_o} \left(\nabla P_o + \rho_o g \nabla D \right) \right) + \nabla \cdot \left(\rho_g y_{g,g} \frac{kk_{rg}}{\mu_g} \left(\nabla P_g + \rho_g g \nabla D \right) \right)$$
$$= \frac{\partial}{\partial t} \left(\phi_o \rho_o y_{g,o} S_o \right) + \frac{\partial}{\partial t} \left(\phi_g \rho_g y_{g,g} S_g \right) + q_g \qquad (2.42)$$

for the gas component. A set of relationships is required from which the values of the $y_{c,p}$ terms can be obtained.

2.2 Fluid flow through fractured reservoirs

In this section the fluid flow concepts developed in the first part of the chapter are extended to deal with reservoirs containing networks of fractures. The flow of fluids through an individual fracture is addressed first by idealising the fracture as a smooth-walled slit. The equations describing flow of a viscous, compressible fluid are discussed, as are complicating factors such as wall roughness and friction. This is followed by a discussion on the flow through a network of interconnected fractures. Finally, the porous medium and the fracture network theories are combined, and the flow of fluid through an interconnected fracture network in a porous and permeable matrix is addressed.

2.2.1 Flow through a single fracture: the slit approximation

This section begins with a definition of the problem in the form of a derivation of the governing equations, followed by a discussion of special cases and physical phenomena relating to the specific problem addressed in this thesis. The section is concluded with an historical overview.

Derivation of the governing equations

Consider the flow of fluid down the length of a fracture, represented by a long, narrow slit of width w, height h and length l with the selection of coordinates shown in Figure 2.1. The flow of fluid is described by the equation of continuity (the mass balance equation), and by an equation of motion (the momentum balance equation, which is analogous to Darcy's law for the flow through a porous medium). Typically, in a fractured reservoir, the width of the slit would be in the order of 1mm or less, the height perhaps 1m and the length, perhaps 100m. Due to vast differences in the three dimensions of the fracture, the boundary conditions that most strongly influence the behaviour of the fluid are determined by the width of the slit, rather than by the height and length. The physics of this process is described by Newton's law of viscosity, discussed in the first part of this section.

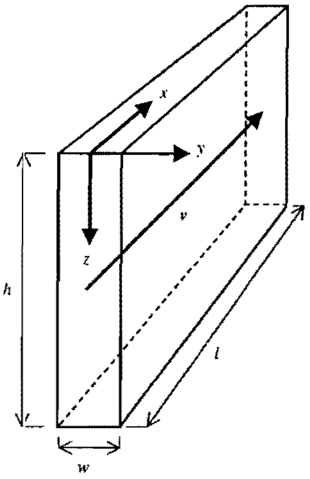

Figure 2.1: *Representation of a single fracture by a slit.*

The equation of continuity: mass balance. The derivation of the mass balance equation for the flow of fluid in a single slit follows the same route as that for flow through a porous medium (with the difference that the porosity of the slit has a constant value equal to 1). The resulting equation, analogous to equation (2.14), is therefore

$$-\nabla\cdot(\rho v)=\frac{\partial\rho}{\partial t}+q\,. \tag{2.43}$$

The source-sink term, q, may represent the gain of fluid from, or loss of fluid to, the surrounding porous rock matrix.

Viscosity of a Newtonian fluid. The behaviour of petroleum can adequately be approximated by that of a Newtonian fluid. For fluid flowing down the length of a slit as illustrated in Figure 2.1, the two components of stress of significance are the shear stress $\tau_{yx}(x,y,t)$, exerted in the x-direction on a fluid surface of constant y, given by (Bird, Stewart and Lightfoot, 1960),

$$\tau_{yx}(x,y,t)=-\mu\frac{\partial v_x(x,y,t)}{\partial y}, \tag{2.44}$$

where μ is the fluid viscosity and $v_x(x,y,t)$ is the velocity of the fluid in the x- direction, and the normal stress $\tau_{xx}(x,t)$ acting in the x-direction on a surface perpendicular to the x-axis, given by (Bird, Stewart and Lightfoot, 1960, p79; and Lai, Rubin and Krempl, 1993, p401)

$$\tau_{xx}(x,t)=-\left(\frac{4}{3}\mu+\kappa\right)\frac{\partial v_x(x,y,t)}{\partial x}, \tag{2.45}$$

where κ is the bulk viscosity.

The equation of motion: momentum balance. Momentum balance is given by the Navier-Stokes equation (Bird, Stewart and Lightfoot, 1960, p78)

$$\frac{\partial}{\partial t}(\rho v) = -\nabla \cdot \rho v v - \nabla \cdot \tau - \nabla P + \rho g , \qquad (2.46)$$

where τ is the stress tensor, and $\rho v v$ is the convective momentum flux, which is the dyadic product of ρv and v. The component of this equation in the x-direction is

$$\frac{\partial}{\partial t}(\rho v_x) = -\frac{\partial}{\partial x}(\rho v_x^2) - \frac{\partial}{\partial x}(\tau_{xx}) - \frac{\partial}{\partial y}(\tau_{yx}) - \frac{\partial}{\partial x}(P) + \rho g_x . \qquad (2.47)$$

By combining equation (2.47) with (2.44) and (2.45), and assuming constant viscosity, we obtain

$$\frac{\partial}{\partial t}(\rho v_x) = \left(\frac{4}{3}\mu + \kappa\right)\frac{\partial^2 v_x}{\partial x^2} - \frac{\partial}{\partial x}(\rho v_x^2 + P) + \mu\frac{\partial^2 v_x}{\partial y^2} + \rho g_x . \qquad (2.48)$$

By re-arranging this and incorporating the mass balance equation (2.43) in which the source-sink term is ignored, we obtain

$$\rho\frac{Dv_x}{Dt} = \left(\frac{4}{3}\mu + \kappa\right)\frac{\partial^2 v_x}{\partial x^2} - \frac{\partial P}{\partial x} + \mu\frac{\partial^2 v_x}{\partial y^2} + \rho g_x , \text{ where} \qquad (2.49)$$

$$\frac{Dv_x}{Dt} = \frac{\partial v_x}{\partial t} + v_x\frac{\partial v_x}{\partial x} \qquad (2.50)$$

is the material derivative. This equation describes the laminar flow of a single-phase, compressible and viscous fluid subjected to the force of gravity and a pressure gradient, through a regular slit under isothermal conditions.

Some special cases of flow through a single slit

Steady state flow of viscous, incompressible fluid. If it is assumed that the gravitational forces can be ignored, the fluid is incompressible, the slit has constant width and the motion is steady state, then the velocity in the x-direction does not vary in space or time, and expression (2.47) can be simplified and integrated with respect to y to give

$$\tau_{yx}(y) = -y\frac{\partial P(x)}{\partial x} . \qquad (2.51)$$

If this is substituted into (2.44) and the resulting expression integrated with respect to y then

$$v_x(y) = \frac{y^2}{2\mu}\frac{\partial P(x)}{\partial x} + C . \qquad (2.52)$$

The integration constant C is eliminated by imposing the non-slip boundary condition that the x-direction velocity is zero where the fluid is in contact with the walls of the slit, namely

$$v_x\left(\pm\frac{w}{2}\right) = 0 . \qquad (2.53)$$

Hence,

$$v_x(y) = -\frac{\partial P(x)}{\partial x}\frac{w^2}{8\mu}\left(1 - \left(\frac{2y}{w}\right)^2\right) . \qquad (2.54)$$

The average velocity in the slit is determined by integrating the velocity over the cross sectional area of the slit and dividing by that area, to give

$$\langle v_x \rangle = \frac{1}{wh}\int_0^h \int_{-\frac{w}{2}}^{\frac{w}{2}} -\frac{\partial P(x)}{\partial x}\frac{w^2}{8\mu}\left(1-\left(\frac{2y}{w}\right)^2\right)dydz = -\frac{w^2}{12\mu}\frac{\partial P}{\partial x}. \tag{2.55}$$

If an analogy is drawn between this expression and Darcy's law (2.19) without the gravity term, then an expression for the permeability of a single fracture emerges which is

$$k_{fr} = \frac{w^2}{12}. \tag{2.56}$$

This is the equation commonly used for determining the 'permeability' of individual fractures. A fracture with a width of 1mm, would therefore have a 'permeability' of 83,000,000*10^{-15}m^2 (approximately 83,000,000mD). If the fracture spacing is say, 1m, then the porosity of the fracture network is approximately 0.1%. The macroscopic permeability of the fracture network, obtained by multiplying the permeability of a single fracture with the porosity, is therefore approximately 83000*10^{-15}m^2 (approximately 83000mD). Porous sandstone typically has a permeability of around 100*10^{-15}m^2 (approximately 100mD). Clearly the presence of fractures has a profound effect on the productivity of a reservoir.

Steady state flow of inviscid (ideal), compressible fluid. A limitation of the equations derived in the previous section is that they are restricted to incompressible fluids. If both the bulk and Newtonian viscosities are sufficiently low, the first term on the righthand side of equation (2.49) can be ignored. Then for steady state flow in which gravity and source terms are also ignored, Bernoulli's equation,

$$\int_{x_0}^{x} v_x \frac{\partial v_x}{\partial x}dx + \int_{x_0}^{x}\frac{1}{\rho}\frac{\partial P}{\partial x}dx = 0 = \frac{1}{2}v_x^2(x) - \frac{1}{2}v_x^2(x_0) + \int_{x_0}^{x}\frac{\partial P}{\rho}, \tag{2.57}$$

results. If the expressions for compressibility (2.13a) and (2.13b) are incorporated into this then the integration can be performed, leading to

$$v_x(x) = \sqrt{v_x^2(x_0) + \frac{2}{c\rho(x_0)}\left(exp\left(-c\left(P(x) - P(x_0)\right)\right) - 1\right)}. \tag{2.58}$$

Comparison between Darcy and Bernoulli flow. Bernoulli's equation shows that if a uniform pressure gradient exists along the length of the slit, the velocity of the fluid will increase as it moves along the slit under the influence of a uniform pressure gradient. This is contrary to what occurs when the fluid is governed by Darcy's law, which causes the fluid to move with a uniform fluid velocity in a uniform pressure gradient. Neither equation is altogether satisfactory. The permeability used in Darcy's law is dominated by the width of the slit as well as the viscosity, neither of which occurs in Bernoulli's equation. The velocity forecast by the use of Bernoulli's equation contains the effect of compressibility and density of the fluid, neither of which plays a role in Darcy's equation. The acceleration effect forecast by Bernoulli's equation becomes significant at high values of compressibility and when large pressure gradients prevail, as is the case in close proximity to gas wells.

The Forchheimer equation. The Bernoulli equation accounts for the acceleration that is caused by expansion of fluid as it moves from a high pressure location to one of lower pressure, a consequence of its compressibility, but has limited practical use due to the inherent assumption that the fluid is inviscid. In practical reservoir engineering, the effect of convective acceleration is dealt with through the application of the Forchheimer (1901) equation, which results in a modified version of Darcy's law (Dake, 1978)

$$\frac{\partial P}{\partial x}=-\frac{\mu}{k}v_v-\beta\rho v_x^2, \qquad (2.59)$$

where β is the coefficient of internal resistance and has dimensions of L^{-1}. The consequence of the additional term $-\beta\rho v_x^2$, often referred to as the 'non-Darcy' component, is that for a given pressure gradient, the fluid velocity is lower that that predicted by Darcy's equation. The value of β must be determined experimentally. Dake (1978) showed experimental evidence demonstrating that the value of β is a function of absolute permeability.

A comparison between predictions made using the Darcy and the Forchheimer equations respectively, of the relationship between pressure gradient and fluid velocity, is shown in Figure 2.2. Two values of permeability have been considered, a high value of $1*10^{-12}m^2$, with the corresponding value for β of $4.5*10^7m^{-1}$, and a low value of $1*10^{-15}m^2$, with the corresponding value for β of $9*10^{10}m^{-1}$. The values of β were obtained from Dake (1978. p259, Figure 8.8). It is evident that the Forchheimer effect results in a greater pressure gradient being required for a given velocity and that this effect only becomes significant at high velocities. Pressure gradients in petroleum reservoirs are unlikely to exceed values of around 10MP/m, except possibly in close vicinity to wells. In low permeability reservoirs the velocities are unlikely to reach levels where the Forchheimer effect needs to be considered, while in high permeability reservoirs, the velocities may attain values that require the Forchheimer effect to be considered.

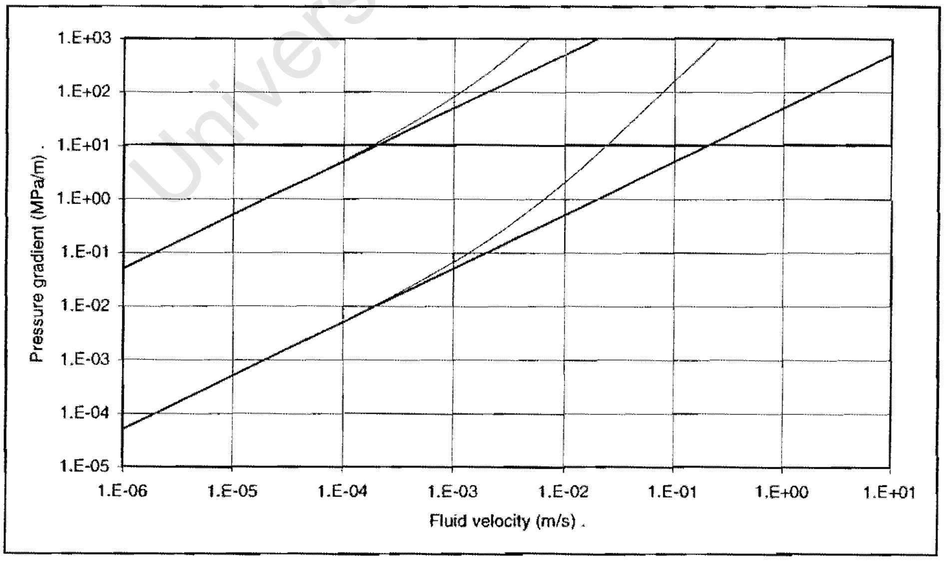

Figure 2.2: *Relationship between one-dimensional pressure gradient and fluid velocity predicted by the Darcy equation (bold curves) and by the Forchheimer equation (thin curves). The two pairs of curves presented are for permeability values of $1*10^{-15}m^2$ (upper pair) and $1*10^{-12}m^2$ (lower pair).*

Steady state flow of a viscous, compressible fluid. For steady state flow in which the gravity term is ignored, assuming that the pressure, and hence the density, are functions of x only, and assuming also that the viscosity is a constant, the equation of motion (2.48) becomes

$$\left(\frac{4}{3}\mu+\kappa\right)\frac{\partial^2 v_x}{\partial x^2}-\frac{\partial}{\partial x}\left(\rho v_x^2+P\right)+\mu\frac{\partial^2 v_x}{\partial y^2}=0. \tag{2.60}$$

The use of this expression would provide an accurate estimate of the behaviour of compressible fluid flowing along a smooth-walled slit under steady state conditions. However, this version of the Navier-Stokes equation is computationally challenging to solve and the improved accuracy afforded by the use of this more rigorous description of the problem is unlikely to justify the extra effort required to obtain a solution. This view is supported by the fact that two important additional physical phenomena, namely turbulence and friction, are not addressed by this formulation.

Turbulence. In this section, the transition between laminar and turbulent flow is examined for a smooth-walled slit. The dimensionless Reynold's number for a slit (Bird, Stewart and Lightfoot, 1960, p 203) is given by

$$Re=\frac{w\rho}{\mu}\langle v_x\rangle. \tag{2.61}$$

When turbulence occurs, the x-velocity v_x is replaced by the time smoothed x-velocity $\bar{v}_x$, defined (Bird, Stewart and Lightfoot, 1960, p 156) as the time average of v_x over a time interval which is large with respect to the time of turbulent oscillation but small with respect to the time relating to the pressure drop causing the flow. Likewise, the width averaged velocity $\langle v_x\rangle$, is replaced by $\langle\bar{v}_x\rangle$. If expressions (2.55) and (2.60) are combined, the Reynold's number for single-phase flow of incompressible fluid in a smooth-walled slit is

$$Re=-\frac{w^3\rho}{\mu^2}\frac{\partial P}{\partial x}. \tag{2.62}$$

The value of the Reynold's number is dominated by the width of the fracture and to a lesser extent by the viscosity of the fluid. Fluid flow is laminar at low values of the Reynold's number and turbulent at high values. For a smooth-walled circular tube, the transition between laminar and turbulent flow occurs at approximately 2000 (Bird, Stewart and Lightfoot, 1960, p 155). In Figure 2.3A, fluid velocity as a function of slit width according to equation (2.60), is shown for a Reynold's number of 2000. Curves for two fluid types, namely low viscosity (0.02*10^{-3}Pas) gas and high viscosity (1.0*10^{-3}Pas) oil are illustrated. Assuming that the transition between laminar and turbulent flow in a slit occurs at approximately the same Reynold's number as it does for a circular tube, the region above each curve represents the conditions for which flow is turbulent, while lamina flow occurs for conditions in the region below the curve.

Figure 2.3B similarly shows the relationship between pressure gradient and slit width according to equation (2.61). Within a petroleum reservoir, the conditions are such that both turbulent and laminar flow can occur, due to the wide range of fracture widths, fluid types and pressure gradients that can exist. This is true, even if the value of the Reynold's number at which the transition takes place is significantly different from 2000.

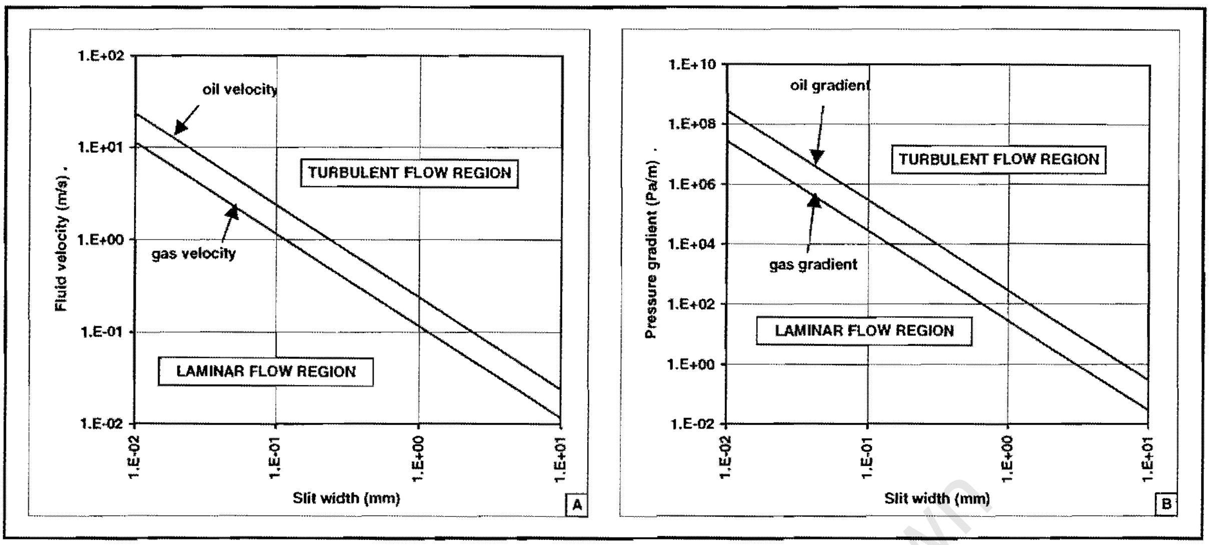

Figure 2.3: *Relationship between slit width and fluid velocity (diagram A) and between pressure gradient and slit width (diagram B), for which Reynold's number is equal to 2000.*

Friction. The equations developed in preceding sections apply to flow in a slit with smooth-walls. The walls of a fracture may be very rough, and frictional effects significant. Fluid flowing through a slit imposes a force on the walls that is the sum of a static force and a kinetic force (Bird, Stewart and Lightfoot, 1960, p181). The kinetic force can be expressed as

$$F_k = AKf \tag{2.63}$$

in which f is the dimensionless friction factor. Appropriate expressions for the characteristic area A, and the kinetic energy per unit volume, K, are

$$A = 2l(h+w) \approx 2lh \text{ and} \tag{2.64a}$$

$$K = \frac{1}{2}\rho\langle v_x\rangle^2 . \tag{2.64b}$$

If expressions (2.63) and (2.64) are incorporated into (2.62) and equated to an expression for the force balance along the length of the horizontal slit, then by re-arranging we obtain

$$\langle v_x\rangle = \frac{w^2}{\mu \, Re\, f}\frac{\partial P}{\partial l} . \tag{2.65}$$

This expression allows the friction factor to be determined experimentally. Alternatively, if the expression for velocity from the definition of Reynold's number (2.60), is substituted into this, an expression ensues from which the value of the Reynold's number can be determined experimentally. Expression (2.65) is analogous to Darcy's law (2.19), from which an expression for the permeability of the slit,

$$k = \frac{w^2}{Re\, f} , \tag{2.66}$$

can be deduced. If this expression is compared with (2.56), then it is clear that the permeability derived through the assumption of laminar flow in a smooth-walled slit is consistent with (2.66) provided that $Re f = 12$.

Historical overview: flow through a single fracture

Equation (2.55) describing the flow of viscous, incompressible fluid through smooth parallel plates has been used by Lamb (1932), Muskat (1937), Huitt (1956), Irmay (1965) and Parsons (1966), amongst others, and has subsequently become widely accepted. It is used extensively in geohydrology for modelling flow of water through fractured rock (Wilson and Witherspoon, 1974), but is even used for problems involving flow of highly compressible fluids such as gas. Barenblatt (1960), Barenblatt and Zheltov (1960) and Barenblatt, Zheltov and Kochina (1960), who pioneered much of the theory of fluid flow through fractured rock and introduced the 'dual porosity' concept, advocated the use of Darcy's equation to describe the flow through the fracture network. They did not, however, provide any expression for the fracture permeability. Warren and Root (1963), who popularised the concept of dual porosity, also did not provide an expression for the fracture permeability.

Asfari and Witherspoon (1973) used finite element techniques to investigate the relative steady state contribution to flow of discrete and isolated fractures imbedded in a porous medium. They reported a nonlinear relationship between the degree of anisotropy and the ratio of fracture length to lateral separation of the fractures. They defined anisotropy as the ratio of the overall permeability determined in a direction parallel to the fracture orientation, to the matrix permeability. on the one hand, Gureghian (1975) modelled the flow of incompressible water through fractures. He used a finite element model to study the steady state flow through a porous medium containing a single fracture of finite dimensions in the vicinity of a well. He studied the effects of varying fracture orientation and geometry, and concluded that a fracture had to be intersected by a well before any appreciable improvements in the flow characteristics were evident.

Jones, Wooten and Kaluza (1988) performed laboratory experiments to assess the effects that the roughness of the walls of the fractures have on the flow patterns. They reviewed two important papers (Lomize, 1951 and Louis, 1969) in which the authors presented experimental data from which friction factors were determined. They presented empirical relationships between Reynold's number and friction factor for laminar and turbulent flow conditions. Jones, Wooten and Kaluza (1988) proposed a modification to the equation for fracture permeability (2.56) with experimentally derived friction factors to account for the roughness of the fracture walls. In one example, they showed a 60% reduction in effective permeability between the smooth-walled theoretical value and that of a rough-walled fracture derived from experimentation. They concluded that the critical Reynold's number at which the onset of turbulence occurred was not a constant, but decreased as the width of the fracture decreased, or as the surface roughness or friction factor increased. Their experiments showed critical Reynold's numbers as low as 350. They also made the important observation that for rough-walled fractures, the transition from laminar to turbulent flow occurred at lower velocities, than generally reported in the literature.

McDonald *et al.* (1991) provided further experimental data of friction factor vs. Reynold's number for various media, including sand, granular soils, and naturally fractured chert at various apertures. They showed experimentally derived $Re\,f$ products ranging from 16 to 35 for fracture widths ranging from 0.3 to 0.06mm in naturally fractured chert, compared with the theoretical value of 12 for a perfectly smooth-walled slit. Muralidhar (1989) studied flow through a single fracture with varying apertures and containing a distribution of contact areas where the fracture width became zero. He considered the single-phase flow of an incompressible fluid under steady state conditions. Muralidhar demonstrated that the requirement for the fluid to flow around the areas where the walls of the fracture were in contact, or where local changes in the width of the fracture occurred, resulted in a greater pressure drop for a given velocity than that predicted by Darcy's equation. Muralidhar compared the equivalent permeability for the two cases and showed that where distinct contact areas were present, representing 18% of the total surface area of the fracture, neglect of the tortuosity term resulted in a velocity which was a factor of three too great.

Rossen and Kumar (1992 and 1994) studied the flow of non-Newtonian fluids through fractures. They considered a power law fluid and a Bingham plastic. The question of whether cases exist where petroleum reservoir fluids can be considered to be non-Newtonian was also addressed by Wu, Pruess and Witherspoon (1992). They cited examples of heavy oils that were better described as Bingham fluids. They gave numerous references to reports in the literature of cases of non-Newtonian fluid flow being encountered in reservoir engineering problems.

Duguid and Lee (1977) also argued that the flow of incompressible fluid in a single fracture tubule was better described through the use of the Navier-Stokes equations. They demonstrated that a general form of Darcy's law could be derived from this when the fractured medium was considered on a bulk scale, and space-averaged values were used. This in turn led to an expression for the effective permeability. However, their expression contained the time derivative of the velocity term. Due to the inherent difficulties associated with determining this permeability from basic data, Duguid and co-workers proposed that the value of the bulk fracture permeability should instead be derived from an analysis of reservoir performance.

Rossen and Kumar (1992) studied two-phase flow of fluids through a single fracture. They viewed the fracture as a two-dimensional network of apertures and constrictions. They pointed out that, due to the wide range of pressure gradients and fracture apertures found in reservoirs, different multi-phase flow regimes could occur, ranging from viscous-pressure dominated flow (wide fractures, high pressure gradients and high velocities) to capillary dominated flow (narrow fractures, low pressure gradients and low velocities). Rossen and Kumar (1994) extended their work by considering the case in which simultaneous two-phase flow was made possible by the flow of the wetting phase as a film against the walls of the fracture, while the non-wetting phase occupied the central part of the fracture.

Zimmerman and Bodvarsson (1996), in a review article on fluid flow through a single fracture, discussed the different models for dealing with wall roughness. They defined a new parameter, w_h, the hydraulic aperture, to replace w in expression (2.55), and evaluated different expressions for this parameter. They concluded that use of the mean aperture width would not give accurate results and that the effect of wall rugosity was to reduce the value of the hydraulic aperture below the mean. Their study was based on the Reynold's lubrication, a simplification of the Navier-Stokes equation, valid for low flow rates under steady state conditions. They demonstrated that the lubrication equation could be used provided that the ratio of wavelength of wall perturbations to aperture width was greater than about three.

In an attempt to determine the range in value of the hydraulic aperture, the performed an analytical analysis of walls with sinusoidal perturbations in one direction. They demonstrated that the hydraulic aperture could be approximated by the arithmetic mean of the varying apertures when the fluid flow direction was transverse to the direction of the perturbations, or by the harmonic mean for flow parallel to the direction of the perturbations.

They also studied the effects of areas of closure of the fractures using the Hele-Shaw model, solving Laplace's equation for flow between a pair of parallel plates joined in places by cylinders. They concluded that the tortuosity effect caused by regions where the rock walls were in contact with each other could be accounted for by simple correction factors dependant upon the fractional amount of the contact area.

Concluding remarks. Current ideas regarding the flow of fluid through a single fracture, and the application of these ideas in the modelling of petroleum reservoir problems, are greatly influenced by the study of the flow of fluid through idealised slits. The most common problem studied in this regard is that of incompressible fluid flowing through a smooth walled slit of constant dimensions. This has lead to expression (2.55) and (2.56), which are analogous to Darcy's law, being used extensively in the industry to model fluid flow through individual fractures and through fracture networks alike. The physics of fluid flowing through real fractures is likely to be significantly more complex than suggested by these expressions. Numerous researchers have attempted to quantify the effects of wall rugosity, variable fracture dimensions, and fluid characteristics, and have demonstrated the potential for large errors in numerical modelling results if these effects are ignored. However, considering the inherent difficulty of characterising the fractures in a reservoir, the fracture permeability remains a parameter with a large degree of uncertainty in its value and is often considered a history matching variable.

2.2.2 Flow through a network of fractures

The modelling of fluid flow in a discrete fracture was dealt with in the previous section (2.2.1), and the modelling of the combined fracture network and porous and permeable rock matrix will be dealt with in the following section (2.2.3). This short section deals with the flow of fluid through a fracture network on its own. On the scale of a reservoir, the fracture network is seen as a continuum and this forms the basis for the ensuing discussion.

The governing equations have been developed on the premise that an analogy can be drawn between a piece of porous and permeable rock on a small scale, and a volume of rock containing fractures on a much larger scale. In this analogy, the grains of sand are replaced by the chunks of matrix rock, and the interconnected pore spaces by the interconnected fractures. Pursuing this analogy, precisely the same equations that govern the flow through a porous and permeable rock matrix should apply to the fracture network continuum. If we adopt the same expressions for mass balance, Darcy's law and compressibility described in Section 2.1.3, and replace the physical properties of the porous medium with appropriate properties for the fracture network continuum, then the governing equation for single-phase isothermal flow of compressible fluid through a fracture network under the influence of pressure gradients and gravity, which is entirely analogous to equation (2.23), can be written as

$$\nabla \cdot \left(\frac{\rho k_f}{\mu} \left(\nabla P + \rho g \nabla D \right) \right) = \rho \phi_f \left(c_{fl} + c_f \right) \frac{\partial P}{\partial t} + q , \tag{2.67}$$

where subscripts f and fl indicate fracture and fluid respectively. If the magnitude of the fracture permeability developed in the previous section, expression (2.56), is assumed for the fracture continuum, and the tensor nature of the fracture permeability is ignored, then this equation becomes

$$\nabla \cdot \left(\frac{\rho \phi_f w^2}{12\mu} \left(\nabla P + \rho g \nabla D \right) \right) = \rho \phi_f \left(c_{fl} + c_f \right) \frac{\partial P}{\partial t} + q . \tag{2.68}$$

2.2.3 The fracture network in a porous and permeable medium

In previous sections, governing equations were developed to describe the flow of fluid through a porous and permeable formation (2.23) and through a fracture network (2.67). This section comprises a review of the methods for combining the two theories to form a set of equations describing the flow of fluids through a reservoir made up of a porous and permeable rock matrix permeated by networks of fractures. Fluid flow through such a fractured porous medium has traditionally been modelled numerically by making use of the so-called 'dual porosity' model, or of some variation of this model, illustrated in Figure 2.4.

The basic premise of this approach is that the fracture network provides the conduits through which the reservoir fluid is transported while the porous matrix material provides the storage space. Of particular importance is the coupling between the two systems. The section begins with an explanation of the meaning of terms and underlying principles, and proceeds to the historical overview.

Modelling terms and principles

This discussion covers the dual porosity model, the analytical transfer function, the dual porosity dual permeability model, the single continuum model, and two forms of numerical transfer functions. These models and parameters all relate to the two equations developed in previous sections describing the isothermal flow of single-phase, compressible fluid in the matrix and fracture network respectively (2.23 and 2.67).

The conventional dual porosity model. The dual porosity model is based on the premise that fluid can flow between the isolated matrix blocks and the fracture network, but that the bulk transport of fluid through the reservoir occurs via the fracture network only. While the fractures form the flow conduits, the matrix material forms the storage space. The conventional approach to numerical simulation is to define two overlapping continua, one representing the fracture network, and the other representing the porous matrix, illustrated in Figures 2.4. Equation (2.23) is not normally used in this form and is replaced by some 'transfer function'. The most common approach is to track a single value of 'average' pressure for all the physical matrix blocks that occur within any given simulation grid block or cell as a function of time, effectively eliminating the possibility of capturing transient effects.

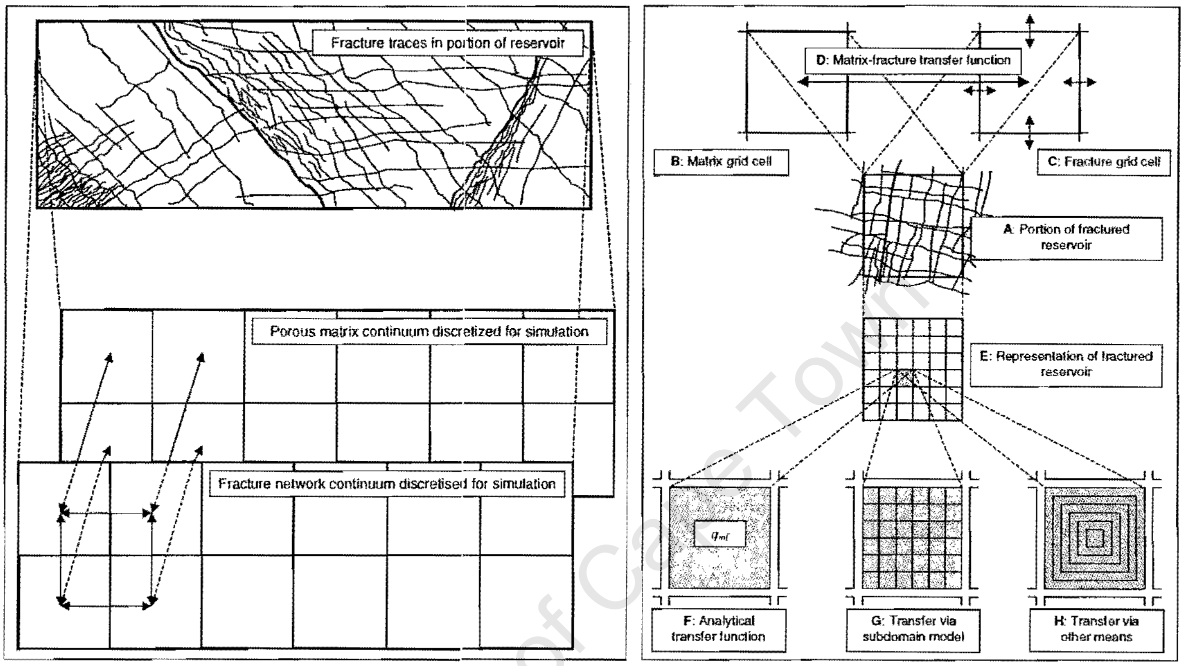

Figure 2.4: *<u>On the left:</u> Portion of reservoir showing fracture traces, together with representation for numerical simulation of discretized porous matrix and fracture network continua. Arrows indicate possible fluid flow routes for the dual porosity model. <u>On the right:</u> A portion of fractured reservoir (A) is discretized for numerical simulation. Two grid cells are needed to represent the porous matrix system (B), and the fracture network (C). Flow between the grids is according to some transfer function (D). The transfer function depends upon the idealised size and shape of the physical matrix blocks within the fracture network (E). The transfer function may be analytical (F), or numerical, employing further discretization via a sub-domain model (G), such as the multiple interacting continua model (MINC), (H).*

The analytical matrix-fracture transfer function and the geometric factor. Much of the literature on the subject of fractured reservoirs deals with the transfer function and there is a lack of consistency regarding nomenclature of the components of the transfer function. Most of the discussion is based on the assumption that the fluid is only slightly compressible, or incompressible. This results in a simplification to equations (2.23) and (2.67), made possible by dividing both sides by the density of the fluid. For consistency in this thesis, where this has been done, the associated transfer function is designated Q_{mf}, with dimensions [T^{-1}], in order to distinguish its meaning from the transfer function appropriate for a compressible fluid, designated q_{mf} with dimensions [$ML^{-3}T^{-1}$].

The equations incorporate a term referred to as the 'geometric factor', a component of the transfer function, which is still the subject of controversy, and much work relating to this parameter, particularly for multi-phase flow, is being undertaken. In this thesis, the geometric factor has been given the symbol α, and is a dimensionless quantity relating the difference between the average pressure in a matrix block and the average pressure in the fractures surrounding the block, to the rate of expulsion of fluid from the block (2.69). The value of α depends upon the size and shape of the matrix block. A variation on the basic definition, identified as α^*, has dimensions of inverse area [L^{-2}] and is also used. Where authors have referred to the geometric factor with different symbols or definitions, these have been re-formulated to remain consistent with the definitions used in this thesis. A much used symbol for the geometric factor is σ which is also referred to as the 'shape factor'. Another term often used is the 'geometric leakage factor' Γ.

A further subject of debate relates to the selection of appropriate values of pressure for both the matrix and fracture, needed to solve the transfer function at any given time. These are most commonly assumed to be the average pressure values estimated from the simulation cells in which the matrix block and its corresponding portion of fracture network are located respectively. The widely accepted form of the transfer function developed by Barenblatt (1960), Barenblatt and Zheltov (1960) and Barenblatt, Zheltov and Kochina (1960) is

$$q_{mf} = \frac{\rho\alpha}{\mu}\left(\overline{P}_m - \overline{P}_f\right), \text{ or} \qquad (2.69)$$

$$Q_{mf} = \frac{\alpha}{\mu}\left(\overline{P}_m - \overline{P}_f\right) = \Gamma\left(\overline{P}_m - \overline{P}_f\right). \qquad (2.70)$$

An alternative approach involves taking any reference to permeability out of α and including it in the expression for the transfer function explicitly, leading to

$$q_{mf} = \frac{\rho k_m \alpha^*}{\mu}\left(\overline{P}_m - \overline{P}_f\right), \text{ or} \qquad (2.71)$$

$$Q_{mf} = \frac{k_m \alpha^*}{\mu}\left(\overline{P}_m - \overline{P}_f\right). \qquad (2.72)$$

The numerical value of the geometric factor α intuitively includes the permeability of the matrix block together with some characteristic length (l_c) associated with the size and shape of the matrix block,

$$\alpha = C\frac{k_m}{l_c^2}, \text{ or} \qquad (2.73)$$

$$\alpha^* = C\frac{1}{l_c^2}, \qquad (2.74)$$

in which C is some constant. The expression derived by Warren and Root (1963) for the geometric factor of single-phase flow based on semi-steady state flow assumptions is

$$\alpha^* = \frac{4N(N+2)}{l_c^{\,2}}, \qquad (2.75)$$

where N is the number of normal sets of fractures (1, 2 or 3) and

$$l_c = l_x \text{ for } N = 1, \qquad (2.76)$$

$$l_c = \frac{2l_x l_y}{\left(l_x + l_y\right)} \text{ for } N = 2\text{, and} \tag{2.77}$$

$$l_c = \frac{3l_x l_y l_z}{\left(l_x l_y + l_y l_z + l_z l_x\right)} \text{ for } N = 3\text{,} \tag{2.78}$$

and where l_x, l_y and l_z are the dimensions of a typical block. Kazemi *et al.* (1976) proposed a formula of the form

$$\alpha^* = 4\left(\frac{1}{l_x^{\ 2}} + \frac{1}{l_y^{\ 2}} + \frac{1}{l_z^{\ 2}}\right). \tag{2.79}$$

For systems with anisotropic permeability, Kazemi *et al.* suggested that expression (2.79) could be modified to

$$\alpha = 4\left(\frac{k_x}{l_x^{\ 2}} + \frac{k_y}{l_y^{\ 2}} + \frac{k_z}{l_z^{\ 2}}\right). \tag{2.80}$$

Thomas, Dixon and Pierson (1983) proposed a formula of the form

$$\alpha^* = \frac{A}{l_c V_m} \tag{2.81}$$

where A is the interface area and V_m is the volume of the matrix block.

The transient equations

The discussion in previous paragraphs relating to the transfer function was based on the assumption that pseudo-steady state conditions prevail. When this is not the case, and transient effects must be considered, the derivation of an appropriate analytical solution is much more difficult. An approximation of the effects of transient behaviour can be analysed by considering a much simplified model. If the fluid is assumed to be slightly compressible, then the nonlinear term of equation 2.32 can be dropped, leading to a linear differential equation describing the pressure distribution $P_m(\boldsymbol{x}_m, t)$ within a matrix block as a function of time,

$$\nabla^2 P_m(\boldsymbol{x}_m, t) = \frac{\phi_m \mu c_{mt}}{k_m} \frac{\partial P_m(\boldsymbol{x}_m, t)}{\partial t}, \tag{2.82}$$

where c_{mt} is the total compressibility of the matrix system. When the initial condition,

$$P_m(\boldsymbol{x}_m, 0) = P_{m0}, \tag{2.83}$$

where P_{m0} is the constant initial pressure in the matrix block, and the boundary condition,

$$P_m(\boldsymbol{x}_s, t) = P_f\text{, for } t > 0, \tag{2.84}$$

where P_f is the constant pressure in the fracture surrounding the matrix block, are met, then a solution can be obtained (Crank. 1975) in terms of the average pressure in the matrix block $\overline{P}_m$, of the form

$$\overline{P}_m(t) = P_{m0} + \left(P_f - P_{m0}\right)\left(1 - \frac{C}{\pi^2}\sum_{n=1}^{\infty}\frac{1}{n^2} exp\left(-\frac{n^2\pi^2 k_m t}{\phi_m \mu c_{mt} l_m^2}\right)\right), \tag{2.85}$$

where C is a constant that depends on the geometric form, and l_m is a characteristic length of the matrix block. This expression describes how the average pressure in the matrix block changes with time after the fracture pressure has been instantaneously reduced to, and maintained at, some new pressure. The equation contains the effects of pressure gradients that exist in the matrix block during the transient phase. The values of C and l_m depend on the geometry of the matrix block. In the case of a sphere, for example, C has a value of 6, and l_m is the radius of the sphere.

The dual porosity-dual permeability model. The dual porosity-dual permeability model differs from the dual porosity model in that it permits bulk flow of fluid through the reservoir to take place through both the fracture network and through the porous matrix. It is assumed that either the matrix blocks are in contact with one another and form a true continuum, or that the fluid flowing out of one matrix block can subsequently pass into and move through another matrix block.

The single continuum model. This is an alternative to the dual porosity and dual porosity dual-permeability approaches. The fracture and matrix continua are combined into a single continuum and no distinction between fracture and matrix flow is made. The flow is then simulated as if it were occurring in a conventional porous reservoir with modified porosity and permeability distributions. This model is likely to be applicable when the fractures are isolated.

Numerical transfer functions via sub-domain models. In order to account for variations in pressure and saturation (in the case of multi-phase models) within the matrix blocks, various researchers (Saidi, 1983, Gilman, 1986 and Gilman and Kazemi, 1988) have advocated further discretization of the matrix blocks. Such models are occasionally referred to as 'extended dual porosity models'. These methods have not gained popularity due to their longer computational time.

Numerical transfer functions via the multiple interacting continua method (MINC). The multiple interacting continua model, referred to as MINC, is a special case of the subdomain group of models in which the subdomains consist of nested grid blocks or nested volume elements. It is probably the most widely used of the subdomain models. This method of discretization of the matrix blocks was proposed by Pruess and Wu (1989), used by Gilman (1986), and subsequently used by numerous other workers.

Historical overview

Barenblatt (1960), Barenblatt and Zheltov (1960) and Barenblatt, Zheltov and Kochina (1960) first presented an elegant theory in support of the use of dual porosity models. They were the first to propose the use of Darcy's equation to describe the macroscopic flow of fluids through the fracture network. They defended their assumption by drawing the analogy between a porous medium and the fracture network described in Section 2.2.2. Their reasoning led to expressions (2.69) and (2.73), the first reported expression for the matrix-fracture transfer function. They simplified the governing equations (2.23) and (2.67) by assuming that the fracture continuum was homogenous, isotropic and incompressible, that the fluid was incompressible or only slightly compressible and that the fluid viscosity was not a function of pressure.

Warren and Root (1963) developed further the dual porosity concept proposed by Barrenblatt and his various co-workers in 1960. Their work was aimed primarily at interpreting well tests conducted in fractured reservoirs containing slightly compressible fluid. They presented an analytical solution for single-phase, unsteady, radial flow in a naturally fractured reservoir. They derived formulae for the shape factors for a series of identical homogeneous and isotropic parallelepiped matrix blocks within an orthogonal fracture system in multiple dimensions. Warren and Root used the geometric factor with units of inverse area, i.e. α^*, and gave expressions (2.75) to (2.78) for determining its value. In their assessment of well tests, their model demonstrated that at early and late times, the semi-log plot of dimensionless pressure drop versus time portrayed two displaced straight lines with the same slope, the magnitude of which depended upon the permeability of the fracture system.

Bai and Roegiers (1994) and Bai, Elsworth and Roegiers (1993) extended the idea of a dual porosity system to one containing multiple porosity and permeability components, as would be the case in a reservoir with several different fracture sets at different scales. Bai and Roegiers (1994) studied the effects that the nonlinear terms in the flow equations, analogous to convective transport, have on the simulation results. They demonstrated that the appearance of 'dual porosity behaviour' of naturally fractured reservoirs, namely, three distinct lines on semi-log pressure build up plots could be largely due to the degree of convective flow, and not to the inter-porosity flow, as was usually assumed to be the case. Bai, Ma and Roegiers (1994) also considered the dual porosity dual permeability model, and emphasised the need to consider the effect that fracture closure resulting from pressure depletion had on the interpretation of well test data.

Duguid and Lee (1977) studied the flow of slightly compressible water through the fractured reservoir, using a modified version of Darcy's law derived from the Navier Stokes equation. This led them to define a transient transfer function between a given matrix block and its surrounding fractures, the solution of which was not unique as it required (subjective) selection of some characteristic length.

Pruess and Narasimham (1985) studied numerical alternatives to the analytical transfer functions and championed the use of the multiple interacting continua method (MINC). Matrix blocks were discretized into a sequence of nested shells. They demonstrated that the appropriate selection of shell dimensions led to an accurate replication of the results achieved using an analytical function based on pseudo-steady state assumptions made by Warren and Root. Pruess and Wu (1989) continued this work but reverted to the use of semi-analytical methods.

Bossie-Codreanu, Bia and Sabathier (1985) proposed an innovative alternative to the numerical implementation of the dual porosity model that did not require significant modification to a conventional single porosity simulator. Each grid block was populated according to whether it represented a portion of matrix or a portion of the fracture network, resulting in a checkerboard distribution of matrix blocks surrounded by fracture blocks within a single grid. Although the concept was simple, the application led to inefficient usage of grid blocks. They suggested that an advantage of their approach was the elimination of the transfer function. However, their approach required a 'scaling factor', which itself contained elements of the transfer function.

Gilman (1986) presented results of work on the numerical modelling of single-phase compressible flow in fractured reservoirs using finite differences and subdivided matrix blocks for enhanced representation of the transfer of fluids under transient conditions. He demonstrated that significant errors resulted from the incorrect assumption of pseudo-steady state conditions. Wu and Pruess (1988) extended this work and applied the method to the recovery of oil by water imbibition and for water coning studies. Their work emphasised the difficulties in obtaining accurate results for reservoirs in which transient effects were important, such as in very low permeability matrix or where matrix blocks were large. They demonstrated that the assumption of pseudo-steady state resulted in overestimation of recovery from a block through the process of imbibition and advocated the use of a subdomain model. Pruess and Wu (1989) presented analytical transfer functions derived from their MINC formulation. They suggested the use of subdomain models for problems involving high fluid viscosity, large matrix blocks, or low matrix block permeability.

Chen, Poston and Raghavan (1990 and 1991) modelled the flow of slightly compressible fluid into the well bore in a fractured reservoir. They presented an analytical expression for the transient transfer function. Their expression still contained an unidentified 'characteristic length', making it difficult to implement. McDonald *et al.* (1991) proposed the use of a single porosity model in which the volume weighted average of the matrix and fracture permeability values was used.

Zimmerman *et al.* (1993), in their study of slightly compressible water, attempted to improve the transfer function under nonlinear conditions by integrating the expression for pressure over the matrix blocks. The derived an approximate equation for the rate of change of average pressure within a spherical matrix block surrounded by a fracture with a specified pressure, that took account of the pressure gradient existing within the matrix block. They replaced the conventional Warren and Root pseudo-steady state equation with this expression in a dual porosity simulator and reported an improvement in accuracy over the Warren and Root algorithm by comparing both sets of results with those obtained from a finely meshed simulation model.

In an important paper, De Swaan and Raimirez-Villa (1993) developed a time-dependent equation (based on work done by Pollard, 1953) to describe the single-phase flow from a single matrix block. They made use of analytical solutions governing heat flow in solids to derive estimates for the geometric factors for a cube and for a slab. They reported values for α^* of 60 and 15 respectively for a unit cube and for an infinite slab with thickness equal to one half of unity. Onur and Satman (1993) presented well test type-curves for dual porosity reservoirs for the pseudo-steady state flow model of Warren and Root and for the transient flow model of Kazemi and de Swaan. Their study was aimed at identifying those elements of a pressure build up plot that characterised the dual porosity system. Their study emphasised the importance of a model's ability to replicate transient effects if it was to be used for any quantitative interpretation of well test data.

Lough, Lee and Kamath (1996) proposed an alternative to the dual porosity modelling techniques that made use of either a continuum or a discrete fracture approach. They argued that the fracture permeability used in the continuum approach could not do justice to the complexities of the fracture system, while the discrete model could possibly represent individual fractures and geometry accurately but was impractical for modelling the entire reservoir. They combined the two techniques, by first modelling a small representative section of the reservoir populated with discrete fractures to determine an effective permeability, which included contributions from both the fractures and the matrix using a boundary element code. This permeability was then incorporated into a conventional single porosity model. This approach allowed very irregular fracture patterns to be modelled. They assumed that the flow in individual fractures was governed by Darcy's law. The model of Lough, Lee and Kamath (1996) was essentially the single porosity model for which the effective permeability was determined in a fairly sophisticated fashion.

Zimmerman and Bodvarsson (1995) studied liquid imbibition and solute absorption in their work on nuclear waste disposal in fractured volcanic tuff. They demonstrated that matrix block size and geometry were both important parameters. They simplified their equations by eliminating nonlinear terms and their reservoir model comprised a distribution of spherically shaped block of varying size. They demonstrated that for early time behaviour, the distribution of matrix block sizes could be approximated by a single sphere with radius equal to the volume weighted geometric mean of the radii. They were not able to find a satisfactory approach for dealing with late time effects.

Immiscible flow. The imbibition process whereby water enters the matrix blocks and expels oil is an important recovery mechanism in dual porosity oil reservoirs (Chen, Miller and Sepehrnoori, 1995), in which capillary action plays a major role (Kazemi and Merrill (1979), Beckner *et al.* (1987), Douglas, Arbogast and Paes (1989), Bech, Jensen and Nielson (1991), Dutra and Aziz (1992)). Kazemi and Merrill (1979) modelled two-phase flow with a finely gridded matrix block in order to improve definition of the imbibition process. Thomas, Dixon and Pierson (1983) developed a fully implicit, three dimensional, multi-phase simulator based on the dual porosity approach. They made provision for matrix-fracture transfer in the presence of pressure gradients in the fracture. Saidi (1983) introduced the subdomain model for multi-phase flow.

Gilman and Kazemi (1983) and Gilman (1986), considered a refinement of the matrix block which allowed saturation fronts to exist within the block and improved the accuracy of the fluid transfer in cases where transient effects existed. Gilman and Kazemi (1988) refined the work further by including the ability to deal with pressure gradients in the fractures, including dynamic gravity effects. Beckner *et al.* (1987) modelled an advancing fracture water level around a single matrix block with a very fine grid and proposed a revised transfer function. Ishimoto (1988) proposed an adjustment to the conventional expression for Kazemi's shape function to account for nonlinear pressure distribution between the centre of the matrix block and the matrix-fracture interface. Further investigations into the shape factor were undertaken by Ueda *et al.* (1989), Rossen and Shen (1989) and Kazemi and Gilman (1992).

Beckner, Chan and McDonald (1991), identified 'representative matrix blocks' which they subdivided into rectangular rings and layers, to enhance pressure and saturation gradient resolution within the blocks. They showed differences of up to 35% in cumulative oil production between forecasts made using either discretized or unrefined matrix block models. Dutra and Aziz (1992) considered the slow immersion of an oil saturated matrix block into water, with the aim of deriving an analytical transfer function. Similar work was undertaken by De Swaan and Raimirez-Villa (1993). In a comprehensive review paper, Fung (1993) suggested that the dual porosity model was fundamentally inappropriate, as it was physically impossible that matrix blocks were not in contact with one another, and hence there was likely to always be some transfer of fluids between matrix blocks, making the dual porosity-dual permeability model more appropriate.

Chen, Miller and Sepehrnoori (1995) studied counter-current imbibition. Other workers who made important contributions to the two-phase flow problem include Sonier, Souillard and Blaskovich (1986), Litvak (1985) and Saidi (1983).

Miscible flow. While imbibition is the dominant physical process controlling immiscible displacement of one fluid by another in a fractured reservoir, so the molecular diffusion process dominates when the fluids are miscible. Diffusion is facilitated by the rapid dispersive flux through the fractures which exposes fluids of different molecular diffusion potential to each other over large contact areas. Da Silva and Belery (1989) described the process and developed a dual porosity simulator incorporating Fick's molecular diffusion potential. They concluded that transient effects were negligible when gas displaced gas, but could be significant when liquid displaced liquid. Coats (1989), Riazi, Whitson and da Silva (1994) further demonstrated the importance of accounting for molecular diffusion and concluded that transient effects could be significant.

Tan and Firoozabadi (1995a and b) considered viscous and gravity cross flow in their study of the displacement of in situ fluid by injected fluid. They concluded that the most important parameters controlling the physical processes in the fractured reservoir were gravity and fracture spacing. Dindoruk and Firoozabadi (1996a and 1996b) used an analytical model based on the method of characteristics to study the effect that cross flow had on recovery. They considered cross flow caused by gravity and viscous forces, and highlighted the difficulties of attempting to solve the equations numerically.

Concluding remarks. The dual-porosity model of a fractured reservoir first developed by Barenblatt and his co-workers in 1960 is still regarded as the most practical approach for the modelling of fractured petroleum reservoirs. Refinements to the concept have been made by numerous researchers over the years, particularly through the study of multi-phase flow. The single most important component of the dual porosity model is that which describes the link between a matrix block and the surrounding fractures, namely the 'transfer function'. In the case of the most commonly used approach, in which a single average pressure is assigned to a matrix block, and a single average pressure is assigned to the fractures surrounding the block, and in which the flow of fluid between the matrix and the fractures is assumed to take place under pseudo-steady state conditions, the transfer is determined by a single parameter, the geometric factor, α, defined by expression (2.73). In order to model the process of fluid transfer between the matrix block and the fracture network more accurately, particularly when the pseudo-steady state assumptions are broken, the transfer function is inadequate, and the equations governing the flow of fluid throughout each matrix block must be solved in some way. This is the approach implemented in the MINC method, and is the approach adopted in this work.

2.3 Summary of governing equations

In this work, the emphasis is on the study of flow of single phase, compressible gas through fractured reservoirs, particularly reservoirs that have low matrix permeability. The model is restricted to two dimensions, and gravity effects can consequently be ignored. The equation governing flow through the fracture network follows from expression (2.67) and is given by

$$\nabla\cdot\left(\frac{\rho k_f}{\mu}\nabla P\right)=\rho\phi_f c_{ft}\frac{\partial P}{\partial t}+q_{mf}-q_{cf}\ , \tag{2.86}$$

where $c_{ft}=c_{fl}+c_f$ is the total compressibility of the fracture system, comprising the fluid (c_{fl}) and fracture (c_f) compressibility. For the problem considered in this study, c_{fl} is orders of magnitude greater than c_f. Extraction of gas from the reservoir through the wells is assumed to take place via the fracture network, and is accounted for in the sink term $-q_{cf}$. The source term q_{mf} accounts for the transfer of gas from the matrix blocks into the fracture network.

The equations governing the flow of fluid through the matrix material follows from equation (2.23) and is given by

$$\nabla\cdot\left(\frac{\rho k_m}{\mu}\nabla P\right)=\rho\phi_m c_{mt}\frac{\partial P}{\partial t}-q_{mf}\ , \tag{2.87}$$

where $c_{mt}=c_{fl}+c_m$ is the total compressibility of the matrix system, comprising the fluid (c_{fl}) and matrix (c_m) compressibility. For the problem considered in this study, c_{fl} is orders of magnitude greater than c_m. The only destination for gas leaving the matrix block is the fractures, accounted for by the sink term $-q_{mf}$.

When applied to the particular problem of this study, the coefficients in expressions (2.86) and (2.87) differ in two significant instances. The fracture porosity (ϕ_f) is generally far smaller in magnitude than the matrix porosity (ϕ_m), while the fracture permeability (k_f) is generally far greater in magnitude than the matrix permeability (k_m). Pressure is a function of space and time, porosity is a function of space and pressure and permeability is a function of space. The fluid properties, density (ρ) and viscosity (μ) are both functions of pressure.

CHAPTER 3

THE FINITE ELEMENT METHOD

Application of the finite element method (FEM) to the problem of modelling fractured reservoirs is discussed in this chapter in three sections. In the first, an historical overview of the use of the FEM for solving both unfractured and fractured reservoir problems is given. This is followed by a formulation of the FE algorithms for a range of elements for the specific governing equations of fluid flow used in this study. The section ends with a discussion of the system equations that are implemented in the computer program. In the final section, the unique approach developed during the course of this research for modelling a range of fractured reservoir problems, including transient behaviour, through the use of multiple FE meshes is described, and the computer program developed for this purpose is discussed.

3.1 Historical overview

This literature review is intended to describe the evolution of the finite element method in the petroleum industry for the simulation of fluid flow problems, and sets the scene for the section that follows, namely the development of a finite element solution for the governing equations. The use of finite elements for solving petroleum reservoir flow problems is not nearly as widespread as the use of finite difference methods. This work is therefore a departure from the more popular approaches and the literature survey is intended to provide justification for this departure. The literature review gives insight into the difficulties, and the advantages, of using the finite element method for this type of problem in addition to covering numerous issues that are essential ingredients to any simulation effort, such as the treatment of wells in simulators and time stepping.

Finite element methods, originally developed to solve mechanical engineering problems, began to find application in a broader range of disciplines in the early 1970s. During this period of diversification, FEMs were applied to the study of the flow of fluids through porous media in both the petroleum and groundwater industries. The use of FEMs became entrenched in the study of groundwater movement while their use in the petroleum industry waned after an initial flurry of interest as the focus of research shifted to the use of finite difference methods (FDMs). Work on FD schemes in the petroleum industry continued and the FDMs are widely used for this purpose today. The greater complexity of FE modelling undoubtedly favoured the use of FDMs. This was particularly the case in the earlier days when computing costs were high. In addition, FDMs are in general intuitively simpler to comprehend and apply.

By contrast, the groundwater modellers retained their interest in FEMs and today groundwater modelling is done almost exclusively with the use of FE techniques. Research into the use of FEMs for reservoir simulation did continue in the petroleum industry, albeit at a slow pace. Where the FEM has been applied in the petroleum industry, it was restricted almost entirely to the single porosity problem, and limited research results have been published on the use of FEMs for modelling dual porosity reservoirs.

This historical overview is presented in two sections, dealing with conventional porous media and fractured porous media respectively. The aim is to highlight the issues that have relevance to the research results presented in this thesis, and to demonstrate the place that this work has in the industry. Some of the modelling approaches mentioned here are only remotely related to FEMs. Such methods have been described here in order to draw attention to alternative approaches for addressing specific problems. The method most widely used by the petroleum industry, the FDM, is mentioned here in as much as a comparison between the FEM and FDM is valuable.

3.1.1 Simulation of flow in a porous medium

The application of FEMs to the study of flow of fluids in porous media received much attention in the early 1970s. At a conference held in 1974 on FEMs in flow problems (Oden *et al.*, 1974), numerous papers dealing with the flow of fluids through porous media and related subjects were presented, representing the state of the art in the subject.

Zienkiewicz (1966*)* applied the FE technique to the general problem of potential flow. Doctors (1970) considered two-dimensional inviscid flow. Gray and Pinder (1974) developed a FEM for integrating time in ground water problems. Reachford (1976) presented the status of the use of variational methods in the petroleum industry. The paper addressed the different approaches for applying the FEM to steady state problems. Sincovec (1977) used a collocation method to solve the nonlinear problem of single-phase, compressible fluid flow as well as the miscible displacement of one fluid by another. Sincovec compared the efficiency of the collocation method to that of a second order FD approach in terms of computer time and storage requirements for a given degree of accuracy. Cheng (1978) published a comprehensive account of the use of FEMs in groundwater and surface water problems, including several complex case studies.

Lewis and Schrefler (1987) coupled the fluid flow equations with the laws governing stress-strain behaviour of the porous medium. They developed FEMs to study consolidation and subsidence caused by the depletion of aquifers and reservoirs and extended the formulation to include thermal effects. This work, associated principally with the application of FEMs to model fluid flow in deformable porous media, has been extensively expanded upon over the years. Schrefler and Xiaoyong (1993) studied two-phase flow involving water and air in deformable porous media, and included capillary pressure effects. Gawin and Schrefler (1996) developed a model in which the coupled flow of heat, water and gas was considered. Lewis, Schrefler and Rahman (1998) studied three-phase flow, and included relative permeability effects. Schrefler and Scotta (2001) presented detailed results of the modelling of the flow of water and air under different physical conditions. They considered the drainage of a soil column, the storage of air in an aquifer and the dynamic analysis of a sand column subject to a step load.

Finite element verses finite difference methods. Khataniar and Peters (1991) published a comparison between the results of the application of the two methods to problems involving viscous fingering. Comparisons were in terms of mesh orientation effects, computational efficiency and solution quality. The FEM with Gauss quadrature showed the least mesh orientation effects. The FDM and the FEM with Lobatto quadrature showed similar degrees of mesh orientation effects, with the FDM slightly better than the FEM. When fine meshes were used, mesh orientation effects were reduced significantly in all cases, with the FEM using Gauss quadrature still giving the best results. The FEM took more than twice as long as the FDM to complete a simulation run.

Spatial discretization. Chase (1979) simulated chemical flood processes and found that the use of the FEM and the ease with which the method could accommodate varying mesh parameters made it very suitable for modelling this type of problem, the solution of which includes the presence of sharp fronts. Mulder and Gmelig Meyling (1991) modelled incompressible, immiscible two-phase flow in three dimensions and included the facility for dynamically adapted local refinement. Deb *et al.* (1995) developed an advanced simulator to deal with the problem of modelling changes in local precision requirements by using an *h-p* FE framework that allowed both local mesh size refinement and local polynomial enrichment.

Carey *et al.* (1985) made use of moving FE meshes for tracking sharp fronts in convective dominated problems, particularly those relating to chemical injection. Farmer, Heath and Moody (1991) used a FEM to meet detailed geometric modelling requirements in fluid flow problems, such as complex reservoir boundaries, regions where abrupt changes in permeability or other rock properties existed, or where structural elements such as faults or lineaments transected the reservoir.

Voronoi or perpendicular bisection (PEBI) meshes are among a new generation of flexible meshing systems gaining popularity in the petroleum industry. The advantage of these is that the mesh points can be specified anywhere in the domain regardless of the location of any other point. Significant contributions to the subject have been made, amongst many others, by Heineman and Brand (1988) and Heineman *et al.* (1989, 1991) and Palagi and Aziz (1991, 1994). Heineman and Brand (1988) first introduced Voronoi or PEBI meshes to the petroleum industry. Heinemann *et al.* (1991) showed several examples of the use of Voronoi meshes to model practical problems using their integrated FD, or control volume method.

Amado and Pedrosa (1993) also used the finite volume approach with triangular cells. This resulted in control volumes that were similar in nature to the Voronoi or PEBI meshes with a FD discretization described by Heinemann *et al.* (1991). Palagi and Aziz (1991 and 1994) provided a useful guide to the practical implementation of the Voronoi meshing approach, addressing issues such as the selection of mesh points, the assignment of properties and the well model.

In recent years, much attention has been given to the use of Control Volume Finite Elements (CVFE). The CVFE method uses finite elements to solve the pressure equation. In addition to the finite element mesh, the domain is divided into control volumes, each centred on a nodal point. The conservation equations are solved in this control volume grid using a finite difference method. The CVFE method was developed to derive benefit from the flexible meshing capabilities of the FEM, and the local mass conservative properties of the FDM. Forsyth (1989), Gottardi and Dall'Olia (1992), Fung, Hiebert and Nghiem (1992), Fung, Bachanan and Sharma (1994), Sonier (1993) and Eymard and Sonier (1994), applied the technique to a range of problems.

Forsyth (1989) introduced CVFEs primarily as a means for bridging the gap between a regional coarse mesh and a locally refined mesh for thermal reservoir simulation problems. Gottardi and Dall'Olia (1992) used linear triangular elements to model two-phase, two-dimensional, immiscible flow in conjunction with control volumes. They included the effects of capillary pressure, compressibility and gravity. Eymard and Sonier (1994) demonstrated that the stability of the CVFE scheme came from honouring local balances of all components. They also derived convergence criteria for the case of two-phase, multi-dimensional flow of incompressible fluids in the absence of gravity and capillary terms. They performed a comparison with FD schemes (more appropriately control volume FD (CVFD) schemes) via the eighth SPE comparative project (Quandale, 1993).

Fung, Buchanan and Sharma (1994) extended the work on CVFE methods to develop a range of specialised hybrid meshes, specifically to allow detailed description in the vicinity of different types of wells. They formulated the problem in the general context of the method of weighted residuals (MWR) from which the integral FD (IFD), the Petrov-Galerkin FE (PGFE) and the CVFE could be derived. They demonstrated that the CVFE method encompassed the perpendicular bisection method (PEBI), Voronoi meshes, and Cartesian FDs as special cases. Arbogast, *et al.* (1995) considered single-phase flow through an anisotropic porous medium. They used mixed FEs as these conserved mass locally and gave a good approximation to the flux variable.

Rozon (1989) presented a finite volume discretization method for single-phase flow using a cartesian mesh with a bi-linear pressure profile. This led to a nine point discrete equation that differed from the conventional nine point FD equation in that it did not have diagonal terms. Santos, Pedrosa and Correa (1992) used finite volumes to deal with the miscible displacement problem. The result was a five point discretization of the pressure equation and a nine point discretization of the concentration equation.

Leventhal, Klein and Culham (1985) used curvilinear co-ordinate transformations designed to eliminate mixed derivative terms to model complex reservoir shapes. The resulting system of differential equations was solved using finite elements. Kocberber (1995) made use of the meshing capabilities of the FE technique to improve the numerical description of the reservoir in the vicinity of sloping faults.

Wells. Due to the small area that the well bore occupies relative to the reservoir, it is generally impractical to model the well bore explicitly in full field models. The treatment of wells in FD reservoir simulators has followed the approach developed by Peaceman (1978). Peaceman developed a relationship between the average pressure in a (large) FD grid block, and the appropriate pressure to attribute to the well bore of a flowing well completed in that block, based on the assumption of steady state flowing conditions. Shaw (1993) used Peaceman's approach in a FE simulator and confirmed the results obtained for relating bottom hole flowing pressure to the pressure in the cell.

Time stepping. FD time stepping routines are commonly used for the nature of the problem studied here, although other schemes have been used. Van Leer (1977) studied convection of compressible fluid and used a second order upstream centre scheme. The true initial value distribution per mesh was replaced by a simple approximation function and then the result was convected exactly.

Russelll (1982) considered a simple diffusion-convection problem as a precursor to the two-phase miscible displacement problem. He used the method of characteristics to model convection, and a FEM to model diffusion and dispersion, thereby treating each physical process with an appropriate numerical technique. Russell observed that at a given time step, the Darcy velocity field represented convective flow. The solution at that time step was moved along the velocity field to the next time step, and then a FE approach was used to deal with the diffusion and dispersion. In his application of the method of characteristics, he fixed points in the advanced time step and then searched for their location at the current time step. A similar approach was expanded upon and reported by Ewing, Russell and Wheeler (1983) in their effort to develop a method for modelling convection dominated flow of the miscible displacement problem that reduced numerical dispersion and mesh orientation effects.

Chiang, Wheeler and Bedient (1989) applied the concept of the modified method of characteristics to the modelling of solute transport in groundwater. Moissis, Miller and Wheeler (1989) extended the concept to model the effects of gravity and heterogeneity on the miscible viscous fingering phenomenon. Russell (1989) made use of an adaptive implicit method (AIM) for time stepping in a FD simulator. His work dealt with multi-phase flow, and offered a compromise between the fully implicit method (FIM) and the IMPES (implicit pressure, explicit saturation) approach.

Single-phase compressible flow. In single-phase flow problems, the emphasis of modelling is on the correct representation of transience and compressibility. Due to its simplicity relative to multi-phase flow problems, the single-phase flow problem was the first to be addressed historically. The work of Zienkiewicz and Cheung (1965) on the use of FEs in heat flow problems provided a sound basis for subsequent researchers who were able to apply such methods to the problem of fluid flow in porous media.

Javandel and Witherspoon (1968) used the Rayleigh-Ritz variational method to model single-phase transient flow of a slightly compressible fluid in a porous medium. They considered a two-dimensional cross section of a layered reservoir intersected by a well and studied the transient radial flow into the well. Their research provided important groundwork for the further use of FEs in the industry.

Dalen (1979) used FEMs to model fully compressible gas flow. He defined a “pseudo-potential” which he substituted for pressure in the governing equations in an attempt to deal with the nonlinearity caused by compressibility of the gas. Logan, Lee and Tek (1985) developed a simulator designed to model well tests using a two-dimensional radial co-ordinate system. The differential equations were partially linearised by substituting the real gas pseudo-pressure for the actual pressure.

Convection-diffusion problems. The differential equations dealt with in this work can be re-arranged in a form that portrays the convection-diffusion nature of the problem, discussed in Chapter 2 (equation (2.34)). Depending upon the magnitude of the Peclet number (equation (2.35)), the problem may be primarily parabolic (diffusion dominated) or hyperbolic (convection dominated).

The standard finite element methods for hyperbolic problems often give results that exhibit spurious oscillations when the exact solution is not smooth. This effect can be reduced by refinement of the mesh, leading to excessive computational costs. Numerous techniques have been developed to deal with this problem, including upwind differencing of the convective term as opposed to central differencing (Hughes, 1978 and Hughes, Liu and Brooks, 1979), the introduction of artificial diffusion (Kelly *et al.,* 1980), or the use of discontinuous trial functions (Johnson, 1987).

While central differencing is second-order accurate, upwind differencing is only first-order accurate, and its use leads to diffuse solutions. The same effect can be obtained by adding diffusion to a central differencing scheme. Brooks and Hughes (1982) developed the streamline upwind/Petrov-Galerkin method, maintaining the robustness of the upwind method but without the diffusive characteristics. The principle was to add diffusion acting only in the flow direction. The standard Galerkin weighting functions were modified by incorporating a streamline upwind perturbation.

Diaz-Munio and Wellford (1981a and 1981b) showed improvements in the accuracy of results for steady state compressible fluid flow problems dominated by convection when they used singular-perturbation basis functions. Jensen and Finlayson (1980) provided criteria for the Peclet number for which oscillations were likely to occur. They reported that when using a FEM to solve the one-dimensional steady state equation using either linear or quadratic basis functions, oscillations could occur when the product of the Peclet number and the mesh spacing was greater than 2, which was similar to the criterion that applied to the FD method.

Miscible displacement and compositional models. Of all the types of petroleum reservoir problems, the miscible displacement problem has attracted most attention from the FE community. The governing equations are truly convective in nature and the numerical issues such as dispersion and mesh orientation effects discussed in the previous section therefore also apply here. The requirement to occasionally track the hydrocarbon components in addition to the physical phases (compositional models) adds complexity to the problem.

Darlow, Ewing and Wheeler (1982) used mixed FE methods to compute simultaneous solutions to the velocity and pressure fields, with the aim of obtaining more accurate estimates of the velocity. Ewing and Heinemann (1983) used a mixed FE approach to improve the accuracy of the phase velocities by considering the Darcy velocities as primary variables. The velocities derived in this manner were then incorporated into a FD simulator for the remainder of the simulation. They reported a reduction in numerical dispersion, resulting in an improvement in the definition of fronts and better defined fingering when compared with more standard techniques, but noted that the method still suffered from mesh orientation effects.

Ewing, Russell and Young (1989) extended their previous work on miscible displacement to address the issues of reservoir heterogeneity and viscous fingering. Their aim was to replicate the results of fine meshing with a coarse mesh by making use of an anisotropic dispersion term. Kelkar and Gupta (1991) used a FE routine to study the development of instabilities, or fingering, in miscible displacement processes caused by unfavourable mobility ratios.

Durlofsky and Chien (1993) developed a fully compositional mixed FE based simulator in which they expressed the three-phase, multi-component flow equations in terms of a global pressure equation, consisting of a total velocity Darcy equation and total mass balance equations, together with a sequence of component mass balance equations. This separated the governing equations into parabolic and hyperbolic sets, each of which could then be solved with an appropriate method. The parabolic pressure equation was solved using mixed FEs while the hyperbolic component mass balance equations were solved using finite volume methods.

Immiscible flow. Mc Michael and Thomas (1971, 1973) developed a FEM to model multi-dimensional, multi-phase flow of compressible fluids. Their results were reportedly superior to those obtained using FDMs, but suffered from the usual negative consequences of excessive computational cost. FE techniques were further developed by Spivak, Price and Settari (1976, 1977) for modelling the Buckley-Leverett problem. They obtained good agreement with analytical results for the water saturation front. Lewis, Norris and France (1975) reviewed the modelling of the movement of the gas-water interface resulting from withdrawal of gas from a well located at the centre of a radial reservoir. They modelled each of the two phases, compressible gas and incompressible water, separately, and coupled the two solutions via the boundary conditions.

Chavent *et al.* (1980) used mixed FEs to model a water flood in two dimensions, with both the water and the oil assumed to be incompressible. Their novel approach was to define only two dependent variables governing the average oil and water flow vector, namely the reduced water saturation and a fictitious pressure, referred to as the 'global pressure'. These variables were then solved with a mixed FEM. Chavent and Jaffre (1986), in a text on the subject, demonstrated the use of the method for multiple dimensions and a variety of fluid descriptions.

Gottardi and Mesini (1987) modelled a two-dimensional, two-phase problem involving gas and oil in which they solved oil pressure and saturation simultaneously. Kukreti *et al.* (1988) modelled two-phase flow of immiscible and incompressible fluids moving through a compressible reservoir in which they solved oil pressure and water saturation.

Kaluarachchi and Parker (1989), in their study of groundwater contamination, modelled the simultaneous flow of water and oil using FEMs. They used both the Picard and the Newton-Raphson schemes for iteration and reported comparable convergence performance provided that upstream weighting was used with the Picard scheme, allowing significant reduction in computing time. Khataniar and Peters (1990) modelled two-phase flow using FEMs. The transmissibility was evaluated at the upstream node of each element rather than at quadrature points. They modelled the well known one-dimensional Buckley-Leverett displacement. They reported a significant improvement in the match in the simulated results when upstream weighting was used.

Langtangen (1990), in a thorough investigation into the subject, discussed the various numerical approaches in use for modelling immiscible, two-phase incompressible flow. He used the Newton-Raphson iteration method and applied ILU preconditioned conjugate gradient like methods to the non-symmetric matrix system in each iteration. Sukirman and Lewis (1993) presented an iterative scheme for simultaneously solving the highly nonlinear, fully coupled equations describing three-phase flow of compressible fluids in a compressible reservoir.

Improvements in efficiency. Peters and Kasap (1986), in their work on miscible displacement, considered ways of reducing the computational burden of FEMs. They evaluated the transport properties at the centre of each element, rather than at the Gauss points. They reported a 30% decrease in computational time requirements. They also reported less mesh orientation effects. Sagar (1978), in a study of groundwater, demonstrated the use of a method that incorporated geological uncertainty into the FE algorithm and produced a probability distribution of the output.

In more recent years parallel computing has received much attention. Coutinho and Alves (1996) developed a parallel FE technique for miscible displacement. The pressure was approximated by a FEM, and the velocity approximated through a post-processing approach that ensured the required degree of accuracy. The pressure, velocity and concentration linear system of equations were solved with parallel element by element iterative techniques.

3.1.2 Simulation of flow in a fractured reservoir

The dual porosity model with incompressible or slightly compressible water. The research of Duguid and his co-workers undertaken in the early 1970's resulted in two published works (Duguid and Lee, 1977 and Duguid and Abel, 1974) which are recognised as milestones in the application of FE techniques to fluid flow in naturally fractured rock formations. The research findings of Duguid and co-workers have formed the basis for most subsequent work in groundwater applications and are cited extensively in the literature. They built on the theoretical work of Warren and Root (1963), and of Odeh (1965), to develop a FEM for modelling the flow of incompressible water through fractured media. They modelled the fractured reservoir with two continua, linked via a semi-analytical transfer function, in a routine that could be classified within the broader definition of a dual porosity-dual permeability model.

Huyakorn, Lester and Faust (1983) used a FEM to model the flow of incompressible water in the fracture network of an aquifer. They investigated a discrete fracture model and two approaches for dealing with the transfer function in a dual porosity model, namely a FD scheme and a convolution integral. The dual porosity approaches were used to model unsteady state flow from spherical and from prismatic matrix blocks. They reported greater accuracy in results obtained using the combined FE convolution integral approach compared with those obtained using the combined FE-FD approach.

This was due to the steep gradients existing at the matrix-fracture interface at early times that could not easily be captured in the FD model.

Lewis *et al.* (1998) presented a dual porosity model for single-phase flow in a fractured reservoir, coupled to the equations governing deformation, with the purpose of determining the influence that fractures have on the consolidation of a column.

Dual porosity petroleum models. Lefebvre and Weill (1974) used a front tracking method to model the migration and deformation of the water-oil interface within fractures during production. They modelled the reservoir as two continuous media. The FE mesh was adjusted to coincide and track the oil-water contact as it migrated through the reservoir.

Douglas *et al.* (1987) proposed a method for modelling a single-phase fluid of constant compressibility flowing through a fractured porous medium with FEs. Their approach was to adopt the conventional dual porosity model (see Section 2.2.3). They provided an excellent description of the process to follow, but did not present the results of any implementation of the technique. Bhatia, Advani and Lee (1989) used FEs to model two-phase, immiscible and incompressible, or slightly compressible, flow in a one-dimensional dual porosity-dual permeability representation of a fractured reservoir. They made use of a conventional transfer function.

Explicit fractures. Asfari and Witherspoon (1973) utilised the meshing flexibility of the FEM to model discrete fractures, embedded in a matrix continuum, explicitly. They used the conventional fracture permeability (equation (2.56)) and successfully applied the FEM to study the influence of fracture spacing and density on reservoir permeability anisotropy under steady state flowing conditions. Gureghian (1975) studied the effects of the orientation of fractures in proximity to, and also of fractures intersecting, a flowing well. He considered a single-phase, incompressible fluid and modelled the matrix using tetrahedral volume elements with the fractures explicitly modelled as triangles coinciding with the edges of the tetrahedra. He used linear basis functions to approximate the potential.

Kelkar and Zyvoloski (1991) developed a three-dimensional FE simulator in which individual fractures were modelled explicitly. Their formulation allowed fracture aperture and consequently permeability and porosity to vary according to pressure and temperature changes resulting from the injection of cold water into petroleum reservoirs. Kikani (1991) studied the flow in a single fracture, with special attention being paid to the tips of a fracture of finite length, the objective being to understand the distribution of flux along the length of the fracture. He used a variety of higher order elements and discretization approaches.

Associated problems. Besides the FEM and the FDM, several alternative approaches that are mostly variations on these two primary techniques, have been proposed to solve fractured reservoir problems. Narasimham (1982) used an integral FD scheme that allowed the use of a flexible mesh, suitable for modelling discrete fractures. Shapiro and Andersson (1983) modelled water flow through a series of discrete fractures under steady state conditions using a boundary element method.

FEMs have also been used to solve other types of transport problems in fractured reservoirs. In their study of nuclear waste disposal, Huyakorn, Lester and Mercer (1983a and b) used FEMs to model the movement of solutes through the fractures and into the matrix. Within the fracture network, they considered an advection-dispersion equation which they solved using upstream weighting to control oscillations. Diffusion of solute into matrix blocks was solved using a conventional FE technique. They approximated the matrix blocks with spheres and prisms, represented with one-dimensional elements. Elsworth (1986 and 1987) used a combination of FEs and boundary elements to model water flow in aquifers in his study of toxic waste disposal. Elsworth utilised FEs in those regions for which available data justified a detailed description such as discrete fractures, and the boundary element approach to the remaining regions of poor definition. Gerke and van Genuchten (1993) used a dual porosity-dual permeability model to evaluate the movement of water and solutes in fractured reservoirs. Transport of solute was modelled with the convection-dispersion equation.

3.1.3 Concluding remarks

Finite element methods have not been used as extensively as finite difference methods for solving petroleum reservoir flow problems in general, and fractured reservoir problems in particular, due primarily to their historically greater computational overheads and to the intuitively simpler approach of the finite difference method when applied to this type of problem. In contrast, finite element methods are routinely used for the modelling of incompressible single phase groundwater problems, although these have mostly been restricted to single porosity problems. The research in this area is highly advanced and provides useful insight into the challenges encountered in this type of problem.

The convective nature of many petroleum related problems, particularly the miscible displacement problem, requires special attention when the finite element method is being used, as the results may exhibit spurious oscillations when the exact solution is not smooth. Much of the research on finite element methods has been dedicated to this problem, and has included work relating to mesh refinement, upwind differencing, the introduction of artificial diffusion and the use of discontinuous trial functions.

Where finite element methods have been used for modelling fractured reservoirs, this work has been largely restricted to the application of the conventional dual porosity model within a finite element context. Additionally, these models have been restricted to incompressible or slightly compressible fluids.

3.2 A finite element solution for the governing equations

The governing equations that were derived and discussed in Chapter 2 are recounted here in an appropriate form, and then it is shown how the FEM is used to obtain an approximate solution to the general form of these equations. Development of the formulation follows a conventional route and reference is made throughout to the texts of Burnett (1987), Zienkiewicz and Taylor (1967) and Dhatt and Touzot (1984). Challenges encountered in the development of the numerical technique which are particular to this problem include the need to deal with nonlinearities together with the coupling of the matrix and fracture algorithms into a single algorithm which represents a novel application of the FEM.

3.2.1 Summary of the governing equations

In this work the fracture network is modelled with at most a two-dimensional representation, while each matrix block is reduced to a one-dimensional model. It is convenient to distinguish between the fracture network and the matrix model by electing to use the x-y plane for representing the two-dimensional fracture network and the z-axis for the independent spatial co-ordinate of the matrix block(s). The governing equation for the fracture network in two dimensions follows from equation (2.86) and has the form

$$-\left(\frac{\partial}{\partial x}\left(\alpha_{fx}\frac{\partial P_f}{\partial x}\right)+\frac{\partial}{\partial y}\left(\alpha_{fy}\frac{\partial P_f}{\partial y}\right)\right)+\beta_f\left(\frac{\partial P_f}{\partial t}\right)=f_f, \tag{3.1}$$

in which

$$P_f = P_f(x,y,t),$$

$$\alpha_{fx,y}=\alpha_{fx,y}(x,y,P_f(x,y,t))=\frac{\rho(P_f(x,y,t))k_{fx,y}(x,y)}{\mu(P_f(x,y,t))}, \tag{3.2}$$

$$\beta_f=\beta_f(x,y,P_f(x,y,t))=\rho(P_f(x,y,t))c_{ft}\phi_f(x,y,P_f(x,y,t)) \text{ and} \tag{3.3}$$

$$-f_f=-f_f(x,y,t)=q_{mf}(x,y,t)-q_{cf}(x,y,t). \tag{3.4}$$

The corresponding equation in one dimension used for modelling the matrix blocks comes from equation (2.87) and has the form

$$-\frac{\partial}{\partial z}\left(\alpha_{mz}\frac{\partial P_m}{\partial z}\right)+\beta_m\left(\frac{\partial P_m}{\partial t}\right)=f_m, \tag{3.5}$$

in which

$$P_m = P_m(z,t),$$

$$\alpha_{mz}=\alpha_{mz}(z,P_m(z,t))=\frac{\rho(P_m(z,t))k_m(z)}{\mu(P_m(z,t))}, \tag{3.6}$$

$$\beta_m=\beta_m(z,P_m(z,t))=\rho(P_m(z,t))c_{mt}\phi_m(z,P_m(z,t)) \text{ and} \tag{3.7}$$

$$-f_m=-f_m(z,t)=-q_{mf}(z,t). \tag{3.8}$$

Henceforth in this chapter, the subscripts m (matrix) and f (fracture) are dropped from the equations for simplicity. The (x,y) co-ordinate system describes the fracture network, the (z) co-ordinate describes the matrix material, and where equations are generic and apply to either co-ordinate system, the $(\mathbf{x})$ co-ordinate is used.

3.2.2 The Galerkin method of weighted residuals

Expressions 3.5 and 3.1 describing the initial boundary value problem in one and two dimensions respectively can be written in the form

$$A(P) = f_{\Omega}, \text{ on domain } \Omega, \tag{3.9}$$

in which the variable P is a function of geometric position and time, and A is a nonlinear partial differential operator representing the lefthand side of (3.5) or (3.1). Additionally, boundary conditions must be specified over the whole boundary S, of Ω for $t > t_0$, or

$$S(P) = f_S. \tag{3.10}$$

These can be in the form of a condition on P, (Dirichlet or Essential Boundary Conditions, (EBCs)), or in the form of a condition on the flux, $\boldsymbol{n} \cdot \nabla P$ (Neuman or Natural Boundary Conditions (NBCs)), or a combination of both types.

Typically, an EBC would be used to describe a constant pressure boundary brought about by a pressure maintenance program in a reservoir. NBCs may be concentrated at points or distributed along part or all of the boundary. An NBC would be specified to describe influx of water from an active aquifer, or conversely, the presence of a no-flow boundary. In addition, Internal Load Conditions (ILCs) may be defined that describe the flux to or from the domain other than through the boundary. Typically, ILCs would be used to model the extraction of reservoir fluids via a production well or the injection of fluids via an injection well.

Finally, initial conditions

$$P = P_0 \text{ on } \Omega \text{ for } t = t_0, \tag{3.11}$$

are required to solve for P in space and time.

The residual function R is defined by

$$R(Q) = A(Q) - f_{\Omega}, \tag{3.12}$$

for any function Q. Clearly R vanishes when $Q = P$, the solution of equations (3.9), (3.10) and (3.11). Rather than solving the partial differential equations (3.9), (3.10) and (3.11) directly, the weighted residual method involves searching for a solution $\tilde{P}$ that satisfies the integral equation

$$W = \int_{\Omega} \Psi R(\tilde{P}) d\Omega = 0, \tag{3.13}$$

where Ψ is a set of weighting functions. An approximate solution is sought of the form

$$\tilde{P}(\boldsymbol{x}, t) = \sum_{j=1}^{N} a_j(t) \psi_j(\boldsymbol{x}), \tag{3.14}$$

in which the basis functions, ψ_j, are algebraic expressions, typically polynomials, and a_j are time dependent parameters. In the Galerkin method of weighted residuals, the weighting functions of expression (3.13) are selected to be the basis functions of expression (3.14). This leads to

$$W_i = \int_{\Omega} \psi_i \left(A(\tilde{P}) - f_{\Omega} \right) d\Omega = 0, \text{ for } i = 1 \text{ to } N, \text{ or} \tag{3.15}$$

$$W_i = \int_{\Omega} \psi_i \left(A\left(\sum_{j=1}^{N} a_j \psi_j \right) - f_{\Omega} \right) d\Omega = 0, \text{ for } i = 1 \text{ to } N. \tag{3.16}$$

The two-dimensional fracture network equations

If A is taken to be the operator defined by (3.1), then (3.15) becomes

$$W_i = \iint_{\Omega} \left(-\frac{\partial}{\partial x}\left(\alpha_x \frac{\partial \tilde{P}}{\partial x}\right) - \frac{\partial}{\partial y}\left(\alpha_y \frac{\partial \tilde{P}}{\partial y}\right) + \beta \frac{\partial \tilde{P}}{\partial t} - f \right) \psi_i dxdy = 0 \text{, for } i = 1 \text{ to } N. \tag{3.17}$$

If the chain rule for differentiation is applied to the first two terms of the integrand, then

$$W_i = -\iint_{\Omega} \left(\frac{\partial}{\partial x}\left(\alpha_x \frac{\partial \tilde{P}}{\partial x}\psi_i\right) + \frac{\partial}{\partial y}\left(\alpha_y \frac{\partial \tilde{P}}{\partial y}\psi_i\right)\right) dxdy$$
$$+\iint_{\Omega} \left(\left(\alpha_x \frac{\partial \tilde{P}}{\partial x}\right)\frac{\partial \psi_i}{\partial x} + \left(\alpha_y \frac{\partial \tilde{P}}{\partial y}\right)\frac{\partial \psi_i}{\partial y} + \beta\psi_i \frac{\partial \tilde{P}}{\partial t} - f\psi_i \right) dxdy = 0 \text{, for } i = 1 \text{ to } N. \tag{3.18}$$

If the divergence theorem is applied to the first integral of expression (3.18), it becomes

$$-\oint_{S} \left(\alpha_x \frac{\partial \tilde{P}}{\partial x}\psi_i n_x + \alpha_y \frac{\partial \tilde{P}}{\partial y}\psi_i n_y \right) ds, \tag{3.19}$$

where ds is the co-ordinate along the surface (boundary) of the domain Ω, and n_x and n_y are directional cosines of the outward normal to the surface (Figure 3.1).

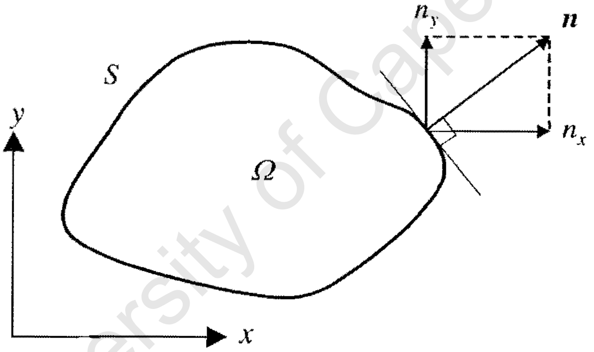

Figure 3.1: *Example of a domain Ω with a surface S.*

The components of the flux term are defined as

$$\tilde{\tau}_x = -\alpha_x \frac{\partial \tilde{P}}{\partial x} \text{, and } \tilde{\tau}_y = -\alpha_y \frac{\partial \tilde{P}}{\partial y}, \tag{3.20}$$

while the outward normal component of the flux is

$$\tilde{\tau}_n = \tilde{\tau}_x n_x + \tilde{\tau}_y n_y. \tag{3.21}$$

By combining expressions (3.19), (3.20) and (3.21) into (3.18) and rearranging, we get

$$W_i = \iint_{\Omega} \left(\beta\psi_i \frac{\partial \tilde{P}}{\partial t} \right) dxdy + \iint_{\Omega} \left(\left(\alpha_x \frac{\partial \tilde{P}}{\partial x}\right)\frac{\partial \psi_i}{\partial x} + \left(\alpha_y \frac{\partial \tilde{P}}{\partial y}\right)\frac{\partial \psi_i}{\partial y} \right) dxdy$$
$$= \iint_{\Omega} f\psi_i dxdy - \oint_{\Omega} \tilde{\tau}_n \psi_i ds \text{, for } i = 1 \text{ to } N. \tag{3.22}$$

If the general form of the solution (3.14) is used in (3.22), then this becomes

$$W_i = \sum_{j=1}^{n}\left(\iint_{\Omega} \psi_i \beta \psi_j dxdy\right)\frac{\partial a_j}{\partial t} + \sum_{j=1}^{n}\left(\iint_{\Omega} \frac{\partial \psi_i}{\partial x}\alpha_x \frac{\partial \psi_j}{\partial x} dxdy + \iint_{\Omega} \frac{\partial \psi_i}{\partial y}\alpha_y \frac{\partial \psi_j}{\partial y} dxdy\right)a_j$$
$$= \iint_{\Omega} f\psi_i dxdy + \oint_{\Omega} \tilde{\tau}_{-n}\psi_i ds \text{, for } i = 1 \text{ to } N. \tag{3.23}$$

These equations (3.23) can be expressed in the matrix form

$$\boldsymbol{C}(\boldsymbol{a}(t))\frac{d\boldsymbol{a}(t)}{dt} + \boldsymbol{K}(\boldsymbol{a}(t))\boldsymbol{a}(t) = \boldsymbol{F}(t,\boldsymbol{a}(t)), \tag{3.24}$$

in which $\boldsymbol{a}$ is a vector with components a_j and the 'capacity' and 'stiffness' matrices and the 'load' vector are defined by

$$C_{ij}(\boldsymbol{a}(t)) = \iint_{\Omega} \psi_i(x,y)\beta(x,y,\boldsymbol{a}(t))\psi_j(x,y)dxdy, \tag{3.25}$$

$$K_{ij}(\boldsymbol{a}(t)) = \iint_{\Omega} \frac{\partial \psi_i(x,y)}{\partial x}\alpha_x(x,y,\boldsymbol{a}(t))\frac{\partial \psi_j(x,y)}{\partial x}dxdy$$
$$+\iint_{\Omega} \frac{\partial \psi_i(x,y)}{\partial y}\alpha_y(x,y,\boldsymbol{a}(t))\frac{\partial \psi_j(x,y)}{\partial y}dxdy, \tag{3.26}$$

and

$$F_i(t,\boldsymbol{a}(t)) = Ff_i(t) + F\tau_i(\boldsymbol{a}(t))\iint_{\Omega} f(x,y,t)\psi_i(x,y)dxdy$$
$$+\oint_{\Omega} \tilde{\tau}_{-n}(x,y,t,\boldsymbol{a}(t))\psi_i(x,y)ds \text{, for } i,j = 1 \text{ to } N. \tag{3.27}$$

The one-dimensional matrix block equations

Development of the equations for the one-dimensional case proceeds in exactly the same fashion as above, beginning with equation (3.5). The result is a set of equations that is similar to (3.24) but with only one spatial variable, z, so that, for every (x,y) pair,

$$C_{ij}(\boldsymbol{a}(t)) = \int_{\Omega} \psi_i(z)\beta(z,\boldsymbol{a}(t))\psi_j(z)dz, \tag{3.28}$$

$$K_{ij}(\boldsymbol{a}(t)) = \int_{\Omega} \frac{\partial \psi_i(z)}{\partial z}\alpha(z,\boldsymbol{a}(t))\frac{\partial \psi_j(z)}{\partial z}dz \tag{3.29}$$

and

$$F_i(t) = Ff_i(t) + F\tau_i(t,\boldsymbol{a}(t)) = \int_{\Omega} f(z,\boldsymbol{a}(t))\psi_i(z)dz - \left[\tilde{\tau}(z,t,\boldsymbol{a}(t))\psi_i(z)\right]_{\Omega} \text{for } i = 1 \text{ to } N. \tag{3.30}$$

3.2.3 The finite element method

The finite element method provides a means for the systematic construction of the basis functions ψ_j (3.14). This is achieved by dividing the domain Ω into E nonoverlapping subdomains or elements Ω^e, and defining basis functions ψ_j^e on each element individually. In two dimensions the elements are typically triangles or quadrilaterals and provision can be made for curvilinear edges (Figure 3.2).

Nodal points are defined independently and distributed throughout the domain and on its boundary. The vertex of every element must however, be defined by a node. The two-dimensional elements illustrated in Figure 3.2 are 4-node bilinear quadrilateral (A), 8-node serendipity (B), 3-node linear triangular (C) and 6-node quadratic triangular (D) elements. The one-dimensional elements illustrated are 2-node linear (E), 3-node quadratic (F) and 5-node quartic (G) elements.

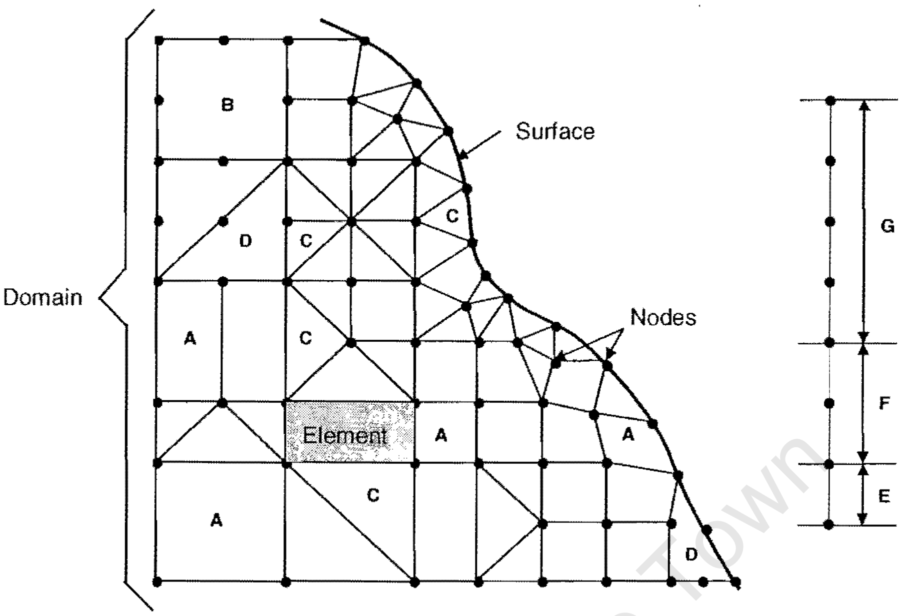

Figure 3.2: *Examples of a two-dimensional domain (lefthand side) and a one-dimensional domain (righthand side) divided into elements with nodal points.*

The basis functions are selected over the entire domain so that

$$\psi_j(x_i) = \delta_{ji}\text{, for } i, j = 1 \text{ to } N, \tag{3.31}$$

where N is the number of nodal points and x_j are their locations. In each element, polynomial basis functions, ψ_j^e, are defined (illustrated in Figure 3.3 in one-dimension) such that

$$\psi_j^e = \psi_j\big|_{\Omega^e}. \tag{3.32}$$

While ψ_j^e is defined on element e only, the basis functions ψ_j are continuous across adjacent elements. Such functions are said to be of class C^n if the function and its first n derivatives are continuous. The basis function illustrated in Figure 3.3 is therefore C^0 continuous.

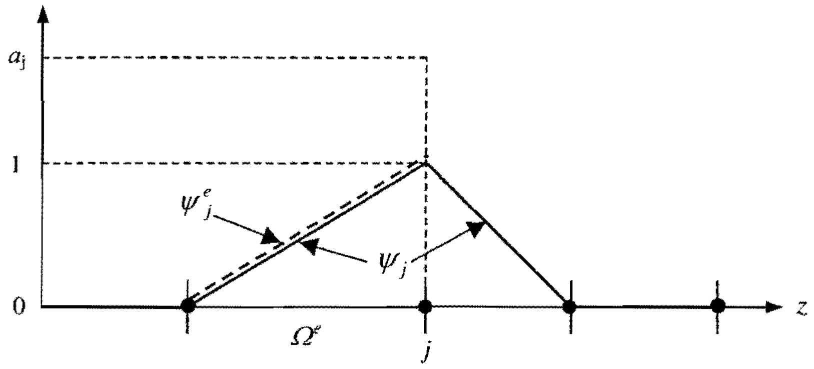

Figure 3.3: *Example of a string of one-dimensional 2-node linear finite elements showing the relationship between ψ_j and ψ_j^e.*

The approximation, $\tilde{P}$, on Ω^e is given by

$$\tilde{P}^e(x,t)=\sum_{j=1}^{N_e}a_j^e(t)\psi_j^e(x), \tag{3.33}$$

where N_e is the number of interpolation nodal points in element e and a_j^e are the nodal parameters of e. The approximation over the whole domain is then

$$\tilde{P}(x,t)=\sum_{e=1}^{E}P^e(x,t). \tag{3.34}$$

From 3.31 to 3.33 it follows that each $a_j(t)$ of expression (3.14) is the value of the function $\tilde{P}(x,t)$ at a nodal point j, or

$$a_j(t)=\tilde{P}(x_j,t)\text{, for } j=1 \text{ to } N. \tag{3.35}$$

Expression (3.13), of the integral over the entire domain is replaced by a summation of sub-domain, or element domain integrals:

$$W=\int_{\Omega}\Psi R(\tilde{P})d\Omega=\sum_{e=1}^{E}W^e=\sum_{e=1}^{E}\int_{\Omega^e}\Psi^e R(\tilde{P})d\Omega=0, \tag{3.36}$$

where

$$W^e=\int_{\Omega^e}\psi_i^e\left(A(\tilde{P}^e)-f_{\Omega^e}\right)d\Omega\text{, for } i=1 \text{ to } N_e\text{, or} \tag{3.37}$$

$$W^e=\int_{\Omega^e}\psi_i^e\left(A\left(\sum_{j=1}^{N_e}a_j^e\psi_j^e\right)-f_{\Omega^e}\right)d\Omega\text{, for } i=1 \text{ to } N_e. \tag{3.38}$$

This assembly of the element equations leads to

$$W=\sum_{e=1}^{E}\boldsymbol{C}^e(\boldsymbol{a}^e(t))\frac{d\boldsymbol{a}^e(t)}{dt}+\boldsymbol{K}^e(\boldsymbol{a}^e(t))\boldsymbol{a}^e(t)-\boldsymbol{F}^e(t,\boldsymbol{a}^e(t)), \tag{3.39}$$

where $\boldsymbol{a}^e(t)$ are the nodal variables associated with Ω^e. In the two-dimensional case,

$$C_{ij}^e(\boldsymbol{a}^e(t))=\iint_{\Omega^e}\psi_i^e(x,y)\beta(x,y,\boldsymbol{a}^e(t))\psi_j^e(x,y)dxdy, \tag{3.40}$$

$$\begin{aligned}K_{ij}^e(\boldsymbol{a}^e(t))=&\iint_{\Omega^e}\frac{\partial\psi_i^e(x,y)}{\partial x}\alpha_x(x,y,\boldsymbol{a}^e(t))\frac{\partial\psi_j^e(x,y)}{\partial x}dxdy,\\&+\iint_{\Omega^e}\frac{\partial\psi_i^e(x,y)}{\partial y}\alpha_y(x,y,\boldsymbol{a}^e(t))\frac{\partial\psi_j^e(x,y)}{\partial y}dxdy,\end{aligned} \tag{3.41}$$

and

$$\begin{aligned}F_i^e(t,\boldsymbol{a}^e(t))=&Ff_i^e(t)+F\tau_i^e(\boldsymbol{a}^e(t))\iint_{\Omega^e}f(x,y,t)\psi_i^e(x,y)dxdy\\&+\oint_{\Omega^e}\tilde{\tau}_{-n}^e(x,y,t,\boldsymbol{a}^e(t))\psi_i^e(x,y)ds\text{, for } i,j=1 \text{ to } N_e.\end{aligned} \tag{3.42}$$

In the one-dimensional case, for each (x,y) pair,

$$C_{ij}^e(\boldsymbol{a}^e(t))=\int_{\Omega^e}\psi_i^e(z)\beta(z,\boldsymbol{a}^e(t))\psi_j^e(z)dz, \tag{3.43}$$

$$K_{ij}^e(t)=\int_{\Omega}\frac{\partial\psi_i^e(z)}{\partial z}\alpha\left(z,\boldsymbol{a}^e(t)\right)\frac{\partial\psi_j^e(z)}{\partial z}dz\,, \tag{3.44}$$

and

$$F_i^e(t)=Ff_i^e(t)+F\tau_i^e\left(t,\boldsymbol{a}^e(t)\right)=\int_{\Omega}f\left(z,\boldsymbol{a}^e(t)\right)\psi_i^e(z)dz-\left[\tilde{\tau}^e\left(z,t,\boldsymbol{a}^e(t)\right)\psi_i^e(z)\right]_{\Omega^e}\,,$$
$$\text{for } i=1 \text{ to } N_e\,. \tag{3.45}$$

3.2.4 Basis functions and development of the element equations

In this section, basis functions are reviewed for three one-dimensional and for three, two-dimensional elements and the corresponding element matrices are built.

One-dimensional C^0 elements

The one-dimensional, linear element. A one-dimensional element of length L with two nodes located at z_1 and z_2 has linear basis functions

$$\psi_1^e(z)=\frac{z_2-z}{z_2-z_1} \text{ and } \psi_2^e(z)=\frac{z-z_1}{z_2-z_1}\,. \tag{3.46}$$

The physical parameters are evaluated in the centre of the element,

$$\alpha^e(t)=\alpha(z_c,t) \text{ and } \beta^e(t)=\beta(z_c,t)\text{, with } z_c=\frac{1}{2}(z_1+z_2)\,. \tag{3.47}$$

By substituting these expressions into the element equations, (3.43) to (3.45), and into the flux equation (3.20), integrating and simplifying we get

$$C_{11}^e(t)=C_{22}^e(t)=\frac{\beta^e(t)L}{3}\,,\quad C_{12}^e(t)=C_{21}^e(t)=\frac{\beta^e(t)L}{6}\,, \tag{3.48}$$

$$K_{11}^e(t)=K_{22}^e(t)=-K_{12}^e(t)=-K_{21}^e(t)=\frac{\alpha^e(t)}{L}\,, \tag{3.49}$$

$$F_1^e(t)=\frac{f^e(t)L}{2}+\tilde{\tau}^e(z_1,t)\,,\; F_2^e(t)=\frac{f^e(t)L}{2}-\tilde{\tau}^e(z_2,t)\text{, with } f^e(t)=f(z_c,t) \text{ and} \tag{3.50}$$

$$\tilde{\tau}^e(z,t)=-\alpha(z,t)\frac{a_2(t)-a_1(t)}{z_2-z_1}\,. \tag{3.51}$$

One-dimensional C^0 isoparametric suite of elements

The isoparametric approach to building elements utilises a single standard 'parent' element that is defined in a convenient fashion in a fictitious co-ordinate system (the parent co-ordinate system), and upon which the basis functions, the trial solution and element equations are defined. The parent element is linked to the real elements defined in the co-ordinate system in which the physical problem exists through a procedure that maps the co-ordinates of the parent element onto each of the real elements via an isoparametric transformation.

The spatial co-ordinate in the parent system is denoted (ζ), to distinguish it from the real co-ordinate, (z). The two co-ordinate systems are linked via a transformation particular to each real element that maps each point in the parent element to a unique point in the real element,

$$z = \chi^e(\zeta) . \tag{3.52}$$

The lower and upper limits of the parent element in this co-ordinate system lie at $\zeta = -1$ and $\zeta = +1$ respectively (Figure 3.4).

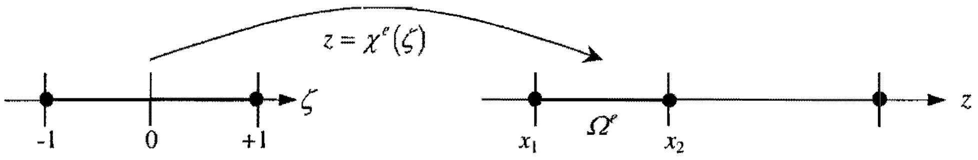

Figure 3.4: *Diagram showing the transformation from the parent co-ordinate system on the lefthand side to the real co-ordinate system on the righthand side.*

The trial solution in the parent element, $\tilde{P}(\zeta,t;a)$, is made up, analogous to expressions (3.33) and (3.34), of basis functions defined in the parent co-ordinate system, $\hat{\psi}_j(\zeta)$, between these limits, so that

$$\tilde{P}(\zeta,t;a) = \sum_{j=1}^{N_e} a_j^e(t)\hat{\psi}_j(\zeta) , \tag{3.53}$$

and

$$\hat{\psi}_j(\zeta) = \psi_j^e(z) . \tag{3.54}$$

The basis functions used here are Lagrange polynomials of general degree p,

$$\hat{\psi}_j = \frac{(\zeta-\zeta_1)(\zeta-\zeta_2)\ldots(\zeta-\zeta_{j-1})(\zeta-\zeta_{j+1})\ldots(\zeta-\zeta_L)(\zeta-\zeta_{p+1})}{(\zeta_j-\zeta_1)(\zeta_j-\zeta_2)\ldots(\zeta_j-\zeta_{j-1})(\zeta_j-\zeta_{j+1})\ldots(\zeta_j-\zeta_L)(\zeta_j-\zeta_{p+1})} , \tag{3.55}$$

with $j = 1,2,3,\ldots,p+1$. For isoparametric mapping, the co-ordinate transformation function is a linear combination of the parent basis functions and the co-ordinates in the real element, or

$$z = \sum_{k=1}^{l} z_k^e \hat{\psi}_k(\zeta) , \tag{3.56}$$

where z_k^e are the co-ordinates of the l nodes of element e. The selection of Lagrange basis functions means that interpolation property

$$\hat{\psi}_j(\zeta_i) = \delta_{ji} = \psi_j^e(z_i) , \tag{3.57}$$

holds in both the parent and the real elements. In order to transform the element equations, the derivative of the basis functions,

$$\frac{d\psi_i^e(z)}{dz} = \frac{d\psi_i^e(\chi^e(\zeta))}{d\zeta}\frac{d\zeta}{dz} = \frac{1}{J^e(\zeta)}\frac{d\hat{\psi}_i(\zeta)}{d\zeta} , \text{ where } J^e(\zeta) = \frac{dz}{d\zeta} , \tag{3.58}$$

the physical properties,

$$\alpha(z,t) = \alpha(\chi^e(\zeta),t) = \alpha^e(\zeta,t) \text{ and } \beta(z,t) = \beta(\chi^e(\zeta),t) = \beta^e(\zeta,t) , \tag{3.59}$$

and the integral itself,

$$\int_{z_1}^{z_3} I(z)dz = \int_{\zeta(z_1)}^{\zeta(z_3)} I(\chi^e(\zeta))J^e(\zeta)d\zeta , \tag{3.60}$$

are evaluated. These expressions are necessary for transforming the element equations from the real co-ordinate system into the parent domain before applying numerical integration. When these transformations are performed, the expressions for the element equations become

$$C_{ij}^e(t)=\int_{-1}^{+1}\hat{\psi}_i(\zeta)\beta^e(\zeta,t)\hat{\psi}_j(\zeta)J^e(\zeta)d\zeta\,, \tag{3.61}$$

$$K_{ij}^e(t)=\int_{-1}^{+1}\left(\frac{1}{J^e(\zeta)}\frac{d\hat{\psi}_i(\zeta)}{d\zeta}\right)\alpha^e(\zeta,t)\left(\frac{1}{J^e(\zeta)}\frac{d\hat{\psi}_j(\zeta)}{d\zeta}\right)J^e(\zeta)d\zeta \text{ and} \tag{3.62}$$

$$Ff_i^e(t)=\int_{-1}^{+1}f^e(\zeta,t)\hat{\psi}_i(\zeta)J^e(\zeta)d\zeta \text{ and } F\tau_i^e(t)=-\left[\tau^e(z,t)\psi_i^e(z)\right]_{z_1}^{z_3}. \tag{3.63}$$

In this work, integration is performed by approximation via the quadrature rule

$$\int_{-1}^{+1}I(\zeta)d\zeta\cong\sum_{l=1}^{n}w_{nl}I(\zeta_{nl}), \tag{3.64}$$

where w_{nl} are weighting factors and ζ_{nl} are Gauss points. In the program developed for this work, Gauss-Legendre quadrature rules have been used, the integration points and weights of which are listed for n=1 to 5, in Burnett (1987), p319. The expression for the flux,

$$\tilde{\tau}^e(z,t)=-\alpha^e(z,t)\sum_{j=1}^{n}a_j(t)\frac{d\psi_j^e(z)}{dz}=-\alpha\left(\chi^e(\zeta)\right)\sum_{j=1}^{n}a_j(t)\frac{d\psi_j^e\left(\chi^e(\zeta)\right)}{d\zeta}\frac{d\zeta}{dz}, \tag{3.65}$$

can be written with reference to the Gauss points as

$$\tilde{\tau}^{(e)}(\zeta,t)=-\alpha^{(e)}(\zeta,t)\sum_{j=1}^{n}a_j(t)\frac{d\hat{\psi}_j(\zeta)}{d\zeta}\frac{1}{J^{(e)}(\zeta)}. \tag{3.66}$$

The one-dimensional C^0 quadratic isoparametric element. The one-dimensional quadratic element has 3 nodes, evenly spaced in the parent co-ordinate system at $\zeta=-1, 0, +1$. The trial and basis functions and their derivatives in the parent element are

$$\begin{aligned}
&\hat{\psi}_1(\zeta)=\frac{1}{2}\zeta(\zeta-1), && \frac{d\hat{\psi}_1(\zeta)}{d\zeta}=\zeta-\frac{1}{2},\\
&\hat{\psi}_2(\zeta)=(1+\zeta)(\zeta-1), && \frac{d\hat{\psi}_2(\zeta)}{d\zeta}=-2\zeta,\\
&\hat{\psi}_1(\zeta)=\frac{1}{2}\zeta(\zeta+1) \text{ and} && \frac{d\hat{\psi}_3(\zeta)}{d\zeta}=\zeta+\frac{1}{2}.
\end{aligned} \tag{3.67}$$

The expression for the Jacobian, J, is

$$J^e(\zeta)=\left(\zeta-\frac{1}{2}\right)z_1^e-2\zeta z_2^e+\left(\zeta+\frac{1}{2}\right)z_3^e. \tag{3.68}$$

By making use of the interpolation property, the boundary load simplifies to

$$F\tau^e=\begin{Bmatrix}\tau^e(z_1)\\0\\\tau^e(z_3)\end{Bmatrix}. \tag{3.69}$$

The optimal flux-sampling points are the Gauss points for the two-point rule, $\zeta = \pm 1/\sqrt{3}$. Nodal fluxes are determined via the straight line interpolation polynomial through these points. At inter-element nodes the element nodal fluxes from adjacent elements are averaged.

The one-dimensional C^0 quartic isoparametric element. The basis functions are fourth degree Lagrange interpolation polynomials and the nodes in the parent element are equally spaced at $\zeta = -1, -1/2, 0, +1/2, +1$. The resulting equations are

$$\begin{aligned}
\hat{\psi}_1(\zeta) &= \frac{2}{3}\left(\zeta+\frac{1}{2}\right)\zeta\left(\zeta-\frac{1}{2}\right)(\zeta-1), & \frac{d\hat{\psi}_1(\zeta)}{d\zeta} &= -\frac{2}{3}\left(4\zeta^3-3\zeta^2-\frac{1}{2}\zeta+\frac{1}{4}\right),\\
\hat{\psi}_2(\zeta) &= -\frac{8}{3}(\zeta+1)\zeta\left(\zeta-\frac{1}{2}\right)(\zeta-1), & \frac{d\hat{\psi}_2(\zeta)}{d\zeta} &= -\frac{8}{3}\left(4\zeta^3-\frac{3}{2}\zeta^2-2\zeta+\frac{1}{2}\right),\\
\hat{\psi}_3(\zeta) &= 4(\zeta+1)\left(\zeta+\frac{1}{2}\right)\left(\zeta-\frac{1}{2}\right)(\zeta-1), & \frac{d\hat{\psi}_3(\zeta)}{d\zeta} &= 4\left(4\zeta^3-\frac{5}{2}\zeta\right),\\
\hat{\psi}_4(\zeta) &= -\frac{8}{3}(\zeta+1)\left(\zeta+\frac{1}{2}\right)\zeta(\zeta-1), & \frac{d\hat{\psi}_4(\zeta)}{d\zeta} &= -\frac{8}{3}\left(4\zeta^3+\frac{3}{2}\zeta^2-2\zeta-\frac{1}{2}\right),\\
\hat{\psi}_5(\zeta) &= \frac{2}{3}(\zeta+1)\left(\zeta+\frac{1}{2}\right)\zeta\left(\zeta-\frac{1}{2}\right) \text{ and} & \frac{d\hat{\psi}_5(\zeta)}{d\zeta} &= \frac{2}{3}\left(4\zeta^3+3\zeta^2-\frac{1}{2}\zeta-\frac{1}{4}\right).
\end{aligned} \tag{3.70}$$

Two-dimensional C^0 elements

The C^0 linear triangular element. The triangular element has corner co-ordinates in the $x-y$ plane at (x_1, y_1), (x_2, y_2), (x_3, y_3) (Figure 3.5).

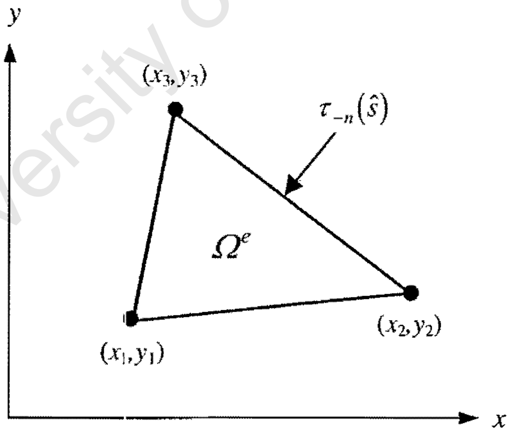

Figure 3.5: *A triangular element with a flux applied along one edge.*

The basis functions and their derivatives for this simplest of two-dimensional elements are

$$\psi_j^e(x,y) = \frac{a_j + b_j x + c_j y}{2\Delta}, \text{ for } j = 1, 2, 3, \tag{3.71}$$

$$\frac{\partial \psi_j^e(x,y)}{\partial x} = \frac{b_j}{2\Delta} \text{ and } \frac{\partial \psi_j^e(x,y)}{\partial y} = \frac{c_j}{2\Delta}, \text{ where} \tag{3.72}$$

$a_j = x_k y_l - x_l y_k$, $b_j = y_k - y_l$, $c_j = x_l - x_k$ with j, k, l cyclically permuted, and

$\Delta = \frac{1}{2}\left((x_2 y_3 - x_3 y_2) - (x_1 y_3 - x_3 y_1) + (x_1 y_2 - x_2 y_1)\right)$ is the area of the triangle.

Clearly, these basis functions possess the interpolation property

$$\psi_j^e(x_i, y_i) = \delta_{ji} . \tag{3.73}$$

Each of the physical properties within a given element is approximated by a single time dependent value determined at the centroid of the triangle,

$$\alpha_x^e(t) \cong \alpha_x(x_c, y_c, t),\ \alpha_y^e(t) \cong \alpha_y(x_c, y_c, t) \text{ and } \beta^e(t) \cong \beta(x_c, y_c, t), \text{ with} \tag{3.74}$$

$$x_c = \frac{1}{3}(x_1 + x_2 + x_3) \text{ and } y_c = \frac{1}{3}(y_1 + y_2 + y_3) . \tag{3.75}$$

The resulting expression for the approximation for each of the element capacity terms is

$$C_{ij}^e(t) \cong \beta^e(t) \iint_{\Omega^e} \psi_i^e(x, y) \psi_j^e(x, y) dxdy . \tag{3.76}$$

The basis functions are identical to the triangle area co-ordinates $\zeta_1, \zeta_2, \zeta_3$ for which the integration formulae are

$$\iint_{\Omega^e} \zeta_1^l \zeta_2^m \zeta_3^n dxdy = \frac{l!m!n!}{(l+m+n+2)!} 2\Delta . \tag{3.77}$$

Triangle area co-ordinates are a set of three co-ordinates, each of which varies linearly from a value of 0 at a side of the triangle to a value of 1 at the opposite vertex. When these integration formulae are applied to (3.76), the capacity matrix terms become

$$C_{ij}^e(t) = \iint_{\Omega^e} \zeta_i \zeta_j dxdy = \begin{cases} \dfrac{\beta^e(t)\Delta}{6} & i = j \\ \dfrac{\beta^e(t)\Delta}{12} & i \neq j \end{cases} , \tag{3.78}$$

and the stiffness matrix becomes

$$K_{ij}^e(t) \cong \frac{\alpha_x^e(t)}{4\Delta} b_i b_j + \frac{\alpha_y^e(t)}{4\Delta} c_i c_j . \tag{3.79}$$

The interior load is approximated by a single value, sampled at the centroid of the triangle,

$$f^e(t) = f(x_c, y_c, t), \text{ leading to} \tag{3.80}$$

$$Ff_i^e(t) \cong f^e(t) \iint_{\Omega^e} \psi_i^e(x, y) dxdy = \frac{f^e \Delta}{3} . \tag{3.81}$$

The boundary flux may be distributed along the side or it may be concentrated at a node. Where the applied natural boundary condition, $\tau_{-n}(\hat{s})$ is distributed along the length of a side of the element (Figure 3.5) bounded by nodes n_1 and n_2, it is evaluated at the midpoint of the side,

$$\tau^e(t) = \tau_{-n}(x_m, y_m), \text{ where} \tag{3.82}$$

$$x_m = \frac{1}{2}(x_{n_1} + x_{n_2}) \text{ and } y_m = \frac{1}{2}(y_{n_1} + y_{n_2}) .$$

The flux integrals become

$$\int_{n_1}^{n_2} \tilde{\tau}_{-n}^e(t) \psi_{n_1,n_2}^e ds \cong \int_{n_1}^{n_2} \tau_{-n}(s,t) \psi_{n_1,n_2}^e ds \cong \tau^e(t) \int_{n_1}^{n_2} \psi_{n_1,n_2}^e ds = \frac{\tau^e(t) L_{n_1 n_2}}{2} . \tag{3.83}$$

When the applied natural boundary condition is concentrated at node n_1, then

$$\tau_{-n}(\hat{s}) = \tau_{n_1}\delta(\hat{s} - \hat{s}_{n_1}), \tag{3.84}$$

and the flux integrals become

$$\int_{n_1}^{n_2} \tilde{\tau}^e_{-n}(t)\psi^e_{n_1} ds = \tau_{n_1} \text{ and } \int_{n_1}^{n_2} \tilde{\tau}^e_{-n}(t)\psi^e_{n_2} ds = 0. \tag{3.85}$$

Expressions for the flux expressions with the optimum flux-sampling point at the centroid of the triangle are

$$\tilde{\tau}^e_x(x,y,t) = -\alpha_x(x,y,t)\sum_{j=1}^{3} a_j(t)\frac{\partial\psi^e_j(x,y)}{\partial x} \cong -\alpha_x(x_c,y_c,t)\sum_{j=1}^{3} a_j(t)\frac{b_j}{2\Delta} \text{ and} \tag{3.86}$$

$$\tilde{\tau}^e_y(x,y,t) = -\alpha_y(x,y,t)\sum_{j=1}^{3} a_j(t)\frac{\partial\psi^e_j(x,y)}{\partial y} \cong -\alpha_y(x_c,y_c,t)\sum_{j=1}^{3} a_j(t)\frac{c_j}{2\Delta}. \tag{3.87}$$

Two-dimensional C^0 isoparametric suite of elements

The two-dimensional parent elements are defined in the (ξ,η) co-ordinate system (Figures 3.6 and 3.7). For each type of parent element, a unique set of basis functions and their derivatives are determined. The isoparametric transformation takes place by using, as for the one-dimensional case, the basis functions themselves,

$$x = \sum_{k=1}^{n} x^e_k\hat{\psi}_k(\xi,\eta) \text{ and } y = \sum_{k=1}^{n} y^e_k\hat{\psi}_k(\xi,\eta). \tag{3.88}$$

The Jacobian,

$$\left|J^e(\xi,\eta)\right| = \frac{\partial x}{\partial\xi}\frac{\partial y}{\partial\eta} - \frac{\partial x}{\partial\eta}\frac{\partial y}{\partial\xi}, \tag{3.89}$$

is evaluated in each case by using the transformation functions and the specific derivatives for that element. Transformation of the capacity, stiffness and load integrals leads to

$$C^e_{ij}(t) = \int_{\eta_1}^{\eta_2}\int_{\xi_1}^{\xi_2} \psi^e_i\beta(t)\psi^e_j\left|J^e\right|d\xi d\eta, \tag{3.90}$$

$$K^e_{ij}(t) = \int_{\eta_1}^{\eta_2}\int_{\xi_1}^{\xi_2} \frac{\partial\psi^e_i}{\partial x}\alpha_x(t)\frac{\partial\psi^e_i}{\partial x}\left|J^e\right|d\xi d\eta + \int_{\eta_1}^{\eta_2}\int_{\xi_1}^{\xi_2} \frac{\partial\psi^e_i}{\partial y}\alpha_x(t)\frac{\partial\psi^e_i}{\partial y}\left|J^e\right|d\xi d\eta \text{ and} \tag{3.91}$$

$$F^e_i(t) = \int_{\eta_1}^{\eta_2}\int_{\xi_1}^{\xi_2} f(t)\psi^e_i\left|J^e\right|d\xi d\eta + \oint_{S^e} \tilde{\tau}^e_{-n}(t)\psi^e_i ds. \tag{3.92}$$

The integration limits of the respective integrals $(\eta_1,\eta_2,\xi_1,\xi_2)$ depend upon the specific parent element.

The C^0 bilinear isoparametric quadrilateral element. The parent element has four nodal points at (ξ,η) values of (-1,-1), (1,-1), (1,1), (-1,1) respectively (Figure 3.6). The basis functions and their derivatives are given by

$$\hat{\psi}_1(\xi,\eta) = \frac{1}{4}(1-\xi)(1-\eta), \qquad \frac{\partial\hat{\psi}_1(\xi,\eta)}{\partial\xi} = -\frac{1}{4}(1-\eta), \qquad \frac{\partial\hat{\psi}_1(\xi,\eta)}{\partial\eta} = -\frac{1}{4}(1-\xi),$$

$$\hat{\psi}_2(\xi,\eta)=\frac{1}{4}(1+\xi)(1-\eta), \quad \frac{\partial\hat{\psi}_2(\xi,\eta)}{\partial\xi}=-\frac{1}{4}(1-\eta), \quad \frac{\partial\hat{\psi}_2(\xi,\eta)}{\partial\eta}=-\frac{1}{4}(1+\xi),$$
$$\hat{\psi}_3(\xi,\eta)=\frac{1}{4}(1+\xi)(1+\eta), \quad \frac{\partial\hat{\psi}_3(\xi,\eta)}{\partial\xi}=\frac{1}{4}(1+\eta), \quad \frac{\partial\hat{\psi}_3(\xi,\eta)}{\partial\eta}=\frac{1}{4}(1+\xi),$$
$$\hat{\psi}_4(\xi,\eta)=\frac{1}{4}(1-\xi)(1+\eta), \quad \frac{\partial\hat{\psi}_4(\xi,\eta)}{\partial\xi}=-\frac{1}{4}(1+\eta) \text{ and } \frac{\partial\hat{\psi}_4(\xi,\eta)}{\partial\eta}=\frac{1}{4}(1-\xi). \qquad (3.93)$$

The integration limits for this element are $\xi_1=\eta_1=-1$, $\xi_2=\eta_2=+1$ (Figure 3.6). The quadrature formula used is

$$\int_{-1}^{1}\int_{-1}^{1} I(\xi,\eta)d\xi d\eta \cong \sum_{k=1}^{n}\sum_{l=1}^{n} w_{nk}w_{nl}I(\xi_{nl},\eta_{nk}). \qquad (3.94)$$

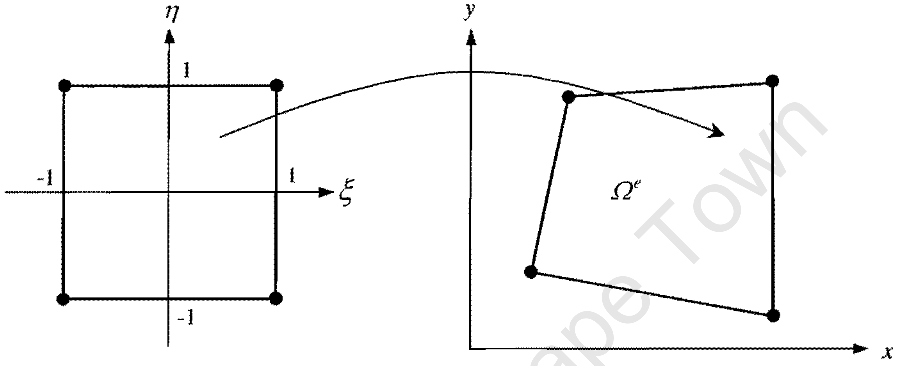

Figure 3.6: *A bilinear isoparametric quadrilateral element showing the transformation from the parent co-ordinate system on the lefthand side to the real co-ordinate system on the righthand side.*

Gauss points and weightings are listed in Burnett (1987), p617. In the program used for this work, the user may elect to use 1*1, 2*2 or 3*3 Gauss points. The element equations are then approximated by

$$C_{ij}^e(t) \cong \sum_{k=1}^{n}\sum_{l=1}^{n} w_{nk}w_{nl}\left(\psi_i^e\beta(t)\psi_j^e\left|J^e\right|\right)_{(\xi_{nl},\eta_{nk})}, \qquad (3.95)$$

$$K_{ij}^e(t) \cong \sum_{k=1}^{n}\sum_{l=1}^{n} w_{nk}w_{nl}\left[\left(\frac{\partial\psi_i^e}{\partial x}\alpha_x(t)\frac{\partial\psi_i^e}{\partial x}+\frac{\partial\psi_i^e}{\partial y}\alpha_y(t)\frac{\partial\psi_i^e}{\partial y}\right)\left|J^e\right|\right]_{(\xi_{nl},\eta_{nk})} \text{ and} \qquad (3.96)$$

$$Ff_i^e(t) \cong \sum_{k=1}^{n}\sum_{l=1}^{n} w_{nk}w_{nl}\left[f(t)\psi_i^e\left|J^e\right|\right]_{(\xi_{nl},\eta_{nl})}. \qquad (3.97)$$

The derivatives are dealt with by using the chain rule which leads to

$$\frac{\partial\psi_i^e}{\partial x}=\frac{1}{\left|J^e\right|}\frac{\partial y}{\partial\eta}\frac{\partial\hat{\psi}_i}{\partial\xi}-\frac{1}{\left|J^e\right|}\frac{\partial y}{\partial\xi}\frac{\partial\hat{\psi}_i}{\partial\eta} \text{ and} \qquad (3.98)$$

$$\frac{\partial\psi_i^e}{\partial y}=-\frac{1}{\left|J^e\right|}\frac{\partial x}{\partial\eta}\frac{\partial\hat{\psi}_i}{\partial\xi}+\frac{1}{\left|J^e\right|}\frac{\partial x}{\partial\xi}\frac{\partial\hat{\psi}_i}{\partial\eta}. \qquad (3.99)$$

As physical parameters are defined in the real co-ordinate system, the value of any physical parameter at a point (ξ,η) is determined by transforming to its corresponding (x,y) location and then establishing the appropriate value. The boundary flux integral is simplified through the assumption that the flux is constant along the side of the element, that the boundary side of the element is straight and that the mid-side node is located at its centre. Then the boundary flux at the two nodes n_1, n_2, along the element edge of length L, located at the boundary domain Γ are given by

$$F\tau_{n_1}^{(e)}(\Gamma)=\frac{1}{2}L\tilde{\tau}^{e}_{-n} \text{ and } F\tau^{e}_{n_2}(\Gamma)=\frac{1}{2}L\tilde{\tau}^{e}_{-n}. \qquad (3.100)$$

The flux is determined in the centre of the element ($(\xi,\eta)=(0,0)$), coinciding with the quadrature point for the one point Gauss rule.

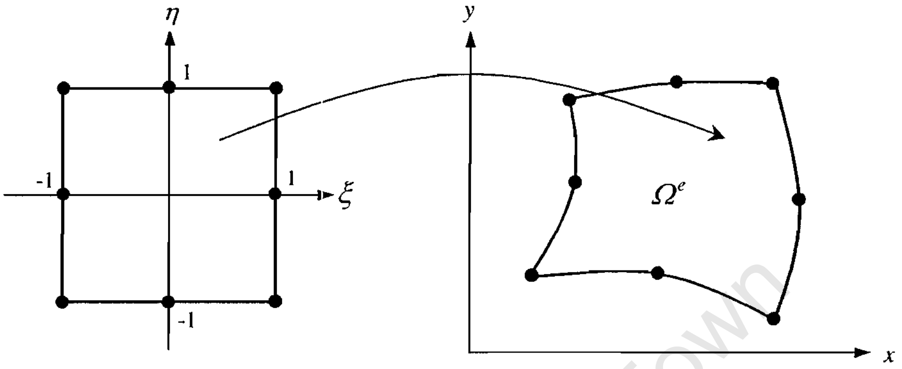

Figure 3.7: *A serendipity element showing the transformation from the parent co-ordinate system on the lefthand side to the real co-ordinate system on the righthand side.*

The C^0 serendipity element. This element has eight nodal points located at (-1,-1), (1,-1), (1,1), (-1,1), (0,-1), (1,0), (0,1) and (-1,0) (figure 3.7). The basis functions are

$$\hat{\psi}_1(\xi,\eta)=\frac{1}{4}(1-\xi)(1-\eta)(-\xi-\eta-1), \quad \hat{\psi}_2(\xi,\eta)=\frac{1}{4}(1+\xi)(1-\eta)(\xi-\eta-1),$$

$$\hat{\psi}_3(\xi,\eta)=\frac{1}{4}(1+\xi)(1+\eta)(\xi+\eta-1), \quad \hat{\psi}_4(\xi,\eta)=\frac{1}{4}(1-\xi)(1+\eta)(-\xi+\eta-1),$$

$$\hat{\psi}_5(\xi,\eta)=\frac{1}{2}(1-\xi^2)(1-\eta), \quad \hat{\psi}_6(\xi,\eta)=\frac{1}{4}(1+\xi)(1-\eta^2),$$

$$\hat{\psi}_7(\xi,\eta)=\frac{1}{4}(1-\xi^2)(1+\eta) \text{ and } \quad \hat{\psi}_8(\xi,\eta)=\frac{1}{2}(1-\xi)(1-\eta^2). \qquad (3.101)$$

Quadrature formulae are the same as those for the bilinear quadrilateral. Boundary flux terms are identical to those of the quadratic triangle. For the flux, optimal flux sampling points are the four quadrature points for the 2*2 Gauss rule.

3.2.5 The system equations

The element equations are assembled to give the set of system equations

$$C(a(t))\frac{da(t)}{dt}+K(a(t))a(t)=F(t). \qquad (3.102)$$

These equations apply equally to the porous and permeable rock matrix and to the fracture network, and therefore the same routines can be used to solve for both systems. Where the dual porosity model is needed, two coupled sets of system matrices must be solved concurrently, the one for the fracture network continuum and the other for each group of matrix blocks.

The expression for the capacity matrix, $\boldsymbol{C}$ contains the physical property β, (expressions (3.25) and (3.28)) which is a function of fluid density, formation compressibility and porosity (equations (3.3) and (3.7)). The fluid density of highly compressible gas varies greatly with pressure, according to the definition of compressibility (equation (2.12)) and the numerical value of fluid compressibility itself may vary with pressure. Additionally, the porosity is a function of pressure according to equation (2.11). The terms of the capacity matrix are therefore functions of the unknown $\boldsymbol{a}(t)$. Likewise, the terms of the stiffness matrix $\boldsymbol{K}$ are functions of the unknown $\boldsymbol{a}(t)$ through the physical property α (expressions (3.26) and (3.29)) which includes density, permeability and fluid viscosity (equations (3.2) and (3.6)). Besides the pressure dependence of the density, fluid viscosity and permeability may also be pressure dependent. Consequently, the set of equations (3.102) are nonlinear and cannot be solved directly for $\boldsymbol{a}(t)$ at any given value of time, as the values of the entries in the matrices $\boldsymbol{C}$ and $\boldsymbol{K}$ are themselves functions of $\boldsymbol{a}(t)$. Solution of this set of equations has to proceed in an iterative fashion.

Time integration is accomplished via a generalised finite difference scheme. If t_n is the time at the start, and t_{n+1} the time at the end of the current time step of length $\Delta t = t_{n+1} - t_n$, then the matrices are evaluated at some time, $t_{n+\theta}$ within the current time step, defined by

$$t_{n+\theta} = (1-\theta)t_n + \theta t_{n+1}, \tag{3.103}$$

where θ takes on a value between 0 and 1, representing a fraction of the length of the time step, and is specified by the user at the start of each time interval. The matrices are evaluated at time $t_{n+\theta}$ as

$$\boldsymbol{C}_{n+\theta}\left[\frac{d\boldsymbol{a}(t)}{dt}\right]_{n+\theta} + \boldsymbol{K}_{n+\theta}\boldsymbol{a}_{n+\theta} = \boldsymbol{F}_{n+\theta}, \tag{3.104}$$

where $\boldsymbol{C}_{n+\theta} = \boldsymbol{C}(t_{n+\theta})$, etc. Any of the vectors or matrices of equation (3.104) can be approximated at time t_θ by linear interpolation between t_{n-1} and t_n with an equation of the form

$$\boldsymbol{M}_{n+\theta} \cong (1-\theta)\boldsymbol{M}_n + \theta\boldsymbol{M}_{n+1}. \tag{3.105}$$

Differentiation of the analogous expression for $\boldsymbol{a}(t)$ leads to

$$\left[\frac{d\boldsymbol{a}(t)}{dt}\right]_{n+\theta} = \frac{1}{\Delta t}\left[\frac{d\boldsymbol{a}(t)}{d\theta}\right]_{n+\theta} \cong \frac{\boldsymbol{a}_{n+1} - \boldsymbol{a}_n}{\Delta t}. \tag{3.106}$$

By incorporating this expression for the derivative of $\boldsymbol{a}(t)$ at time $t_{n+\theta}$ and the linear interpolation expressions for $\boldsymbol{a}_{n+\theta}$ (from 3.105) into the matrix equations (3.104) and rearranging the terms, we get

$$\left(\frac{1}{\Delta t}\boldsymbol{C}_{n+\theta} + \theta\boldsymbol{K}_{n+\theta}\right)\boldsymbol{a}_{n+1} = \boldsymbol{F}_{n+\theta} + \left(\frac{1}{\Delta t}\boldsymbol{C}_{n+\theta} - (1-\theta)\boldsymbol{K}_{n+\theta}\right)\boldsymbol{a}_n. \tag{3.107}$$

This can be rewritten in the simpler from as

$$\boldsymbol{Kef}_{n+\theta}\boldsymbol{a}_{n+1} = \boldsymbol{Fef}_{n+\theta}, \text{ where} \tag{3.108}$$

$$\boldsymbol{Kef}_{n+\theta} = \frac{1}{\Delta t}\boldsymbol{C}_{n+\theta} + \theta\boldsymbol{K}_{n+\theta} \text{ and} \tag{3.109}$$

$$\boldsymbol{Fef}_{n+\theta} = \boldsymbol{F}_{n+\theta} + \left(\frac{1}{\Delta t}\boldsymbol{C}_{n+\theta} - (1-\theta)\boldsymbol{K}_{n+\theta}\right)\boldsymbol{a}_n. \tag{3.110}$$

If expressions (3.109) and (3.110) are expanded to include equation (3.105), then

$$\boldsymbol{Kef}_{n+\theta} = \frac{1}{\Delta t}\left((1-\theta)\boldsymbol{C}_n + \theta\boldsymbol{C}_{n+1}\right) + \theta\left((1-\theta)\boldsymbol{K}_n + \theta\boldsymbol{K}_{n+1}\right) \text{ and} \tag{3.111}$$

$$\boldsymbol{Fef}_{n+\theta} = (1-\theta)\boldsymbol{F}_n + \theta\boldsymbol{F}_{n+1} + \left(\frac{1}{\Delta t}\left((1-\theta)\boldsymbol{C}_n + \theta\boldsymbol{C}_{n+1}\right) - (1-\theta)\left((1-\theta)\boldsymbol{K}_n + \theta\boldsymbol{K}_{n+1}\right)\right)\boldsymbol{a}_n . \tag{3.112}$$

The desired solution at time t_{n+1}, i.e. a_{n+1} is obtained by solving (3.108) together with (3.111) and (3.112). However, these equations cannot be solved directly on account of the presence of $\boldsymbol{C}_{n+1}$ and $\boldsymbol{K}_{n+1}$ on the righthand sides of equations (3.111) and (3.112). The expression for the terms in the matrix $\boldsymbol{C}$ contain the parameter β and in order to solve $\boldsymbol{a}_{n+1}$ from equation (3.108), it is, according to (3.111) and (3.112) necessary to evaluate $\boldsymbol{C}_{n+1}$ which in turn involves evaluating

$$\beta_{n+1}(\boldsymbol{x},\boldsymbol{a}_{n+1}) = \rho_{n+1}(\boldsymbol{x},\boldsymbol{a}_{n+1})c_{f,n+1}(\boldsymbol{a}_{n+1})\phi_{n+1}(\boldsymbol{x},\boldsymbol{a}_{n+1}) , \tag{3.113}$$

requiring *a priori* knowledge of $\boldsymbol{a}_{n+1}$. Likewise, terms in the matrix $\boldsymbol{K}$ contain the parameter α and in order to solve $\boldsymbol{a}_{n+1}$, it is necessary to evaluate $\boldsymbol{K}_{n+1}$, which in turn involves evaluating

$$\alpha_{n+1}(\boldsymbol{x},\boldsymbol{a}_{n+1}) = \frac{\rho_{n+1}(\boldsymbol{x},\boldsymbol{a}_{n+1})\boldsymbol{k}_{fx,y,n+1}(\boldsymbol{x},\boldsymbol{a}_{n+1})}{\mu_{n+1}(\boldsymbol{a}_{n+1})} , \tag{3.114}$$

once again requiring *a priori* knowledge of $\boldsymbol{a}_{n+1}$. At the start of each new time step, therefore, an initial estimate is made of the value of the solution at the end of the time step, $\boldsymbol{a}_{n+1}^{0}$ and this is used in expressions (3.113) and (3.114) to estimate the values of the terms of the matrices. The matrices are then built and solved, giving an improved estimate of the solution, $\boldsymbol{a}_{n+1}^{1}$. This is repeated until the solution converges. The detail of this procedure is described in Section 3.3.2.

3.3 A finite element simulator for the fractured reservoir

The description of the finite element simulator is accomplished in three parts. In the first sub-section, the conceptual algorithm is described and developed. The second sub-section deals with the numerical implementation of the algorithm, and the third is a description of the FEFRES computer program developed during the course of this research. A logical flow diagram of the algorithm is included in appendix B.

3.3.1 The conceptual algorithm

In this sub-section, the modelling concept is discussed and the algorithm needed to solve the coupled, nonlinear system equations describing flow in the matrix and fractures, developed in sub-section 3.2.5, is developed.

The simulator solves the governing equations discretized in two mesh complexes, referred to here as the primary and secondary mesh complexes respectively (Figures 3.8 and 3.9). The primary mesh complex conforms to the physical geometry of the hydrocarbon-bearing reservoir and is the more general of the two. It is referred to as a mesh complex as it can represent different entities within a single reservoir model. It may be used to model only the fracture network continuum, or only the nonfractured porous and permeable rock matrix, or a combined fracture network and matrix rock continuum, or porous and permeable rock matrix with embedded, explicitly defined fractures. In addition, the primary mesh complex accommodates the boundary and load conditions imposed upon the reservoir as a whole. The distinguishing characteristic of the primary mesh is that it represents the continuously connected domain of the reservoir. When and where the dual porosity model is invoked, the primary mesh describes the fracture network continuum.

Wells can be modelled in the primary mesh explicitly using internal boundaries with the appropriate boundary conditions set according to the manner in which production from the well is being controlled (essential boundary conditions or natural boundary conditions), or simply by imposing internal load conditions on those cells in which wells are located. The external boundaries of the reservoir can be no-flow boundaries, constant pressure boundaries representing for example, aquifer pressure support, or there may be reason to specify some value for the rate of fluid influx across a boundary. The primary mesh can be constructed using any combination of the two-dimensional elements as well as any of the one-dimensional elements as needed for example, for the explicit representation of fractures. In whichever mode the primary mesh is used, it can accommodate heterogeneity and anisotropy of the entity being modelled.

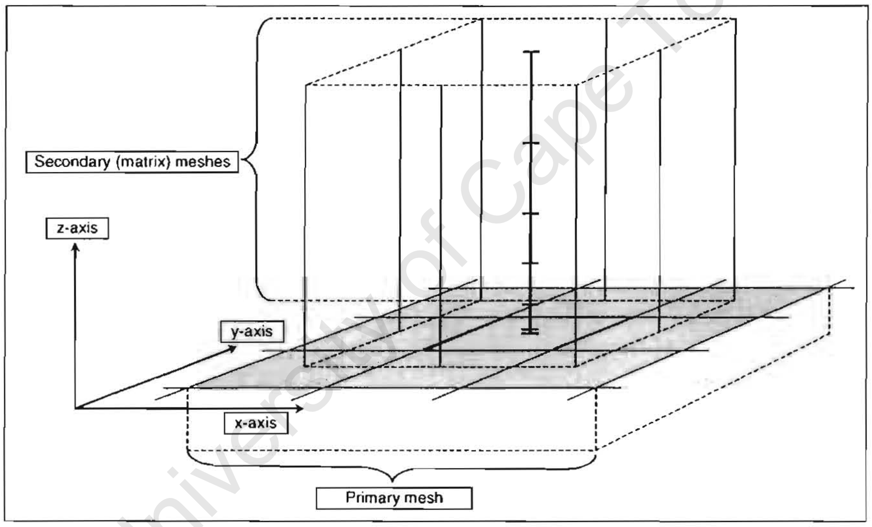

Figure 3.8: *Illustration of mesh definitions for the dual porosity model. The two-dimensional primary mesh is used to model the continuous component of the reservoir, which is the fracture system in the dual porosity model. The matrix blocks are modelled using a series of one-dimensional meshes (the secondary mesh(es)) that are coupled to the primary mesh. Each vertical line displayed in the secondary mesh domain represents a one-dimensional sequence of cells associated with a given primary mesh cell.*

The secondary mesh complex is specialised and is used exclusively to model the porous and permeable blocks of rock matrix that are surrounded and isolated by the fracture network in the dual porosity model. The secondary mesh complex is composed of a large number of individual one-dimensional meshes, each of which is solved independently and linked to a specific primary cell. Each primary cell may have none, one or many secondary meshes associated with it. A secondary mesh is utilised when dual porosity behaviour is expected to occur. A separate mesh is defined to represent every group of matrix blocks which are either distinct in terms of one or more of the essential parameters influencing behaviour of the matrix block, namely size, geometry, orientation or physical properties, or in terms of the expected boundary conditions that will be imposed on that group of matrix blocks in the future. Thus two adjacent primary mesh cells may represent portions of the reservoir in which the matrix blocks are physically and geometrically similar, but may nonetheless be assigned different secondary meshes as they may experience significantly different pressure histories which in turn impose different boundary conditions on the secondary meshes at any given time.

Likewise, it is not at all unlikely that a single fracture cell may represent a portion of the reservoir which is characterised by a bi-, or multi-modal distribution of matrix block sizes. In this instance, the cell in the primary mesh would have two (or if needs be, more) secondary meshes associated with it, each with its own physical characteristics. Each secondary mesh comprises a set of one-dimensional elements. The construction of such a one-dimensional mesh is such that it is possible to make a distinction between a range of matrix block shapes, and orientations and matrix physical properties. Examples of the construction of such meshes are demonstrated in Section 4.2.

In addition to the elements needed to model a matrix block itself, a final 'control' element with very small dimensions is added to the series to represent the fracture. This element provides the link between the two meshes and is not counted as one of the elements making up the matrix mesh. Its purpose is exclusively to provide the mechanism for dealing with boundary conditions. All boundary conditions imposed upon the secondary mesh are done so via the control element, and the output from the matrix mesh from which the controlling input into the primary mesh is determined, is likewise obtained via the control element. Whenever the fracture network equations have been solved, the outcome is a new pressure field in the fracture network. This pressure field forms the essential boundary conditions to be imposed upon the control element of the secondary meshes for the subsequent solution of the matrix equations. Whenever the matrix equations have been solved, the outcome is a flux of fluid into or out of the control element. This flux forms the interior load conditions to be imposed on the primary mesh cell for the subsequent solution of the fracture equations.

When the dual porosity mode is invoked, the primary and secondary meshes are linked. The manner in which the reservoir is being managed determines the boundary conditions that are imposed upon the primary mesh complex. The simulation proceeds in time via a series of time intervals. Each time interval represents a period during which the boundary conditions remain fixed. Each time interval is divided into a number of time steps. Solution of the equations proceeds in time with a finite difference approach from one time step to the next.

Within every time step, the system equations and boundary conditions governing the primary mesh must be solved. Included in these equations is a set of interior load conditions imposed upon the primary elements by the secondary mesh complex. This represents the volume of gas that is expected to flow from (or into) those matrix blocks that are located within the geographical boundaries represented by each primary cell, into (or from) that primary cell during the time step in question. This flux is determined by solving the equations that govern the secondary meshes together with the constraints imposed on them.

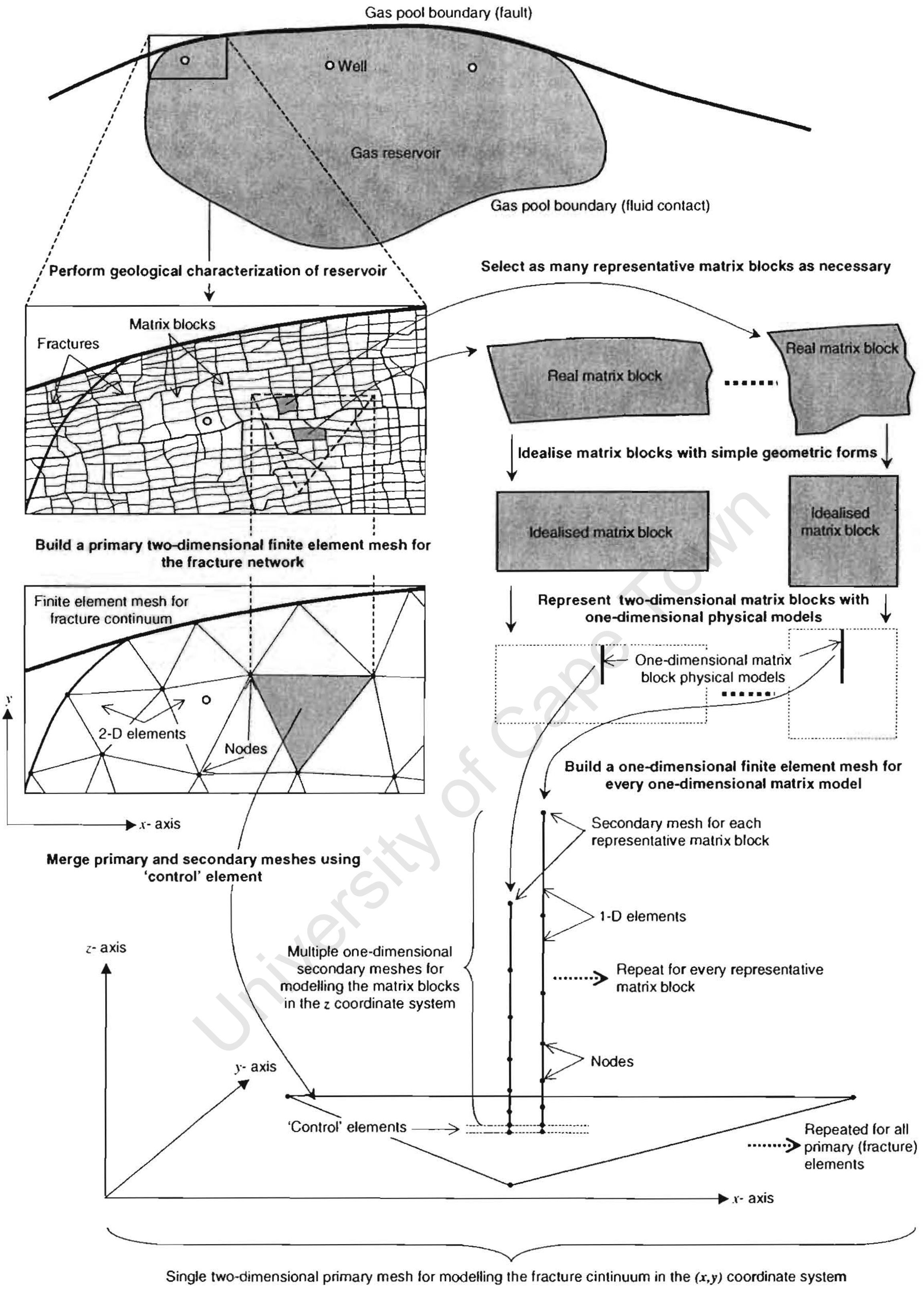

Figure 3.9: *Modelling concept for dual porosity finite element simulator.*

The only constraint experienced by a secondary mesh comes in the form of an essential boundary condition, imposed upon the final node in the string of matrix elements (both nodes of the control element). This node represents the outer edge of the matrix block that is coincidental with the fracture wall. For the time step in question, this boundary condition is the pressure estimated to prevail in the primary cell at the end of the time step. In order to determine this value, the primary mesh must be solved. To progress the simulator through this time step, an iterative process is required which is referred to here as the 'coupled iteration', a term used to distinguish it from the 'nonlinear iteration', which refers to the iterative process used to solve the primary mesh.

3.3.2 Numerical implementation of the algorithm

In this sub-section, it is shown how the system equations developed in section 3.2.5 are incorporated into the conceptual algorithm developed in sub-section 3.3.1 to form the numerical procedure that forms the basis for the FEFRES computer program. Various issues such as boundary conditions, data storage, physical and fluid properties and input/output procedures are elaborated on.

Numerical solution procedure

If $\boldsymbol{X}^{j(i)}_{p.n(m)}$ is a matrix or vector associated with the primary (subscript p) mesh and is evaluated at the start of the jth nonlinear iteration (J is the total number of nonlinear iterations) of the ith coupled iteration (I is the total number of coupled iterations) at time t_n which is the start of time step number n (N is the total number of time steps) of time interval number m (M is the total number of time intervals), then equations (3.108), (3.111) and (3.112) for the primary mesh become

$$\boldsymbol{Kef}^{j(i)}_{p.n+\theta(m)}\boldsymbol{a}^{j(i)}_{p.n+1} = \boldsymbol{Fef}^{j(i)}_{p.n+\theta(m)}, \tag{3.115}$$

$$\begin{aligned}\boldsymbol{Kef}^{j(i)}_{p.n+\theta(m)} &= \frac{1}{\Delta t}\left((1-\theta)\boldsymbol{C}^{j(i)}_{p.n(m)}\left(\boldsymbol{a}^{j(i)}_{p.n(m)}\right) + \theta\boldsymbol{C}^{j(i)}_{p.n+1(m)}\left(\boldsymbol{a}^{j(i)}_{p.n+1(m)}\right)\right)\\ &\quad +\theta\left((1-\theta)\boldsymbol{K}^{j(i)}_{p.n(m)}\left(\boldsymbol{a}^{j(i)}_{p.n(m)}\right) + \theta\boldsymbol{K}^{j(i)}_{p.n+1(m)}\left(\boldsymbol{a}^{j(i)}_{p.n+1(m)}\right)\right) \text{ and}\end{aligned} \tag{3.116}$$

$$\begin{aligned}\boldsymbol{Fef}^{j(i)}_{p.n+\theta(m)} &= (1-\theta)\boldsymbol{F}^{j(i)}_{p.n(m)}\left(\boldsymbol{a}^{j(i)}_{p.n(m)}\right) + \theta\boldsymbol{F}^{j(i)}_{p.n+1(m)}\left(\boldsymbol{a}^{j(i)}_{p.n+1(m)}\right)\\ &\quad +\left(\frac{1}{\Delta t}\left((1-\theta)\boldsymbol{C}^{j(i)}_{p.n(m)}\left(\boldsymbol{a}^{j(i)}_{p.n(m)}\right) + \theta\boldsymbol{C}^{j(i)}_{p.n+1(m)}\left(\boldsymbol{a}^{j(i)}_{p.n+1(m)}\right)\right)\right)\boldsymbol{a}^{j(i)}_{p.n(m)}\\ &\quad -\left((1-\theta)\left((1-\theta)\boldsymbol{K}^{j(i)}_{p.n(m)}\left(\boldsymbol{a}^{j(i)}_{p.n(m)}\right) + \theta\boldsymbol{K}^{j(i)}_{p.n+1(m)}\left(\boldsymbol{a}^{j(i)}_{p.n+1(m)}\right)\right)\right)\boldsymbol{a}^{j(i)}_{p.n(m)}.\end{aligned} \tag{3.117}$$

Likewise, if $\boldsymbol{X}^{i}_{s.l(n(m))}$ is a matrix or vector associated with the secondary (subscript s) mesh system and is evaluated after the ith coupled iteration at the end of time sub-step number l (L is the total number of time sub-steps) of time step number n of time interval number m, then for the secondary mesh system, equations (3.108), (3.111) and (3.112) become

$$\boldsymbol{Kef}^{i}_{s.l(n(m))}\boldsymbol{a}^{i}_{s.l(n+1)} = \boldsymbol{Fef}^{i}_{s.l(n(m))}, \tag{3.118}$$

$$\boldsymbol{Kef}^{i}_{s.l(n(m))} = \frac{1}{\Delta t}\left(\boldsymbol{C}^{i}_{s.l(n(m))}\left(\boldsymbol{a}^{i}_{s.l(n(m))}\right)\right) \text{ and} \tag{3.119}$$

$$\begin{aligned}\boldsymbol{Fef}^{i}_{s.l(n(m))} &= \boldsymbol{F}^{i}_{s.l(n(m))}\left(\boldsymbol{a}^{i}_{s.l(n(m))}\right)\\ &\quad +\frac{1}{\Delta t}\left(\boldsymbol{C}^{i}_{s.l(n(m))}\left(\boldsymbol{a}^{i}_{s.l(n(n))}\right)\right)\boldsymbol{a}^{i}_{s.l(n(m))} - \boldsymbol{K}^{i}_{s.l(n(m))}\left(\boldsymbol{a}^{i}_{s.l(n(m))}\right)\boldsymbol{a}^{i}_{s.l(n(m))}.\end{aligned} \tag{3.120}$$

If e indicates element number and d indicates node number, and there are D_p nodes in the primary mesh and $D_{s(e_p)}$ nodes in the secondary mesh associated with primary element e_p, and there are E_p

elements in the primary mesh and $E_{s(e_p)}$ elements in the secondary mesh associated with primary element e_p, then $\boldsymbol{Kef}_p$ is a $D_p * D_p$ matrix, $\boldsymbol{a}_p$ is a $D_p * 1$ matrix and $\boldsymbol{Fef}_p$ is a $1 * D_p$ matrix. Expression (3.118) typically comprises E_p matrix equations, in each of which $\boldsymbol{Kef}_s$ is a $D_{s(e_p)} * D_{s(e_p)}$ matrix, $\boldsymbol{a}_p$ is a $D_{s(e_p)} * 1$ matrix and $\boldsymbol{Fef}_p$ is a $1 * D_{s(e_p)}$ matrix.

In the computer program, at the start of a new time step, the first iteration is initiated by solving the secondary mesh first, using as the essential boundary condition, an estimate of the pressure that will prevail in its associated primary cell at the end of this time step (***step 1*** below). This estimate of pressure is made by linearly extrapolating the two sets of pressure fields from the end of each of the previous two time steps. If this is the first time step of a new interval, then the pressure field determined at the end of the last time step from the last time interval is used as an estimate without any extrapolation (3.121). If this is the second time step of the time interval, then the pressure field determined at the end of the previous time step (the first time step of the interval) is used without any extrapolation (3.122). The reason for this is that a new time interval may be associated with very different load and boundary conditions (such as the shutting in of a well) which can cause a rapid reversal of trends, and therefore extrapolation from a previous time interval may not be appropriate.

For subsequent time steps, the first estimate of the primary cell pressure at the end of the current time step for the first coupled iteration within this time step, is estimated by linearly extrapolating the final pressure fields determined at the ends of the previous two time steps (3.123). If this is anything but the first iteration of a new time step, then of course no extrapolation is required as the primary solution would have been completed during the previous iteration of this time step, and an estimate of the pressure field in the primary mesh at the end of the time step will be readily available.

Step 1: *At the start of a new time step,* n *in time interval* m*, estimate the solution to the primary mesh at the end of the time step, i.e.* $\boldsymbol{a}^{1(1)}_{p,n+1(m)}$.

If this is the first time step of a new time interval ($n(m) = 1$), $\boldsymbol{a}^{1(1)}_{p,2(m)} \cong \boldsymbol{a}^{J+1(I+1)}_{p,N+1(m-1)}$, *or* (3.121)

if this is the second time step of the time interval ($n(m) = 2$), $\boldsymbol{a}^{1(1)}_{p,3(m)} \cong \boldsymbol{a}^{J+1(I+1)}_{p,2(m)}$, *or,* (3.122)

if this is any other time step in the time interval, $\boldsymbol{a}^{1(1)}_{p,n+1(m)} \cong \frac{1}{2}\left(\boldsymbol{a}^{J+1(I+1)}_{p,n(m)} + \boldsymbol{a}^{J+1(I+1)}_{p,n-1(m)}\right)$. (3.123)

In this algorithm, a single value for the pressure in each primary cell is used as a boundary condition for all the secondary meshes associated with that cell (***step 2***). The pressure at the centroid of the primary cell is determined for this purpose using an basis function (3.124).

Step 2: *Use* $\boldsymbol{a}^{1(1)}_{p,n+1(m)}$ *to define essential boundary conditions for the secondary mesh system,*

$$\boldsymbol{P}^{1}_{s,L+1(n(m))} = f\left(\boldsymbol{a}^{1(1)}_{p,n+1(m)}\right), \tag{3.124}$$

where f *is a function that determines an average value of the pressure for each primary cell from the cell's nodal pressure values.*

Once the boundary conditions for the secondary mesh complex for this iteration of this time step have been defined, the secondary mesh is ready to be solved (***steps 3 to 5***). This proceeds by way of a series of time sub-steps which are peculiar to the secondary mesh (typically 10 sub-steps per time step). Boundary conditions are imposed by ramping through the sub-steps (see next section for explanation). The secondary matrices are solved in an explicit fashion (forward time differencing) through each of these sub-steps. However, due to the nonlinear nature of the governing equations, the pressure-dependent coefficients are still revised at the beginning of each time sub-step based on the predicted pressure fields forecast during the previous time sub-step and the matrices are rebuilt to accommodate these changed values. Each of the secondary meshes is time sub-stepped through this iteration in turn.

Step 3: *Build the system matrices for the secondary meshes* $\boldsymbol{Kef}^{1}_{s,1(n(m))}$ *(equation (3.119)) and* $\boldsymbol{Fef}^{1}_{s,1(n(m))}$ *(equation (3.120)) and apply the essential boundary conditions via the ramping formula (3.131) over the time step.*

Step 4: *Solve for* $\boldsymbol{a}^{1}_{s,2n(m)}$ *using equation (3.118).*

Step 5: *Repeat steps 3 and 4 for* $l = 2$ *to* L*, leading to an estimate of the solution for the secondary mesh at the end of the current time step,*

$$\boldsymbol{a}^{1}_{s,1(n+1(m))} \cong \boldsymbol{a}^{1}_{s,L+1(n(m))}\,. \tag{3.125}$$

At the end of each sub-step, the flux from each of the final elements is determined, multiplied by the length of the sub-step and incremented so that once the end of the time step is reached, the total mass of fluid extruded from each of the secondary meshes is known (***step 6***). Using the nodal pressure values at the beginning and end of the time step, together with the pressure adjusted physical parameters, a material balance calculation is performed and checked against the calculated flux for each secondary mesh. The values are reported for quality control purposes and to help in selecting time sub-step lengths. An estimate of the flux from each secondary mesh is stored (***step 7***), to be used as an internal load condition for each of the primary cells (3.126). Each series of elements in a secondary mesh represents a single matrix block and there may be many such matrix blocks within the geographical area represented by the primary cell. The total flux is determined by multiplying the flux from the representative matrix block by the number of such matrix blocks present in the primary cell.

Step 6: *From the results obtained after step 5, estimate the flux from each of the secondary meshes over the duration of the current time step according to equations (3.51) or (3.66),* $\tau^{1}_{s,2\to L+1(n(m))}$.

Step 7: *Use the results from step 5 to define an interior load condition for each of the primary mesh elements,*

$$\boldsymbol{F}^{1(1)}_{p,n\to n+1(m)} = f\left(\tau^{1}_{s,2\to L+1(n(m))}\right). \tag{3.126}$$

Once the secondary mesh complex has been solved for this coupling iteration in this time step, the primary mesh can be solved (***steps 8 to 10***), honouring the fluxes forecast by the secondary mesh (3.126). At the same time, all other boundary conditions and loads imposed on the reservoir and specified by the user are solved. The primary mesh is solved for this coupling iteration for this time step by using an implicit or semi-implicit time stepping algorithm to proceed across the whole time step. The degree of implicitness depends upon the value of θ, which is defined for each time step, and can have different values for different steps. In practice, θ can take on any value between 0 (forward time differencing) and 1 (backward differencing). When a forward differencing approach is used, the solution procedure follows that described above for the secondary meshes, except that the matrices are solved over the entire step in one go (no sub-stepping).

Coefficients and the ensuing matrices are updated and rebuilt for pressure dependence at the beginning of each time-step, based on the forecasts made during the previous time step. When any value of θ other than 0 is used, then the procedure is further complicated by the need to evaluate the coefficients at some unknown pressure field which will prevail at a time as determined by the value of θ during the course of the current time step. This is accomplished via an iterative process, referred to here as the 'nonlinear' iteration to distinguish it from the outer, 'coupling' iteration. Within the given coupling iteration then, secondary mesh imposed loads are kept constant, and the matrices associated with the primary mesh are repeatedly solved (the nonlinear iterations). The iteration process first requires an estimate of the primary pressure field expected at the end of the current time step.

For the first iteration of the first two time steps of an interval, a similar process is used for estimating the pressure field expected at the end of this time step in the primary mesh as was described above for the secondary mesh. For all time steps within a time interval other than the first two, the first estimate of the pressure field at the end of the time step for the first nonlinear iteration of that time step is obtained via a linear extrapolation of the pressure fields from the ends of the previous two time-steps. Over the first two time steps of a time interval, the pressure field from the end of the previous time step is used as the initial estimate of the pressure field at the end of this time step without any extrapolation, in order to initiate the first nonlinear iteration of this time-step. For subsequent nonlinear iterations in this program use has been made of a direct (Picard) method to search for the solution at the end of the time step.

During every iteration then, the program has estimates of the pressure fields prevailing at the start of the time step, and an estimate of the pressure field expected at the end of the time step from some source or other. The program then determines the pressure field associated with the current value of θ via linear extrapolation. This pressure field is then interpolated where necessary and used to recalculate the values of all pressure dependent coefficients in the governing equations. Where necessary, the element and system matrices are reconstructed and the equations solved. Nonlinear iterations are continued until convergence criteria are met (3.127 and 3.128).

Step 8: *Build the primary mesh system matrices (3.115) to (3.117), using the approximation of* $\boldsymbol{a}_{p.n+1(m)}^{1(1)}$ *from step 1, and either* $\boldsymbol{a}_{p,n+1(m-1)}^{I+1(J+1)}$*, the final primary mesh solution from the end of the previous time interval if this is the first time step of a new interval, or* $\boldsymbol{a}_{p,n(m)}^{I+1(J+1)}$*, the final primary mesh solution from the end of the previous time step, as the case may be. Apply boundary and load conditions, including the interior load conditions defined in step 7.*

Step 9: *Solve for* $\boldsymbol{a}_{p.n+1(m)}^{2(1)}$ *by inverting the system equations built in step 8.*

Step 10: *Using* $a^{2(1)}_{p,n+1(m)}$ *as a new approximation to the solution of the primary mesh at the end of this time step, repeat steps 8 and 9, and continue to repeat consecutively, for* $j = 2$ *to* $J+1$*. This constitutes the nonlinear iteration loop. Check for convergence after each iteration, and continue with the iterations until either*

$$\sum_{d}^{D_p} \left| a^{j(1)}_{d(p),n+1(m)} - a^{j-1(1)}_{d(p),n+1(m)} \right| \leq C_1 \text{, or} \tag{3.127}$$

$$Max\left[\left| a^{j(1)}_{d(p),n+1(m)} - a^{j(1)}_{d(p),n+1(m)} \right|_{d=1\to D_p} \right] \leq C_2 \text{,} \tag{3.128}$$

holds, where C_1 *and* C_2 *are values specified by the user, or the maximum number of iterations, specified by the user, is reached.* J *is therefore either the maximum permissible number of iterations or the number of iterations after which convergence criteria have been satisfied. The end result is a converged solution* $a^{J+1(1)}_{p,n+1(m)}$ *consistent with the load conditions determined in step 7.*

Once convergence of the nonlinear iterations has been achieved, the primary pressure fields are stored and the program reverts to the coupling iteration. The next loop of the coupling iteration begins with the revised primary pressure field being used as a set of essential boundary conditions for the secondary meshes. This entire process is repeated until convergence is reached (***step 11***). The parameters for two sets of convergence criteria are specified by the user, which may be different for different time steps. The first set relates to the nonlinear iterations ((3.127) and (3.128)) and the second to the coupling iterations ((3.129) and (3.130)).

In both cases the criteria are firstly a limit on the sum over all nodes in the primary mesh of the absolute change in pressure from one iteration to the next ((3.127) and (3.129)), referred to as the global criteria, and secondly, a limit on the maximum absolute change in pressure at any node in the primary mesh during an iteration ((3.128) and (3.130)), referred to as the local criteria. In the practical application, nonlinear iteration criteria are stricter than those imposed on the coupling iterations. In addition, the numbers of coupling and nonlinear iterations permitted per time step are limited. The status of all convergence parameters can be reported for quality control measures.

In addition to these controls, a limit is imposed on the absolute value of the calculated flux permitted from any of the secondary meshes during any given time step. In the event that the calculated flux exceeds this value, the flux is 'pruned' to the maximum value and the pressure profile in the secondary mesh is re-determined to be consistent with this value (via a material balance calculation). This is reported and in the event that the flux from any secondary mesh still needs pruning after all the iterations within the coupling iteration loop have been concluded, then a warning is issued. This is not a convergence test, but is used to impose a dampening effect and prevent undue numerical oscillations following a sudden change in reservoir control. If this occurs repeatedly, then either the time step needs to be shortened or the number of cells in the offending secondary mesh need to be increased. The maximum allowable flux is determined by the user specifying a factor (≥1.0) which is applied to the flux from each secondary mesh determined during the previous time step.

Step 11: *Use the result of step 10, i.e.* $\boldsymbol{a}_{p,n+1(m)}^{J+1(1)}$*, as a new approximation for solution to the primary mesh at the end of this time step, and repeat steps 1 to 10 to obtain* $\boldsymbol{a}_{p,n+1(m)}^{J+1(2)}$*. Continue repeating these steps consecutively for* $i = 2$ *to* $I + 1$*. This constitutes the coupling iteration loop. Check for convergence after each set of coupling iterations, and continue iterating until,*

$$\sum_{d}^{D_p} \left| a_{d(p),n+1(m)}^{J+1(I+1)} - a_{d(p),n+1(m)}^{J+1(I)} \right| \le C_3 \text{ , or} \tag{3.129}$$

$$Max\left[\left| a_{d(p),n+1(m)}^{J+1(I+1)} - a_{d(p),n+1(m)}^{J+1(I)} \right|_{d=1 \to D_p} \right] \le C_4 , \tag{3.130}$$

where C_3 *and* C_4 *are values specified by the user, or until the maximum number of coupling iterations, specified by the user, is reached.* I *is therefore either the maximum permissible number of coupling iterations or the number of coupling iterations after which global convergence criteria have been satisfied. The end result is a converged solution* $\boldsymbol{a}_{p,n+1(m)}^{J+1(I+1)}$ *for the primary mesh and a corresponding consistent solution for the secondary mesh,* $\boldsymbol{a}_{s,L+1(n+1(m))}^{I+1}$*. These are the final solutions applicable at the end of time step* n*.*

Within a given time step then, there is a loop of coupling iterations in which the primary and secondary mesh complexes are successively solved and which terminates once a consistent set of pressures and fluxes have been obtained. The secondary meshes provide the fluxes needed by the primary mesh, and the primary mesh provides the pressures needed by the secondary meshes. Within each coupling iteration, the nonlinear matrix equations in the secondary meshes are solved by a forward differencing algorithm using small time steps while the nonlinear equations in the primary mesh are solved either explicitly, or implicitly within a secondary loop of nonlinear iterations. This procedure is repeated for each time step of each time interval (*steps 12 and 13*).

Step 12: *For the next time step, (step number* $n+1$*), repeat steps 1 to 11, and continue to repeat for all time steps in this time interval, i.e. for* $n = 2$ *to* N*. The result at the end of this is the set of solutions* $\boldsymbol{a}_{p,N+1(m)}^{J+1(I+1)}$ *and* $\boldsymbol{a}_{s,L+1(N+1(m))}^{I+1}$*.*

Step 13: *Repeat steps 1 to 12 for the next time interval* $(m+1)$ *and continue for all time intervals, i.e. for* $m = 1$ *to* $M+1$*. The final set of results are* $\boldsymbol{a}_{p,N+1(M+1)}^{J+1(I+1)}$ *and* $\boldsymbol{a}_{s,L+1(N+1(M+1))}^{I+1}$*.*

The load vector and the lumped capacity matrix

User defined internal loads and natural boundary conditions are applied at the end of the time interval for which they are specified and interpolated linearly over the time interval. Likewise, loads imposed on the primary mesh by the secondary mesh (see next section) are applied at the end of each time step and distributed over the time step such that the total mass flow during the time step is conserved.

Where a forward differencing scheme is used ($\theta = 0$), the effective stiffness matrix contains only the capacity matrix and the element capacity matrices are therefore lumped or diagonalised before being assembled, to give $C_{lump}(t)$, thereby improving efficiency of the equation solving process.

Essential boundary conditions

Essential boundary conditions are applied via a ramping formula over a time interval given by

$$P_{n+1}^{i} = P_{1}^{i} + n * delP^{i} , \tag{3.131}$$

where P_{n+1}^{i} is the essential boundary condition to be applied to node i at the end of time step number n of this time interval, P_{1}^{i} is the essential boundary condition applied to node i at the start of the first time step of this time interval, and

$$delP^{i} = \frac{1}{N}\left(P_{N+1}^{i} - P_{1}^{i}\right), \tag{3.132}$$

where N is the number of time steps in this time interval and P_{N+1}^{i} is the essential boundary condition to be applied to node i at the end of the Nth time step of this time interval, i.e. at the end of this time interval. When the essential boundary conditions are applied, a ramping form of expression (3.108) results, given by

$$\boldsymbol{K}_{ef}\boldsymbol{P}_{n+1} = \boldsymbol{K}_{efP_1} + n\boldsymbol{K}_{efdP}\text{, where} \tag{3.133}$$
$$\boldsymbol{K}_{efP_1} = \boldsymbol{K}_{ef}\boldsymbol{P}_1 \text{ and } \boldsymbol{K}_{efdP} = \boldsymbol{K}_{ef}\boldsymbol{delP},$$

in which $a(t_n)$ has been replaced with P_n.

Internal data storage

The sparse stiffness matrix that results after the system equations have been assembled is condensed to the minimum number of columns to accommodate the bandwidth. Due to the need for iterative solving of the equations, more than one solution must be in storage at any given time. For the primary matrix, within any given time step, this includes the pressure field at the beginning of the time step, together with the pressure field at the beginning of the previous time step, the latter only until the first nonlinear iteration has been completed. Thereafter the solution at the beginning of the current time step and the two most recent iteration solution estimates for the end of the current time step must be kept. For the secondary mesh, the pressure field at the beginning of the time step, and the two most recent solutions at the end of the time step must be stored. Contemporary solutions of all secondary meshes are stored in the same matrix, with one index referencing the primary mesh cells and the second, the secondary mesh nodal points.

Physical and fluid properties

Physical properties of both the primary and secondary meshes are input as two- and one-dimensional quadratic equations respectively, allowing heterogeneity to be modelled.

In the two-dimensional case, permeability anisotropy can be modelled by assigning different values to the coefficients of each of the orthogonal components of permeability. The physical properties at the initial pressure are determined, as

$$k_x(x,y) = a_{kx}(x,y) + b_{kx}(x,y)x + c_{kx}(x,y)y + d_{kx}(x,y)x^2 + e_{kx}(x,y)y^2 + f_{kx}(x,y)xy ,$$
$$k_y(x,y) = a_{ky}(x,y) + b_{ky}(x,y)x + c_{ky}(x,y)y + d_{ky}(x,y)x^2 + e_{ky}(x,y)y^2 + f_{ky}(x,y)xy ,$$
$$k_z(x,y,z) = a_{kz}(x,y) + b_{kz}(x,y)z + d_{kz}(x,y)z^2 ,$$

$$\phi_p(x,y)=a_{p\phi}(x,y)+b_{p\phi}(x,y)x+c_{p\phi}(x,y)y+d_{p\phi}(x,y)x^2+e_{p\phi}(x,y)y^2+f_{p\phi}(x,y)xy \text{ and}$$
$$\phi_s(x,y)=a_{s\phi}(x,y)+b_{s\phi}(x,y)z+d_{s\phi}(x,y)z^2 . \qquad (3.134)$$

The subscripts p and s refer to the primary and secondary mesh systems respectively. As indicated, the coefficients can have different values in different regions of the reservoir. Co-ordinates (x,y) indicate distribution in the primary mesh system, while the z co-ordinate indicates distribution in the secondary mesh system. Pressure dependence of the porosity term is dealt with separately via the definition of rock compressibility (2.11). The rock matrix and the fracture network are each assigned a constant but different value of rock compressibility.

Upon initialisation, a single value for the pressure is assigned throughout the primary and secondary meshes. Likewise, a single corresponding value for fluid density is assigned to all parts of the reservoir. The pressure dependence of the fluid density is dealt with via the definition of compressibility (2.13a). The fluid compressibility itself is assumed to have a constant numerical value. Fluid viscosity is allowed to vary with changing pressure according to the 'viscosibility', which has a definition analogous to that of the compressibility. The numerical value of viscosibility is assumed to remain constant.

Input/output

Data are read from a single file divided into two parts. The first deals with geometric information for both mesh complexes and physical and fluid properties. The second part contains time stepping information. The program has limited automatic mesh generation capabilities, allowing the input data to be limited to control lines. For each time step, the number and length of time steps are specified, together with convergence criteria, internal load conditions, essential boundary conditions and natural boundary conditions to be applied during the time step.

3.3.3 The FEFRES computer program

This sub-section comprises a description of the computer program developed during the course of this research, christened FEFRES (Finite Element Fractured REservoir Simulator). The numerical simulator is very general and is able to accommodate a variety of requirements associated with modelling fractured or nonfractured reservoirs.

Where a single porosity model is appropriate, the dual porosity component can simply be switched off. In this case, the single porosity properties are assigned to the primary mesh. Examples of such cases are described in section 4.1 of the next chapter. Where the dual porosity model is appropriate, the primary mesh represents the fracture continuum, and the secondary meshes are built according to the properties of the blocks of matrix material. Examples of such cases are shown in section 4.3 of the next chapter.

The algorithm for modelling a matrix block with a string of one-dimensional finite elements allows transient effects that may exist within the matrix block to be replicated. This is demonstrated in section 4.2 of the next chapter. It is also possible to capture geometrically important characteristics of the matrix block (size and shape) in the one-dimensional representation. Examples of the importance of being able to do this, and how it is achieved, are shown in section 4.2 of the next chapter. It is possible to assign multiple sets of secondary meshes to a single primary element. This would be necessary, for example, if multiple fracture sets were present, resulting in multiple matrix block geometries within the domain covered by any particular primary element.

Fractures can also be modelled explicitly with the use of one-dimensional elements embedded in the two-dimensional primary mesh. In this case the primary mesh is assigned the properties of the matrix material.

Where different regions of the reservoir have different modelling requirements, all of the above-mentioned features, namely single porosity, multiple fracture sets and discrete fractures can be incorporated into a single simulation model.

The FEFRES program is capable of dealing only with two-dimensional reservoirs. It is therefore a prerequisite that it is geologically sensible to represent the fracture network as a two-dimensional continuum. Likewise, the matrix blocks in this system must also clearly be two-dimensional. The program can only accommodate a single phase and deals equally well with water, oil or gas. All that is required is that the correct fluid properties are used. When the fluid is compressible, this fact is honoured fully and the non-linear forms of the governing equations are solved repeatedly until convergence is achieved.

The fracture continuum can be discretized using the variety of two-dimensional elements discussed in section 3.2 of this chapter. Likewise, the matrix blocks can be modelled with any of the one-dimensional elements described in section 3.2. Wells are modelled explicitly within the primary mesh through refinement of the mesh about the wells, or alternatively, by applying internal load conditions to each primary elements covering the domain where a well is located. No-flow boundaries in the reservoir are modelled by specifying natural boundary conditions. Constant pressure boundaries, or the consequences of aquifer support, are approximated by applying natural boundary conditions. Complex reservoir geometries are easily replicated through the flexible meshing capabilities of the finite element method.

Multiple fracture sets can be incorporated by identifying and defining more than one representative matrix block within the area of reservoir represented by any fracture cell.

The basis for the computer code is the UNAFEM program presented in Burnett (1987). During the course of this research the original program was extensively rewritten and modified. However, a number of the underlying principles have been retained. In particular, the modular approach to subroutine construction has formed the basis for FEFRES. The manner in which individual element subroutines are written to be accessible from any part of the program is very efficient and provides a flexible chassis for further development.

Besides the rewriting of the code according to a different programming style, there have been three significant changes made to the original UNAFEM code. The first was the process of customisation needed to deal with the particular governing equations and type of problem used in this work. The second was to incorporate the ability to deal with the nonlinear aspects of the problem. This required the introduction of the nonlinear iteration routines to solve the matrices and the facility to determine the values of pressure dependant coefficients at any point in the program. The result of this was a complete re-organisation of the program's logical sequence caused by the need to update element matrices every time that a new estimate of pressure becomes available. The third major change has been the introduction of the concept of multiple meshes needed to solve the dual porosity problem. This was accompanied by the introduction of the coupling iteration routines and a complete re-organisation of data storage. FEFRES has been developed on a PC and runs under DOS for improved efficiency.

CHAPTER 4

NUMERICAL IMPLEMENTATION AND RESULTS

The modelling approach, algorithms and computer program developed in the previous chapters are applied here to a variety of dual porosity related problems. Numerical results are presented in this chapter in three sections. The first deals with fluid flow in a single porosity system and the results obtained from numerical simulation are compared with analytical solutions for a variety of problems with the objective of verifying the correctness of the numerical simulator.

The second section of this chapter deals with the single matrix block. Comparisons between numerical results obtained using finely meshed two-dimensional models and the corresponding one-dimensional representations are presented with the objective of verifying the one-dimensional model concept and identifying the limitations in the use of such an approach. Numerical results from the simulation of a variety of matrix block geometric shapes, sizes and physical property values and flow regimes are presented.

In the final section numerical simulation results are presented for the combined porous matrix and fracture flow problem. A range of reservoir characteristics are considered and the numerical results are used to improve understanding of the behaviour of fractured reservoirs and to identify the most appropriate modelling approach for any particular set of circumstances.

4.1 Flow through the single porosity system

In this section, three examples of highly compressible gas flowing through a two-dimensional porous and permeable continuum are considered. The objective of this section is to validate the simulator for the single porosity model. This is achieved by comparing the simulation results with analytical solutions. The first example is an elongated reservoir for which the simulation output can be verified with material balance and analytical steady state calculations. The second example is that of flow through a square domain, which demonstrates the effects of heterogeneity and for which the results are verified through material balance calculations. The third example is a well test in a finite radial reservoir that takes advantage of the finite element method's (FEM) flexible meshing capabilities to provide mesh refinement where it is needed, which demonstrates the suitability of higher order elements for this problem. For this example, numerical results are verified by comparison with transient and pseudo-steady state analytical solutions to the radial diffusivity equation.

4.1.1 An elongated reservoir

Problem description and physical properties

The model considered here is that of an elongated reservoir, 1000m long, 100m wide and 1m thick, with homogenous and isotropic properties (Figure 4.1). Two wells, a producer and an injector, are each located 50m from an end, along the centre line of the reservoir. Porosity and permeability (Table

4.1) are typical of a porous and permeable clastic rock matrix. Fluid properties in this example most closely resemble those of oil, although with an exceptionally high value of compressibility. With these parameters, the reservoir contains a volume of 20 000m^3 of fluid which at initial reservoir conditions equates to a mass of 14.416*10^{6}kg. The sequences of flow and injection rates used in the simulation are listed in Table 4.2.

Table 4.1: *Reservoir and fluid properties for the elongated reservoir example.*

Parameter	Symbol	Value	In Oilfield units	Value	in SI units
Matrix permeability	k	**20.0**	mD	**19.7385*10^{-15}**	m^2
Matrix porosity	ϕ	**0.20**	fraction	**0.20**	fraction
Fluid density	ρ	**45.0**	lbft^{-3}	**720.831**	kgm^{-3}
Fluid compressibility	c	**100*10^{-6}**	psi^{-1}	**14.5038*10^{-9}**	Pa^{-1}
Fluid viscosity	μ	**0.20**	cP	**0.20*10^{-3}**	Pas
Initial pressure	P_i	**5000.5**	psi	**34.477*10^6**	Pa

Table 4.2: *Control sequence for the elongated reservoir example.*

Sequence	Injector rate (kg/s)	Production rate (kg/s)	Duration (days)	Elapsed time (days)
1	shut in	shut in	30	30
2	shut in	**0.114**	360	390
3	shut in	shut in	360	750
4	**0.114**	shut in	360	1110
5	shut in	shut in	360	1470
6	**0.266**	**0.266**	360	1830
7	shut in	shut in	360	2190

The numerical model

The problem was solved using the finite element code (FEFRES) described in Chapter 3 with the secondary mesh complex dormant. The reservoir was discretized into 10 square cells, each with dimensions 100m by 100m (Figure 4.1).

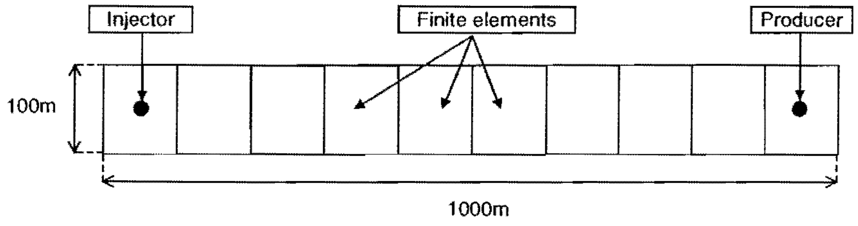

Figure 4.1: *Elongated reservoir with an injector at one end and a producer at the other, discretized into ten square finite elements.*

Both four-node bilinear quadrilateral and eight-node serendipity elements were used. Constant time steps of 1hr. were used throughout. Both forward and backward differencing were used. Due to the simple nature of the problem, convergence was achieved at each time step after at most four iterations.

Some useful analytical expressions

In preparation for the following section in which the numerical results are compared with analytical solutions, important analytical expressions are derived here.

The material balance calculation. In this and subsequent sections, material balance forms an important component of the process of verifying numerical results. The procedure and steps for performing the material balance calculations are outlined below:

The initial pore volume of the reservoir is

$$PV(t_0) = \iint_V \phi(x, y; t_0) dV . \tag{4.1}$$

The initial mass of fluid in the reservoir is

$$M(t_0) = PV(t_0)\rho(t_0) . \tag{4.2}$$

The total mass of fluid produced by time t *is*

$$M_p(t) = \int_{t_0}^{t} Q_m(t) dt . \tag{4.3}$$

The total mass of fluid remaining in the reservoir at time t *is*

$$M_r(t) = M(t_0) - M_p(t) . \tag{4.4}$$

The volume that this remaining mass would occupy at the initial pressure and density is

$$PV^* = \frac{M_r(t)}{\rho(t_0)} . \tag{4.5}$$

If this volume is expanded to fill the original pore volume, the ensuing pressure at time t can be determined by re-arranging the expression for the definition of compressibility (2.13b) and integrating, to give

$$\overline{P}(t) = P(t_0) + \frac{1}{c} ln \frac{PV^*}{PV(t_0)} . \tag{4.6}$$

Expression (4.6) allows the average reservoir pressure to be determined at any time.

The steady state flow equations. During the sequence of flow periods prescribed for this example, steady state conditions become established. From Darcy's law (2.19), the mass flow rate of gas at a point x along the conduit with a constant cross-sectional area of A is

$$q_m(x) = -\frac{kA\rho(x)}{\mu} \frac{\partial P(x)}{\partial x} , \tag{4.7}$$

and the average mass flow rate across the length of the conduit is therefore given by

$$\overline{q}_m = \frac{1}{L}\int_0^L q_m(x)dx = -\frac{kA}{\mu L}\int_{P(0)}^{P(L)} \rho(x)dP \,. \tag{4.8}$$

From the definition of compressibility (2.13a), it follows that

$$\rho(x) = \rho_R \, exp(-c(P(x) - P_R)), \tag{4.9}$$

where ρ_R is a reference density defined at reference pressure P_R. By substituting this into expression (4.8) and performing the integration, we obtain

$$\overline{q}_m = \frac{kA}{\mu L}\frac{\rho_R \, exp(cP_R)}{c}\left(exp(-cP(L)) - exp(-cP(0))\right). \tag{4.10}$$

This expression gives the relationship between the pressure at either end of a conduit with rectangular cross section containing porous and permeable material, and the rate of fluid flowing through the conduit under steady state conditions.

Results

Figure 4.2A shows the average pressure in each of the two end cells (in which the producer and injector are completed respectively) while Figure 4.2B shows the corresponding rate of pressure change. Each of the seven sequences is discussed in turn with reference to these diagrams.

Sequence 1: Both wells inactive. During the first 30d period, pressures remain constant at the initial pressure as neither the producer nor the injector are active.

Sequence 2: Producer active. As the producer is opened (elapsed time 30d), the producer cell experiences immediate and rapid pressure decline. The injector cell also experiences pressure decline but the onset of decline in this cell is delayed with respect to the producer cell. The initial rate of pressure decline in the injector cell is lower than what it is in the producer cell. As time progresses, the rate of decline in the injector cell increases but this rate always remains less than the rate of decline seen in the producer cell and the decline rates in the two cells never converge. In addition, within each of the two cells, the individual rates of decline are not constant, despite the fact that the flow rate is constant, as a consequence of the nonlinear compressibility of the fluid.

Sequence 3: Both wells inactive. After an elapsed time of 390d, the producer is shut in and the pressure trend in the producer cell is immediately reversed. The injector cell, in which the pressure is above the average reservoir pressure at this stage, exhibits a more sluggish response in the form of a gradual slowing down of its decline rate. Pressures in the two cells converge and differ by approximately 0.02MPa at the end of the sequence, with an average value of 14.935MPa forecast by the simulator. The material balance calculation for the reservoir at this stage, following the procedure described in equations (4.1) to (4.6) suggests that the theoretical average reservoir pressure should be 15.022MPa. The value of 14.935MPa determined by the simulator is in good agreement with this figure. The theoretical drop in average pressure from the initial pressure, namely 34.477MPa-15.022MPa=19.455MPa differs by only 0.45% from that forecast by the simulator, namely 34.477MPa-14.935MPa=19.542MPa.

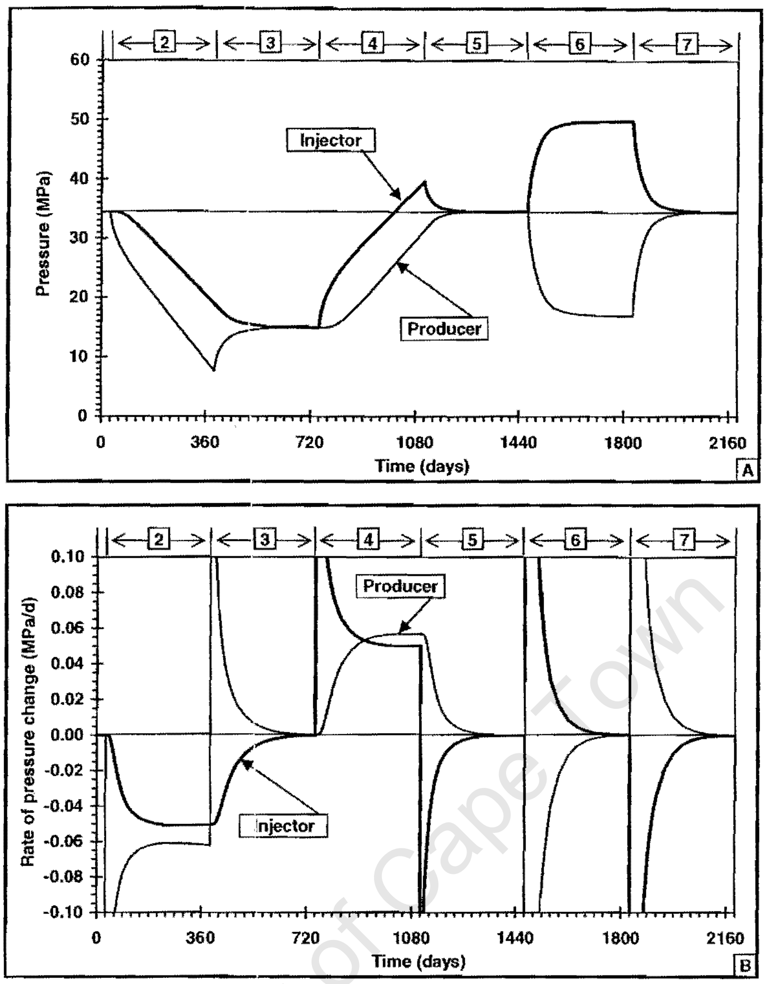

Figure 4.2: *Pressure profiles (diagram A) and rates of change of pressure (diagram B) at either ends of an elongated reservoir containing a producer at one end and an injector at the other for the sequence shown in Table 4.2. Time sequence numbers are shown at the top of the diagrams. The thick curves show the average pressure (diagram A) and rate of change of average pressure (diagram B) of the cell in which the injector is completed as a function of time. The thin curves show the corresponding pressure profile (diagram A) and rate of change of pressure (diagram B) in the producer cell.*

Sequence 4: Injector active. During this sequence, the producer remains inactive and fluid is injected at the same rate that it was extracted during sequence 3. The outcome, evident in Figure 4.2A, is the reverse of the pressure trends observed during sequence 3.

Sequence 5: Both wells inactive. By the end of the previous sequence, a mass of fluid had been extracted from the reservoir, and then the same mass had been replaced. By the end of sequence 5, the reservoir has equalised to an average pressure forecast by the simulator to be 34.415MPa. This is less than 0.2% below the theoretical value of 34.477MPa.

Sequence 6: Both wells active. The producer and the injector are activated at identical absolute rates of 0.266kgs^{-1}. The producer cell experiences an immediate and rapid pressure decline, while the injector cell experiences the reverse. The pressure profiles of the two cells are not mirror images of each other about the initial pressure of 34.477MPa, due to the compressibility of the gas. In both cells, the rates of pressure change decrease until the pressures in the two cells stabilise at values of 49.797MPa and 16.923MPa respectively, representing steady-state conditions. Adopting the initial pressure and the corresponding density as the appropriate reference values, the average mass flow rate according to equation (4.10) should be 0.267kgs^{-1}. The actual value, 0.266kgs-1, differs by 0.37% from this value.

Sequence 7: Both wells inactive. In the final sequence, both wells are shut in simultaneously. The injector cell experiences an immediate and rapid pressure decline, as its pressure is significantly above the average reservoir pressure by the end of the previous sequence while the opposite holds for the producer cell. Eventually the pressure throughout the reservoir equalises to a constant value of 34.411MPa, less then 0.2% different from the theoretical value of 34.477MPa.

Conclusions

- Detail of pressure profiles forecast by the simulator can be interpreted in a way that makes intuitive and logical sense, suggesting that the simulator is not making gross errors in modelling the overall behaviour of a single porosity reservoir.
- During the periods when both wells are shut in and the reservoir pressure stabilises, analytical material balance calculations confirm the average reservoir pressure forecast by the simulator.
- During the period when steady state conditions are established, the analytical solution confirms that the combination of pressure gradient and flow rate forecast by the simulator is consistent.

4.1.2 A heterogeneous square reservoir

Problem description and physical properties

In this section, a square, heterogeneous reservoir, measuring 1000 by 1000m with a single producer well located in the lower lefthand corner (Figure 4.4), 50m distant from the two closest edges, is considered. The physical and fluid properties are the same as those assumed for the previous example (Section 4.1.1), listed in Table 4.1, except that the permeability, given by

$$k_x = k_y = \left(\frac{1}{2}\right)^{\left(\frac{x}{100}\right)} 714 * 10^{-15}\ \text{m}^2, \tag{4.11}$$

and illustrated in Figure 4.3 on a semi-log plot, is heterogeneous (but isotropic).

With the parameters listed in Table 4.1, the reservoir initially holds a mass of 144.16*10^{6}kg of fluid. The well is opened at a rate of 0.61kgs^{-1} for a period of 360d before being shut in for an equivalent length of time.

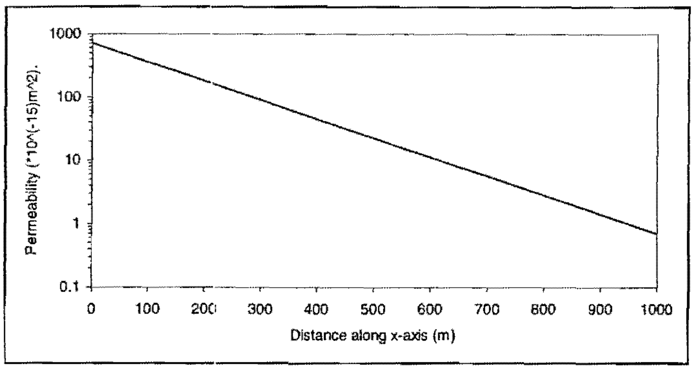

Figure 4.3: *Permeability distribution in the x -direction for the heterogeneous square reservoir model.*

The numerical model

Discretization and elements. The reservoir was discretized into one hundred square cells, each measuring 100 by 100m and modelled with 8-node serendipity elements.

Time stepping. Time stepping was performed with a range of values for θ. It was found that for forward time differencing (θ=0), severe numerical instabilities occurred during early times (up to several days) following a change in the flowing status of the well if the length of the time step was increased beyond 60s, resulting in excessive run times. When backward time differencing was used (θ=1), it was found that the length of the time step could be increased progressively following a change in the flowing status of a well, from an initial value of 60s to 1d over a short period of time and still remain stable, with the pressure field converging to within the specified tolerance levels within 3 nonlinear iterations. Equivalent accuracy in results were obtained using the two time stepping routines but with the forward differencing runs taking up to 4 times longer than the backward time differencing runs. These results confirm the standard criterion that unconditional stability is achieved when θ has a value between ½ and 1. Performance of the Crank-Nicolson method was similar to that of the backward time differencing method, but required slightly more stringent selection of time step sizes and marginally longer run times to achieve the same level of accuracy.

Results

The pressure distribution existing in the reservoir after the 360d flow period is shown as a contour map in diagram A of Figure 4.4 and is clearly dominated by the strongly heterogeneous nature of the reservoir. The pressure field at the end of the one year shut in period is shown in diagram B of Figure 4.4. The heterogeneous nature of the reservoir still influences the pressure distribution, although after this length of time, the pressure has almost equalised throughout the reservoir.

Material balance. Following a similar sequence of material balance calculations to that described in the previous section (equations (4.1) to (4.6)), the final average pressure in the reservoir should be 24.745MPa. The drop in average pressure forecast by the simulator (34.477-24.708=9.769MPa) differs by less than 0.4% from that predicted by material balance calculations (34.477-24.745=9.732MPa).

Conclusions

- Inspection of the pressure contour maps shows that the simulator honours the permeability heterogeneity and that the overall trend forecast by the simulator makes intuitive sense.
- The final average reservoir pressure forecast by the simulator is confirmed with analytical material balance calculations.

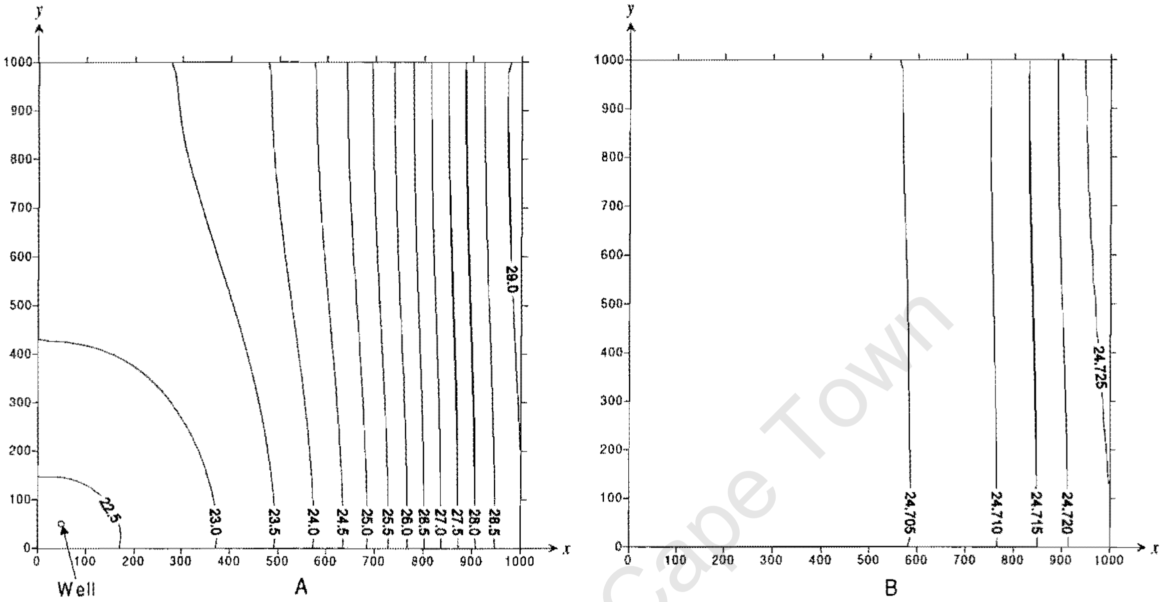

Figure 4.4: *Pressure contours (MPa) in an anisotropic, two-dimensional reservoir after 360 days of production from a well located in the lower lefthand corner (A) and subsequently 360 days after the well has been shut in (B).*

4.1.3 Radial flow: the well test

Problem description and physical properties

The reservoir is assumed to be a homogenous and isotropic circular domain (Figure 4.5). The physical properties of the reservoir and fluid are listed in Table 4.3. The 500m radius reservoir, which is 1m thick and has a porosity value of 0.1, is intersected by a 31.12cm (12.25in.) diameter well at its centre. The reservoir has a high value for permeability and the fluid properties are typical of gas. The initial fluid density referred to in Table 4.3 is the density at reservoir conditions at the initial pressure. These properties result in an initial mass of $19.635*10^6$kg of gas in place (approximately equal to 0.7Bscf of gas).

The sequence that has been modelled (Table 4.4) is typical of a well test. The well is flowed for a fixed period (12hours) referred to as the 'draw down', at a high and constant rate (19.571kgs^{-1}, or approximately 60MMscf/d). The well is then shut in by closing a choke located down hole for a period referred to as the 'build up' period, which should be at least as long as the draw down (12-hours).

Pressure gauges located as close to the sand face as possible record the pressure in the well bore as a function of time, during both draw down and build up.

Table 4.3: *Reservoir and fluid properties for the radial well-test problem.*

Parameter	Symbol	Value	Oilfield units	Value	in SI units
Reservoir radius	r_e	**1640.4**	ft	**500**	m
Well bore radius	r_w	**0.511**	ft	**0.156**	m
Matrix permeability	k	**1013.3**	mD	**$1.0*10^{-12}$**	m^2
Matrix porosity	ϕ	**0.10**	fraction	**0.10**	Fraction
Initial fluid density	ρ	**15.6**	$lbft^{-3}$	**250**	Kgm^{-3}
Fluid compressibility	c	**$103.4*10^{-6}$**	psi^{-1}	**$15*10^{-9}$**	Pa^{-1}
Fluid viscosity	μ	**0.04**	cP	**$40*10^{-6}$**	Pas
Initial pressure	P_i	**5000.5**	psi	**$40*10^{6}$**	Pa

Table 4.4: *Control sequence for the radial flow example.*

Sequence	Duration (hours)	Production rate (kg/s)	Production rate[1] (MMscf/d)
Draw down	12	19.571	30
Build up	12	0.000	360

NOTE: [1] Production rate in oilfield units is approximate

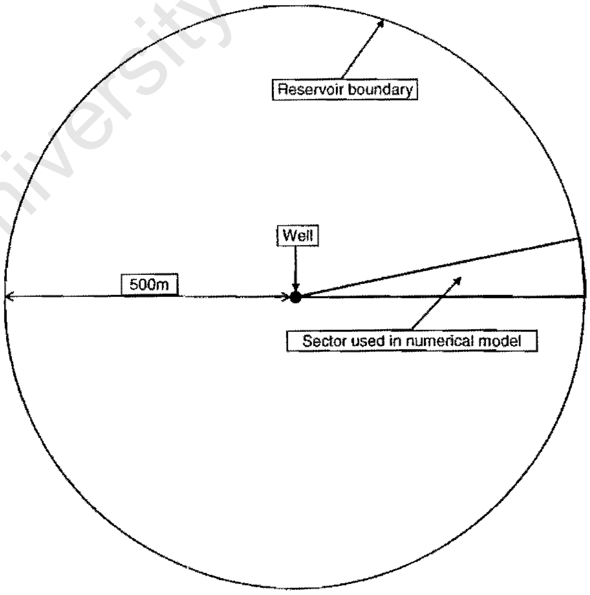

Figure 4.5: *Circular reservoir with a well at its centre, showing the sector used for numerical simulation.*

The numerical model

Due to the radial symmetry of the reservoir considered in this example, the problem is one-dimensional, but is treated here as two-dimensional. In this example, a sector comprising 1/32nd of the full circle (11.25 degrees) is considered (Figures 4.5 and 4.6). A sector of this specific size is most suitable for this problem as it can be discretized with a single row of elements and at the same time allow both an optimal rate of increase in the dimension of successive elements as a function of the radial distance from the centre of the well bore to be achieved, and a minimum degree of distortion of quadrilateral elements from the shape of a square to be maintained.

Discretization. A single row of elements has been used to model the sector. The mesh is generated by constructing $N+1$ circular arcs with radii

$$r_i = r_w \left(\frac{r_e}{r_w} \right)^{\frac{i}{N}}, \text{ for } i = 0 \text{ to } N, \tag{4.12}$$

where r_w is the radius of the well, r_e is the outer radius of the reservoir and N is the number of elements, in this case, 40. The innermost element has dimensions of approximately 3.5cm (Figure 4.6, diagram B), while the outermost cell has dimensions of approximately 91.5m (Figure 4.6, diagram A). The outer cell therefore represents a pore volume approximately 6 to 7 orders of magnitude greater than the pore volume of the innermost cell. The extremely fine meshing in the vicinity of the well bore is necessary to capture the rapid changes that take place in this area immediately after a well is either opened or shut.

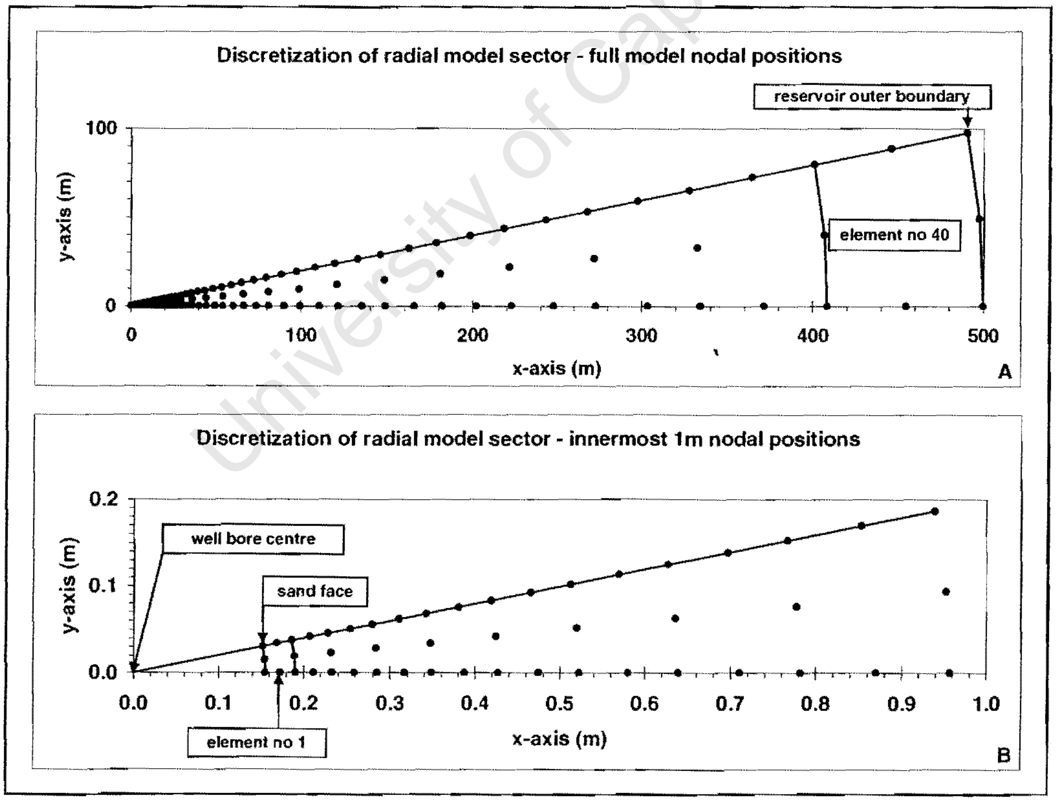

Figure 4.6: *Discretization of a 1/32 (11.25degree) sector of a circular reservoir with a diameter of 500m showing the nodal points for 8-node serendipity elements (diagram A) and the innermost 1m of the discretized sector of diagram A showing the relationship between the innermost cell and the well bore (diagram B).*

Boundary Conditions. Flow into the well bore is accounted for via distributed natural (flux) boundary conditions. The reservoir is therefore considered to flow under depletion drive conditions, with no pressure maintenance from an outside source and no influx of fluids into the reservoir. The flow rate specified in Table 4.4 of 19.571kgs^{-1} represents the total flow rate into the well bore from the entire circumference. The sector being modelled contributes 1/32 of that through an element edge of total length 0.0306m, resulting in a distributed flux along the edge of 20.0kgs^{-1}m^{-1}.

Time stepping and convergence. Time stepping has been selected to allow accurate definition of early time changes after the flowing status of the well is altered. The first time interval comprises 100 steps of 0.0001s, totalling 0.01s. Time steps are thereafter successively increased by a factor of $\sqrt{2}$, with the same number of steps (100) in each interval, until the time interval reaches a length of 1 hour. Thereafter, all intervals are 1 hour long, comprising 60, one minute steps. The same time stepping is repeated for each of the two, twelve hour long sequences. Each 12-hour sequence therefore consisted of 47 time intervals and 4320 time steps. The simulator was run with backward differencing ($\theta = 1.0$). Convergence criteria were set to allow a maximum global error of 1000Pa (C_1 in equation 3.127 and C_3 in equation 3.129) and a maximum local error of 100Pa, (C_2 in equation 3.128 and C_4 in equation 3.130) or a maximum of 10 nonlinear iterations (refer to Section 3.3.2), whichever was achieved first. Convergence criteria were always met within the specified maximum number of iterations.

Some useful analytical expressions

Both pseudo-steady state and transient flow conditions are identified and discussed in the next section dealing with the results. In preparation for this, the required analytical solution methods are stated here. Analytical approximations to the radial diffusivity equation for (slightly) compressible fluid in a circular domain have been extensively investigated by numerous workers over the years in the effort to interpret well-tests and thereby gain insight into the characteristics of the reservoir. Analytical solutions for infinitely acting radial transience and pseudo-steady state (pseudo-steady state) behaviour that are appropriate for the problem being dealt with in this section are discussed below. The concept of the real gas pseudo-pressure is also described here in anticipation of its use for Horner analysis of the build up.

The radial diffusivity equation. The differential equation (2.32) for a radially symmetric problem is

$$\frac{\partial^2 P}{\partial r^2} + \frac{1}{r}\frac{\partial P}{\partial r} + c\left(\frac{\partial P}{\partial r}\right)^2 = C\frac{\phi \mu c}{k}\frac{\partial P}{\partial t}, \qquad (4.13)$$

where C is a constant. This expression is difficult to solve analytically due to the last term on the lefthand side. If the fluid compressibility or the pressure gradient are small this term may be ignored, permitting an analytical solution to be developed. An estimate of the relative importance of the terms of equation (4.13) for the example under consideration can be made by using the simulator output during the transient stage when changes are taking place very rapidly, after an elapsed time of 34s (end of time interval 21) and at a distance of 1m from the centre of the well bore (cell number 9).

Under these conditions, the terms on the lefthand side of expression (4.13) have the approximate values

$$\left|\frac{\partial^2 P}{\partial r^2}\right| = 0.48, \ \left|\frac{1}{r}\frac{\partial P}{\partial r}\right| = 0.46 \text{ and } \left|c\left(\frac{\partial P}{\partial r}\right)^2\right| = 0.0036. \qquad (4.14)$$

This suggests the despite the highly compressible nature of the fluid, ignoring the third term on the righthand side of equation (4.3) still allows a reasonable approximation to be made for this specific example.

Infinitely acting radial transient behaviour. The solution to equation (4.13) (in which the nonlinear term has been dropped) for transient behaviour is effected by applying the initial condition and two boundary conditions. The initial condition states that the pressure is equal to P_i at time $t = 0$. The one boundary condition states that the pressure at the outer edge of the reservoir remains at the initial pressure, while the constant rate at the sand face is according to Darcy's law. Mathews and Russel (1967) provided a solution (Craft and Hawkins, 1991, p235) of the form

$$P(r,t) = P_i - C\frac{q\mu}{\rho kh}\left(-E_i\left(-C_1\frac{\phi\mu c_t r^2}{kt}\right)\right), \qquad (4.15)$$

where $P(r,t)$ is the pressure at a radial distance r from the centre of the well bore at time t, P_i is the initial reservoir pressure, q is the flow rate into the well bore, E_i is the exponential integral and C and C_1 are constants. This is the line source solution to the diffusivity equation. When the value of the argument is less than 0.01, the exponential integral can be approximated by

$$-E_i(x) = -ln(x) - 0.5772. \qquad (4.16)$$

This leads to an analytical approximation, which, expressed in units of this work is

$$P(r,t) = P_i - 0.1833\frac{q\mu}{\rho_0\, exp\left(c\left(P(r,t) - P_i\right)\right)kh}\left(log\left(\frac{kt}{\phi\mu c r^2}\right) + 0.3489\right), \qquad (4.17)$$

where ρ_0 is the reference fluid density and h is the reservoir thickness. Expression (4.17) provides a reasonable estimate provided that

$$0.2511\frac{\phi\mu c r^2}{kt} < 0.01, \qquad (4.18)$$

a condition imposed by the approximation for the exponential integral (expression (4.16)). At the sand face, therefore, the approximation is valid provided the time is greater than 0.036s. Equation (4.17) and subsequent expressions have been adapted from equations reported in Craft and Hawkins (1991, p239), which are expressed in oilfield units and relate to liquid volumetric flow rates reported at surface conditions. The equations shown here have been adjusted to be compatible with the unit system used in this work and with the gas flow rates reported in mass units.

Pseudo-steady state behaviour. Pseudo-steady state behaviour becomes established once the pressure pulse has intersected the outer boundary of the reservoir. A full description of the difference in behaviour between infinitely acting radial transient and pseudo-steady state flowing conditions is described in the following sections dealing with the numerical results. Derivation of the pseudo-steady state equation follows a similar route to that of the infinitely acting radial transient equation, but with different boundary conditions, namely that the radial pressure gradient is equal to zero at the edge of the reservoir, which is compatible with the no flow boundary assumption. The resulting expression is

$$P(r,t) = P_i - 0.1833\frac{q\mu}{\rho_0\, exp\big(c\big(P(r,t) - P_i\big)\big)kh}\left(log\left(\frac{\pi r_e^{\,2}}{C_A r_w^{\,2}}\right) + 0.3514\right) - \frac{qt}{\rho_0\, exp\big(c\big(P(r,t) - P_i\big)\big)\pi r_w^{\,2} h\phi c}, \tag{4.19}$$

in which C_A is a dimensionless shape factor that takes on the value of 31.62 for a circular domain. This relationship has once again been adapted from the equations in oilfield units reported in Craft and Hawkins (1991, p243).

The real gas pseudo-pressure formulation. In order to model the behaviour of a real gas more accurately, the 'real gas pseudo-pressure' can be substituted for pressure in the radial diffusivity equations, allowing the analysis to be performed without any limiting assumptions concerning compressibility of the gas. The real gas pseudo-pressure ($m(P)$) is defined (Dake, 1978, p247) as

$$m(P) = 2\int_{P_R}^{P}\frac{P}{\mu Z}dP. \tag{4.20}$$

The real gas Z-factor is included in the gas law to account for the deviation in behaviour of a real gas from that of an ideal gas at high pressure, viz.

$$PV = ZnRT. \tag{4.21}$$

By combining this with the definition of compressibility (2.8), rearranging and integrating, it follows that

$$Z = \frac{Z_0}{P_0}P\, exp\big(c(P_0 - P)\big), \tag{4.22}$$

where Z_0 is a known value at some pressure P_0. By including this in expression (4.20), assuming that the viscosity remains constant, and performing the integration, we obtain an expression for real gas pseudo-pressure, in the form

$$m(P) = \frac{2P_0}{c\mu Z_0}exp\big(c(P - P_R - P_0)\big). \tag{4.23}$$

If this is incorporated into equation (4.13) then one obtains the radial diffusivity equation for $m(P)$, that is

$$\frac{\partial^2 m(P)}{\partial r^2} + \frac{1}{r}\frac{\partial m(P)}{\partial r} = \frac{\phi\mu c}{k}\frac{\partial m(P)}{\partial t}. \tag{4.24}$$

Provided that viscosity and compressibility are constant, an approximate solution to this equation can be obtained through the use of the exponential integral.

Results: The well bore temporal response

In this first of two sections dealing with results for the modelling of the well test, the pressure response within the well bore itself as a function of time is analysed. Pressure as a function of time in the well bore over the full 24 hour duration of the test is illustrated in Figure 4.7. Inspection of the draw down shows two distinct periods. The first spans the time during which rate of change of pressure in the well bore is not constant. During this period, pressure changes rapidly, particularly during the first few seconds after the well has been opened. The rate at which the pressure changes itself decreases in absolute terms as a function of time. This is referred to as the period of 'transient' behaviour. During the second period, pressure in the well bore continues to change, but the rate of change is approximately constant (i.e. the well bore pressure is an approximately linear function of time). This is referred to as the period of 'pseudo-steady state' or 'semi-steady state' behaviour.

The transient period itself may be further divided into two parts, often referred to as early and late transience. During early transience, the pressure pulse travels radially outward from the well bore, and has not yet reached the outer boundary of the reservoir. For all practical purposes the reservoir is infinite in extent, as the position of the outer boundary has not yet begun to influence pressure recorded in the well bore. This period is often referred to as the 'infinite acting' period. Once the first sign of pressure change occurs at the outer boundary, this period of early transience ends, and is followed by a period of stabilization prior to pseudo-steady state becoming fully established. This period of stabilization is also strictly transient in nature, and is often referred to as the 'late transient' period. There is some controversy as to the existence and nature of so called late transience, particularly in a radially symmetric reservoir such as this (Dake (1994), p163). However, for the purpose of analysing the well test, the early transient period, or infinitely acting period, is most important as it is possible to approximate this period analytically. To avoid confusion, the so-called early transient period will be referred to as the 'infinitely acting radial transient' (IRT) period, which describes this period unambiguously.

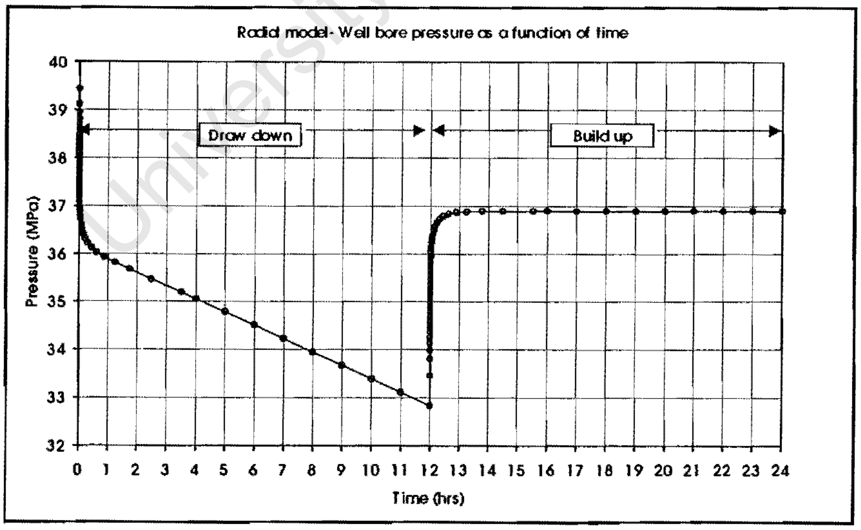

Figure 4.7: *Pressure response in the well bore in the centre of a circular reservoir subjected to a 12-hour flow period followed by a 12-hour shut in period.*

The pseudo-steady state period occurs after the pressure pulse has reached all the boundaries, the shape of the pressure profile has become reasonably stable, and the reservoir pressure throughout is declining in an approximately uniform fashion. This behaviour differs from real steady state behaviour for which the pressure profile remains static in time and for which the outer boundary of the reservoir must be a constant pressure boundary, rather than a no flow boundary.

During the build up, which should be regarded merely as a change in rate, a similar process to that described above occurs, in that the pressure disturbance created by changing the rate of the well at first travels radially outwards from the well bore, following infinitely acting transient behaviour, then goes through a transition phase as the pulse reaches the outer limits of the reservoir, and eventually follows pseudo-steady state behaviour. As the reservoir pressure has been altered from its original uniform state due to the preceding draw down, the response at the well during the build up is a superposition of events, and the individual flow regimes are not immediately apparent on the linear scales of Figure 4.7. During the initial seconds of the build up, the pressure recorded in the well bore changes very rapidly. This rate of change slows down and eventually the pressure in the reservoir stabilises to a value that is determined by the material balance.

Comparison between analytical and numerical results for the draw down. Analytical solutions for both infinitely acting radial transient and pseudo-steady state conditions (4.17) and (4.19), together with the output from the numerical simulator are illustrated for the first three hours of draw down on a linear time scale in Figure 4.8. Close inspection of the listing of the numerical results reveals that the outer cell (number 40) first begins to experience a change in pressure after time interval 31, which corresponds to 18.646 mins. Up to this point it can be stated with a high degree of confidence that the reservoir must exhibit infinitely acting radial transient behaviour. The rate of draw down has become approximately constant by the time interval 35 is reached, which corresponds to a total elapsed time of 78mins, after which it is clear that the reservoir exhibits pseudo-steady state behaviour.

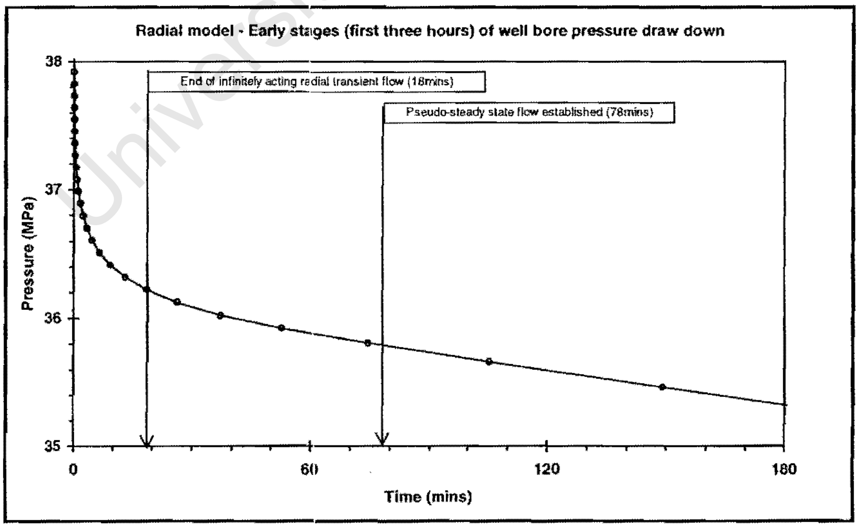

Figure 4.8: *Pressure response in the well bore in the centre of a circular reservoir during the first 3 hours of pressure draw down. The solid line is the output from the numerical simulator. The circles are the approximations obtained by using the analytical solution for infinitely acting radial transient behaviour.*

There is very good agreement in Figure 4.8 between the infinitely acting radial transient analytical solution and the numerical approximation for the first 18mins, and between the pseudo-steady state solution and the numerical approximation after an elapsed time of 78mins. The time at which pseudo-steady state has become established (78mins) was confirmed using the expression presented in Craft and Hawkins (1991, p217) which, in the units of this work, is

$$t_{PSS} = 0.3164\frac{\phi\mu c r_e^{2}}{k}. \tag{4.25}$$

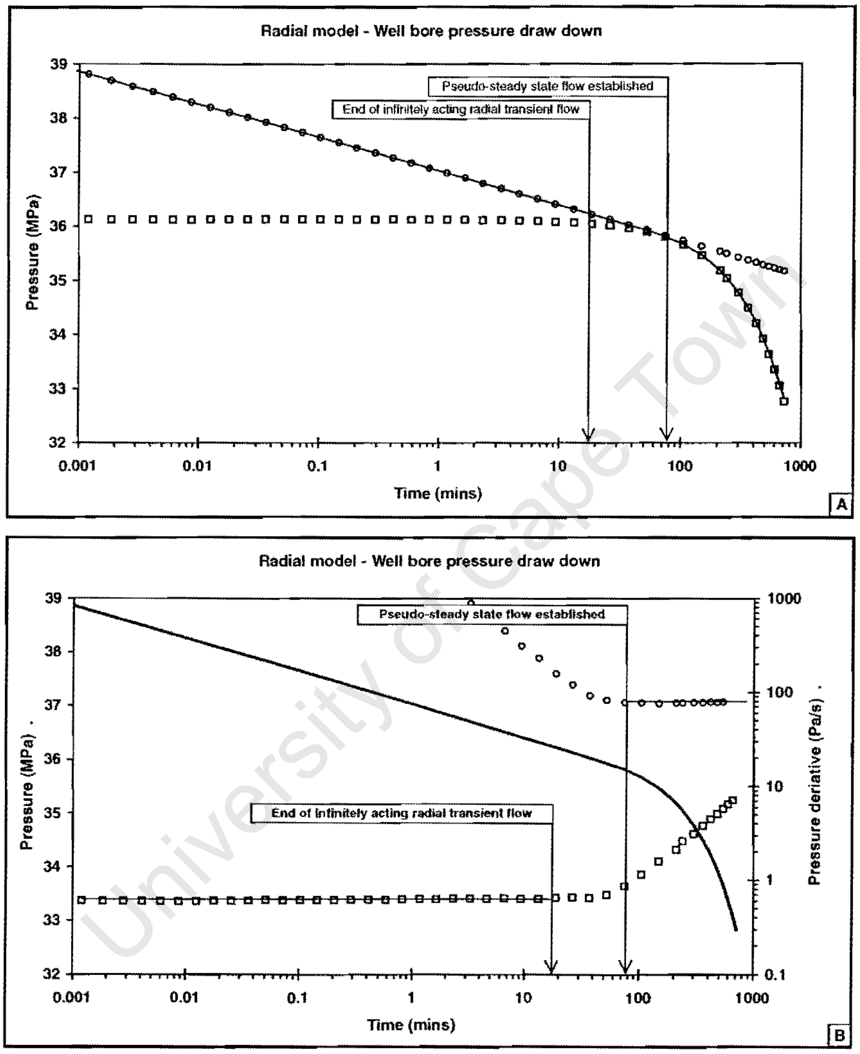

Figure 4.9: *Pressure response in the well bore in the centre of a circular reservoir during a 12-hour draw down against a logarithmic time scale. The solid line is the output from the numerical simulator. In diagram A, the circles are the approximations obtained by using the analytical solution for infinitely acting radial transient behaviour. The squares are the approximations obtained by using the analytical solution for pseudo-steady state behaviour. In diagram B, the circles are the derivatives of the simulator output with respect to time. The squares are the derivatives of the simulator output with respect to logarithmic time.*

The full draw down period is illustrated in Figure 4.9A on a logarithmic time scale that stretches the early time. Agreement between the numerical and each of the analytical solutions is good during those periods for which the respective analytical solutions are appropriate. Clearly the use of either of the analytical solutions beyond the limits of the period for which it is appropriate results in errors.

Further definition of the flow regimes is illustrated in Figure 4.9B where the numerical results are shown for the full draw down period, together with derivatives of this pressure with respect to time and with respect to logarithm of time. The time interval over which the derivative of pressure with respect to time remains reasonably constant is expected to define the period over which the well follows pseudo-steady state behaviour (from equation (4.19)). The time interval over which the derivative of pressure with respect to logarithmic time remains reasonably constant is expected to identify the period during which the well exhibits infinitely acting radial transient behaviour (from equation (4.17)).

Horner build up analysis. So far, only the pressure draw down period has been considered. In practice, due to the noise associated with flowing a well, the pressure data recorded down hole during the draw down period is often inferior to that recorded during the build up period. The most popular method of analysing build up data is with the use of Horner plots (Horner, 1951; Dake, 1994, p190), and involves plotting the pressure as a function of the dimensionless Horner time, defined as

$$t_H = log\frac{t + \Delta t}{\Delta t} \qquad (4.26)$$

in which t is the elapsed time from when the well was shut in and Δt is the length of the preceding flow period. On a Horner plot, transience appears as a straight line with constant slope. Once the limits of the reservoir have been 'seen', the absolute value of the slope begins to decline and reaches a value of zero at the time that the flow is pseudo-steady state.

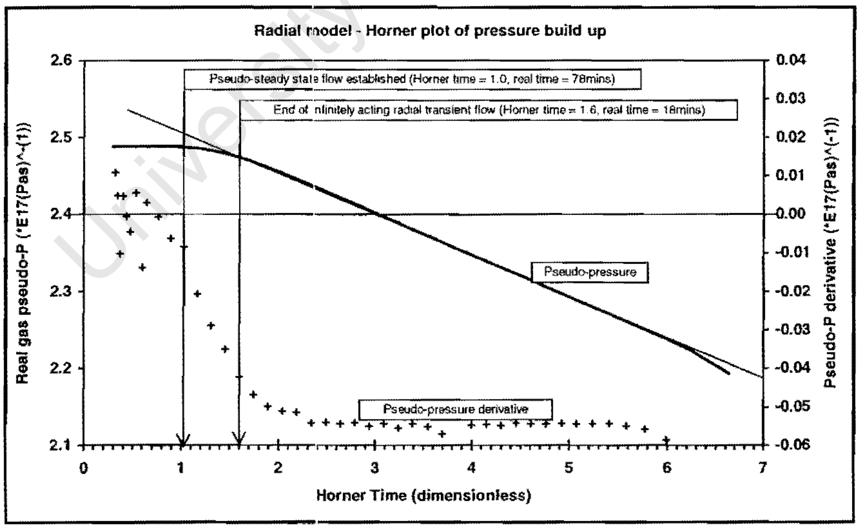

Figure 4.10: *Horner plot for the build up sequence following a 12-hour draw down sequence for a well completed in the centre of a circular reservoir.*

The real gas pseudo-pressure has been used in the construction of the Horner plot illustrated in Figure 4.10. The derivative of the real gas pseudo-pressure with respect to the Horner time is also included. Note that real time increase from the right to the left of the abscissa with infinite shut in time occurring at a Horner time of 0. The period during which the derivative maintains a constant value (of between -

0.05 and -0.06) which corresponds to the infinitely acting radial transient behaviour, is evident. Thereafter the derivative begins to change at a Horner time of approximately 1.6, which corresponds to a real time of 18min. The derivative is seen to change rapidly, reducing in absolute magnitude to reach a value of about 0 at a Horner time of approximately 1.0, which corresponds to a real time of 78mins. The flat section of the Horner plot from this point onwards (to the left) is indicative of pseudo-steady state behaviour. This analysis of the build up and the agreement with the observations made under the discussion pertaining to the draw down period add confidence that the numerical simulator is providing a reliable reflection of the reservoir response.

Material balance. From Figure 4.6, it is clear that the final, stabilised pressure is considerably lower than the initial pressure. The material balance for this test follows the steps described in Section 4.1.1, (expressions (4.1) to (4.6)). By applying the procedure to this problem it appears that the final average reservoir pressure should be 37.07MPa. Inspection of the detailed output of the simulator reveals that the average pressure in the reservoir after the 12-hour shut in period is 36.90MPa. There is thus a 5.5% difference in the amount that the pressure has fallen from its initial value, between the material balance calculations and the simulator forecasts, or conversely, a 0.5% difference in the final absolute pressure values. When the material balance adjustment option in the simulator is applied, the simulator of course gives a result which is identical to that of the material balance calculation.

Results: The spatial response

In this second of the two sections dealing with results for the modelling of the well test, the pressure in the reservoir as a function of the radial distance from the centre of the well bore is analysed, at a number of selected values of elapsed time. In each of the diagrams that follows, curves for up to seven different values of elapsed time, identified according to Table 4.5, are illustrated.

Table 4.5: *Elapsed times at which pressure profiles are illustrated in Figure 4.11 and 4.12.*

Reference curve	Time interval no.	End of time interval.	Status
1	11	1.1secs	infinitely acting radial transient
2	21	34.9secs	infinitely acting radial transient
3	26	3.3mins	infinitely acting radial transient
4	31	18.6mins	Last of infinitely acting radial transient
5	35	74.6	Near pseudo-steady state
6	41	6hrs	pseudo-steady state
7	47	12hrs	pseudo-steady state

The pressure as a function of radial distance from the well bore is plotted for each of the 7 selected times after the well has been opened for the draw down sequence (Figures 4.11 and 4.12).

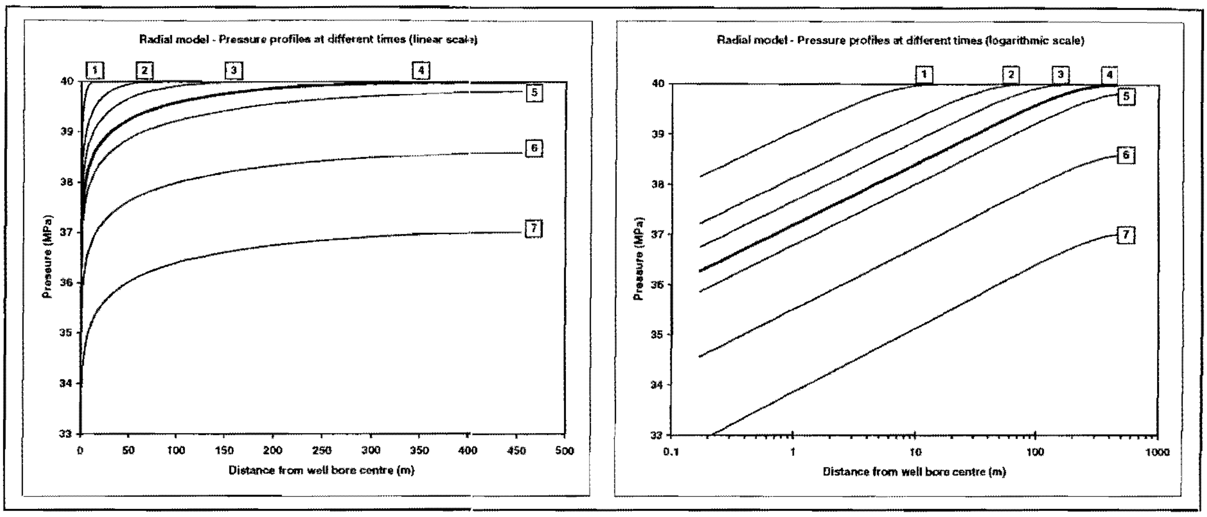

Figure 4.11: *Pressure forecast by the simulator as a function of radial distance from the centre of a well bore located in a circular reservoir. Each profile corresponds to a different time (see Table 4.5) after the well has been shut in following a 12-hour flow period. A linear distance scale is used in the diagram on the left, and a logarithmic scale in the diagram on the right.*

Transient behaviour exists for the first 4 selected time intervals. The migration of the pressure pulse away from the well bore as time progresses, is evident. The pressure pulse reaches the limit of the reservoir at the time corresponding to curve number 4. In the case of curve number 5, pseudo-steady state is becoming established and in the final two curves, pseudo-steady state behaviour is evident, with the pressure declining uniformly throughout the reservoir. For that time during which infinitely acting radial transient behaviour occurs, the analytical approximations (4.17) are included in Figure 4.12 as circles.

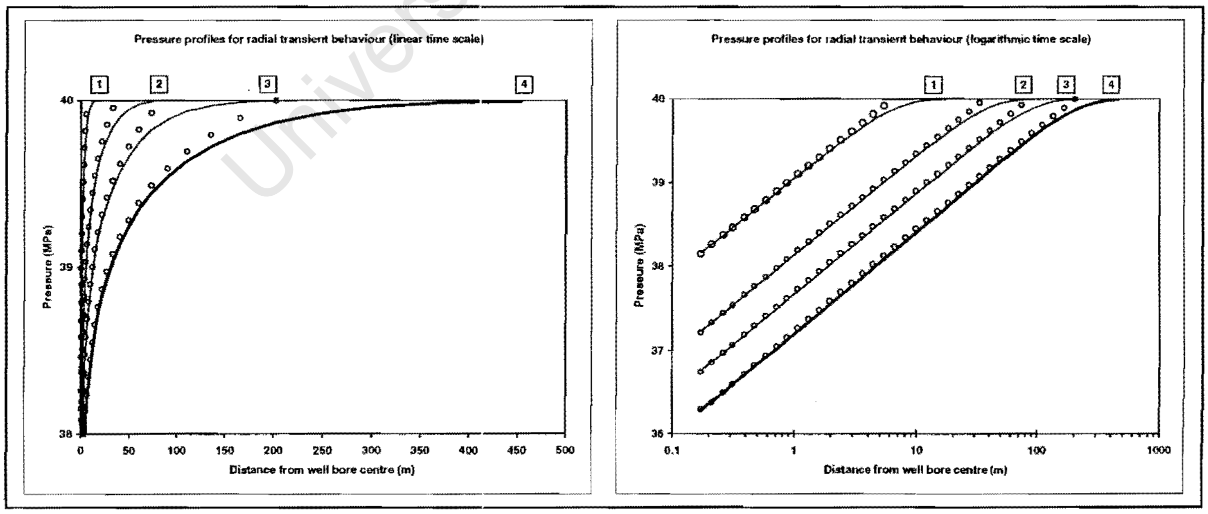

Figure 4.12: *Pressure as a function of radial distance from the centre of a well bore located at the centre of a circular reservoir. Each profile corresponds to a different time, and the sequence covers the period during which infinitely acting radial transient behaviour is observed (see Table 4.5) after the well has been shut in following a 12-hour flow period. The solid curve is the output from the numerical simulator. The circles represent the analytical solution.*

4.2 Flow from an individual matrix block

In this section, the flow of fluid from an individual matrix blocks is analysed. The shape, size and physical properties of the matrix block are varied, and expulsion of gas under different flowing conditions is compared for different solution techniques. The fractures are not modelled explicitly in this section, and are dealt with by imposing boundary conditions on the matrix block models.

In the first part, the process of reducing the matrix block to a one-dimensional representation is described. A reference matrix block, typical of a low matrix permeability fractured gas reservoir is modelled. Besides the reference block, several other geometric shapes are considered, and their corresponding one-dimensional representations are described. This is followed by a section in which the different solution methods are discussed: a finely meshed two-dimensional numerical solution, the numerical solution of the one-dimensional representation, and an analytical solution. In the next section comparisons are made between results obtained from various combinations of matrix block characteristics and solution techniques for pseudo-steady state flow conditions. Finally, these comparisons are repeated, where appropriate, for transient flow conditions. In addition, the effect of refinement of the discretization of the one-dimensional model is considered.

4.2.1 One-dimensional conceptual models for differently shaped blocks

The concept of reducing differently shaped matrix blocks to one-dimensional representations is developed in this section. A square matrix block is considered first, which is referred to subsequently as the 'reference' matrix block. The concept is extended to cover rectangular, triangular, and ribbon-shaped blocks. Additionally, the problem of dealing with anisotropy is addressed. The reference matrix block is a homogenous and isotropic, two-dimensional (1m thick) square block saturated with gas. The properties of the matrix material and the gas are shown in Table 4.6.

Table 4.6: *Parameters of the reference matrix block and its saturating fluid.*

Parameter	Symbol	Value	Oilfield units	Value	SI units
Lengths	a	32.808	ft	10.0	m
Thickness	c	3.2808	ft	1.0	m
Permeability	$k_{m,x}, k_{m,y}$	0.00101325	mD	$1.0{*}10^{-18}$	m^{2}
Porosity	ϕ_m	0.10	fraction	0.10	fraction
Fluid viscosity	μ	0.40	cP	$0.40{*}10^{-3}$	Pas
Fluid compressibility	c	$103.4{*}10^{-6}$	psi^{-1}	$15.0{*}10^{-9}$	Pa^{-1}
Initial fluid density	ρ	15.607	lbft^{-3}	0.250	gcm^{-3}
Initial pressure	P_{mi}	5801.5	psi	$40.0{*}10^{6}$	Pa

Reduction of the reference block to a one-dimensional problem

The two-dimensional matrix block and its one-dimensional representation are illustrated in Figure 4.13. the length of a side of the matrix block is a. For the purpose of this discussion, the x-axis has been selected to coincide with the preferred orientation of the one-dimensional model with respect to the two-dimensional block. In this, and all subsequent examples, the variable x is the spatial co-ordinate of the one-dimensional matrix block, and takes on values between 0 and D. D is the value of x at the boundary of the matrix block, which, in the case of the reference block, is equal to $\frac{a}{2}$.

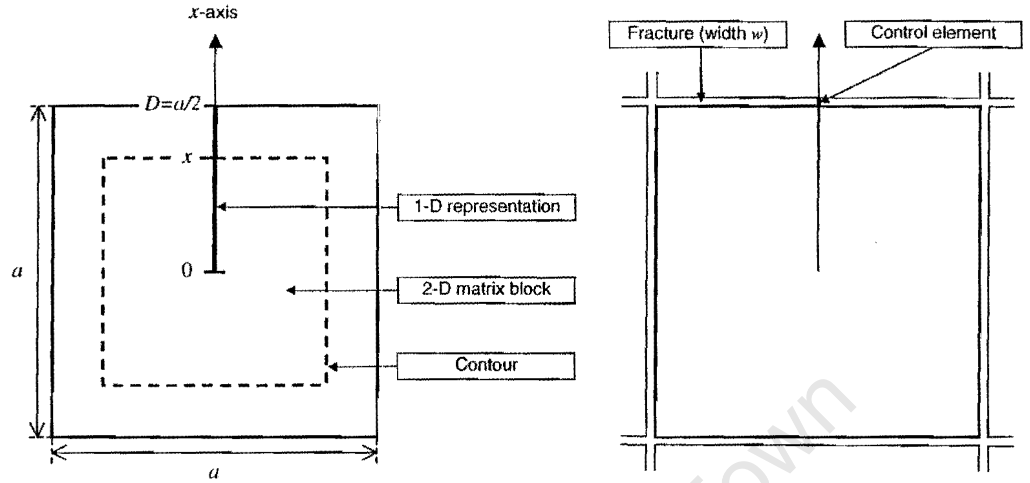

Figure 4.13: *The reference matrix block and its one-dimensional representation are shown on the lefthand side. The relationship between the matrix block representation and the fractures is illustrated on the righthand side.*

Reduction of the multi-dimensional matrix block to a one-dimensional model is based on the premise that the most important property determining the behaviour of the expulsion of gas from an isotropic and homogenous matrix block is the distribution of the volume of gas as a function of distance from the outer surface. Use is made of the concept of a 'contour' $l(x)$, illustrated in Figure 4.13 and defined as the loci of all points that are equidistant from the nearest edge. The value of $l(x)$ varies between 0 where x=0, and the total circumference of the two-dimensional matrix block, where $x = D$. The matrix material is then modelled with finite elements defined along the spatial co-ordinate x, between 0 and D. The 'control element', introduced in section 3.3 and used to describe the fracture at the end of the one dimensional matrix block, is modelled as an additional element located between $x = D$ and $x = D + w$, where w is the width of the fracture.

In general, the reduction to a one-dimensional model is approximated by replacing both the permeability and the porosity with the product of the respective parameter and an appropriate value for the length of the contour, giving

$$k_m'(x) \approx \int_0^{l(x)} k_m(s)ds\text{, and} \tag{4.27}$$

$$\phi_m'(x,t) \approx \int_0^{l(x)} \phi_m(s,t)ds\text{,} \tag{4.28}$$

where $l(x)$ is the total length of the contour passing the x-axis at the point x. The multi-dimensional governing equation (2.23) without the gravity term is

$$\nabla \cdot \left(\frac{\rho k_m}{\mu} (\nabla P_m) \right) = \phi_m \rho c_m \frac{\partial P_m}{\partial t} . \tag{4.29}$$

The one-dimensional version of this equation is

$$\frac{\partial}{\partial x} \left(\frac{\rho(x,t) k_m'(x)}{\mu(x,t)} \left(\frac{\partial}{\partial x} P_m(x,t) \right) \right) = \phi_m'(x,t) \rho(x,t) c_{m,t}(x,t) \frac{\partial P_m(x,t)}{\partial t} . \tag{4.30}$$

In the event that the matrix block is homogenous and isotropic, or is isotropic with properties that vary with x, then expressions (4.27) and (4.28) reduce to

$k_m'(x) \approx k_m l(x)$, and (4.31)

$\phi_m'(x) \approx \phi_m l(x)$ respectively. (4.32)

The expression for the length of the contour of the unit square, illustrated in Figure 4.13 by the dashed line, is

$$l(x) = 8x . \tag{4.33}$$

In order to implement this procedure numerically, the expression for the pore volume encompassed within the circumference $l(x)$ is required, which, for the square matrix block, is

$$PV(x) = \int_0^D \int_0^{l(x)} \phi_m(s) ds dx . \tag{4.34}$$

When the matrix block is homogenous, with a single value of porosity throughout, this reduces to

$$PV(x) = A(x) \phi_m . \tag{4.35}$$

The expressions for the area encompassed by the contour of a general isotropic and heterogeneous, unit square is

$$A(x) = 4x^2 . \tag{4.36}$$

Variety in matrix block geometry and properties

Fracture sets that break the rock matrix into blocks generally have well defined orientations determined by the tectonic forces that induced the fracturing and by the fabric of the formation. Within a given reservoir, several fracture sets may exist, with different orientations and fracture spacing, resulting in a large range of possible geometric forms for the matrix blocks. In this section, geometric forms are considered that idealise many shapes that are likely to occur in nature.

What distinguishes one geometric form from another during the simplification process from a multi- to a single-dimensional representation is the expression for $l(x)$. Based on the premise that the most important parameter determining the evolution of the pressure at a given point within the matrix block is that point's location relative to the closest edge, the path followed in determining the expression for $l(x)$ is that which ensures that the distance to the nearest edge from every point on $l(x)$ is a constant value for any given value of x. The matrix block geometric forms considered here were selected to cover a range of expressions for $l(x)$ that would test the sensitivity and robustness of the numerical solution to this parameter.

Although a large number of geometrical shapes is theoretically possible, the matrix blocks must all fit together to fill the reservoir. If the fracturing is random and results in many different block sizes and shapes, then for practical reasons it will be necessary to determine a representative geometry. The value of the parameter $l(x)$ can then be regarded as a history matching parameter, in much the same way as the conventional geometric factor is considered a history matching parameter in conventional dual porosity simulators.

The bulk reservoir rock that later becomes fractured may be significantly anisotropic with respect to permeability, and significantly heterogeneous with respect to both permeability and porosity. However, over the range of matrix block sizes for which dual porosity behaviour in a reservoir is important, heterogeneity in plan view is often not significant when considering individual matrix blocks, i.e., in general, the scales of the matrix blocks are far smaller than the horizontal scales of heterogeneity. This is not always the case, however, and where heterogeneity is important on the scale of the matrix block, average properties must be applied, which may degrade the accuracy of a one-dimensional representation. Anisotropy, on the other hand, may be independent of scale, and therefore can occur equally in individual matrix blocks as it does in the bulk reservoir. Anisotropy therefore requires consideration in the development of the one-dimensional model.

The rectangle. Rectangular matrix blocks are common and occur when two fracture sets with different fracture spacing intersect at right angles. The expression for $l(x)$ (Figure 4.14) in this case becomes

$$l(x) = 2(a-b) + 8x\,, \tag{4.37}$$

while the area enclosed within the contour for the general homogenous rectangle is

$$A(x) = 2(a-b+2x)x\,. \tag{4.38}$$

In this study, the specific example of a rectangle with dimensions 20 by 5m has been considered (see Table 4.7).

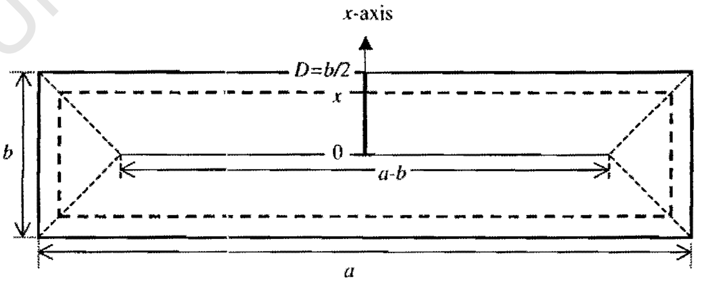

Figure 4.14: *Reduction of a two-dimensional rectangular matrix block to a one-dimensional representation.*

The right angled triangle. Right angled triangular shaped matrix blocks can occur when two fracture sets orientated at right angles to each other, are intersected by a third, oblique fracture set. Consider a general right angled triangle where the sides at right angles to each other have lengths a and b. The origin of the x-axis along which the one-dimensional representation is defined is positioned equidistant (D) from the three sides and is orientated as illustrated in Figure 4.15.

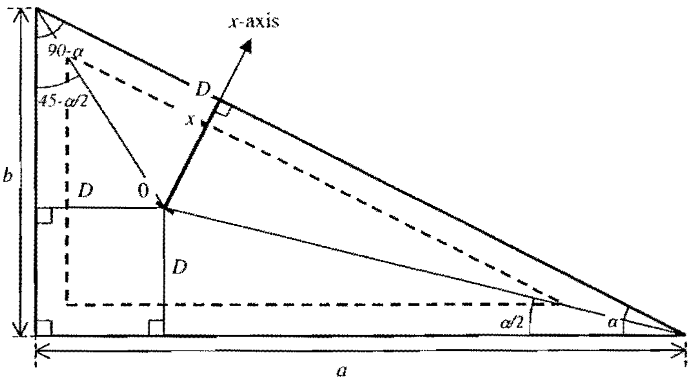

Figure 4.15: *Reduction of a two-dimensional right angled triangular matrix block to a one-dimensional representation.*

The total dimension of the one-dimensional representation is therefore

$$D = \frac{a}{1 + cot(\beta)}, \text{ with } \beta = \frac{\alpha}{2}. \tag{4.39}$$

The appropriate expression for the length of the contour, $l(x)$ is

$$l(x) = \left(2 + cot(\beta) + cot(45 - \beta) + \sqrt{(1 + cot(\beta))^2 + (1 + cot(45 - \beta))^2} \right) x. \tag{4.40}$$

The area enclosed by the contour as a function of x for the general homogenous triangle is

$$A(x) = \frac{1}{2}(1 + cot(\beta))(1 + cot(45 - \beta))x^2. \tag{4.41}$$

The approach presented here can be extended to any arbitrary triangle. It must be borne in mind, however, that the range of triangles is limited to those which can be pieced together to fill a space. In this study, two right triangles have been considered, one in which the value of α is 45°, and the other, an acute angled triangle for which the long edge is twice that of the short edge and for which the value of α is therefore approximately 14° (see Table 4.7).

The infinitely long ribbon. In this example, the reservoir is characterised by a single fracture set which divides the reservoir into a series of parallel ribbons that are, for practical purposes, infinitely long. Figure 4.16 shows a representation of such a block.

The block has a width equal to b, and an arbitrary section of length a is considered here. As gas flows parallel to the x-axis, the expression for $l(x)$ is simply

$$l(x) = 2a. \tag{4.42}$$

The general expression for the area enclosed by the contour of such a block is

$$A(x) = 2ax. \tag{4.43}$$

For this study, a 10m length of an infinitely long, 10m wide ribbon is considered.

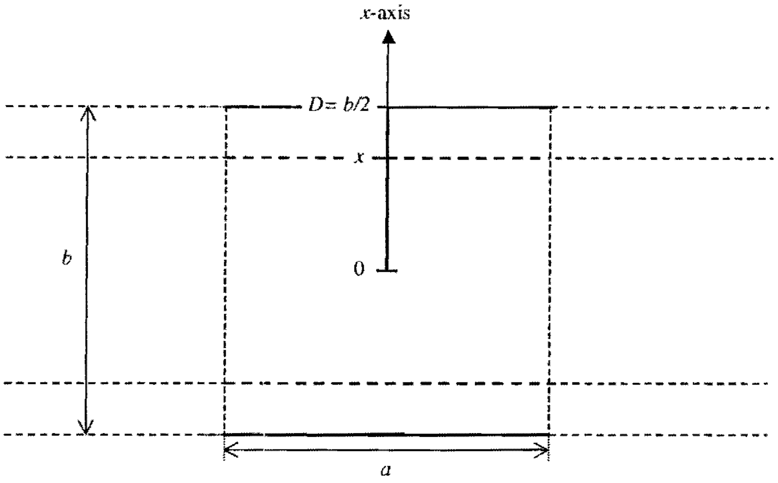

Figure 4.16: *Reduction of a section of an infinitely long two-dimensional matrix block to a one-dimensional representation.*

The anisotropic square. It is common for the matrix permeability to be anisotropic. In this example, a square matrix block is assumed to have different values for two orthogonal components of the permeability. It is further assumed that the principal permeability directions are aligned parallel to the edges of the matrix block. This is not unusual, as permeability anisotropy is often related to rock strength, which in turn has a strong influence on the orientation of fracture propagation. The degree of anisotropy is defined as

$$\varphi = \frac{k_{my}}{k_{mx}}. \tag{4.44}$$

The isotropic reference block can be considered to lie at one end of the anisotropy scale ($\varphi = 1$), while the infinitely long block approximates the other extreme end of the scale in which permeability in one direction is effectively zero ($\varphi = 0$).

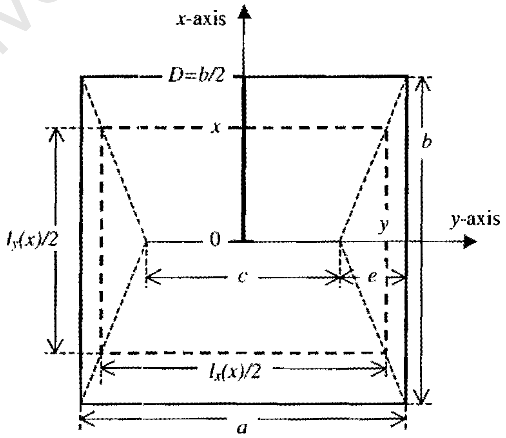

Figure 4.17: *Reduction of a two-dimensional anisotropic square matrix block to a one-dimensional representation.*

In the anisotropic case, the contour is defined as the loci of all points for which the product of the distance to the edge and the permeability in that direction, is constant. The implication of this is that for the anisotropic square matrix block, $l(x)$ is not represented by a series of concentric squares as x

varies, but rather by a series of rectangles which have aspect ratios that change progressively from 0 to 1 as x increases from 0 to D. The expressions that apply in this case are

$$a = b\,,\ e = \varphi\frac{a}{2} \text{ and } y = \frac{a}{2}(1-\varphi) + \varphi x\,. \tag{4.45}$$

The matrix porosity is assumed to remain constant throughout the block and the expression for the pore volume that honours this block's criteria is therefore

$$V_p(x) = 4A(x)\phi_m = 4xy\phi_m = \left(2ax(1-\varphi) + 4\varphi x^2\right)\phi_m\,. \tag{4.46}$$

The corresponding length of the contour surrounding this volume is

$$l(x) = 4x + 4y = 4x(1+\varphi) + 2a(1-\varphi)\,. \tag{4.47}$$

For the purpose of determining the appropriate permeability to use for the one-dimensional model, the expression for the length of the contour must be broken down into two components that are respectively perpendicular to the x-direction and y-direction so that

$$l(x) = l_x(x) + l_y(x)\text{, in which} \tag{4.48}$$

$$l_x(x) = 4y = 2a(1-\varphi) + 4\varphi x \text{ and } l_y(x) = 4x\,.$$

The expression for permeability is then

$$k_m'(x) \approx l_x(x)k_{mx}(x) + l_y(x)k_{my}(x) = \left(8\varphi x + 2a(1-\varphi)\right)k_{mx}\,. \tag{4.49}$$

In the cases studied here, all parameters are identical to those of the reference block except for the degree of anisotropy for which values of $\varphi = 0.5$ and $\varphi = 1.0$ are considered (see Table 4.7).

Specific examples

For the specific geometric examples used in subsequent sections, the parameters are summarised in Table 4.7. All matrix blocks are 1m thick and have the same volume of 100m^3.

Table 4.7: *Parameters for the matrix block geometric forms used in this study.*

Matrix block	*a (m)*	*b (m)*	*D (m)*	*l(x)*	*A(x)*
Square (reference)	10	10	5	$8x$	$4x^2$
Rectangle	20	5	2.5	$30+8x$	$4x^2+30x$
45° triangle	14.142	14.142	4.142	$11.657x$	$5.828x^2$
14° triangle (14.036°)	28.284	7.071	3.100	$20.808x$	$10.404x^2$
Section of infinitely long ribbon	10	10	5	20	$20x$

For the anisotropic square with dimensions of 10m by 10m, the following applies:

Matrix block	$k_{m,x}$ *(m²)*	$k_{m,y}$ *(m²)*	k'_m *(m²)*	*l(x)*	*A(x)*
Anisotropic square ($\varphi = 0.5$)	$1 \cdot 10^{-18}$	$0.5 \cdot 10^{-18}$	$(4x+10) \cdot 10^{-18}$	$6x+10$	$2x^2+10x$
Anisotropic square ($\varphi = 0.1$)	$1 \cdot 10^{-18}$	$0.1 \cdot 10^{-18}$	$(0.8x+18) \cdot 10^{-18}$	$4.4x+18$	$0.4x^2+18x$

4.2.2 Description of numerical and analytical solution procedures

The expulsion of gas from an individual matrix block has been solved (and the results compared in sub-section 4.2.3) using three methods, namely, a finely meshed finite element solution of the two-dimensional problem, a finite element solution of the one-dimensional representation, and an analytical solution of the pseudo-steady state problem. In this section, the approach used for each of these methods is discussed. The results of the modelling are presented in the next section.

(a) Numerical solution of the two-dimensional model

The finite element computer program developed in Chapter 3 was used to solve the equations governing the two-dimensional problem.

Discretization. In the case of the reference block, the 10m*10m square was discretized into 20*20 cells, which were modelled with 4-node bilinear quadrilateral elements. The fracture surrounding the block was represented by a single cell layer, discretized into elongated cells with dimensions of 0.5m and 0.01m and also modelled with 4-node bilinear quadrilateral elements. Additional runs were completed with the block discretized into 10*10 cells and 100*100 cells. The 10*10 mesh gave results which differed slightly from the 20*20 mesh during early transient times. The respective results obtained by using the 20*20 and the 100*100 meshes were very similar and the 20*20 mesh was used further because of its superior run times. Simulations were also completed using 8-node serendipity instead of 4-node bilinear quadrilateral elements. No improvement in the results was evident and the 4-node bilinear quadrilateral elements were therefore used for further work.

Precisely the same discretization and selection of elements were applied to the anisotropic square and to the 10m section of the 10m wide, infinitely long block. In the case of the rectangular block, the same discretization was used, and the cells deformed proportionately (to 1.0m*0.25m rectangles). In the case of the 45° triangular block, the space was filled with a mesh comprising squares and triangles and in the case of the 14° triangular block, the space was filled with rectangles and triangles.

Boundary conditions. For the modelling of pseudo-steady state conditions, approximated by withdrawing gas from the block at a constant mass rate, the appropriate internal load condition was applied to each of the elements representing the fractures that surround that single matrix block. For the purpose of studying transient effects, approximated by maintaining the fracture at a constant pressure, the appropriate essential boundary condition was applied to each of the fracture cells. The pressure in the fractures may vary along the length of a single matrix block, resulting in a geometrically asymmetrical rate of flow from the block. However, due to the relatively far greater permeability of the fracture, compared with that of the matrix material, the effect of the pressure gradient across the dimension of the matrix block is usually negligible. For this reason, the pressure in the fractures surrounding a single matrix block is considered to vary in time only.

Time stepping. Numerous time stepping alternatives were compared to ensure that convergence was taking place. Both an explicit (forward differencing) and an implicit (backward differencing) approach were found to be satisfactory.

(b) Numerical solution of the one-dimensional model

In this section, the process of solving the equations for the one-dimensional representations of the different matrix blocks is discussed. The primary consideration here is the selection of appropriate elements to describe the process. Sufficient accuracy is required, while at the same time the minimum computational effort needs to be established in order to maximise efficiency when these elements are incorporated into the full field model. In this regard, the number of elements, the order of the elements, and the way that the one-dimensional representation is discretized, are important.

Discretization. The most rapid changes take place at and close to the boundary between the matrix block and the fracture, and clearly this is where the smallest element sizes are required. Two approaches were used to discretize the one-dimensional models, namely:

- *Exponential:* cell lengths increase exponentially away from the outer edge.
- *Square rule:* cell lengths increase according to the square of the distance from the outer edge.
- *Equal volume:* all elements represent an equal pore volume (according to expressions in Table 4.7)

For a square, the latter two approaches are identical. For each of the matrix geometry forms, the nodal points that were used in this study according to the above criteria are listed in Table 4.8 .

Table 4.8: *Nodal points for 5 element model of various matrix block geometric forms.*

Matrix block	Type	x_0	x_1	x_2	x_3	x_4	x_5
Square	Equal volume	0.000	2.236	3.162	3.873	4.472	5.000
Rectangle	Equal volume	0.000	0.616	1.155	1.641	2.086	2.500
45° triangle	Equal volume	0.000	1.852	2.620	3.208	3.705	4.142
45° triangle	Exponential	0.000	2.594	3.249	3.642	3.923	4.142
14° triangle	Equal volume	0.000	1.386	1.961	2.401	2.773	3.100
Section of long ribbon	Exponential	0.000	3.417	4.094	4.494	4.779	5.000
Section of long ribbon	Square rule	0.000	2.236	3.162	3.873	4.472	5.000
Anisotropic square ($\varphi = 0.5$)	Equal volume	0.000	1.531	2.623	3.521	4.301	5.000
Anisotropic square ($\varphi = 0.1$)	Equal volume	0.000	1.085	2.122	3.117	4.075	5.000

Table 4.9: *Nodal points for different numbers of elements for square matrix block.*

Number of elements	Type	x_0	x_1	x_2	x_3	x_4	x_5
5	Equal volume	0.000	2.236	3.162	3.873	4.472	5.000
4	Equal volume	0.000	2.500	3.536	4.330	5.000	
3	Equal volume	0.000	2.887	4.082	5.000		
2	Equal volume	0.000	3.536	5.000			
1	Equal volume	0.000	5.000				

In the case of the reference block, the number of elements was also allowed to vary from one to five, the nodal points for which are shown in Table 4.9. In addition, a single 5-node quartic element was used , with the same nodal points as the 4 linear elements. Trials were also completed with five 3-noded quadratic elements. The fracture has been modelled by attaching a small (0.01m long) element to the end of the sequence of elements used to model the matrix block itself.

(c) Analytical solution of the pseudo-steady state equation

The numerous expressions for the geometric factor discussed in Section 2.2.3 were evaluated, and it was found that the expressions (2.75) and (2.77) of Warren and Root (1963), gave results which most closely and consistently matched those of the finely meshed two-dimensional numerical simulation. The analytical solutions presented in subsequent sections are therefore those obtained using these equations of Warren and Root. For the two-dimensional case of a rectangular block with sides of lengths *a* and *b*, Warren and Root's equation becomes

$$\alpha^* = \frac{8(a+b)^2}{a^2 b^2} . \qquad (4.50)$$

For the square and rectangle (the only geometric forms for which the geometric factor of Warren and Root can be directly determined), α^* takes on the values 0.32 and 0.50 respectively.

(d) Analytical solution of the transient equation

The transient equation analysed in this chapter is equation (2.85). The model considered here is that of a circular disk, which is the closest approximation for a square for which the transient equation can be solved. The characteristic length of equation (2.85), l_m, is the radius of the circle that has the same area as all the other geometric shapes considered in this chapter, i.e. 5.64m. The corresponding values of C_1 is 1. Equation (2.85) has bee approximated up to n=20.

4.2.3 Numerical results for pseudo-steady state flow conditions

The objective of this section is firstly to determine the accuracy and limitations of the analytical technique, and secondly, to establish the reliability of the one-dimensional numerical solution for pseudo-steady state conditions. In the first part of this section, comparisons are made between results obtained for the pseudo-steady state expulsion of gas from a variety of matrix block geometric shapes using the analytical solution, two-dimensional finite element numerical simulation, and one-dimensional finite element numerical simulation. The geometric shapes considered in this first part are those for which analytical geometric factors are readily available, namely the square, the rectangle and the section of an infinitely long ribbon. In the second part of this section, the two-dimensional numerical simulation results are compared with one-dimensional numerical simulation results for those geometric forms for which the analytical geometric factors are not readily available, namely the right triangles and the anisotropic block.

Square, rectangular and infinitely long matrix blocks

Matrix block characteristics, and solution techniques are all as described in Section 4.2.2. Results of the modelling of pseudo-steady state expulsion of gas from the 3 matrix block geometric forms are illustrated in Figures 4.18 to 4.20. Each figure contains the following six diagrams:

Diagram A: *'Difference between pressure in matrix and fracture for given flow rate'*: The difference between the average pressure in the matrix block and the fracture pressure is plotted as a function of time for each of the analytical and the two-dimensional numerical approximations respectively for a specified flow rate. For the specified flow rate, see diagram C.

Diagram B: *'Percentage difference in pressure differentials'*: The difference between the two curves of diagram A is plotted as a percentage of the two-dimensional numerical approximation curve of diagram A as a function of time. This diagram accentuates any differences that exist between the curves in diagram A.

Diagram C: *'P_f for given Q_g'*: The absolute pressure in the fracture, required to accommodate a specified flow rate is plotted as a function of post transient time (after 10d) for each of the analytical and the two-dimensional numerical approximations respectively. Also shown is the specified flow rate as a function of time, expressed in units of kg/d and represented by a constant volumetric flow rate of $10m^3$/d at standard conditions.

Diagram D: *'Percentage difference in fracture pressure'*: The difference between the two fracture pressure curves of diagram C is plotted as a percentage of the two-dimensional numerical approximation curve of diagram C, against post transient time. This curve accentuates the differences between the curves of diagram C.

Diagram E: *'G_p for specified P_f*: Cumulative gas produced from the matrix for a specified fracture pressure evolution, namely that determined for the numerical two-dimensional approximation shown in diagram C, and repeated in diagram D, is plotted as a function of post transient time.

Diagram F: *'Percentage difference in cumulative production'*: The difference between the two curves of diagram E is plotted as a percentage of the two-dimensional numerical approximation curve of diagram E, against post transient time. In addition, the difference in cumulative gas determined by the two-dimensional and one-dimensional numerical approximations respectively, expressed as a percentage of the two-dimensional numerical approximation is shown. This diagram accentuates differences between the curves of diagram E and allows comparisons of accuracy amongst the two-dimensional numerical approximation, the one-dimensional numerical approximation and the analytical solution.

Square reference block. Modelling results are shown in Figure 4.18. From diagrams A and B it is clear that there is very good agreement between the analytical solution and the two-dimensional numerical approximation for the matrix/fracture pressure difference values after about the first 10 days. During the first 10 day period, there is very poor agreement. This is due to the fact that the numerical solution captures the early transient effect while the analytical solution does not.

From diagrams C and D it is clear that there is significant divergence (up to 20%) in the fracture pressure values needed to sustain the given rates as determined by the two-dimensional numerical and analytical approaches during late times.

Diagrams E and F show that there is fairly good agreement between the two-dimensional numerical and the analytical approximations of cumulative gas produced as a function of post transient time for a specified history of fracture pressure. The difference is greatest in early times (diagram F) due to the cumulative effect of the preceding transient period. This illustrates that the numerical solution is accurate when pseudo-steady state conditions prevail, but provides poor accuracy during periods of transience, and depending upon the manner in which boundary conditions are specified, may be subject to inaccuracies for some period following the termination of transience. Diagram F illustrates the superior agreement between the two-dimensional and one-dimensional numerical approximations, where differences in forecast cumulative production do not differ by more than 1%. The numerical solution, on the other hand, shows cumulative gas production figures which differ by 3% to more than 10% from the two-dimensional numerical solution, and which take a long time to recover from the effects of transience.

Rectangular matrix block. Diagrams A and B of Figure 4.19 show that there is not good agreement between the analytical and two-dimensional numerical approximations for the difference in pressure between the matrix and the fracture. However, the percentage difference remains fairly constant in the range 26 to 28% after the end of transience (diagram B) and is related to the definition of the average pressure in the matrix rather than to any inherent inaccuracy. A comparison between the diagrams A of Figures 4.18 and 4.19 reveals that in order to sustain a given flow rate, the required pressure drop between the matrix and the fracture is significantly lower for a rectangular block than for a square block of the same volume. This is intuitively correct as the rectangle has a greater surface area and hence all particles lie closer to an edge than is the case with the square block. The remaining diagrams show results that are similar to those for the square block. Diagram F once again shows good agreement between the one-dimensional and two-dimensional numerical approximations, but the agreement is not as good as for the square block. For the rectangular block, differences in cumulative production remain below 3%. For the analytical solution, cumulative gas differs by 2 to 8 % from that of the two-dimensional numerical solution, with the analytical solution still suffering the consequences of incorrect forecasting from the transient period, long after transience has terminated.

Section of infinitely long, ribbon shaped matrix block. The 10m section of an infinitely long, 10m wide block, although it has the same pore volume as the reference block, requires a significantly greater pressure differential between the matrix and the fracture to sustain the same flow rate (compare diagrams A of Figures 4.20 and 4.18). The extent of the transient period is also greater than is the case with the reference block (compare diagrams B of Figures 4.20 and 4.18).

The analytical solution once again provides a reasonably good approximation after transience has ceased. There is, however, as with the reference block, a significant divergence in the fracture pressures required to sustain a given flow rate as determined by the two-dimensional numerical and the analytical approximations (greater than 20% in later times). The order of the projected fracture pressure is also reversed, compared with that of the reference profile, with the analytical solution showing a higher fracture pressure requirement than the two-dimensional numerical approximation.

This degradation is probably due to the expulsion of gas from only two sides of the infinitely long block, which causes greater pressure gradients within the block, which in turn amplifies the effects of nonlinear compressibility, not accounted for fully in the analytical solution.

The diagrams showing cumulative production for a specified evolution of fracture pressure (E and F) illustrate that the one-dimensional numerical approximation once again gives good results, with the difference between the two-dimensional and one-dimensional numerical models maintained at an approximately constant value of about 2%, while the analytical solution differs from the two-dimensional numerical solution by 4 to 5%.

Right triangles and anisotropic matrix blocks

In this part, only the percentage difference in cumulative produced gas as a function of time for a specified fracture pressure is illustrated for each of the geometric forms (equivalent to diagram F of part 1). The comparison presented here is between the results of the two-dimensional and one-dimensional numerical solutions.

45° right triangle. Diagram A of Figure 4.21 shows the percentage difference between the cumulative gas estimated with the two-dimensional and one-dimensional numerical approaches for a specified fracture pressure (also shown in diagram A, Figure 4.21). The difference remains approximately constant, with a value of between 2 and 3%.

14° right triangle. The results for the acute angled triangle are shown in diagram B of Figure 4.21. These are similar to those of the 45° right triangle, with difference in the range of 2 to 3%.

Anisotropic square. A comparison between the two-dimensional and one-dimensional numerical solutions for the anisotropic square ($\varphi = 0.1$) are shown in diagram C of Figure 4.21. Differences remain below 1%.

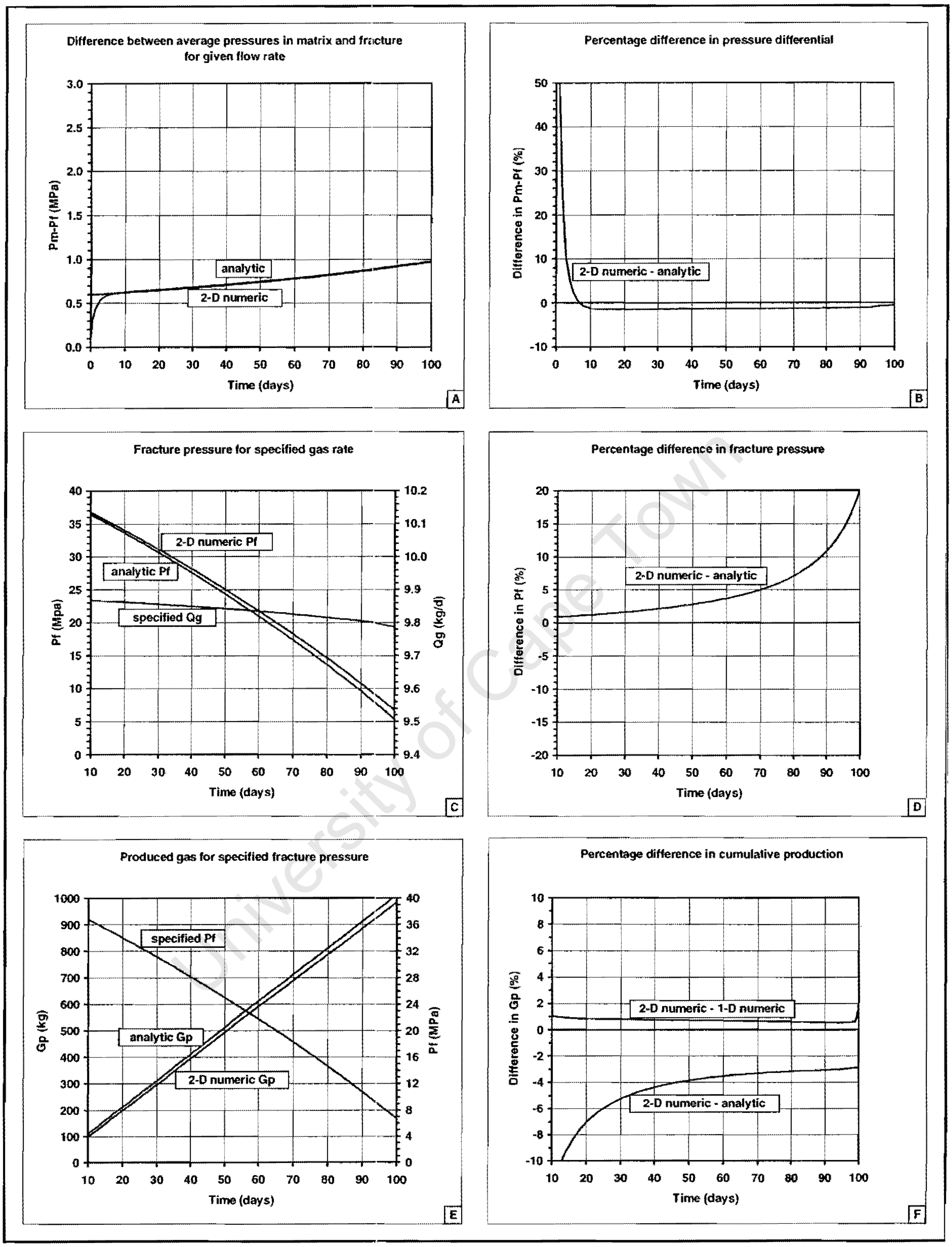

Figure 4.18: *Approximation of pseudo-steady state expulsion of gas from a 10m by 10m square (reference) matrix block. See text for explanation.*

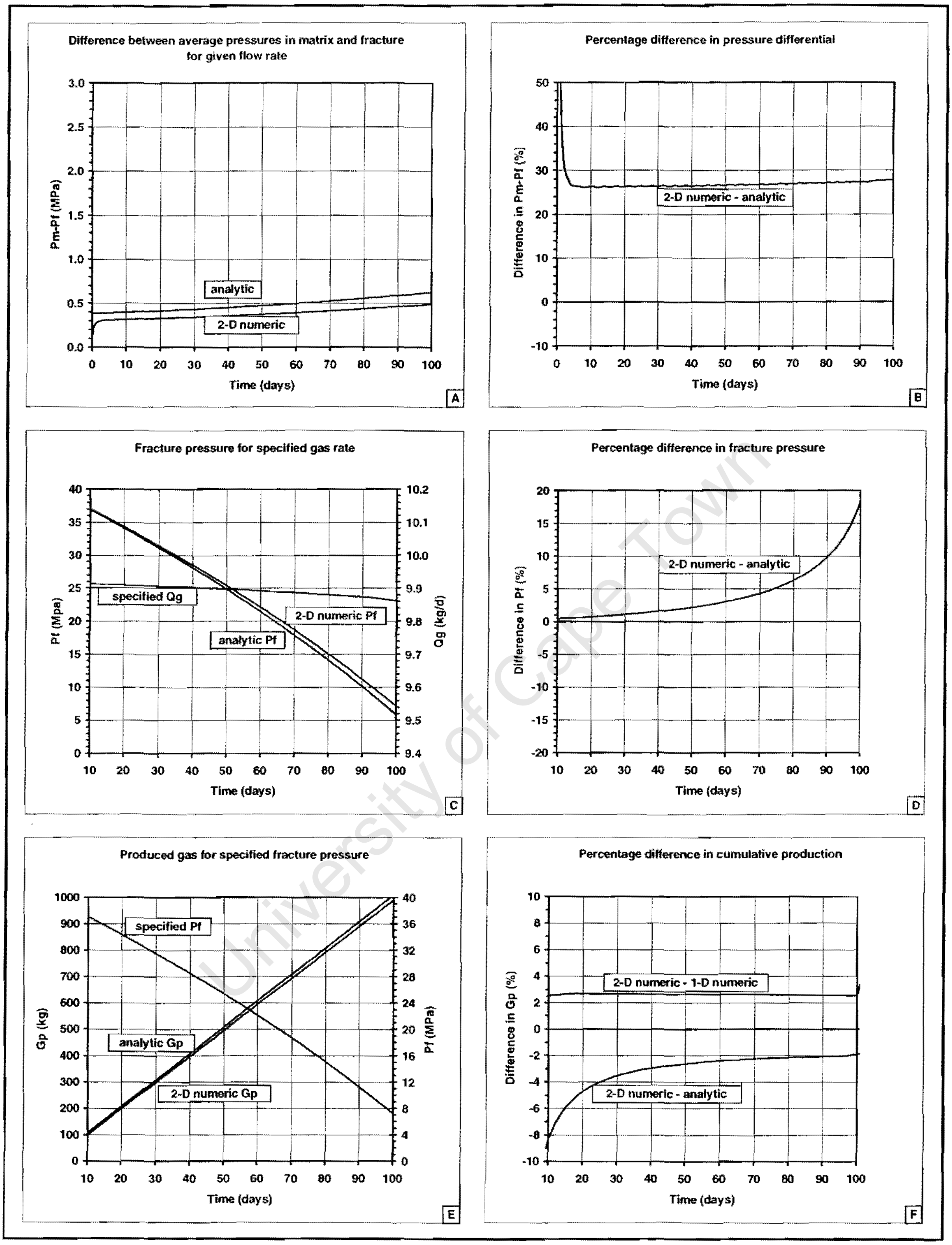

Figure 4.19: *Approximation of pseudo-steady state expulsion of gas from a 20m by 5m rectangular matrix block. See text for explanation.*

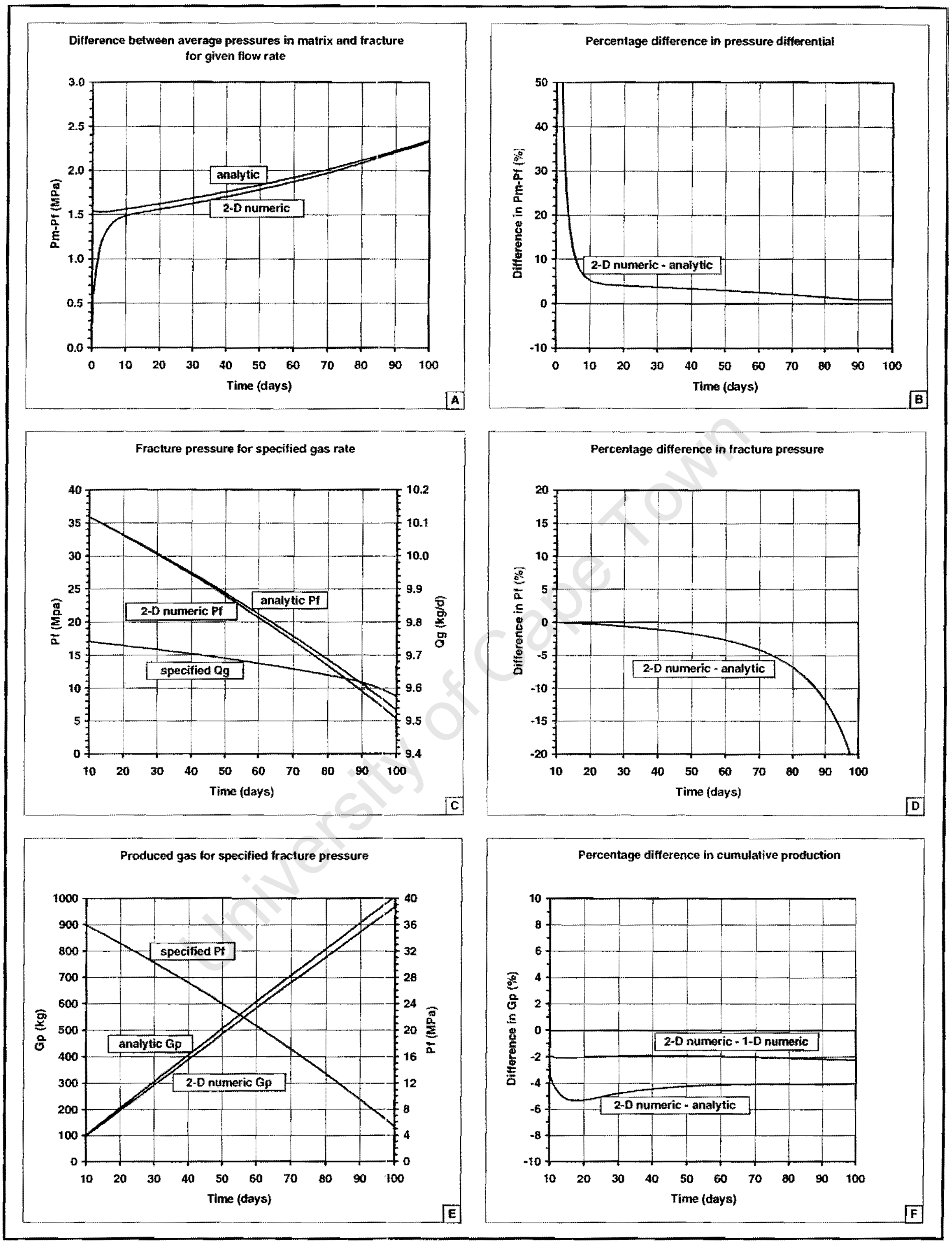

Figure 4.20: *Approximation of pseudo-steady state expulsion of gas from a 10m section of an infinitely long, 10m wide ribbon shaped matrix block. See text for explanation.*

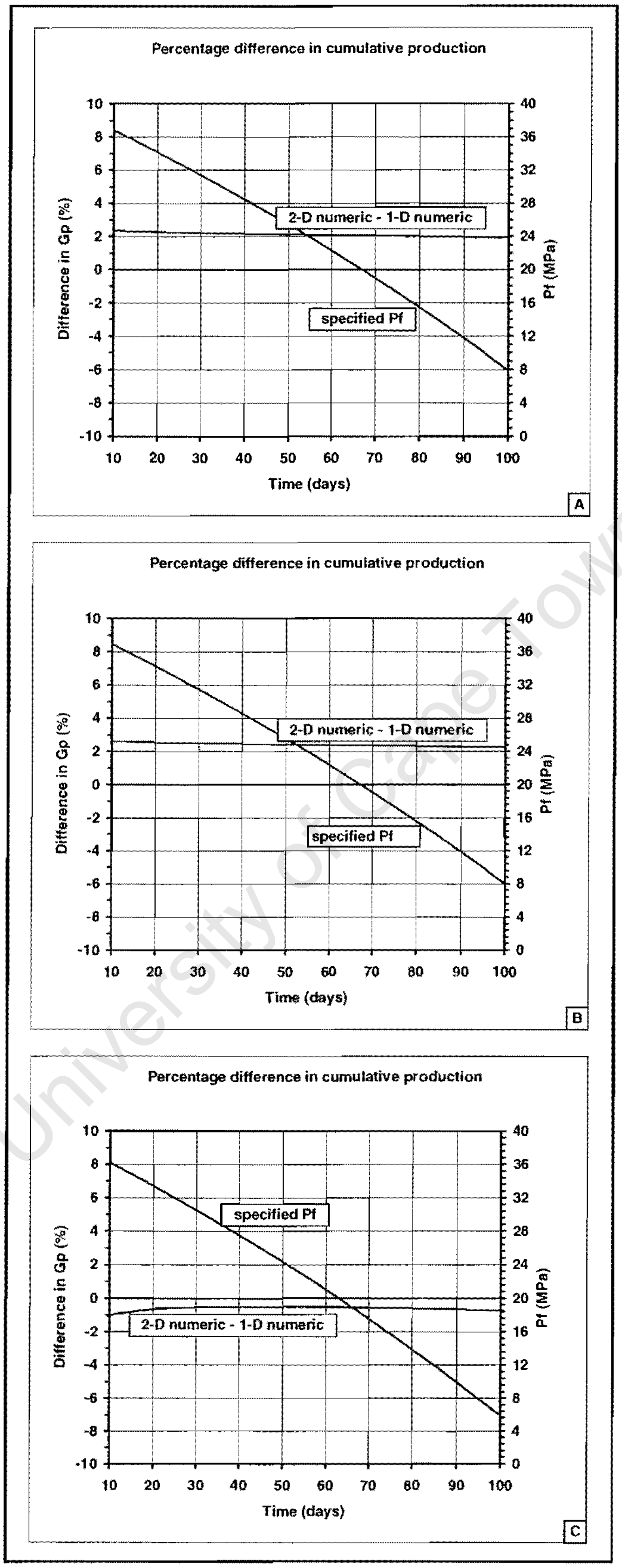

Figure 4.21: *Approximation of pseudo-steady state expulsion of gas from: A) a 45 degree right triangular matrix block, B) a 14 degree right triangular matrix block, and C) an anisotropic ($\varphi = 0.1$) square matrix block See text for explanation.*

Conclusions

- For isotropic square, rectangular and ribbon shaped matrix blocks, the analytical solution for expulsion of gas under pseudo-steady state conditions developed by Warren and Root (1963) compares favourably with finely meshed two-dimensional numerical simulation results while such conditions prevail.
- The most significant difference between the analytical and finely meshed two-dimensional numerical results for pseudo-steady state conditions occurs in the estimate of cumulative gas expelled from the matrix block. This is due to the analytical solution's inability to capture the transient period that inevitably precedes the establishment of pseudo-steady state conditions.
- A two-dimensional block of matrix material can successfully be reduced to a one-dimensional representation for the purpose of numerical modelling.
- The one-dimensional numerical models give results that compare very favourably with finely meshed two-dimensional numerical simulation of pseudo-steady state expulsion of gas from the full range of matrix block geometric shapes considered.
- The one-dimensional numerical models give results that more closely match the finely meshed two-dimensional simulation results than do the analytical solutions while pseudo-steady state conditions prevail for those geometric shapes for which the comparisons were made.
- Under pseudo-steady state flowing conditions, the different geometric forms expel gas in ways that differ significantly, suggesting that the geometric form is an important parameter to be captured during the modelling process.

4.2.4 Numerical results for transient flow conditions

In this section, expulsion of gas from a single matrix block under transient conditions is considered. The section is divided into five parts. In the first, a comparison is made between finely meshed two-dimensional numerical simulation results and the pseudo-steady state analytical solution widely used in full field dual porosity commercial simulators, for a number of geometric forms. The objective is to establish the degree of error introduced by the use of the pseudo-steady state analytical solution in problems that are dominated by transient effects. In addition, a comparison is made between the analytical solution for transient expulsion of slightly compressible fluid from a circular disk and finely meshed two-dimensional numerical simulation results for a simple model.

In the second part, comparisons are made between the two-dimensional numerical simulation results of transient flow from the six different geometric forms. The objective is to establish the extent to which it is necessary to consider geometry as a variable in the modelling process. The third part comprises a detailed comparison between the two-dimensional and one-dimensional numerical simulation results for each of the six geometric forms. The objective is to determine to what extent the one-dimensional representation concept can provide reliable results with the intention of implementing this approach in the full field dual porosity model.

The fourth part of this section consists of comparisons between sets of results from one-dimensional numerical simulation of the reference matrix block for different numbers of elements and types of elements. The objective of this part is to help identify criteria for selecting a one-dimensional model for input into the full field dual porosity model which optimises computational efficiency and accuracy. In the fifth and final part of the section the effects of variations in the two most important matrix block variables other than geometry, namely permeability and matrix block size, are explored. A square matrix block is considered, and the dimensions allowed to vary over 3 orders of magnitude (1m to 100m), while the permeability is varied across eight orders of magnitude ($10^{-14}m^2$ to $10^{-21}m^2$). The objective of this is to establish over what ranges of parameter values it is reasonable to expect that a dual porosity model will be required.

In general, unless otherwise stated, the models are according to the descriptions given in Section 4.2.3. In order to model transience, the fracture pressure is maintained at a constant value of 39MPa, and the matrix block, initially at a constant pressure of 40MPa, is permitted to flow gas into the fracture unconstrained. This results in a very large initial gas flow rate, in the order of several hundreds of kilograms per day, the precise value depending upon the geometry, decreasing rapidly to fractions of a kilogram per day over a 10 day period. This provides a very severe test for the numerical solution techniques.

Limitations of the pseudo-steady state analytical solution

Comparisons are made for the square reference matrix block, the rectangular matrix block, and the section of the infinitely long ribbon. Results are illustrated in Figure 4.22. For each geometry, two diagrams are presented, one showing the gas rate as a function of time for both the pseudo-steady state analytical solution and the two-dimensional numerical simulation, and the other showing the difference between these two curves, expressed as a percentage of two-dimensional numerical simulation gas rate.

From inspection of Figure 4.22 it is clear that the pseudo-steady state solution is unsatisfactory for modelling transience in that it results in unacceptably high errors in the cases studied here. In all three cases, during very early times, the numerical simulation forecasts instantaneous gas rates which are 15 to 40 times greater than those forecast by the analytical solution. As time progresses, the gas rates converge and cross, and the analytical solution begins to forecast higher rates than the numerical simulation (from about 0.3 to 0.8 days onwards, depending on the geometry). The order is once again reversed in the cases of the square and rectangular blocks. This oscillatory effect is analogous to an 'over correction' by the analytical method.

The analytical transient solution for slightly compressible fluids

Also shown in Figure 4.22 is the analytical solution for transient expulsion of slightly compressible fluid from a circular disk. The rate of gas expulsion is shown in diagram A.1, and the percentage difference between this analytical solution and the two-dimensional numerical solution is shown in diagram A.2. During very early times the analytical solution predicts a flow rate that is less than half of that of the

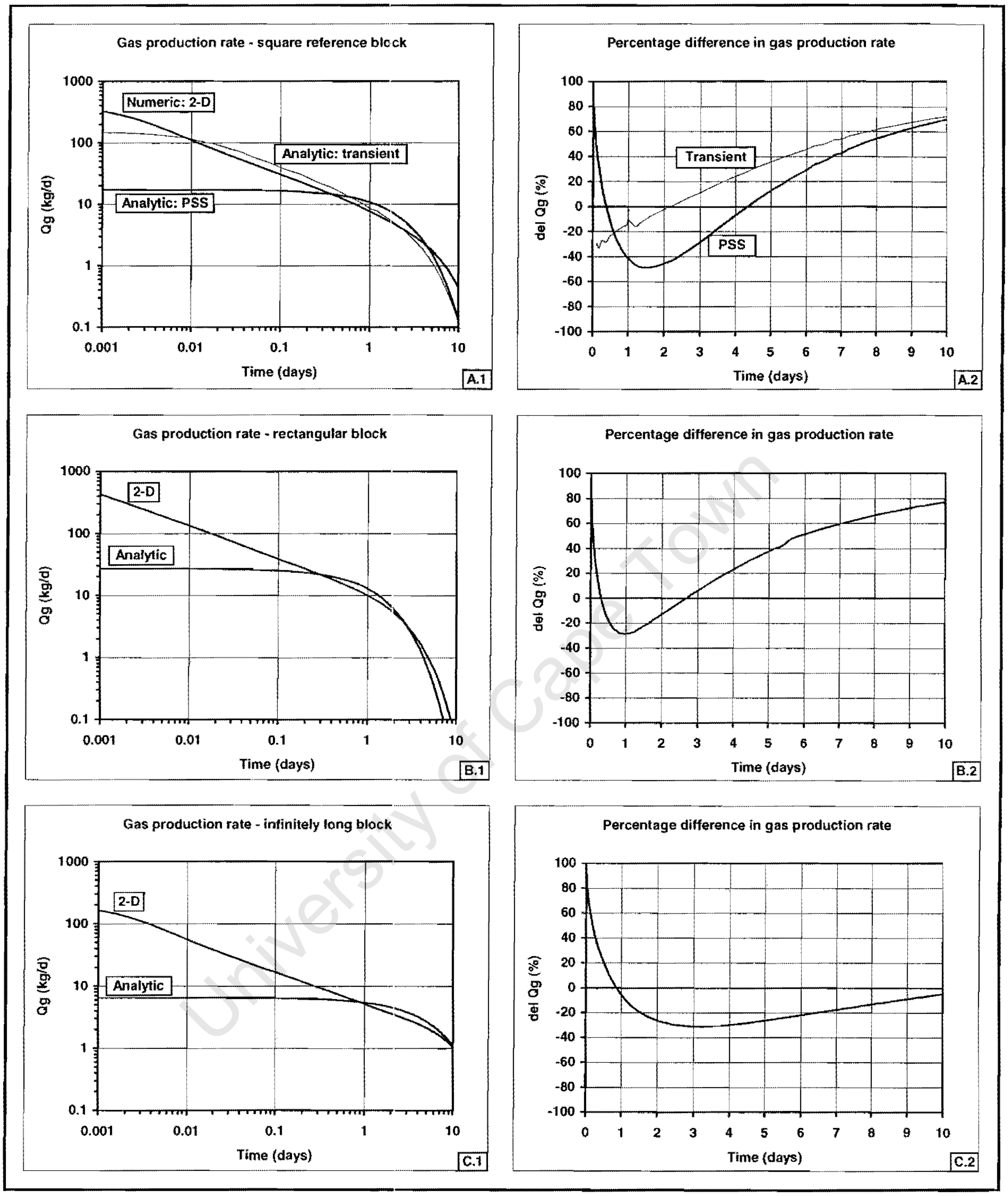

Figure 4.22: *Comparison between results of two-dimensional numerical simulation of the transient expulsion of gas and the pseudo-steady state analytical solution. Diagrams illustrate gas rate as a function of time for the 10m by 10m square reference block (diagram A.1), the 20m by 5m rectangle (diagram B.1) and the 10m section of an infinitely long, 10m wide ribbon (diagram C.1). For each geometry, the difference between the two curves, expressed as a percentage of the two-dimensional numerical simulation results, are shown in diagrams A.2, B.2 and C.2. In addition, the analytical solution for expulsion of slightly compressible fluid from a circlular disk under transient conditions is shown in diagram A.1 and A.2.*

numerical solution. The solutions cross over at about 0.01 days, and again at about two days. In the interval 0.01 to 2 days, the analytical solution is greater than the numerical solution by up to 30%. After 2 days, the transient analytical solution follows the pseudo-steady state solution very closely and they differ from the numerical solution by up to 60% at the end of the ten day period. The transient analytical solution provides a better approximation to the numerical solution than does the pseudo-steady state solution.

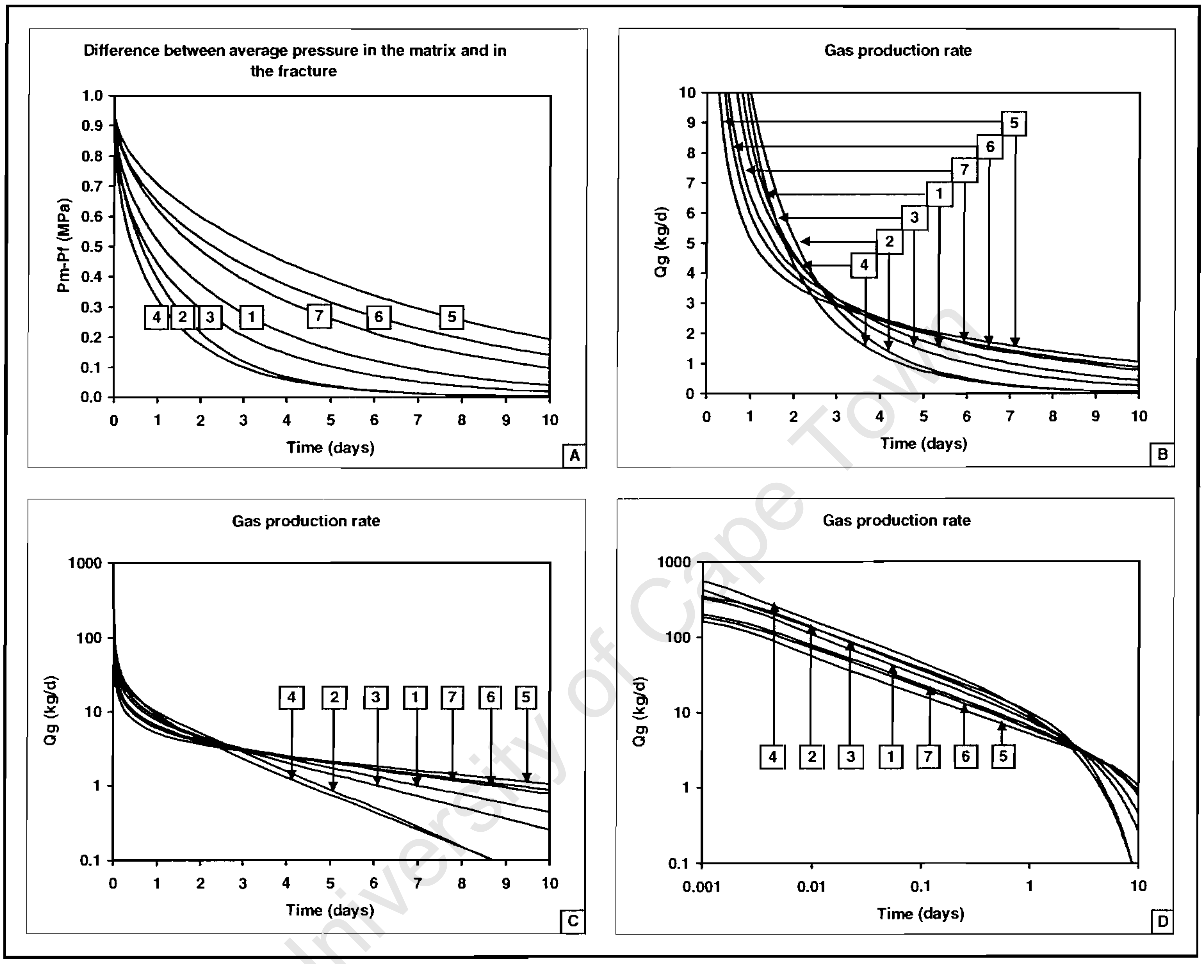

Figure 4.23: *Results of two-dimensional numerical simulation of the transient expulsion of gas from differently shaped matrix blocks. Curves are labelled as follows: 1 is the 10m by 10m reference block, 2 is a 20m by 5m rectangular block, 3 is a 45° right triangular block, 4 is a 14° right triangular block, 5 is a 10m section of infinitely long 10m wide block, 6 is a 10m by 10m anisotropic ($\varphi = 0.1$) block, and 7 is a 10m by 10m anisotropic ($\varphi = 0.5$) block.*

Effect and importance of geometric shape

In this section, the results of two-dimensional numerical simulation for all six of the geometric forms are compared for transient flowing conditions. The matrix models and method of simulating transience are as described in Section 4.2.3. Diagram A of Figure 4.23 shows how the difference between the average matrix block pressure and the fracture pressure changes with time for each of the geometric forms. The responses of the various geometric forms are vastly different, despite the fact that they all have the same properties and all hold the same initial volume of gas. The range of responses is entirely due to differences in geometric shape. The acute angled triangle experiences the most rapid pressure decline, while the section of the infinitely long ribbon experiences the slowest decline.

The rates of pressure decline are clearly related to the rates of gas expulsion. Diagrams B, C and D show the rates of gas expulsion on various combinations of logarithmic and normal axes. The acute angled triangle experiences the most rapid rate of depletion, followed by the rectangle, the 45° triangle, the square reference block, the anisotropic block, and the section of infinitely long ribbon, in that order. The order and variation in the shapes of the profiles are controlled by the relative surface areas exposed to the fractures and the expressions relating gas volume and distance from the nearest edge.

Accuracy of the one-dimensional simplification

The purpose of this section is to evaluate the accuracy of the one-dimensional simulation models of the geometric forms described in Section 4.2.1 under transient flowing conditions. This is achieved by comparisons with finely meshed two-dimensional numerical simulation results. In all these cases, the one-dimensional solutions are as described in Section 4.2.2, i.e. they consist of the 5 linear finite elements with the appropriate nodal spacing and properties for the particular geometry being represented. For each of the geometric cases in the first part, there is a figure containing six diagrams (see figure 4.24):

Diagram A: *'Difference between average pressure in the matrix and in the fracture'*: The difference between the average pressure in the matrix block and the pressure in the fracture is plotted over a period of 10 days for each of the two-dimensional and one-dimensional numerical solutions respectively. The initial pressure difference is 1MPa. As the fracture pressure is maintained at a constant value, the diagram illustrates how the average matrix pressure evolves.

Diagram B: *'Difference in pressure differential'*: The difference between the two curves (two-dimensional pressure minus one-dimensional pressure) of diagram A is shown as a function of time on an expanded scale.

Diagram C: *'Gas production rate'*: The mass rate at which gas is expelled from the block is shown as a function of time on log-log scales. The logarithmic scales permit the inspection of early transient effects.

Diagram D: *'Percentage difference in gas production rate'*: The difference between the gas rates determined from the two-dimensional and the one-dimensional numerical approximations shown in diagram C (two-dimensional minus one-dimensional), is expressed as a percentage of the two-dimensional rate and plotted as a function of time.

Diagram E: *'Cumulative produced gas'*: Cumulative gas is plotted as a function of time for both the two-dimensional and the one-dimensional numerical approximations.

Diagram F: *'Percentage difference in cumulative production'*: The difference between the two curves of diagram E (two-dimensional minus one-dimensional), is expressed as a percentage of the cumulative gas estimated by the two-dimensional numerical approximation and plotted as a function of time.

The square reference block

Modelling results of the expulsion from the square reference block are illustrated in Figure 4.24. Diagram A shows that there is extremely good agreement between the two-dimensional and one-dimensional approximations with respect to the matrix/fracture pressure differential. This is further illustrated in diagram B, where the difference between the two forecasts never exceeds 2%, and remains less than 1% for most of the time. The forecast flow rates from the block estimated by the two methods are also similar (diagram C). The flow rates do not differ by more than 5% over most of the time period (diagram D). Larger discrepancies occur at early times (less than 0.25 days) and at late times, after 8.5 days. At very early times, flow is predominantly from the outer layer of elements and influenced by discretization effects, particularly the size of the outermost cell in the case of the one-dimensional model, or outermost row of cells in the case of the two-dimensional mesh. At late times the flow rates have reached very small values (less than 1% of the initial rate) causing undue amplification of the difference when expressed as a percentage. Cumulative production is similar for the two numerical solution approaches (diagram E). Initially, percentage differences are as high as 4%, but remain close to zero for the bulk of the time.

Rectangular matrix block. Agreement between the results from the two numerical approximations is good as illustrated in Figure 4.25. The pressure differential between the matrix and the fracture never differs by more than 2%. The rate of gas expulsion never differs by more than 10% and the cumulative gas produced never by more than 2%. The difference between the forecast gas rates is erratic, as shown in diagram D, and is sensitive to the numerical approximation technique. The absolute value of the gas rate spans several orders of magnitude over the 10-day period, beginning at about 400kg/d, and reaching a level of less than 0.1kg/d after 10 days. When the gas rates reach very low levels, differences in the rates expressed as a percentage of rate fluctuate wildly, hence these have been omitted from the later times of diagram D. In diagram C, the forecasts made with the two-dimensional and one-dimensional numerical approximations are discernible in early times, but the lines become indistinguishable after 0.1 days. Comparison between diagrams A of Figures 4.24 and 4.25 shows that the pressure differential between the matrix block and the fracture decreases more rapidly in the case of the rectangular block. This is due to a greater surface area, resulting in more rapid expulsion of gas, evident through a comparison of the corresponding diagrams C and D.

45° right triangle. Results are illustrated in Figure 4.26. Good agreement exists between the matrix-fracture pressure differentials forecast by the two approaches. Gas rate differs by up to 10% and the differences in cumulative gas produced stabilises at less than 2% after an initial high value. This initial value is high, partly due to the small volume of gas produced, which magnifies the difference when expressed as a percentage.

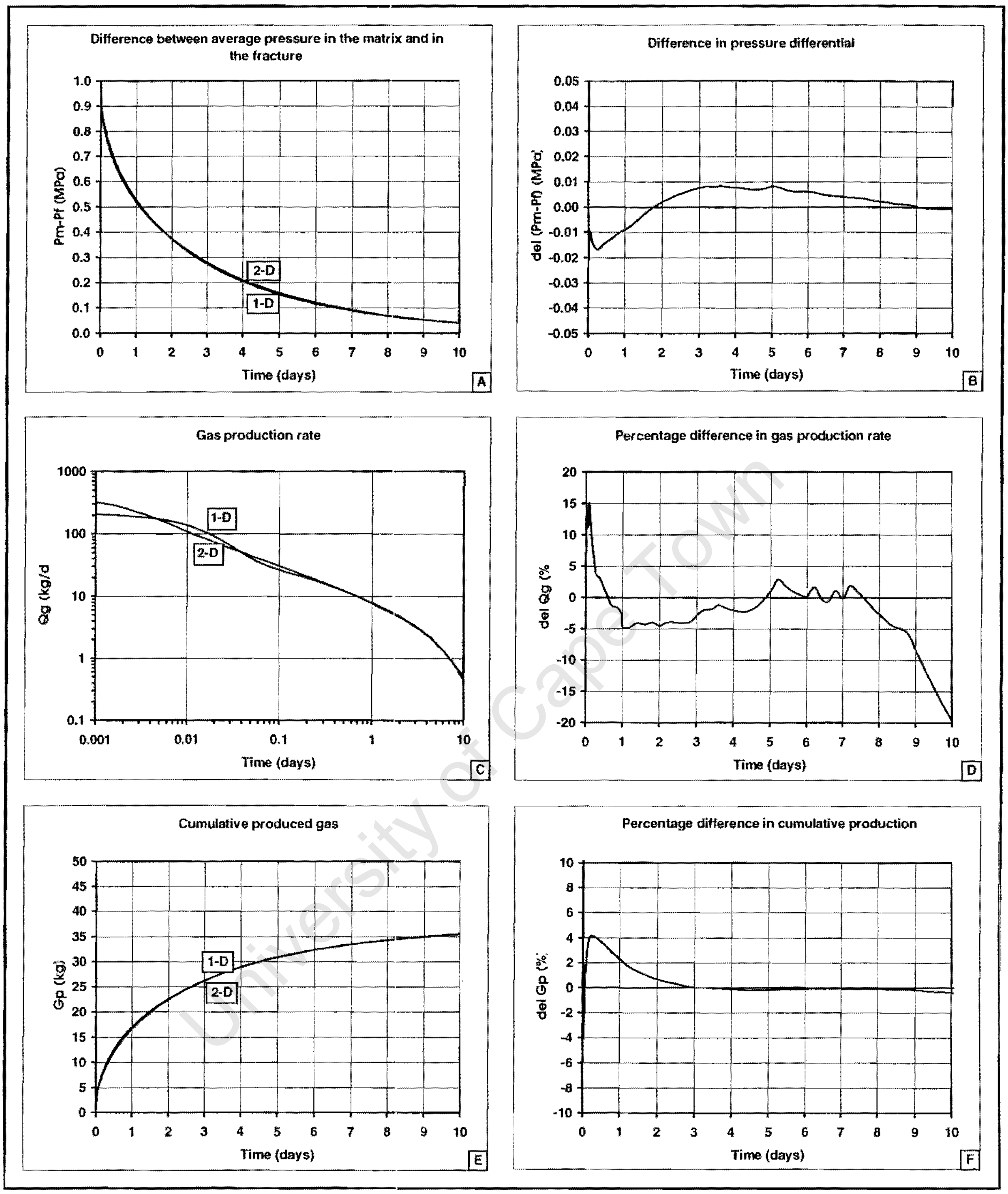

Figure 4.24: *Results for the modelling of expulsion of gas from a 10 by 10m square (reference) matrix block under transient conditions. The comparison is between the numerical solutions obtained from a finely meshed two-dimensional model, and from a one-dimensional representation. In diagrams A and B, pressure profiles are compared, in diagrams C and D, gas flow rates are compared and in diagrams E and F the volumes of cumulative produced gas are compared. Diagrams B, D and F show differences between the curves illustrated in A,C and E. See text for further explanation.*

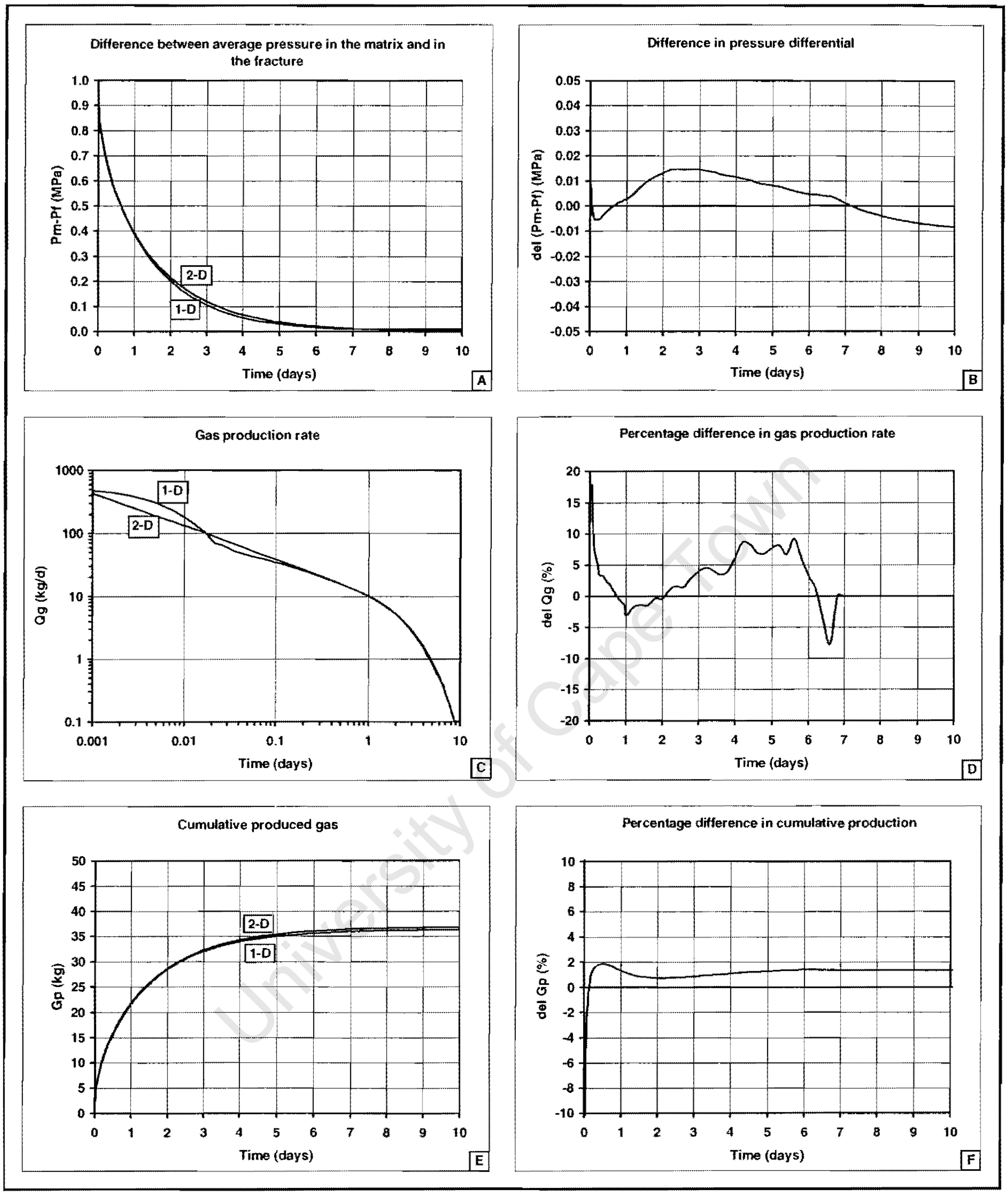

Figure 4.25: *Results for the modelling of expulsion of gas from a 20m by 5m rectangular matrix block under transient conditions. The comparison is between the numerical solutions obtained from a finely meshed two-dimensional model, and from a one-dimensional representation. In diagrams A and B, pressure profiles are compared, in diagrams C and D, gas flow rates are compared and in diagrams E and F the volumes of cumulative produced gas are compared. Diagrams B, D and F show percentage differences. See text for further explanation.*

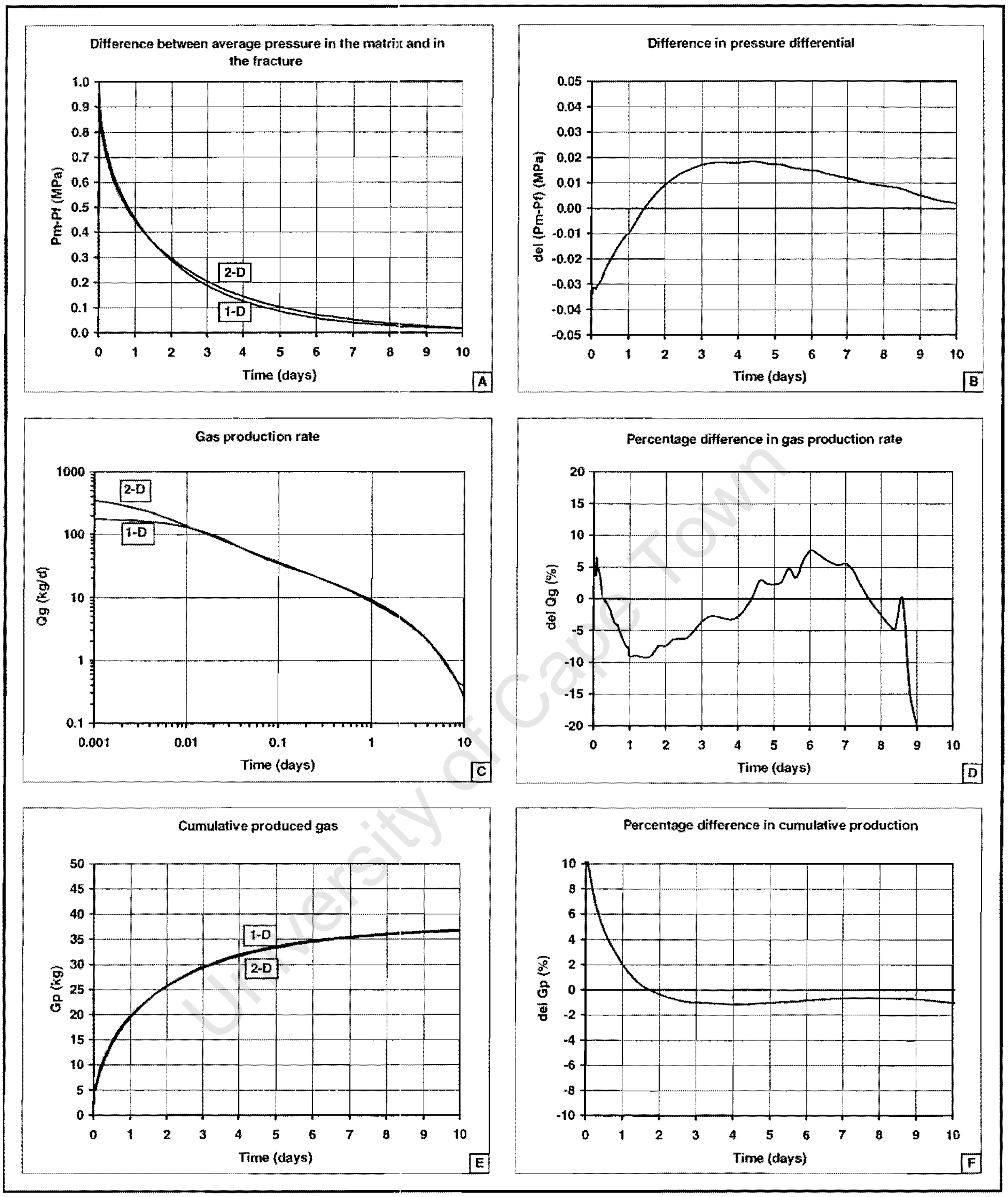

Figure 4.26: *Results for the modelling of expulsion of gas from a 45° right triangular shaped matrix block under transient conditions. The comparison is between the numerical solutions obtained from a finely meshed two-dimensional model, and from a one-dimensional representation. In diagrams A and B, pressure profiles are compared, in diagrams C and D, gas flow rates are compared and in diagrams E and F the volumes of cumulative produced gas are compared. Diagrams B, D and F show percentage differences. See text for further explanation.*

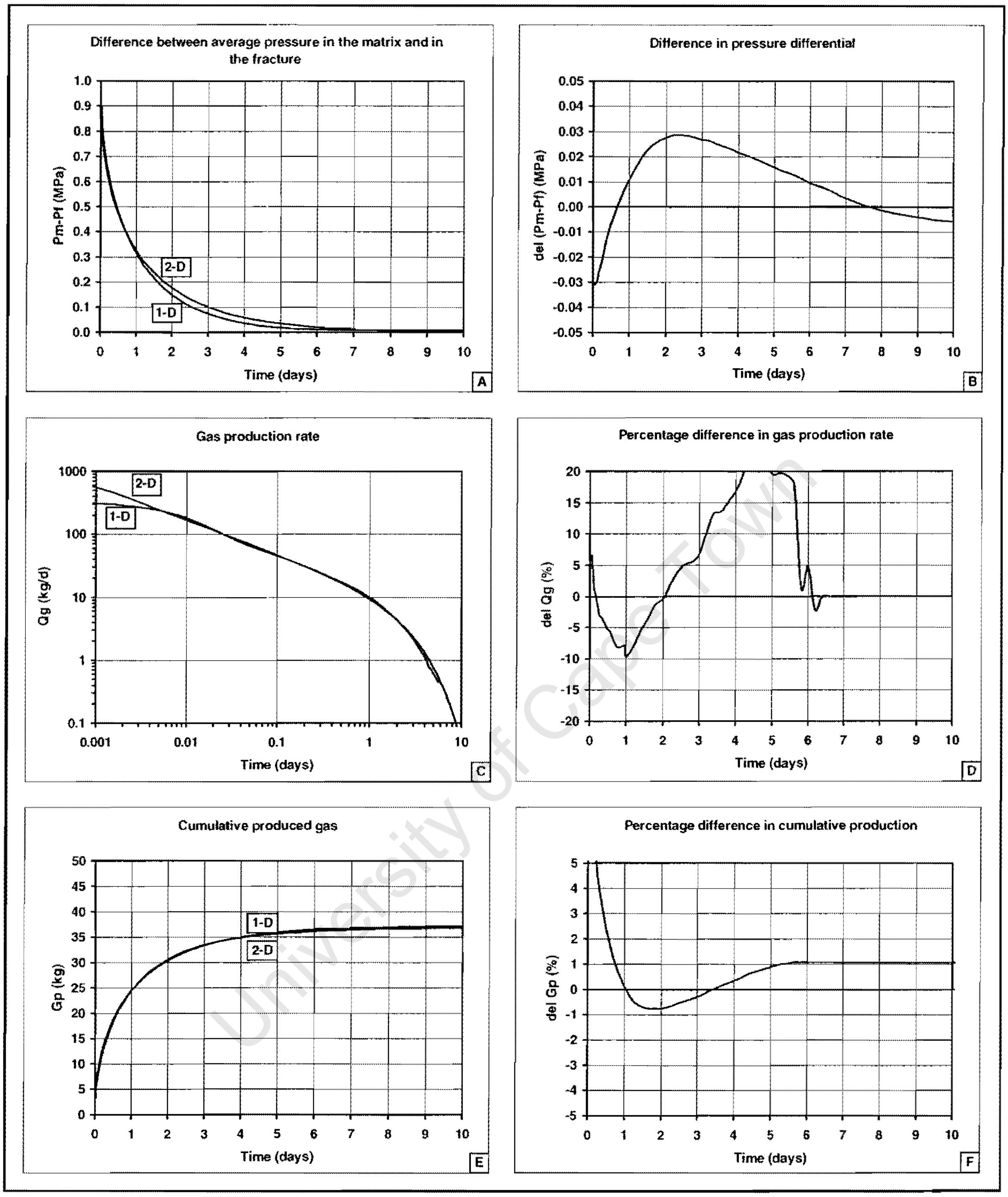

Figure 4.27: *Results for the modelling of expulsion of gas from a 14° right triangular shaped matrix block under transient conditions. The comparison is between the numerical solutions obtained from a finely meshed two-dimensional model, and from a one-dimensional representation. In diagrams A and B, pressure profiles are compared, in diagrams C and D, gas flow rates are compared and in diagrams E and F the volumes of cumulative produced gas are compared. Diagrams B, D and F show percentage differences. See text for further explanation.*

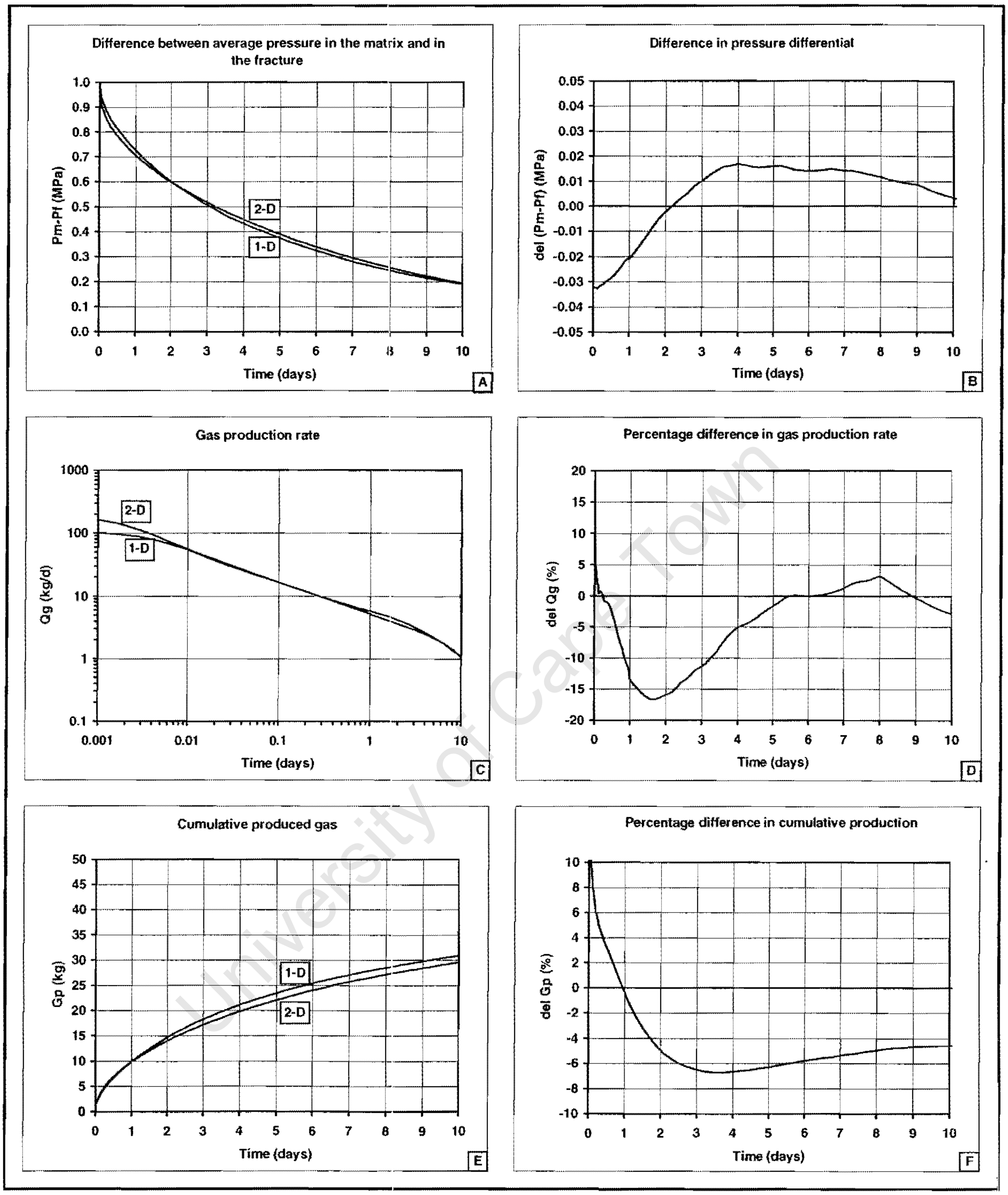
Difference between average pressure in the matrix and in the fracture

Difference in pressure differential

Gas production rate

Percentage difference in gas production rate

Cumulative produced gas

Percentage difference in cumulative production

Figure 4.28: *Results for the modelling of expulsion of gas from a 10m section of an infinitely long, 10m wide ribbon shaped matrix block under transient conditions. The comparison is between the numerical solutions obtained from a finely meshed two-dimensional model, and from a one-dimensional representation. In diagrams A and B, pressure profiles are compared, in diagrams C and D, gas flow rates are compared and in diagrams E and F the volumes of cumulative produced gas are compared. Diagrams B, D and F show percentage differences. See text for further explanation.*

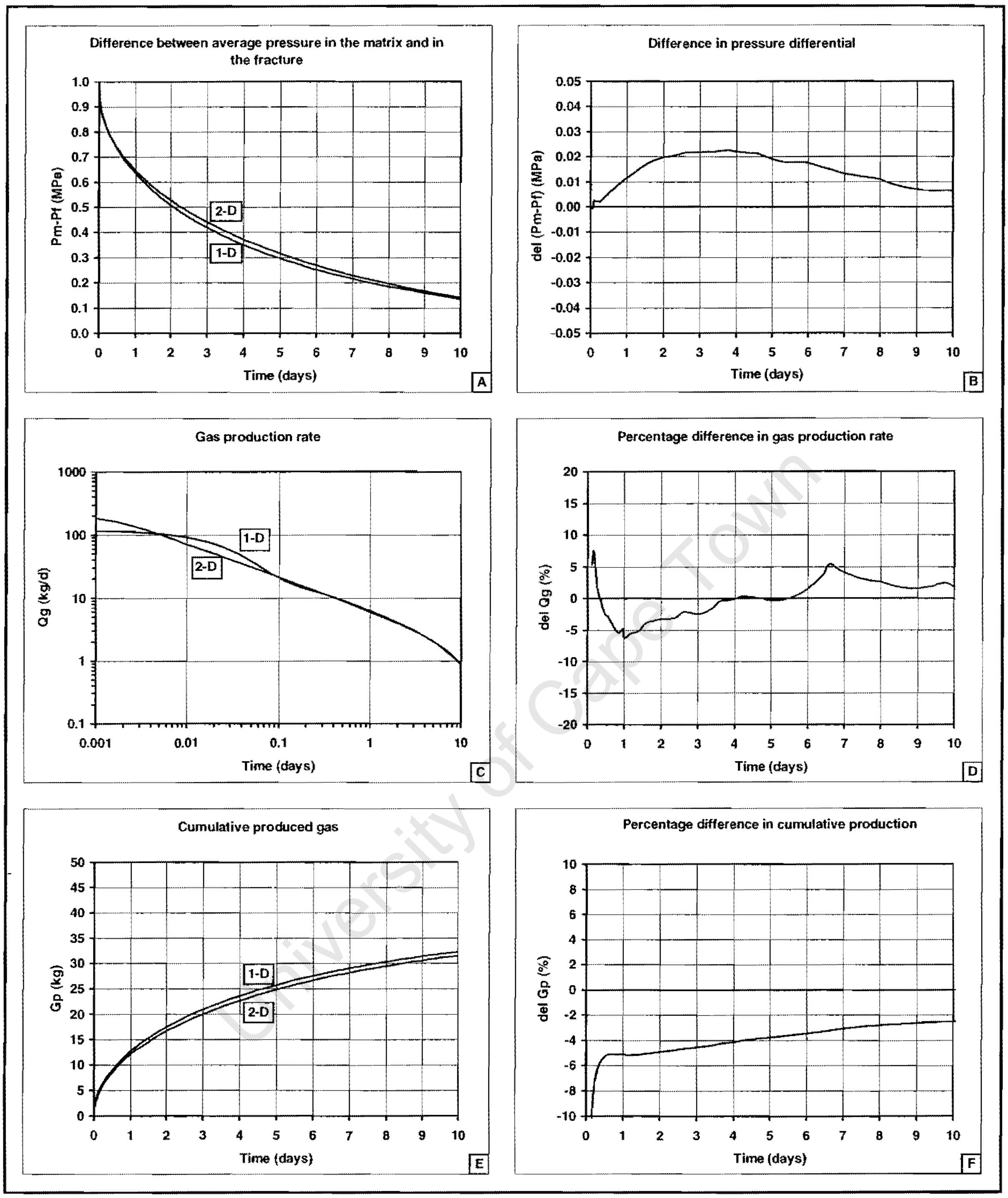

Figure 4.29: *Results for the modelling of expulsion of gas from a 10m by 10m anisotropic square matrix block under transient conditions. The comparison is between the numerical solutions obtained from a finely meshed two-dimensional model, and from a one-dimensional representation. In diagrams A and B, pressure profiles are compared, in diagrams C and D, gas flow rates are compared and in diagrams E and F the volumes of cumulative produced gas are compared. Diagrams B, D and F show percentage differences. See text for further explanation.*

14° right triangle. The modelling results for this case, illustrated in Figure 4.27, show that this geometry is characterised by extremely rapid expulsion of gas, accompanied by a very rapid pressure decline. Fairly large discrepancies in gas rate between the two numerical solutions are evident at very early times. These are manifest in the cumulative gas rate where initial differences are greater than 5% at early times. Differences in cumulative gas stabilise to less than 1% after less than 1 day.

Section of infinitely long ribbon. This model, the results of which are illustrated in Figure 4.28, experiences the slowest decline of pressure, accompanied by the lowest rate of expulsion of gas. This is because only two sides of the block are available for gas expulsion. The one-dimensional model does, however, capture the effects reasonably well, although not as well as in the case of the reference block. Differences in gas rates exceed 15% occasionally, and cumulative gas differs by more than 4% at the end of the 10 day period.

Anisotropic square. Considering that anisotropy is essentially a two-dimensional problem, the one-dimensional representation captures the effects fairly well, as shown in Figure 4.29. Differences in the matrix-fracture pressure differential remain below 0.025MPa, gas rate differences generally below 10% except at very early times, and differences in cumulative gas remain below 6%, except at very early times.

Optimising efficiency of the one-dimensional model

In this section, the effects of mesh refinement and order of polynomial approximation are investigated with the aim of determining minimum requirements to achieve the desired accuracy for implementation in the full field, dual porosity simulator. Figure 4.30 shows comparisons between forecasts made using different numbers of elements to model the one-dimensional representation of the square reference matrix block. Starting with five linear elements, the number of elements is progressively reduced by one. Refer to Table 4.9 for the element properties. Diagram A shows the difference between the average matrix block pressure and the fracture pressure as a function of time. In diagram B the percentage difference between two-dimensional numerical simulation results and each of the curves in diagram A in turn are plotted. From this diagram it appears that the four-element model provides a solution that is comparable with, and for most of the time, slightly better than that obtained using the five-element model. There is increasing degradation in the accuracy of the solution as the number of elements is further reduced.

Diagram C show the gas expulsion rates. The five-element solution provides the smoothest profile but is closely matched by the four-element and even the three-element solutions. This is verified in diagram D in which the percentage difference between the results of the two-dimensional numerical simulation and each of the curves of diagram C in turn, are plotted. Once again the four-element model provides a solution which is comparable to, and over a large portion of the time scale, better, than the five-element model. Clearly the 1 and 2-element models are unsatisfactory. The 1-element model more closely approximates the analytical pseudo-steady state solution. Diagrams E and F show the cumulative gas produced and the percentage difference between the two-dimensional simulation

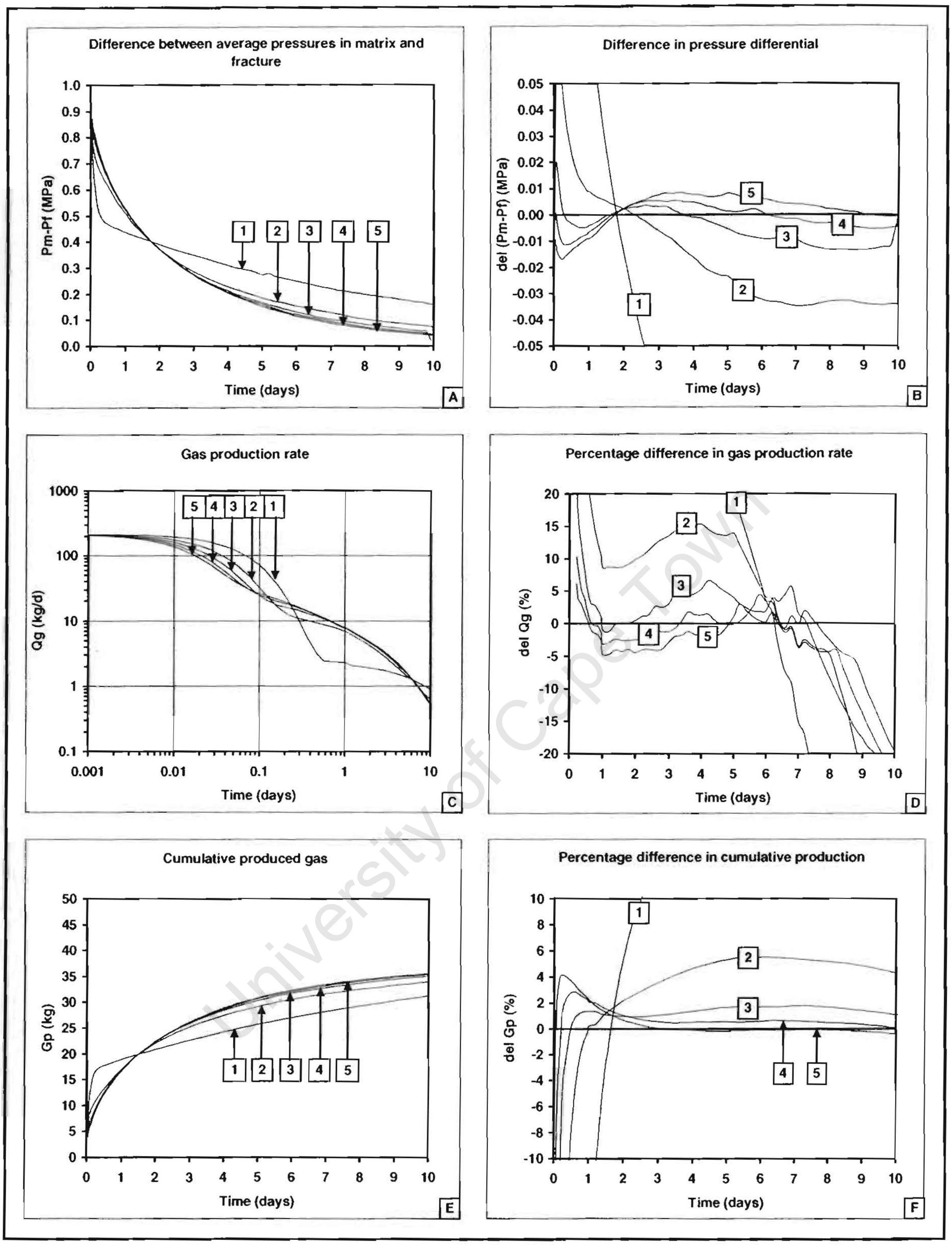

Figure 4.30: *Modelling results for the expulsion of gas from a square reference matrix block under transient conditions. The numbers represent the number of linear finite elements used to model the one-dimensional representation of the block. In diagrams A and B, pressure profiles are compared, in diagrams C and D, gas flow rates are compared and in diagrams E and F the volumes of cumulative produced gas are compared. Diagrams B, D and F show percentage differences. See text for further explanation.*

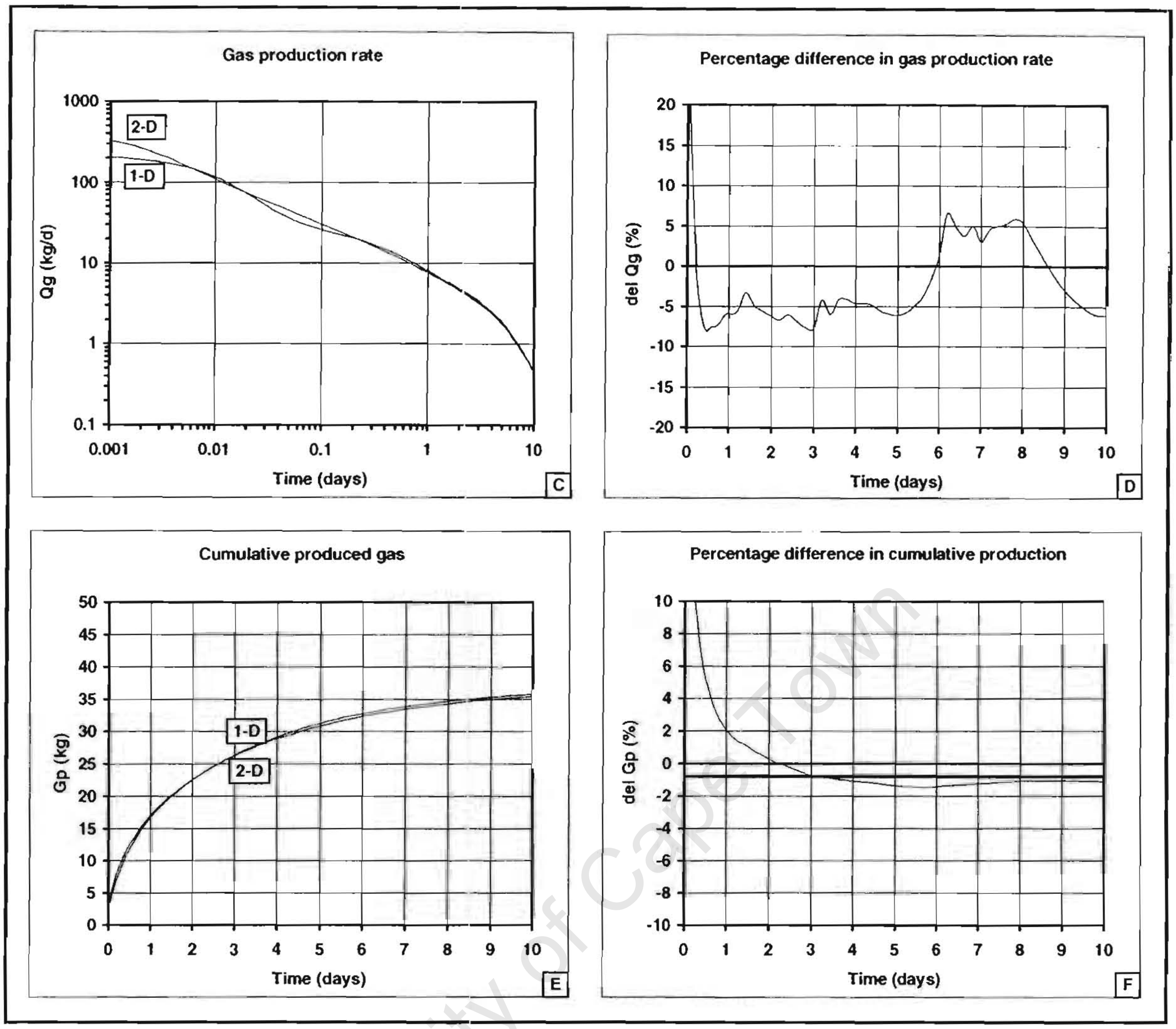

Figure 4.31: *Modelling results for the expulsion of gas from a square reference matrix block under transient conditions. The one-dimensional model consists of a single, five node finite element. In diagrams C and D, gas flow rates are compared and in diagrams E and F the volumes of cumulative produced gas are compared. Diagrams D and F show percentage differences. See text for further explanation.*

and each of the respective one-dimensional models. The five-element model provides the best estimate of cumulative gas, followed closely by the four-element model.

A single five-node finite element was also considered for modelling the one-dimensional representation of the reference matrix block, the numerical results of which are shown in Figure 4.31. The single element gives results that are in close agreement with the two-dimensional numerical model. Gas rate does not differ from the two-dimensional model forecasts by more than 10%, except during early times. The single element gives very good results for late times, better than those obtained using the five linear elements. The early time discrepancy is fairly large, however, and manifests itself in a large error in cumulative gas produced during early times.

Significance of permeability and matrix block size

In all of the preceding sections, the only physical variable considered has been the shape or geometry of the matrix block. None of the other matrix or fluid physical properties, namely porosity, permeability, compressibility, viscosity or block size have been considered. Of these, the greatest variability in nature occurs in permeability, matrix block size and compressibility. Compressibility varies tremendously over the range of reservoir fluids water, oil and gas. For gas the range is, however, not great, and compressibility is therefore not considered further as a variable. In this section, the effects of varying permeability and matrix block size on the performance of the individual matrix block are therefore considered. Three figures are presented (4.32, 4.33 and 4.34) for matrix block sizes of 1m*1m, 10m*10m and 100m*100m respectively. For each matrix block, the value of permeability is varied across seven orders of magnitude with the corresponding curve identification in the figures as set out in Table 4.10.

Table 4.10: *Range of values used to assess importance of matrix permeability.*

Curve (case) number:	1	2	3	4	**5**	6	7	8
Permeability (m^2)	10^{-14}	10^{-15}	10^{-16}	10^{-17}	**10^{-18}**	10^{-19}	10^{-20}	10^{-21}
Permeability (mD*1.01325)	10^{1}	10^{0}	10^{-1}	10^{-2}	**10^{-3}**	10^{-4}	10^{-5}	10^{-6}

In preceding sections, the value of permeability used was that of curve number 5 (the base case). For comparison, note that the reference block of the previous sections corresponds to curve 5 of Figure 4.33. In each of the three figures, four diagrams are presented:

Diagram A: The rate of gas expulsion as a function of time is plotted with log-log scales. The scale limits are the same in all three figures. Inspection of diagrams A for the three matrix block sizes suggests that the initial flow rate from a matrix block is determined primarily by the permeability of the block and to a lesser extent by the size of the block. As the permeability is decreased (increasing curve number), so the initial rate decreases and at the same time, the decline in rate is retarded. Increasing or decreasing the permeability by an order of magnitude causes the initial rate to change accordingly by an order of magnitude. Changing the size of the block, while keeping the permeability constant, does not affect the initial rate to the same extent.

Diagram B: Cumulative gas produced as a function of time is plotted on a log-linear scale system. Note that different scales are used on the ordinates of the three figures as vastly different volumes of gas are recovered. In all three cases, asymptotic values are reached that are proportional to the block sizes (approximately 0.37kg for the 1m*1m block, 37kg for the 10m*10m block, and 3700kg for the 100m*100m block).

Both the size of the block and the permeability dictate the time required for the block to become fully depleted. Although the absolute values differ, all the curves have similar shapes. For the 1m by 1m block with a permeability value of $10^{-19}m^2$, (curve 6), cumulative gas produced reaches its maximum value and the block is fully depleted after slightly longer than 1 day. The 10m by 10m block becomes depleted over the same time scale when the permeability is in the order of $10^{-17}m^2$, (curve 4), and for the 100m by 100m block this occurs for a permeability value of $10^{-15}m^2$ (curve 2). For a given permeability then, the time required to deplete the block is directly proportional to the size of the block. (i.e. increasing the block volume by a factor of 100 means that the permeability must also be increased by a factor of 100 for depletion to occur over the same time in both blocks. This supports the observation that the rate of gas expulsion from the block is influenced more by the permeability than the size of the block.

Diagram C: The average matrix pressure as a function of time is plotted on a log-linear set of axes. Once again, all curves have similar and semi-parallel shapes.

Diagram D: The average matrix pressure as a function of cumulative produced gas is plotted using linear scales. Different scales are used for the abscissa in each of the figures. The fact that all curves for a given block size lie on a common line is a material balance demonstration that the solutions are being performed correctly. This line appears straight over the short interval of pressure change considered here (i.e. from 40 to 39 MPa), but is in fact not, due to nonlinear relationship between pressure and produced volume.

The effect of scale. The curves illustrated in Figures 4.32 to 4.34 have similar shapes. For example, the gas rate profile for the 1m*1m block with a permeability value of $10^{-20}m^2$ (curve 7 in diagram A of Figure 4.32) is similar to the gas rate profile for the 100m*100m block with a permeability value of $10^{-16}m^2$ (curve 3 in diagram A of Figure 4.34) if the latter is divided by 10^4. Because the pressure range over which these numerical results have been obtained is very small (39 to 40MPa), these results are not greatly affected by nonlinearity of the gas compressibility. It would therefore be possible to replicate the results presented in this section with a single, generalised dimensionless solution and to use scaling laws for understanding any particular example (Zimmerman, Bodvarsson and Kwicklis, 1990 and Zimmerman and Bovarsson, 1995). However, the results are presented in this form to support the arguments pertaining to the practical modelling methods for dual porosity reservoirs discussed in subsequent sections.

Machine accuracy. The very large range in the value of permeability investigated in this section imposes high demands on the numerical solution techniques. In particular, accurate results were difficult to obtain for small block sizes and high values of permeability and initial time steps as small as 10^{-3}s were needed.

The 1m by 1m block. Referring to Figure 4.32, it is clear that gas is expelled very rapidly from a 1m by 1m block. At the upper range of matrix permeability values considered here, withdrawal is so rapid that for practical purposes, depletion is instantaneous. This caused numerical difficulties, and simulations could not be completed for the upper two permeability values (cases 1 and 2) due to the excessively high initial flow rates. The highest permeability value for which a successful simulation could be completed is $10^{-16}m^2$ (0.1mD) and despite the fact that this is a relatively low value, depletion of the block has already occurred after about 0.01 days (about 14 minutes). It is only at very low values of permeability that the time taken for the pressure of such a small matrix block to equalise with that of the fracture attains a value which is significant in terms of practical reservoir engineering.

For case 5, where the matrix permeability is $10^{-18}m^2$ (0.001mD), the time taken for equalisation is about 0.5 days. For the lowest permeability value considered here, i.e.$10^{-21}m^2$, (0.000001mD), depletion is extremely slow and has occurred only after about 100 days. An industry 'rule of thumb' is that for non-fractured reservoirs, a permeability value of $10^{-16}m^2$ (0.1mD) is generally regarded as the lower limit for production from a gas reservoir. What is apparent here is that reasonable production is possible from matrix material of several orders of magnitude lower permeability if the rock is fractured into sufficiently small block sizes.

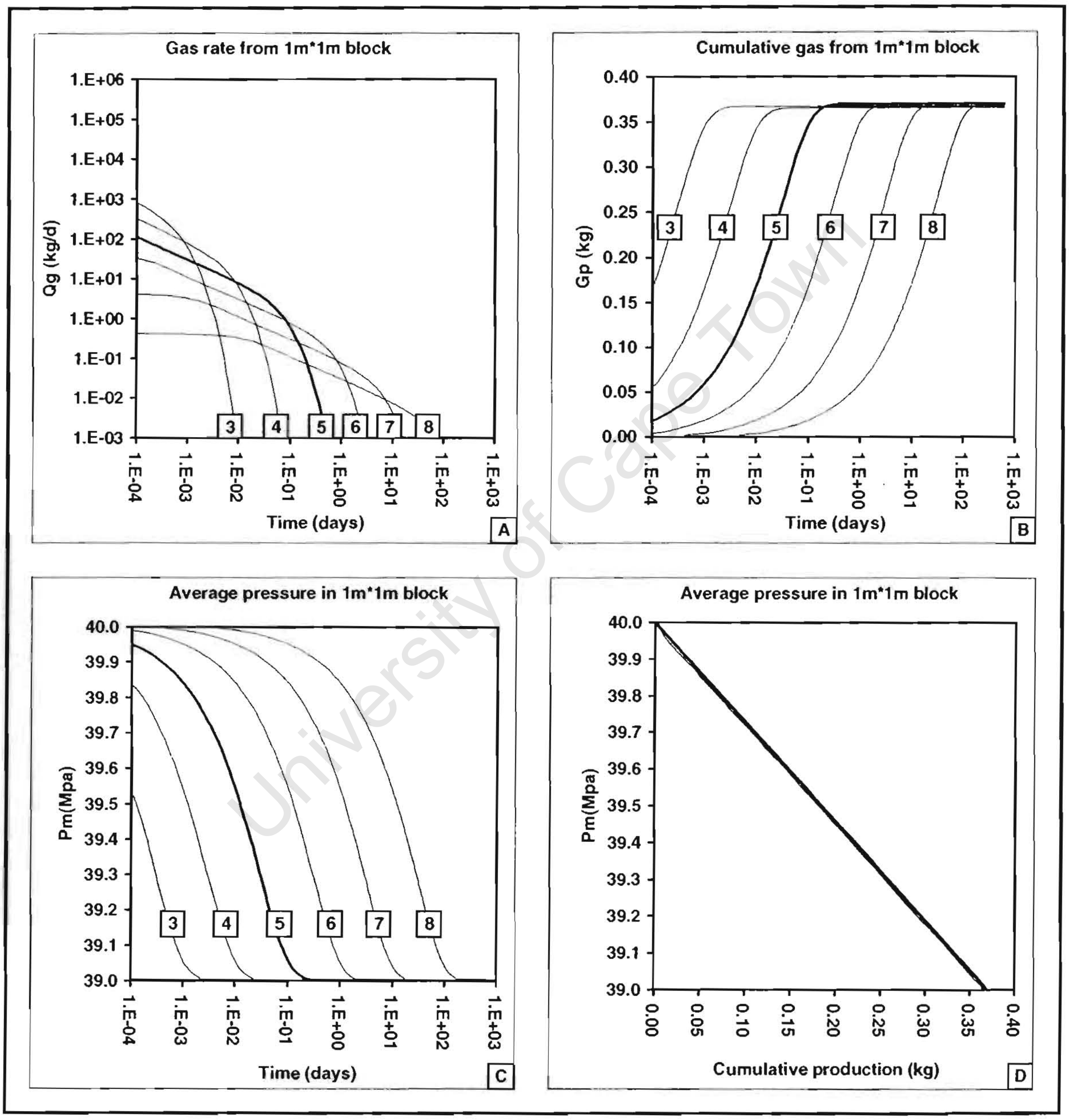

Figure 4.32: *Results of two-dimensional numerical simulation of the expulsion of gas from a 1m by 1m square matrix block for a range of matrix permeability values (see Table 4.10).*

The response of the square block varies so tremendously across the range of permeability values considered here that different approaches are required to cover the range of permeability values for the full field modelling of a fractured reservoir containing matrix blocks of this dimension. Dual porosity behaviour is likely to cease being significant when the matrix permeability exceeds a value of around $10^{-17}m^2$ or $10^{-18}m^2$ (0.01mD or 0.001mD), due to the very rapid rate of depletion of the block. Thus for this range of permeability, it is likely that the reservoir may be adequately modelled using a single porosity model, in which the single continuum is assigned a value for permeability dominated by the fracture network and a value for porosity dominated by the matrix material. Within the range $10^{-18}m^2$ to $10^{-20}m^2$ (inclusive), dual porosity effects are likely to be important and the reservoir should be modelled as such.

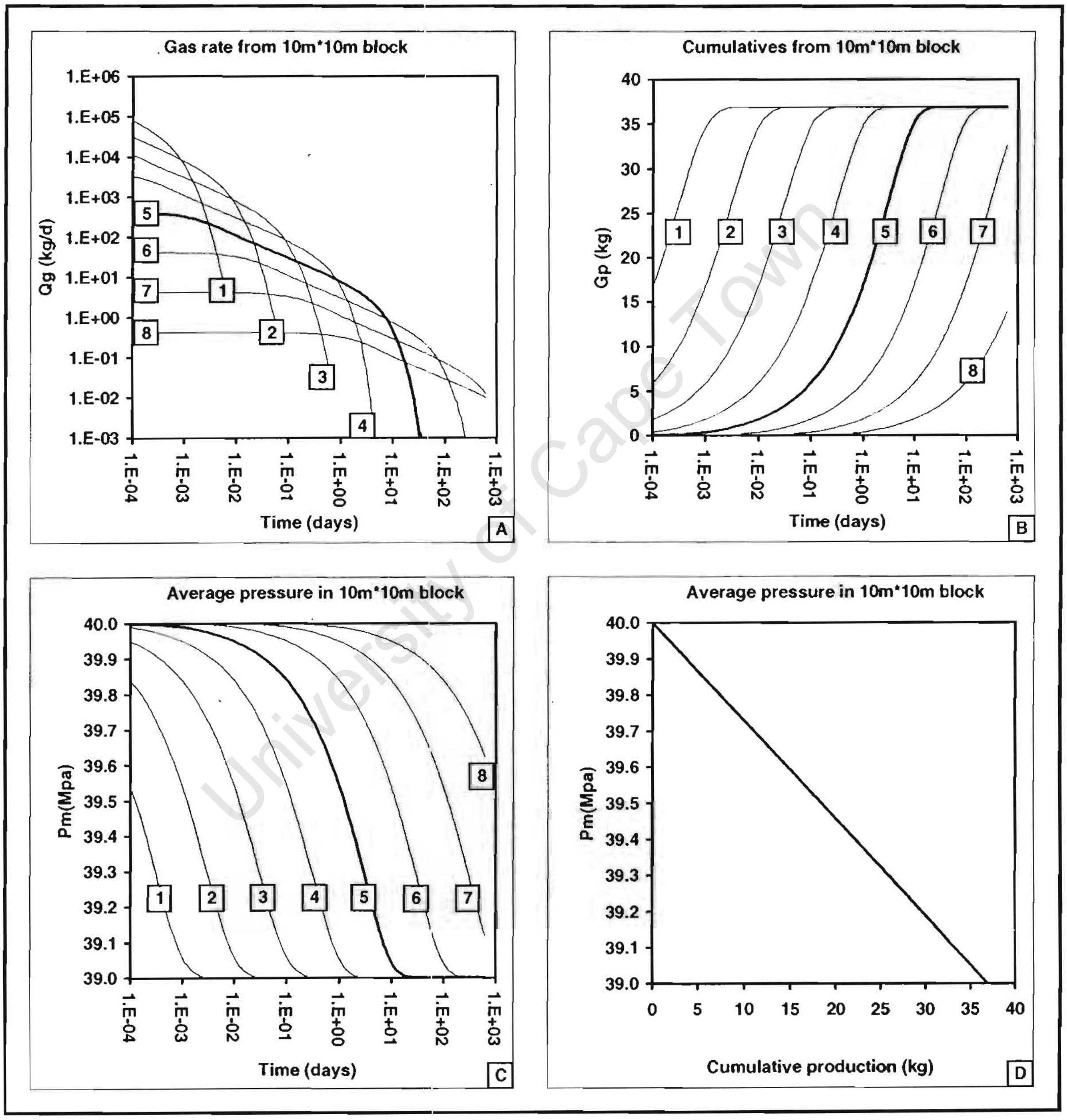

Figure 4.33: *Results of two-dimensional numerical simulation of the expulsion of gas from a 10m by 10m square matrix block for a range of matrix permeability values.*

At the extremely low permeability end of the scale, where the permeability is in the order of $10^{-21}m^2$, the expulsion of gas from the matrix occurs at such a low rate, and depletion is so slow, that the contribution of the matrix to overall reservoir performance is not likely to be significant. With these permeability values, the reservoir can once again be modelled as a single porosity system but with the single continuum being assigned both the permeability and the porosity values pertaining to the fracture network.

The 10m by 10m block. The results of the simulation of expulsion of gas from the 10m by 10m block are illustrated in Figure 4.33. Gas is expelled at very high rates at the higher matrix permeability values, as is the case for the 1m by 1m block. For case 1, with a matrix permeability value of 10^{-14}m^2 (10mD), initial rates are extremely high, in the order of $1*10^5$ kg/d, and the block has become depleted after 0.01 days (14 minutes). At the other end of the scale, for case 8 in which a permeability value of 10^{-14}m^2 is considered, the initial rate is about 0.4kg/d, and the block is only half depleted even after 1000 days.

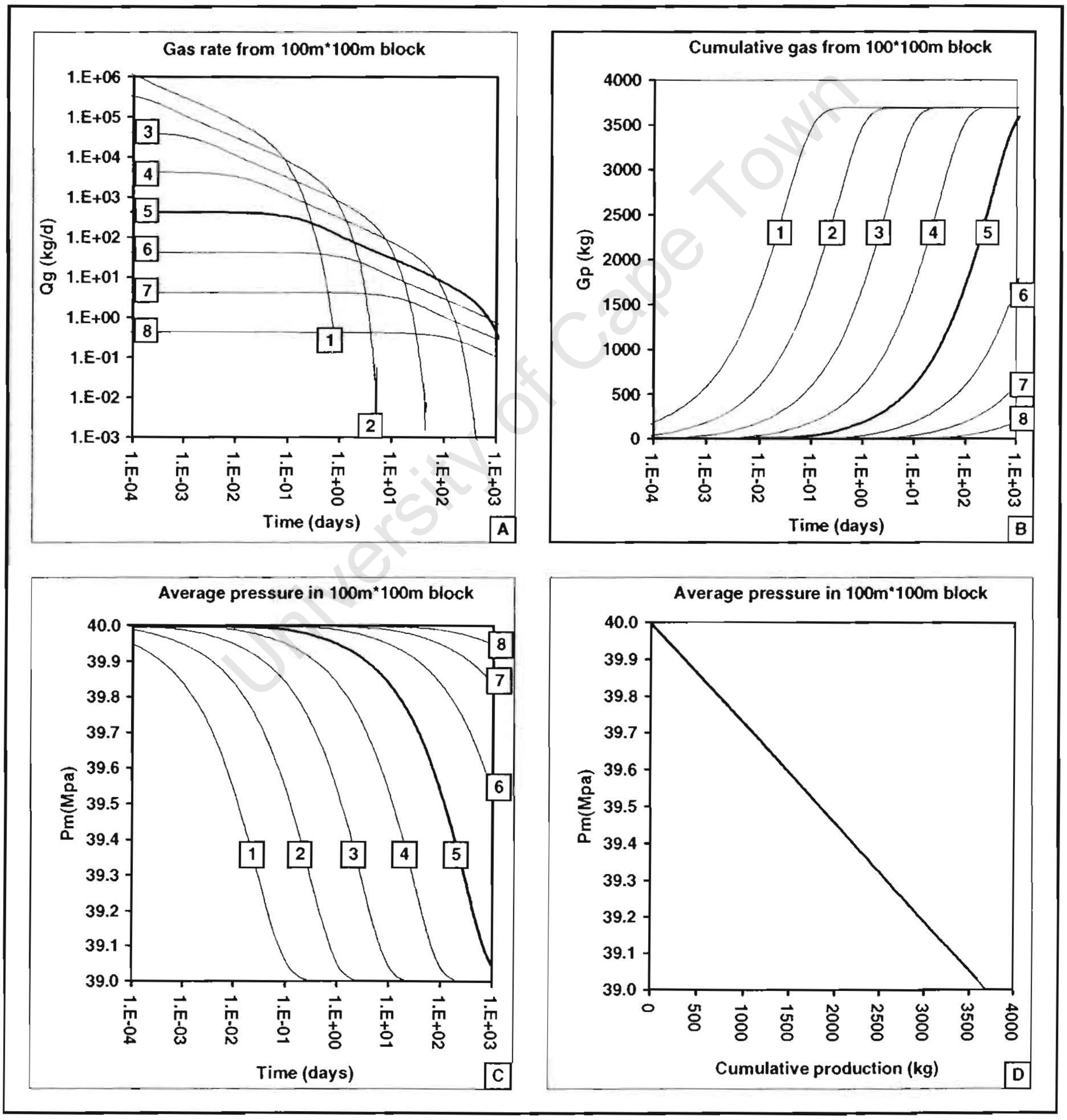

Figure 4.34: *Results of two-dimensional numerical simulation of the expulsion of gas from a 100m by 100m square matrix block for a range of matrix permeability values.*

Similar modelling criteria that apply to the 1m by 1m block also apply to this block, except that the range of permeability values for which dual porosity modelling is likely to be important is shifted by about one order of magnitude to higher values, i.e. over the range $10^{-17}m^2$ to $10^{-19}m^2$. At higher values above this range, the single continuum with fracture permeability and matrix porosity applies, and at lower values below this range, the single continuum with fracture porosity and permeability applies.

The 100m by 100m block. The results of these simulations, presented in Figure 4.34, show similar trends to the previous two examples. Dual porosity behaviour is likely to occur over the permeability range $10^{-16}m^2$ to $10^{-18}m^2$. At the low permeability range, depletion is so slow that the contribution from the matrix to overall production is negligible on a reservoir scale.

Conclusions

- When transient conditions prevail, the analytical solutions for pseudo-steady state flowing conditions give very poor results relative to finely meshed two-dimensional numerical simulation for all those geometric shapes for which analytical solutions were considered. During the transient period, the large degree of divergence is likely to have a negative impact on the analytical solutions' ability to replicate any subsequent pseudo-steady state behaviour.
- The analytical solution for transient flow of slightly compressible fluid gives better results than the analytical solution for pseudo-steady state flow in comparison with the results of finely meshed two-dimensional numerical simulation. In these, the transient equation is applied to a circular disk, while the pseudo-steady state and numerical solutions are for a square matrix block.
- The analytical solution for transient behaviour has limited use in dual porosity simulators as it's application is limited to very idealised shapes, such as spheres or disks, and can only be used under very restrictive boundary conditions, such as a fixed fracture pressure.
- Under transient flowing conditions, the results of finely meshed two-dimensional numerical simulations show that blocks with different geometric shapes respond in significantly differently ways, suggesting that matrix block geometry is an important parameter to consider when modelling fractured reservoirs.
- Simulation results obtained from the use of the one-dimensional models are in very close agreement with the finely meshed two-dimensional model results for all six geometric forms tested for transient flow conditions.
- For the type of problem analysed here, a one-dimensional model comprising five and possibly four, linear, one dimensional elements is adequate for modelling transient flow from a matrix block when compared with finely meshed two-dimensional models. When the number of elements is reduced from 4, the accuracy of the approximation is adversely affected.
- Simulation results using a single, five noded element to represent the matrix block, with nodal spacing selected according to the same criteria as the multiple element model, are in close agreement with finely meshed two-dimensional model results for transient flow conditions.

- Expulsion of gas from a matrix block under transient conditions is greatly affected by the size of the block and the matrix permeability.
- For a matrix block of dimensions 1m*1m, expulsion of gas occurs so rapidly for most values of matrix permeability that any dual porosity effects in a fractured reservoir made up of matrix blocks of this size are only likely to occur when the matrix permeability is extremely low, less than about $5*10^{-18}m^2$ (0.005mD). Matrix blocks of this size can be expected to contribute to production even when the matrix permeability is as low as $5*10^{-21}m^2$ (0.000005mD).
- Expulsion of gas is so slow from a matrix block with dimensions of 100m*100m that dual porosity effects in a fractured reservoir made up of matrix blocks of this size are likely to occur when the matrix permeability is less than about $5*10^{-16}m^2$ (0.5mD). When the matrix permeability is less than about $5*10^{-19}m^2$ (0.0005mD), contribution from the matrix blocks to overall production is expected to be minimal.

4.3 Flow through the fractured reservoir

In this section results of dual porosity modelling are presented. The process involves coupling the fracture network and matrix block models described in Sections 4.1 and 4.2 respectively. A simple elongated fractured reservoir that allows some of the important components of a dual porosity model to be evaluated, is considered. The effects of changing matrix permeability, anisotropy in the matrix permeability, matrix block size, and matrix block shape, are investigated. The study of these models assists in identifying the relative importance of the different parameters.

4.3.1 Model description

The geometric model considered here is similar to that of Section 4.1.1, namely an elongated reservoir, 1000m long (x-axis), 100m wide (y-axis) and 1m thick. The reservoir consists of a fractured network within a porous and permeable rock matrix, and is impregnated with highly compressible gas. A base case model is defined in which the matrix blocks are assumed to be square and the simulation results of this base case model are first discussed in detail. This is followed by a comparison of results in which the matrix permeability is varied between $1*10^{-13}m^2$ (approximately 100mD) and $1*10^{-20}m^2$ (approximately 0.00001mD). The effect of varying the matrix block size between 1m and 50m is discussed next. This is followed by a comparison of the numerical results obtained by using different matrix block shapes.

Problem description and physical properties

A base case model, details of which are presented in Table 4.11, has been defined against which changes made to the model are tested and compared. In the base case it has been assumed that the reservoir contains evenly spaced vertical fracture sets at right angles to each other, effectively dividing the 1000m by 100m area of the reservoir into a series of square matrix blocks, each of which has dimensions of 10m by 10m.

Table 4.11: *Properties for the base case example of an elongated, fractured reservoir.*

Parameter	Symbol	Value	In oilfield units	Value	In SI units
Matrix permeability	k_m	**0.00101**	mD	**$1.0*10^{-18}$**	m^2
Matrix porosity	ϕ_m	**0.10**	fraction	**0.10**	Fraction
Matrix block lengths	a,b	**32.808**	ft	**10**	m
Fracture width	w_{sx}, w_{sy}	**0.00197**	in	**0.0005**	m
Fracture network perm.	k_f	**351.8**	mD	**$347.2*10^{-15}$**	m^2
Fracture network porosity	ϕ_f	**0.0001**	fraction	**0.0001**	fraction
Fluid density	ρ_g	**15.61**	$lbft^{-3}$	**250**	kgm^{-3}
Fluid compressibility	c_g	**$103.4*10^{-6}$**	psi^{-1}	**$15.0*10^{-9}$**	Pa^{-1}
Fluid viscosity	μ_g	**0.04**	cP	**$40.0*10^{-6}$**	Pas
Initial pressure	P_i	**5801.5**	psi	**$40.0*10^{6}$**	Pa

Matrix material base case properties. The matrix material is characterised by a reasonable value for porosity (0.1) and a very low value for permeability ($1*10^{-18}m^2$, or approximately 0.001mD). In the base case model, the permeability in the matrix is considered to be isotropic. The fluid properties listed in Table 4.11 are those of a highly compressible, low viscosity gas. Given the matrix block parameters, the only further requirement is an assumption regarding the fracture width in order for the fracture parameters to be fully determined.

Fracture network base case properties. In this section, the assumption is made that the fractures have a constant width of 0.5mm. According to expression 2.64, an approximation of the absolute permeability of a smooth walled slit of width w under laminar flow conditions is

$$k_s = \frac{w^2}{12} = 20.8333 * 10^{-9} m^2 .$$

This is approximately 21110Darcy, an extremely high value. For the reasons discussed in Section 2.2.1, the effective permeability in practice is likely to be significantly less than this theoretical value. According to the examples cited in Section 2.2.1, a reduction to approximately 1/3 of the theoretical value appears reasonable, and has been used here. In this section, the effect of varying fracture width is not considered, and therefore the value of the permeability of an individual fracture that has been used throughout is

$$k_s' = \frac{20.8333 * 10^{-9}}{3} = 6.944 * 10^{-9} m^2 .$$

As discussed in Section 2.2.1, the concept of fracture permeability, and its implementation in Darcy's law as used in this study has meaning only when the fracture network can be considered to be a hugely up-scaled analogy of a porous rock for which Darcy's law applies. The appropriate permeability to apply in the governing equations is therefore some average value. In general, the appropriate average permeability to use for flow that is parallel to bedding planes is given by the thickness-weighted arithmetic mean,

$$\bar{k} = \frac{\sum_{i}^{N} k_i h_i}{\sum_{i}^{N} h_i}, \tag{4.51}$$

where k_i is the permeability of plane i, h_i is the thickness of plane i, and the summation is over all bedding planes. A similar approach can be applied to the fractured reservoir for the purpose of determining an average value of permeability. For this averaging process, the reservoir can be viewed as being built up of a great many identical units laid side by side. Each unit consists of a single matrix block surrounded on all sides by half widths of fractures, as illustrated in Figure 4.35. In the general case of an anisotropic rectangular block surrounded by fractures which have different widths in each of the two orthogonal directions, the average permeability for the system in each of these two directions will be given by

$$\bar{k}_{mfx} = \frac{k_{mx} b + k_{fx} w_y}{b + w_y} \text{ and } \bar{k}_{mfy} = \frac{k_{my} a + k_{my} w_x}{a + w_x}, \tag{4.52}$$

where $\bar{k}_{mfx}$ and $\bar{k}_{mfy}$ are the average x- and y-components of permeability of the combined matrix-fracture system, k_{mx} and k_{my} are the x- and y-components of permeability of the matrix block, k_{fx} and k_{fy} are the permeability values of single fractures oriented parallel to the x- and y-axes respectively, and which are functions of the widths of the fractures measured perpendicular to either the x- or y-axes, namely w_y and w_x, and b and a are the dimensions of the matrix block measured perpendicular to the x- and y-axes respectively. One of the basic assumptions of the dual porosity model is that bulk flow occurs exclusively through the fracture network and therefore, for this averaging process, the matrix permeability must not contribute to the average permeability, and is assigned a value of nil ($k_{mx} = k_{my} = 0$). In the base case model considered here, the values of the parameters are

$$a = b = 10\text{m},\ w_x = w_y = 0.0005\text{m and } k_{sx} = k_{sy} = 6.944 * 10^{-9}\text{m}^2.$$

The value for the fracture permeability is consequently

$$k_f = \bar{k}_{fx} = \bar{k}_{fy} = 347.20 * 10^{-15}\text{m}^2.$$

The average fracture porosity can be determined from the relationship

$$\phi_f = \frac{(a + w_x)(b + w_y) - ab}{(a + w_x)(b + w_y)}. \tag{4.53}$$

The appropriate value of porosity for the fracture network for the base case model is determined from (4.53) as

$$\phi_f = 0.0001.$$

The values of the various parameters are summarised in Table 4.11. It is noteworthy that the overall permeability of the fracture network is more than five orders of magnitude greater than that of the matrix material, while the porosity of the matrix is three orders of magnitude greater than that of the fracture network.

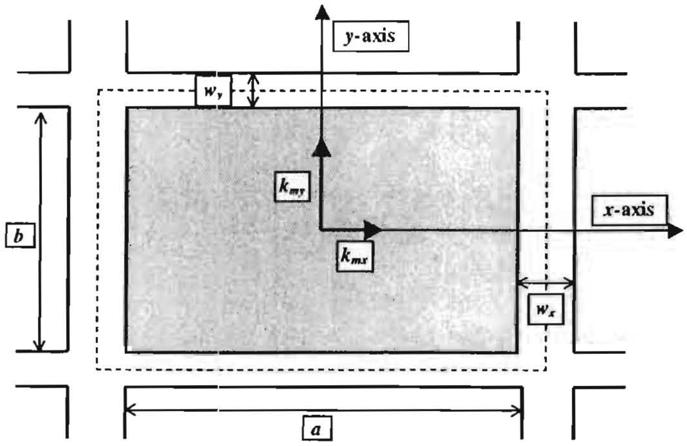

Figure 4.35: *Representation of generalised matrix block surrounded by fractures.*

Initial and boundary conditions. The initial pressure throughout the reservoir, in both the matrix and in the fracture network, is 40MPa. The mass of gas initially in place is distributed as follows:

Gas initially in place in matrix:	$2.5000*10^6$kg	(approximately 88 MMscf)
Gas initially in place in fracture network:	$0.0025*10^6$kg	
Total gas initially in place:	$2.5025*10^6$kg	

All boundaries are considered to be no flow (zero flux) boundaries and there is no artificial pressure maintenance. Gas is extracted from the reservoir via the fracture network out of cell number 1 at a rate of 0.5kgs^{-1} (approximately 1.5MMscf/d). The reservoir model described here can be considered as part of a much larger reservoir, as neither the in situ volumes nor the off-take rate are realistic for a stand alone field development. Relative to the volume of gas in place, the flow rate is extremely high. This creates large pressure differentials appropriate for testing the robustness of the algorithms. Gas is extracted from the reservoir during a 6 day draw down period, followed by 6 days of build up. The total mass of gas extracted from the reservoir during this time is therefore $0.2592*10^6$kg, or approximately 10.3% of the volume initially in place. Following similar material balance arguments to those posed in Section 4.1.1 the average pressure in the reservoir expected to prevail at the end of the sequence is 32.71MPa.

The finite element model

Discretization. The fracture network is modelled with ten side by side cells, each with dimensions of 100m by 100m, constituting the primary mesh (Figure 4.36). These parameters were selected following a process in which a very fine mesh (20m by 20m cells) was progressively coarsened and the results compared. It was found that the relative course mesh of 100m by 100m provided accurate results when used in conjunction with the fine time discretization described in the next section.

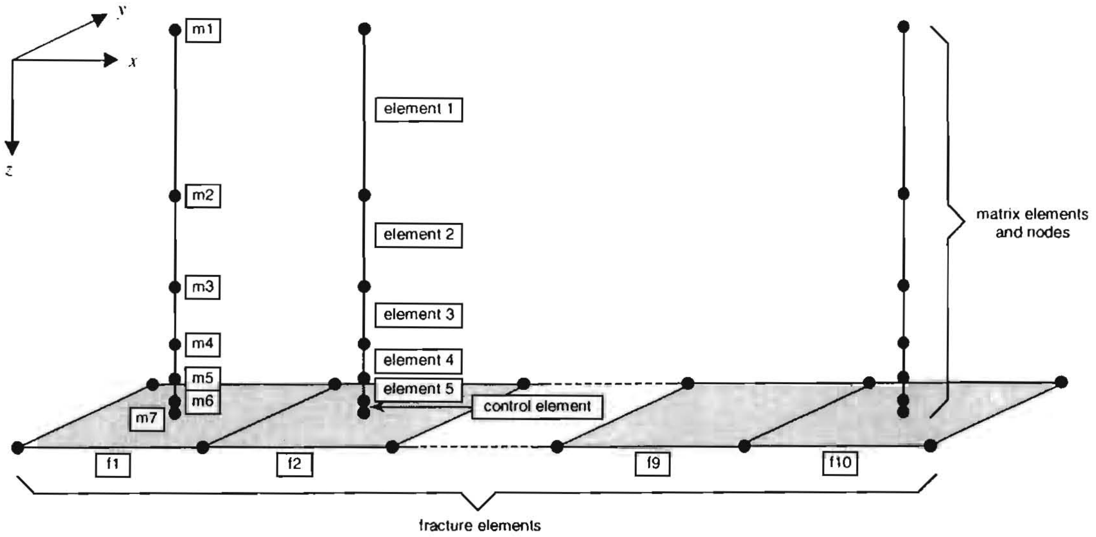

Figure 4.36: *Schematic of the discretization of an elongated reservoir, showing the two-dimensional primary, or fracture mesh, with elements labelled f1 to f10, and the one-dimensional secondary, or matrix meshes, with nodes labelled m1 to m6. (Not to scale.)*

Each matrix block is modelled with five one-dimensional elements as described in Section 4.2.3. These, together with a sixth, control element forming the link between each matrix block and the fractures, as described in Section 3.3.2, complete the secondary mesh system. The length of each element of each secondary mesh is determined according to whether an exponential rule is used or whether each cell is taken to represent a fixed volume of matrix material (Table 4.8). For the base case model, the latter approach is used. Each matrix block represents a gross volume of $100m^3$, and therefore there are 100 matrix blocks per fracture cell. Each primary cell has one representative matrix block associated with it, with its five unique cells. There are therefore ten sets of five cells that comprise the secondary meshes.

For the primary (fracture network) mesh, four-noded bilinear quadrilateral elements are used. For the secondary mesh (matrix block discretization), a series of five, one-dimensional, two-noded linear elements are used to model each representative matrix block associated with each of the primary mesh cells.

Time stepping. The time stepping routine adopted for the primary mesh is similar to that used for the single porosity well test described in Section 4.1.3. The first time interval consists of 100 steps, each of length 0.0001s. In each subsequent time interval, the step length is increased by a factor of $\sqrt{2}$, up to a maximum step length of 180s, while the number of steps in each interval remains constant. Once the step length has reached 180s, the number of steps per interval is increased in steps of ten up to a maximum of 120 steps per interval. Henceforth, a constant interval length of 120 steps of 180s each is maintained until the end of the respective draw down or build up period is reached. Within each primary mesh time step, a fixed number of 10 equal length sub-steps are used to progress the secondary meshes through time. The same time stepping sequence is used for both the draw down and build up periods. For the complete sequence for which the simulation is run, a total of 126 time intervals are used, with a total of 13488 time steps and 134880 sub-steps. The primary mesh is progressed through time using a backward differencing routine while the secondary mesh is solved using forward differencing. The large number of sub-steps used, was to ensure stability of the forward differencing routine.

Convergence. Within each primary time step, the primary mesh is iterated until convergence is achieved using a prediction of the flux that will be derived from each of the representative matrix blocks during that time step. This convergence of the nonlinear primary mesh iterations is controlled by a maximum global rms error of 500Pa and a maximum local (element scale) rms error of 100Pa, or a maximum permitted number of 10 iterations. Once these convergence criteria have been met or the maximum number of iterations exceeded, the secondary mesh is solved using a revised set of essential boundary conditions supplied from the primary mesh and explicit time sub-stepping to revise the forecast of the flux. The primary mesh is then re-solved for the same time step and the process repeated until convergence is achieved. This iteration of the combined primary and secondary meshes is terminated upon meeting the convergence criteria of 1000Pa for the global rms error and 200Pa for the local rms error, or a maximum of 10 iterations. Therefore, for each time step, a maximum of 100 iterations is possible if the rms convergence criteria are not met.

4.3.2 Numerical results of the base case model

Figure 4.37 illustrates the pressure responses associated with the fracture elements f1 and f10. Production of gas takes place from the first cell (f1). Focussing on the matrix pressure profiles associated with fracture cell 1 (diagram A) during the draw down period, it is evident that a large pressure gradient is set up in the matrix block.

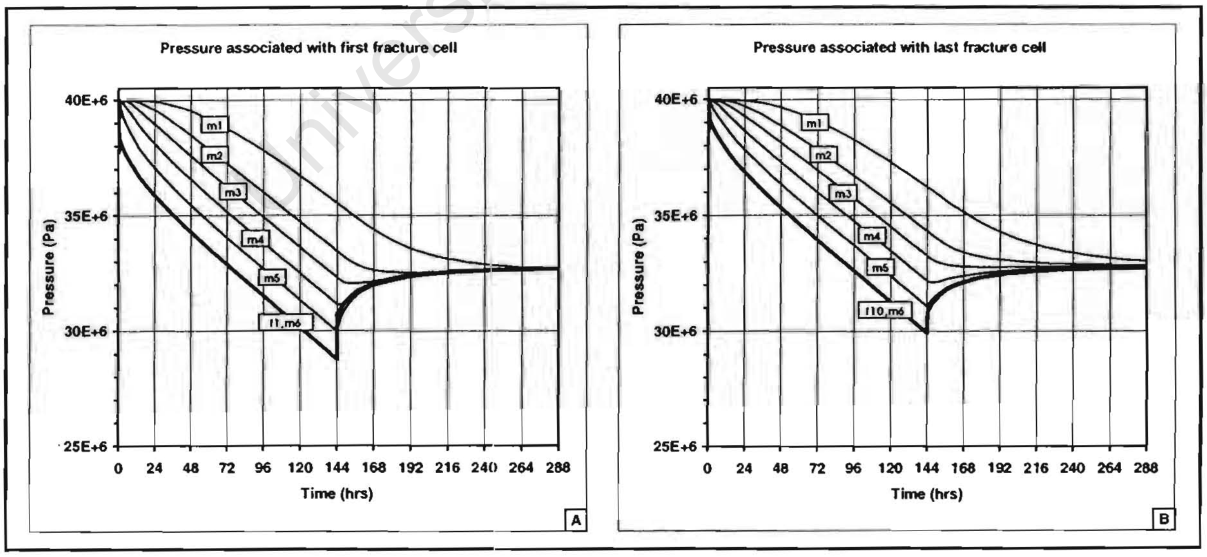

Figure 4.37: *Results of the numerical simulation of a dual porosity model of a reservoir with square matrix blocks. Diagram A shows the pressure responses in the first fracture cell (curve f1) and at the nodal points of its matrix cells (curves m1 to m6). Diagram B shows the corresponding results in the last of the sequence of ten fracture cells (curve f10) and at the nodal points of its matrix cells.*

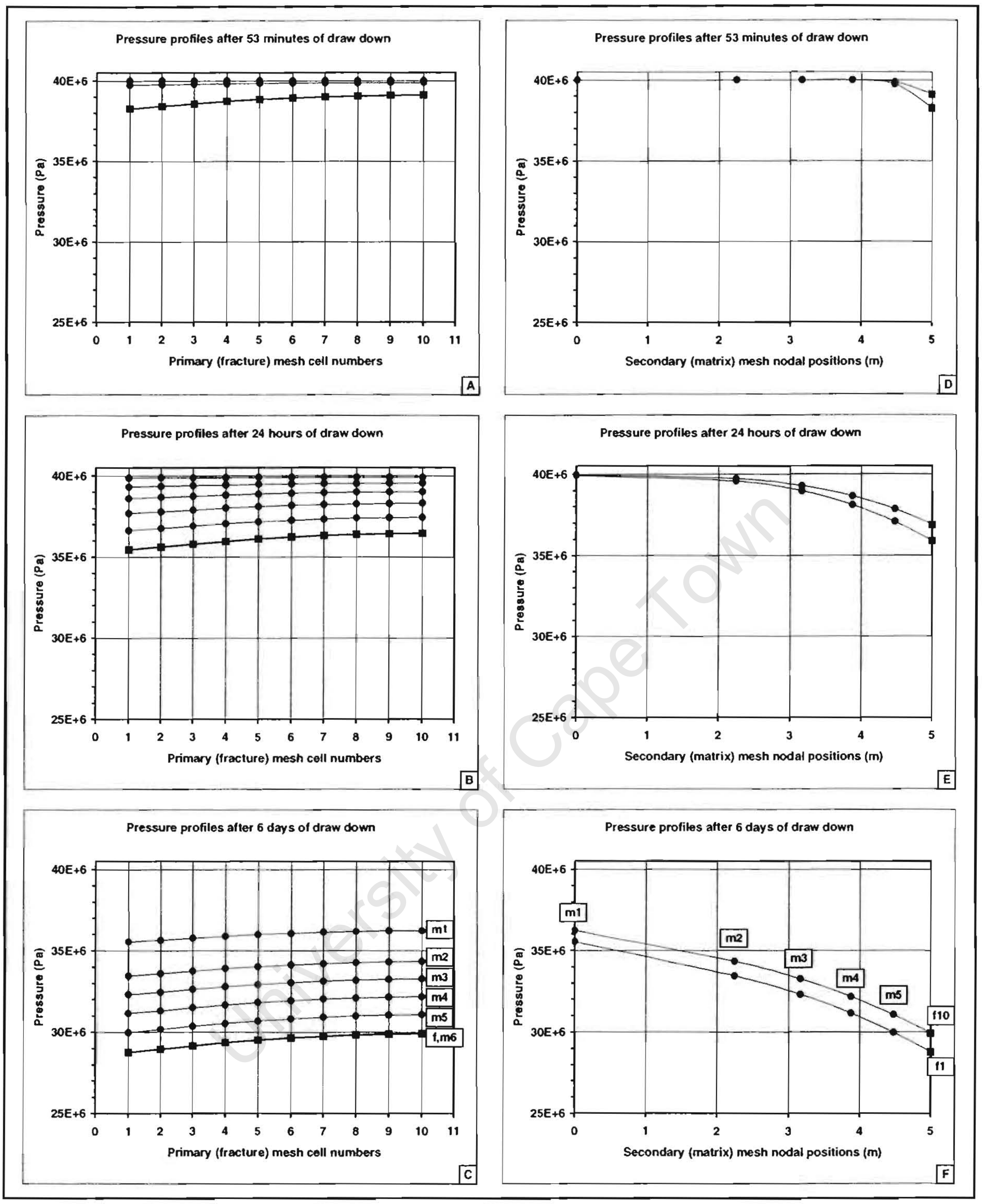

Figure 4.38: ***Diagrams A to C**: Pressure in each of the fracture cells (curve f) and at each fracture cell's associated set of matrix cell nodal points (curves m1 to m6) after 53mins (diagram A), 24hrs (diagram B), and 6days (diagram C) of draw down from an elongated dual porosity reservoir. **Diagrams D to F**: Pressure as a function of distance from the centre of a square matrix block located within the first (curve f1) and last (curve f10) fracture cells at either end of an elongated dual porosity reservoir after 53mins (diagram D), 24hrs (diagram E) and 6days (diagram F) of draw down. Matrix nodal point locations are labelled m1 to m6. The pressure within each fracture cell is annotated with a square and at each matrix nodal point with a circle.*

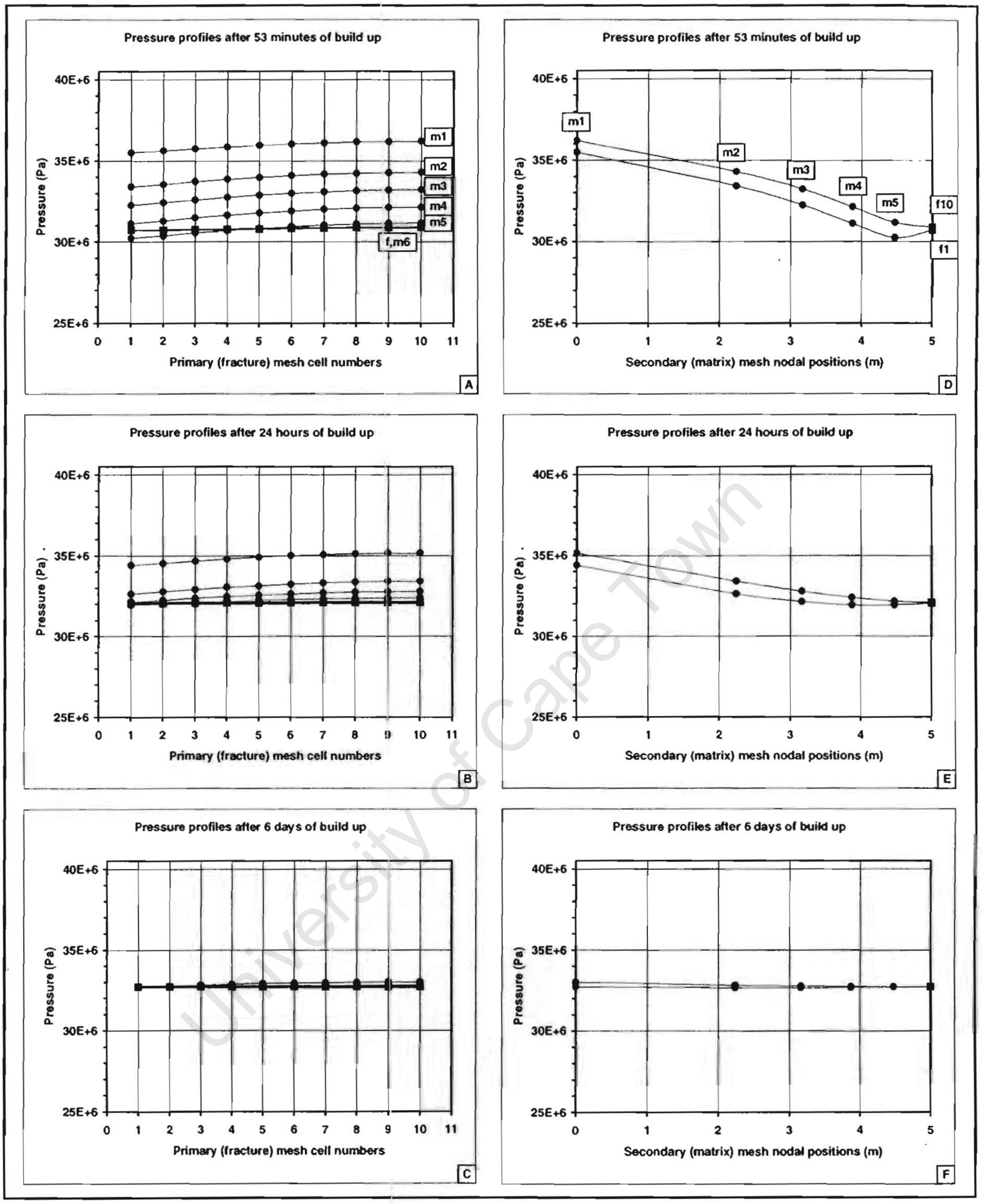

Figure 4.39: ***Diagrams A to C**: Pressure in each of the fracture cells (curve f) and at each fracture cell's associated set of matrix cell nodal points (curves m1 to m6) after 53mins (diagram A), 24hrs (diagram B), and 6days (diagram C) of build up in an elongated dual porosity reservoir. **Diagrams D to F**: Pressure as a function of distance from the centre of a square matrix block located within the first (curve f1) and last (curve f10) fracture cells at either end of an elongated dual porosity reservoir after 53mins (diagram D), 24hrs (diagram E) and 6days (diagram F) of build up. Matrix nodal point locations are labelled m1 to m6. The pressure within each fracture cell is annotated with a square and at each matrix nodal point with a circle.*

The centre of the matrix block, at node m1, is only 5m from the fracture, yet the pressure differential across this distance exceeds 6MPa for a large portion of the draw down period. This is due to the very low permeability of the matrix material. There is also a considerable time delay between the onset of the pressure differential at the edge of the matrix block and the response to this pressure drop at the centre of the matrix block.

The two diagrams of Figure 4.37 show that the first (f1) and last (f10) cells of the fracture mesh respond immediately when the well is shut in. The declining pressure trends established in both cells during the flow period are immediately arrested and reversed when the well is shut in. This is due to the continual feeding of gas from the matrix blocks into the fractures. The pressure throughout the reservoir, in the fractures and in the matrix blocks, has almost converged to a single value at the end of the shut in period.

Draw down sequence. After 53 minutes of draw down (Figure 4.38, diagrams A and D), the pressure throughout the fracture mesh has decreased by between 1MPa and 2MPa. A (small) pressure gradient exists across the fracture network as a result of the finite (but high) permeability of the fracture system. Within each secondary, or matrix mesh, only the cell immediately adjacent to the fracture has experienced some degree of pressure drop (nodes m5 and m6), after 53 minutes. As time progresses, so the pressure in the fractures decreases and the pressure response moves further into the matrix blocks. After about 24hours (diagrams B and E) the innermost nodes (node number 1) of all the matrix meshes begin to experience a change in pressure. Subsequently, the entire system experiences a continual decline until the end of the draw down period is reached (diagrams C and F), portraying a pseudo-steady state behavioural pattern.

Build up sequence. The fracture cells respond immediately to the shut in of the well (Figure 4.37 and Figure 4.39 diagrams A and D) and the pressure gradient across the fracture network is reduced very rapidly. After 53 minutes of build up, the pressure in each of the first 3 to 4 cells representing the fracture network has increased to a value that is greater than the pressure at matrix node m5 associated with that cell. This causes a reversal of the direction of flow, with gas moving from the fractures back into the matrix blocks. Within the matrix blocks themselves, gas continues to flow outwards and accumulates in the cells common to node m5 (cells 4 and 5). This occurrence is absent from the final fracture cell (f10) and its associated matrix cells, where the fluid flow direction is monotone throughout. Ultimately, the pressure throughout the reservoir converges towards a value of 32.7MPa (diagrams C and F), which is consistent with the value determined from material balance calculations.

4.3.3 Numerical results showing the effect of matrix permeability

The influence that permeability has on the numerical forecasts for the dual porosity model is discussed in this section. The matrix permeability has been progressively increased by a factor of 10 from $10^{-20}m^2$ to $10^{-13}m^2$. Besides this, the reservoir model is the same as the base case described in the previous section.

In the first pair of diagrams of Figure 4.40, (A and B), the responses in the first and last fracture cells (f1 and f10) are shown for a single porosity model, in which gas flows only through the fracture network (corresponding to a matrix permeability value of zero). The effective permeability for this example is therefore that of the fracture network, namely $347.2*10^{-15}m^2$. The pressure throughout the fracture network declines rapidly due to the limited volume of gas that can be stored in the fracture network alone and has reached a value of zero after little more than 0.6 hrs.

Diagrams C and D of Figure 4.40 show the pressure responses in the first and last fracture cells, and at the nodal points of the secondary meshes associated with each of these fracture cells, for a matrix permeability value of $10^{-20}m^2$ (approximately 0.00001mD). The pressure in the fracture network declines very rapidly, reaching zero after slightly more than 0.8 hours despite there being a large volume of gas in the reservoir. The permeability is simply too low for the matrix to respond. The pressure at node m6 shows only a small deviation from its initial value (for both fracture cells). A fractured reservoir in which the matrix permeability is as low as of $10^{-20}m^2$ can be modelled as a single porosity reservoir and the contribution from the matrix can be discounted.

The final pair of diagrams of Figure 4.40 (E and F) shows the response for a matrix permeability value of $10^{-19}m^2$. The matrix permeability is sufficiently high to permit some gas to flow out of the matrix block and provide pressure support for the fracture network. The pressure gradient within the matrix blocks is large, up to 36MPa across the 5m depth of the matrix block and the innermost nodes of the matrix blocks only begin to experience observable pressure declines after about 6-hours. In this type of reservoir, transient effects are likely to dominate the expulsion of gas from the matrix blocks.

In the first two diagrams of Figure 4.41 (A and B), a value of $10^{-18}m^2$ is assumed for the permeability of the matrix, corresponding to the base case described earlier. Large pressure gradients exist in the matrix and this type of reservoir must be modelled as a dual porosity reservoir. Furthermore, the sluggish response of the matrix blocks to pressure changes in the fractures means that transient effects remain important.

When the value of the matrix permeability is increased further to $10^{-17}m^2$ (C and D), the response within the matrix block is far more rapid. Pressure gradients of up to 1MPa do still exist within the matrix blocks and the reservoir therefore still exhibits dual-porosity behaviour but transient effects are unlikely to be significant. This is evident during the early stages of the build up period in the last fracture cell, where the pressure is seen to continue its downward trend after the well is shut in, rather than to reverse its direction and climb as is the case with lower matrix permeability examples. This is because the matrix block pressure has closely followed the fracture pressure, and there is very little excess pressure in the matrix to drive gas into the fracture cells.

When the matrix permeability is increased to $10^{-16}m^2$, the response from the matrix blocks is so rapid and the pressure gradients within the matrix blocks so small, that the reservoir can be modelled as a single porosity model. The results of such a single porosity model is illustrated in the final pair of diagrams (E and F) in Figure 4.41.

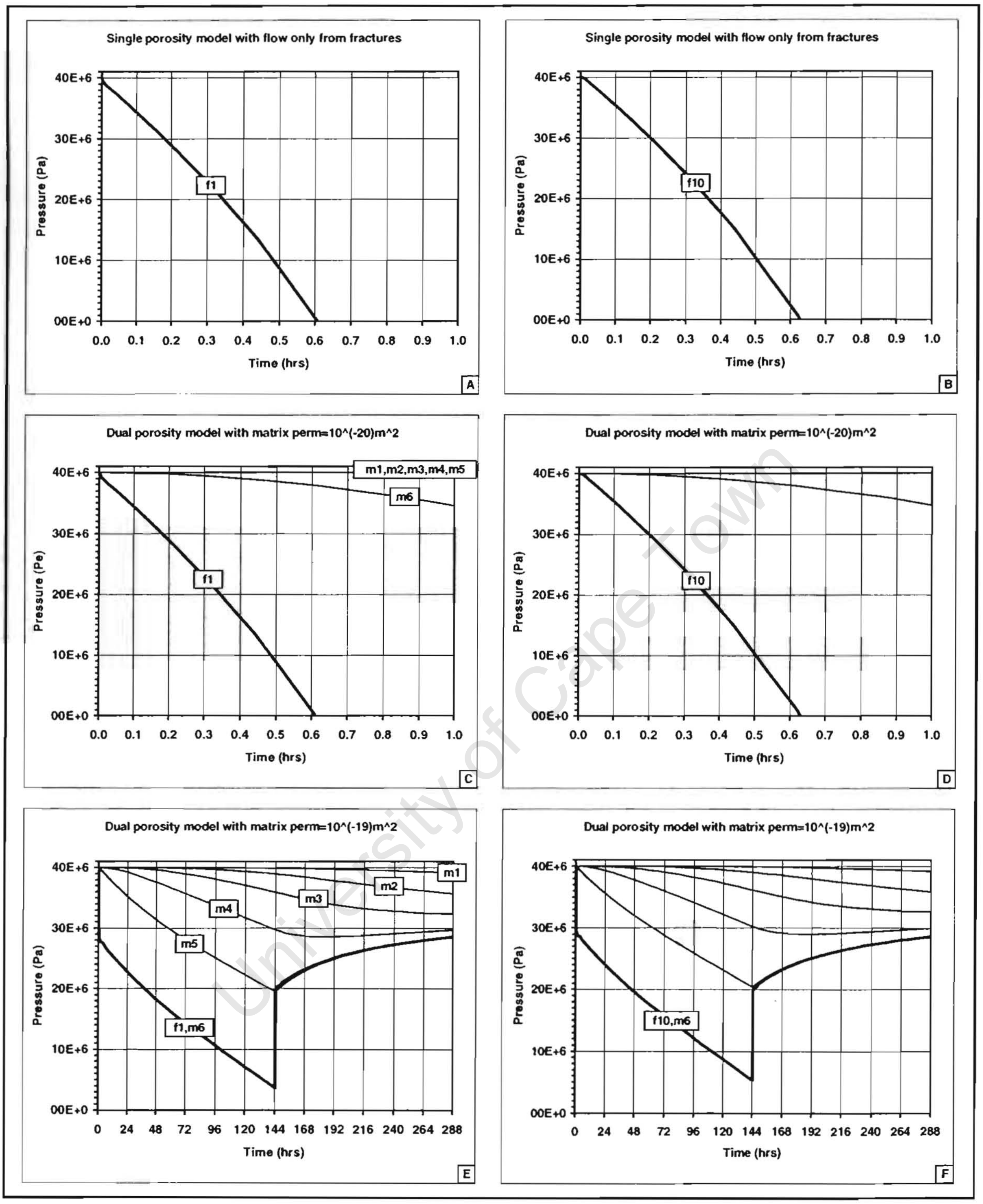

Figure 4.40: *Pressure response in the fracture network (first and last cells) and matrix blocks as a function of time through a 6 day draw down period followed by a 6 day build up period in a dual porosity reservoir. The first pair of diagrams (A and B) show the pressure response as a function of time in the first and last fracture cells (f1 and f10) respectively with no contribution from the matrix. The two remaining pairs correspond to matrix block permeability values of* $1*10^{-20}m^2$ *(diagrams C and D) and* $*10^{-19}m^2$ *(diagrams E and F) respectively.*

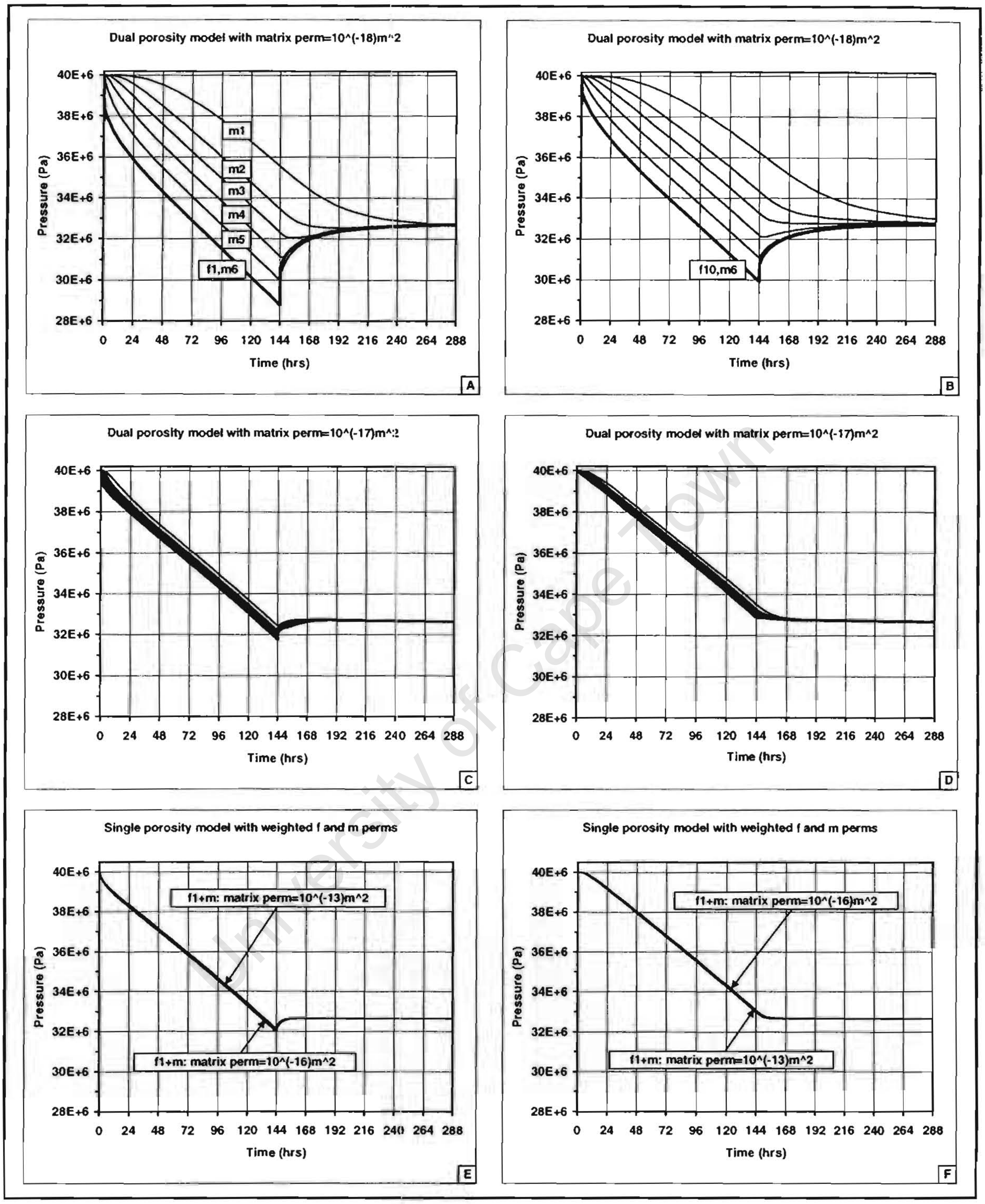

Figure 4.41: *Pressure response in the fracture network (first and last cells) and matrix blocks in a dual porosity reservoir. The first two pairs of diagrams correspond to matrix block permeability values of* $1*10^{-18}m^2$*, (diagrams A and B) and* $1*10^{-17}m^2$ *(diagrams C and D) respectively. Diagrams E and F are single porosity models for which the permeability and porosity are weighted average values of the fracture network and matrix material. The two curves in diagrams E and F correspond to matrix permeability values of* $1*10^{-16}m^2$ *and* $1*10^{-13}m^2$ *respectively.*

The effective porosity for this single porosity model is 0.1001, only 0.1% greater than the matrix porosity, while the permeability is $347.30*10^{-16}m^2$, only 0.03% greater than the fracture permeability. The fractures contribute little to the storage, while the matrix contributes little to the overall permeability. The only requirement for the use of such a single porosity model is that the matrix permeability is sufficiently large that the pressure gradients within the matrix blocks are not significant.

Also illustrated in the lowermost diagrams (E and F) of Figure 4.41 are the forecasts for a single porosity model in which the matrix permeability is significantly higher than in the previous case, namely $10^{-13}m^2$. The pressure profiles in the fracture cells for this case are very similar to those of the previous case, indicating that the response is still dominated by the fracture permeability. The pressure profile for this example in which the matrix permeability is the greater of the two cases lies above the other during the draw down period in the first fracture cell, but lies below it during the draw down period in the last fracture cell. This is because the effect of increasing the average reservoir permeability is to reduce the pressure gradient across the reservoir.

Summary

These examples demonstrate that for the reservoir parameters considered in this example, a fractured reservoir in which the matrix permeability is less than about $10^{-19}m^2$ can be adequately modelled with a single porosity approach in which the reservoir is assigned the properties of the fracture network. When the matrix permeability lies in the range 10^{-19} to $10^{-17}m^2$, the reservoir must be modelled using a dual porosity approach. Additionally, when the permeability lies between 10^{-17} and $10^{-18}m^2$, transient effects are extremely important, while a pseudo-steady state model is likely to provide a good approximation when the permeability is closer to $10^{-17}m^2$. When the matrix permeability is in the order of $10^{-16}m^2$ or higher, a single porosity model suffices, in which the reservoir is assigned the porosity of the matrix and the permeability of the fracture network. This holds true with increasing matrix permeability until the matrix permeability reaches a value that is comparable with that of the fracture permeability after which it must once again be taken into account.

4.3.4 Numerical results showing the effects of matrix block size

In this section the matrix block size is varied from that of the base case (10m*10m). Sizes of 100m*100m, 50m*50m, 5m*m5, 2m*2m and 1m*1m are considered. Altering the matrix block size changes the spacing between fractures and hence the fracture network properties. Appropriately adjusted fracture network properties for the different size matrix blocks are listed in Table 4.12. Results of the modelling are presented in Figure 4.42 for block dimensions of 50m, 20m and 10m and Figure 4.43 for block dimensions of 5m, 2m and 1m. The diagrams are displayed in the same format as in previous sections.

The case for which the block dimension is 100*100m results in very rapid and continual decline of the fracture pressure to a value of zero and the results are not displayed. For the matrix permeability used in this example, a reservoir with matrix blocks of this size is on the limit of what could be regarded as a viable reservoir as the response from the matrix block is so sluggish that it would be difficult to maintain reasonable flow rates. If the matrix permeability is increased, then some point is reached at which a reservoir that contains such large matrix blocks will become exploitable. Generally, reservoirs are discretized for the purpose of full field numerical simulation with meshes that have cell dimensions in the order of 100m. When the matrix block size becomes comparable with that of the primary mesh cell size, the modelling of the reservoir presents new challenges, and different approaches need to be considered.

Table 4.12: *Fracture network properties as functions of matrix block size.*

Matrix block size	**Fracture network permeability**		**Fracture network porosity (fraction)**	**Number of matrix blocks per fracture cell**
	SI units (m^2)	**Oilfield (mD)**		
1m*1m	$3470.49*10^{-15}$	3516.5	0.00100	10000
2m*2m	$1735.68*10^{-15}$	1758.7	0.00050	2500
5m*5m	$694.38*10^{-15}$	703.6	0.00020	400
10m*10m	$347.20*10^{-15}$	351.8	0.00010	100
20m*20m	$173.61*10^{-15}$	175.9	0.00005	25
50m*50m	$69.44*10^{-15}$	70.4	0.00002	4
100m*100m	$34.72*10^{-15}$	35.2	0.00001	1

One approach is to continue to use the dual porosity model in which the number of matrix blocks associated with a fracture cell becomes less than one. This presents difficulties in identifying the appropriate value of fracture pressure to use as a boundary condition for solving the matrix meshes. Pressure gradients within the fracture network across the dimensions of very large matrix block can be significant, resulting in asymmetric expulsion of gas from a symmetrically shaped matrix block.

Another, and preferable, approach, is to model the system with a single porosity model in which the matrix blocks are discretized in the primary mesh, and the fractures are dealt with explicitly. Using a finite element approach, these fractures can then conveniently be modelled using one-dimensional elements. The case to be made for explicitly modelling fractures is strengthened by the observation that the permeability of the fracture continuum steadily decreases as the matrix block size is increased, and the contribution to the overall reservoir permeability made by the matrix becomes significant. Eventually this contravenes the basic assumption of the dual porosity model, namely that bulk fluid flow takes place only via the fracture network.

Casual inspection of Figures 4.42 and 4.43 strengthens the intuitive notion that the degree of pressure draw down in the fracture cells is greatest for the largest matrix block dimension and least for the smallest dimension. This is simply because the total volume of gas exposed to fractures increases as the size of the block decreases. In addition, gas exists at ever greater distances from the fractures as the matrix block size increases and the larger matrix blocks therefore experience longer periods of transience.

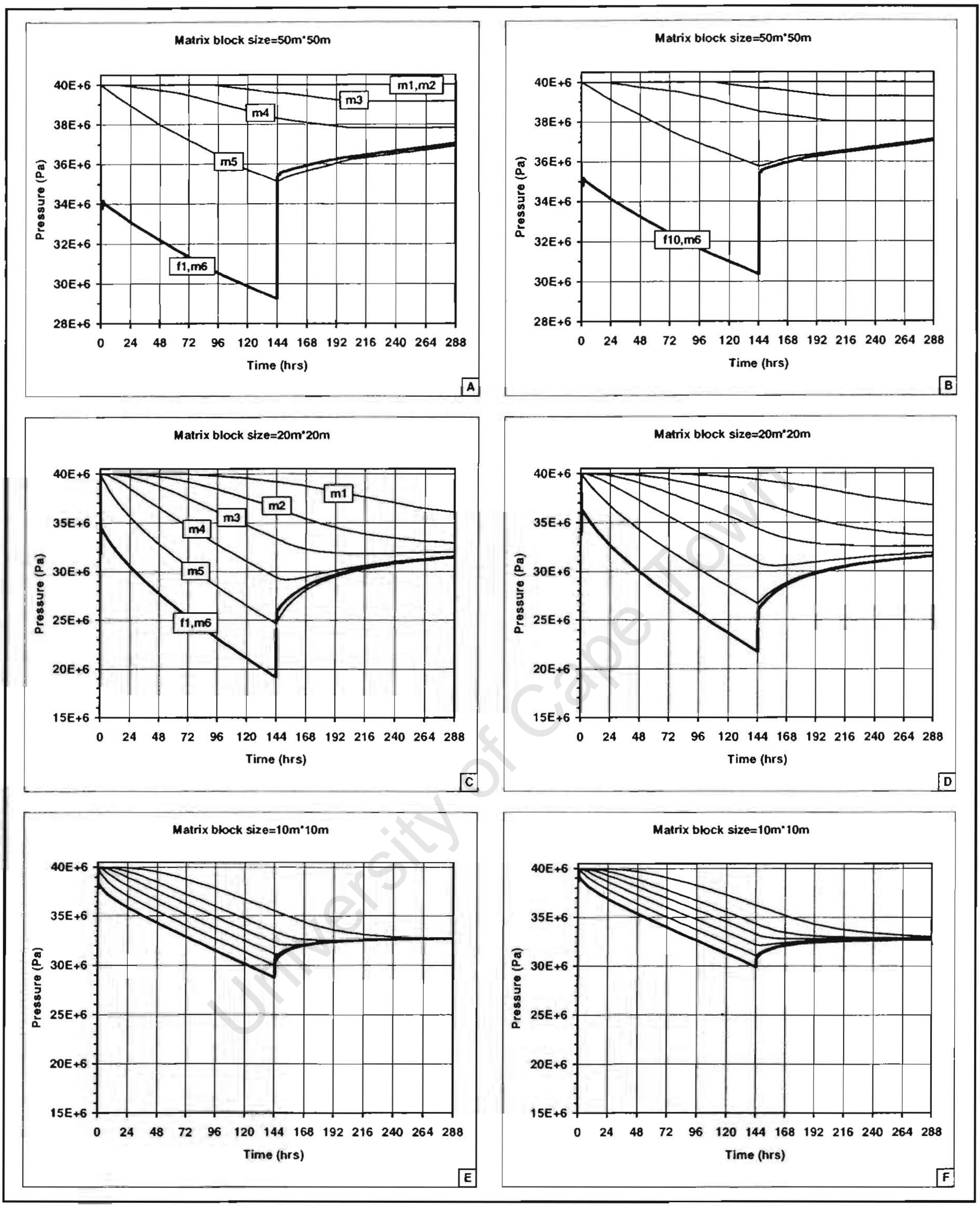

Figure 4.42: *Pressure response in the fracture network and matrix blocks through a 6 day draw down period followed by a 6 day build up period of a dual porosity reservoir. Three different pairs are presented corresponding to matrix block sizes of 50m*50m (diagrams A and B), 20m*20m (diagrams C and D) and 10m*10m (diagrams E and F) respectively. For each pair, the diagram on the left corresponds to the first fracture cell (f1) and the nodes (m1 to m6) of its associated matrix cells, while the diagram on the right corresponds to the last fracture cell and the nodes of its associated matrix cells.*

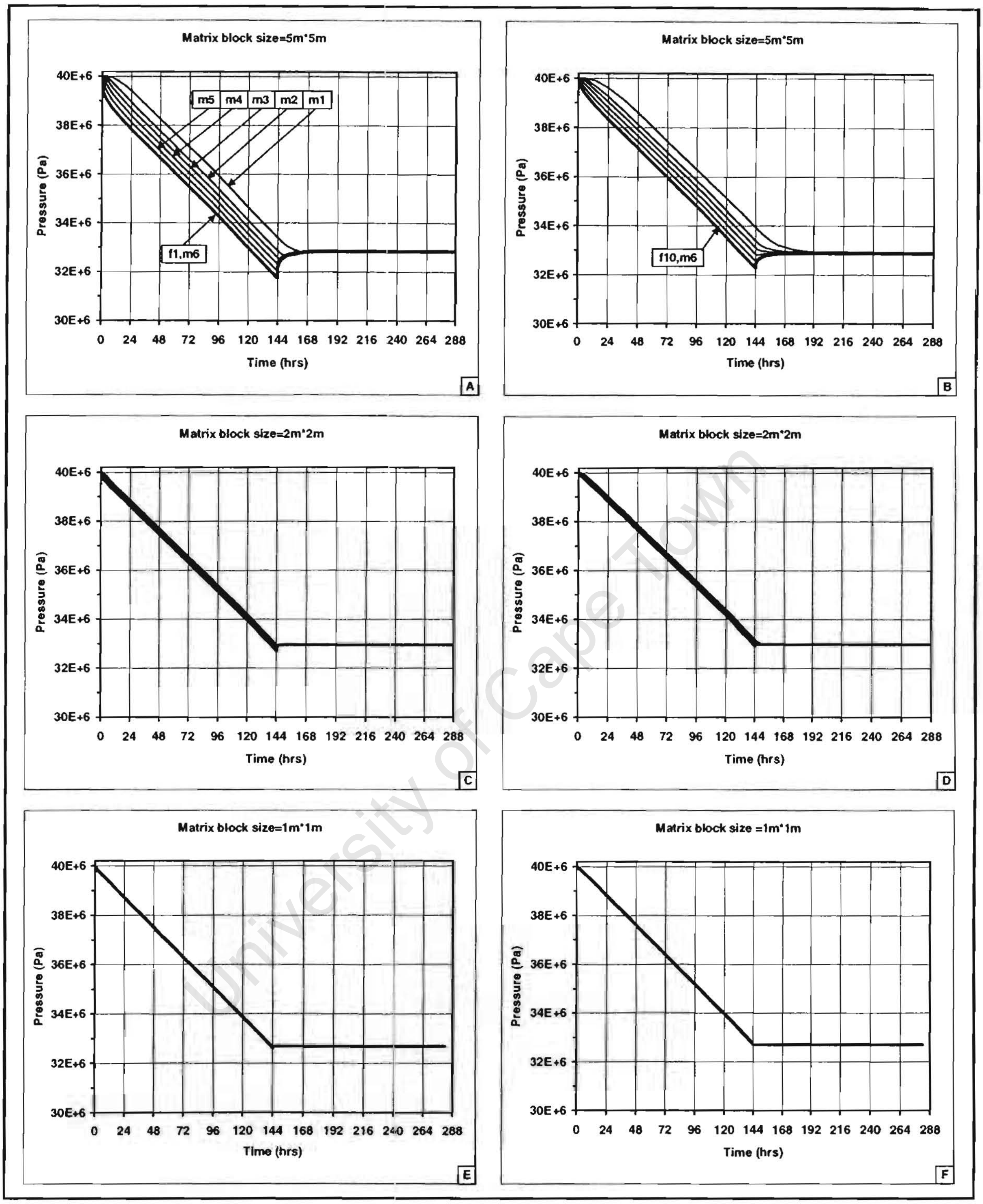

Figure 4.43: *Pressure response in the fracture network and matrix blocks through a 6 day draw down period followed by a 6 day build up period of a dual porosity reservoir. Three different pairs are presented corresponding to matrix block sizes of 5m*5m (diagrams A and B), 2m*2m (diagrams C and D) and 1m*1m (diagrams E and F) respectively. For each pair, the diagram on the left corresponds to the first fracture cell (f1) and the nodes (m1 to m6) of its associated matrix cells, while the diagram on the right corresponds to the last fracture cell and the nodes of its associated matrix cells.*

The pressure gradient across the fracture network is greatest in the case of the largest matrix blocks. This is due to the inverse relationship that exists between matrix block size and the permeability of the fracture continuum.

In the example for which the matrix blocks have dimensions of 50m (Figure 4.42, diagrams A and B), transient effects dominate. By the end of the 12-hour period, the innermost two nodes of the matrix blocks throughout the reservoir have not begun to respond to the pressure drop induced at the block boundary. A reservoir with this block size would therefore necessarily be modelled using a dual porosity approach that can honour transient effects. Similar observations apply to the next two examples in which the matrix block dimensions are assumed to be 20m (Figure 4.42, diagrams C and D) and 10m (Figure 4.42, diagrams E and F) respectively.

When the matrix block size is further reduced to a dimension of 5m, (Figure 4.43, A and B), the pressure gradients that exist within the matrix block are reduced significantly. The modelling of such a reservoir still requires the dual porosity approach, although the transient effects are less important. As the matrix block size is reduced further to 2m (Figure 4.43, diagrams C and D) and then to 1m (diagrams E and F), the reservoir begins to behave more as a single porosity reservoir.

For matrix block sizes of 1m and less, the modelling of the reservoir can be accomplished using a single porosity model for which the appropriate permeability is that of the matrix and the appropriate porosity is the weighted average of those of the matrix and the fracture network. The weighting of the porosity becomes necessary because the value of the fracture porosity becomes comparable with that of the matrix as the matrix block size decreases. The weighting of the permeability is generally not necessary because the fracture permeability increases as the matrix block size decreases and the fractional contribution made by the matrix to the overall permeability consequently decreases.

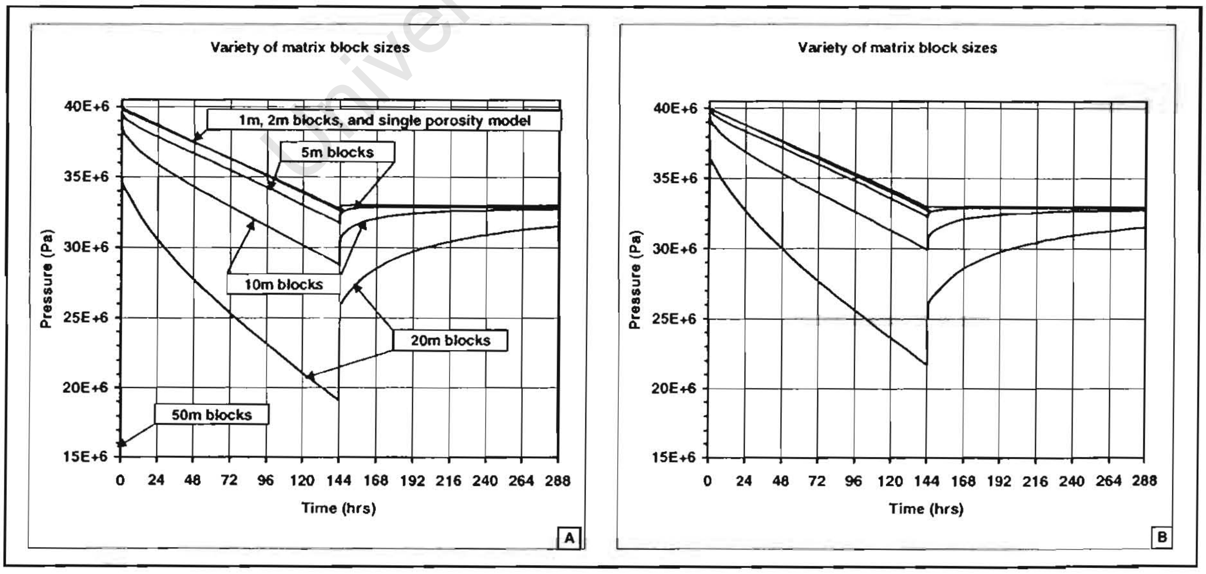

Figure 4.44: *Pressure response in the first (diagram A) and last (diagram B) fracture cells as a function of time through a 6 day draw down period followed by a 6 day build up period from a dual porosity reservoir. Different curves indicate the responses for different matrix block dimensions. All matrix blocks are square.*

Summary

Some of the results presented in the previous section are summarised in Figure 4.44. The pressure profiles in the first (diagram A) and last (diagram B) fracture cells for all the matrix block sizes considered in this study are consolidated. The responses from reservoirs characterised by square matrix blocks with dimensions of 1m and 2m are practically indistinguishable from that of the single porosity model. The dual porosity nature starts to become evident when the matrix block size is increased to 5m and is most significant for matrix block sizes of 10m and 20m. When the matrix block size reaches 50m, the reservoir is unable to sustain the imposed flow rates.

4.3.5 Numerical results showing the effect of matrix block shape

The shape of the matrix blocks can be expected to have a significant impact on the performance of the reservoir as inferred in Sections 4.2. Additionally, those matrix shapes that are not symmetric introduce anisotropy into the fracture continuum permeability that is a function of the orientation of the blocks. Matrix block shapes examined in this section include the square, the rectangle (in two orientations), the 45° right angled triangle, the acute angled triangle, the ribbon that extends along the length of the reservoir and the anisotropic square. All blocks encompass the same volume, namely 100m^3, except the ribbon, which encompasses 10000m^3. The matrix block parameters are identical to those discussed in Section 4.2. The physical properties that must be assigned to the fracture network are affected by the matrix block shapes as listed in Table 4.13.

Table 4.13: *Fracture network properties as a function of matrix block shape.*

Matrix block shape	Matrix block dimensions (m)		Number of matrix blocks per fracture cell	Fracture network permeability (*10^{-15}m^2)		Fracture network porosity (fraction)
	x-comp.	y-comp.		x-comp.	y-comp.	
Square	10	10	100	347.20	347.20	0.000100
Rectangle	20	5	100	694.38	173.61	0.000100
Rectangle	5	20	100	173.61	694.38	0.000100
45° right triangle	14.142	14.142	100	491.03	491.03	0.000121
14° right triangle	28.285	7.071	100	982.02	245.51	0.000161
Ribbon	1000	10	10	0.00	347.20	0.000050
Anisotropic squ.	10	10	100	347.20	347.20	0.000100

It has been assumed that the right angled triangular matrix blocks are oriented such that the sides at right angle to each other are parallel to the x - and y -axes of the reservoir and that in the case of the acute angled triangle, the longer of these two sides is aligned parallel to the x -axis (Figure 4.45). The x - and y -components of the fracture network permeability are then determined by

$$k_x = \frac{k_{f,x} w_y}{w_y + l_y} + \frac{k_{f,\alpha} w_\alpha}{w_\alpha + l_y \cos\alpha} \cos\alpha \text{ and } k_y = \frac{k_{f,y} w_x}{w_x + l_x} + \frac{k_{f,\alpha} w_\alpha}{w_\alpha + l_y \cos\alpha} \sin\alpha , \qquad (4.54)$$

where $k_{f,x}$, $k_{f,y}$ and $k_{f,\alpha}$ are the permeability values of individual fractures oriented parallel to the x-axis, the y-axis and a direction that subtends an angle α with the x-axis, respectively. All other parameters are as illustrated in Figure 4.45.

It is noteworthy that changing the shape of the matrix blocks can cause the permeability of the fracture system to vary over a large range, despite the fact that all the matrix blocks (except the ribbon) occupy the same volume (Table 4.13). The degree of anisotropy caused by the orientation effects of non-symmetrically shaped blocks is also fairly large. Additionally, the fracture network porosity is affected by the matrix block shape, but not to anywhere near the extent that the permeability is.

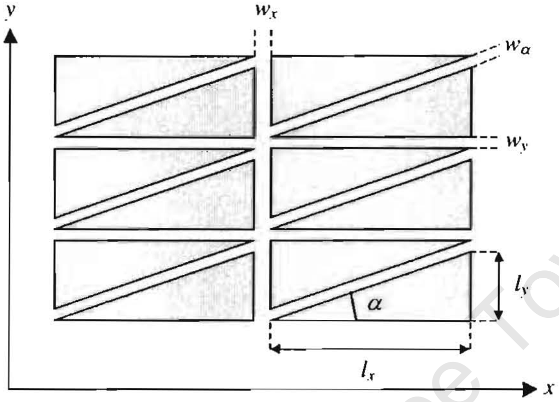

Figure 4.45: *Orientation of triangular shaped matrix blocks.*

It has been assumed that in the case of the ribbons, these are aligned parallel to the x-axis of the fracture network. The anisotropic matrix block is assumed to have an anisotropy of $\varphi = 0.5$, i.e. $k_{my} = 0.5k_{mx}$. Anisotropy in the matrix does not affect the properties of the fracture network.

Square and rectangular matrix blocks. The results of the modelling of fractured reservoirs built up of square and rectangular matrix blocks are presented in Figures 4.46. The pressure profiles in the first and last fracture cells (f1 and f10) are presented together with the profiles at each of the matrix nodes. In the first of these figures, diagrams A and B show the results for the use of the base case square matrix blocks. The next two pairs of diagrams illustrate the results for the use of rectangular matrix blocks, with the blocks orientated parallel (C and D) and perpendicular (E and F) to the direction of elongation of the reservoir respectively.

A striking feature is the difference in the pressure distribution within the matrix blocks as a function of time for the square blocks on the one hand and for the rectangular blocks on the other with the pressure gradient being significantly lower in the case of the rectangular blocks. This is because the surface area for a given volume is greater for the rectangle than what it is for the square. In addition, the greatest distance that any particle of gas can be located from the edge of the rectangular block is half of what it is in the case of the square block.

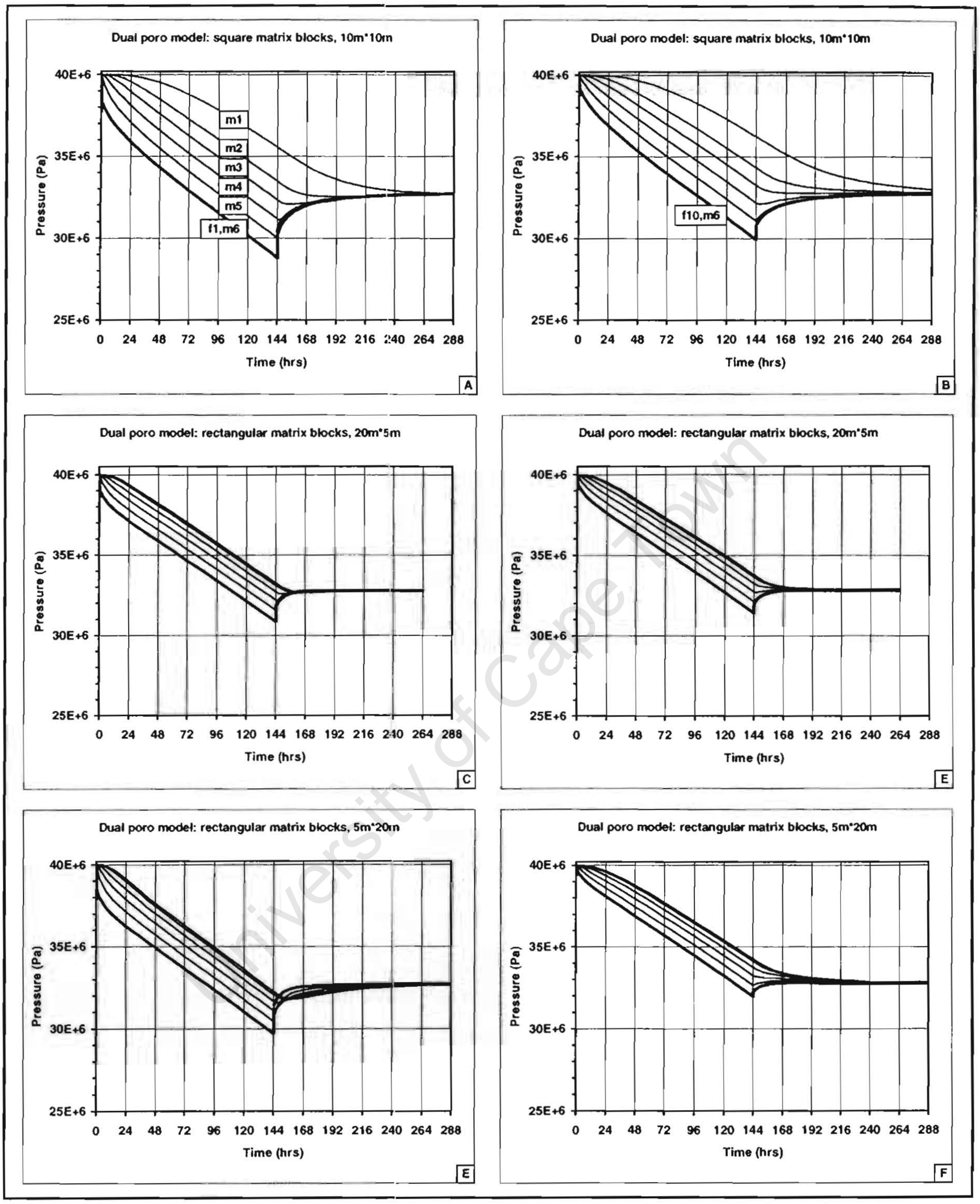

Figure 4.46: *Pressure response in the fracture network and matrix blocks of a dual-porosity reservoir. The three pairs correspond to different matrix block shapes, namely, 10m*10m square blocks (A and B), 20m*5m rectangular blocks orientated parallel to the direction of elongation of the reservoir (C and D) and the same rectangular blocks orientated at right angles to this direction (E and F). For each pair, the diagram on the left corresponds to the first (f1) and that on the right to the last (f10) fracture cells and the nodes of their associated matrix cells.*

From a comparison between diagrams E and F of Figure 4.46 on the one hand, with diagrams C and D on the other, it is clear that the pressure gradient from one end of the fracture network to the other is considerably greater when the matrix block is oriented perpendicular to the direction of elongation of the reservoir. This is due to the way in which the orientation of the rectangular block influences permeability anisotropy of the fracture network. In the case of the transversely oriented matrix blocks, the reversal of flow direction between the matrix block and the fracture network that occurs in the first fracture cell after the well has been shut in is significant while this is not the case for the parallel orientation. This is partly a consequence of the large pressure gradient established across the fracture network in the case of the former. Clearly both the shape and the orientation of the matrix block affects the response of the reservoir.

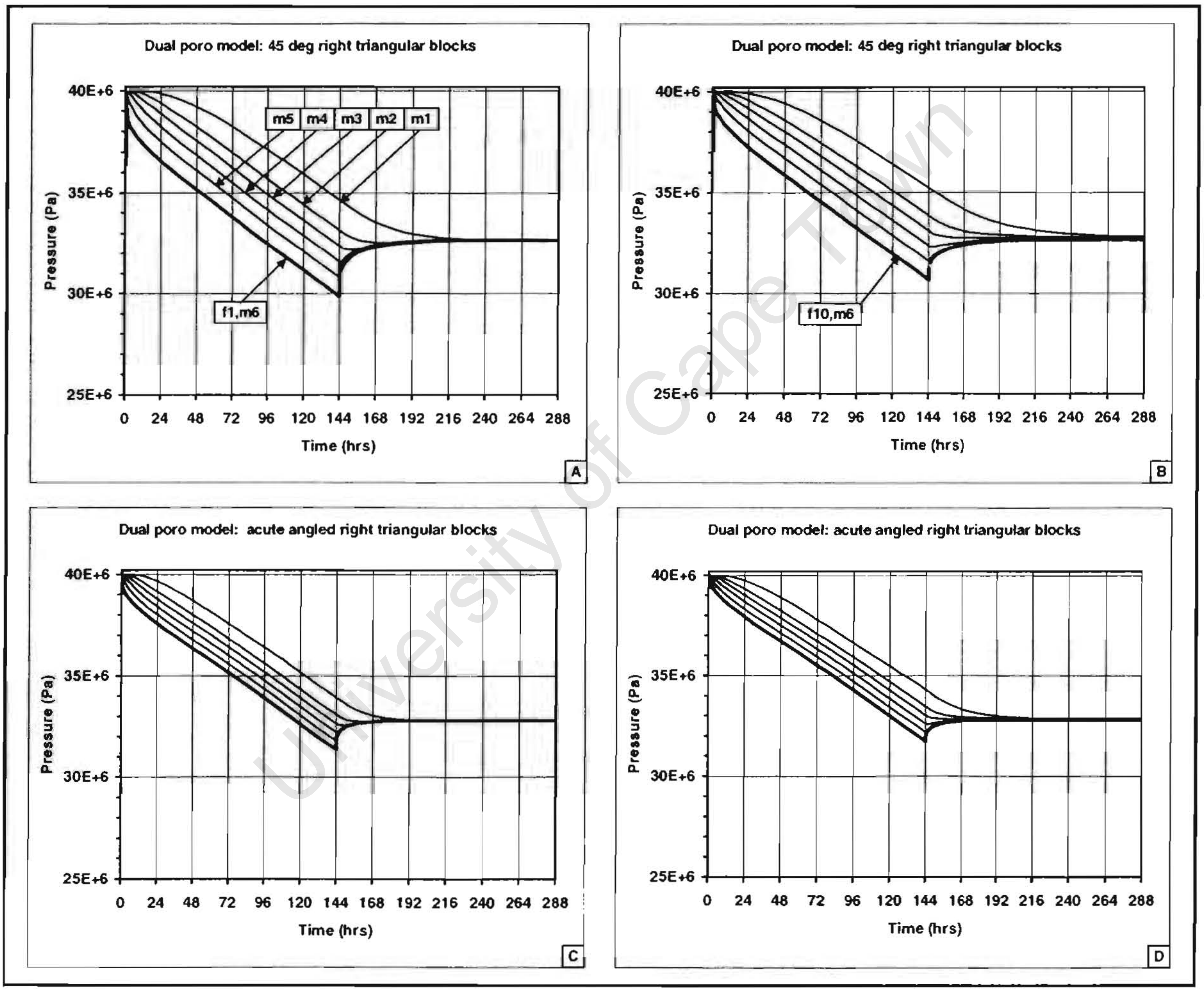

Figure 4.47: *Pressure response in the fracture network and matrix of a dual porosity reservoir. Two different pairs are presented corresponding to different matrix block shapes, namely, 45 degree right triangles (diagrams A and B) and acute angled right triangles (diagrams C and D). For each pair, the diagram on the left corresponds to the first (f1) and that on the right to the last (f10) fracture cells and the nodes of their associated matrix cells.*

Triangular matrix blocks. In Figure 4.47 the results of using the two triangular shaped matrix blocks are shown. The pressure responses within the matrix blocks are quite different for the two respective shapes, with the smaller gradient being experienced in the case of the acute angled triangle. Due to the high fracture permeability associated with the triangles, the pressure gradient across the fracture network is very small in both cases, but particularly so in the case of the acute angled triangle. The pressure gradients within the matrix cells and the degree of draw down in the fracture network are lower for both triangular shapes when compared with the reference square.

Ribbon and anisotropic square shaped matrix blocks. The pressure responses for the examples in which the matrix blocks are ribbons and anisotropic squares are shown in Figure 4.48. The example with ribbons (A and B) experiences the greatest draw down in the fracture network, and the greatest pressure gradient in the matrix blocks of any of the shapes considered here. The response when the matrix blocks are anisotropic squares (C and D) closely resembles that of the ribbon example and represents something intermediate between the ribbon and the reference case.

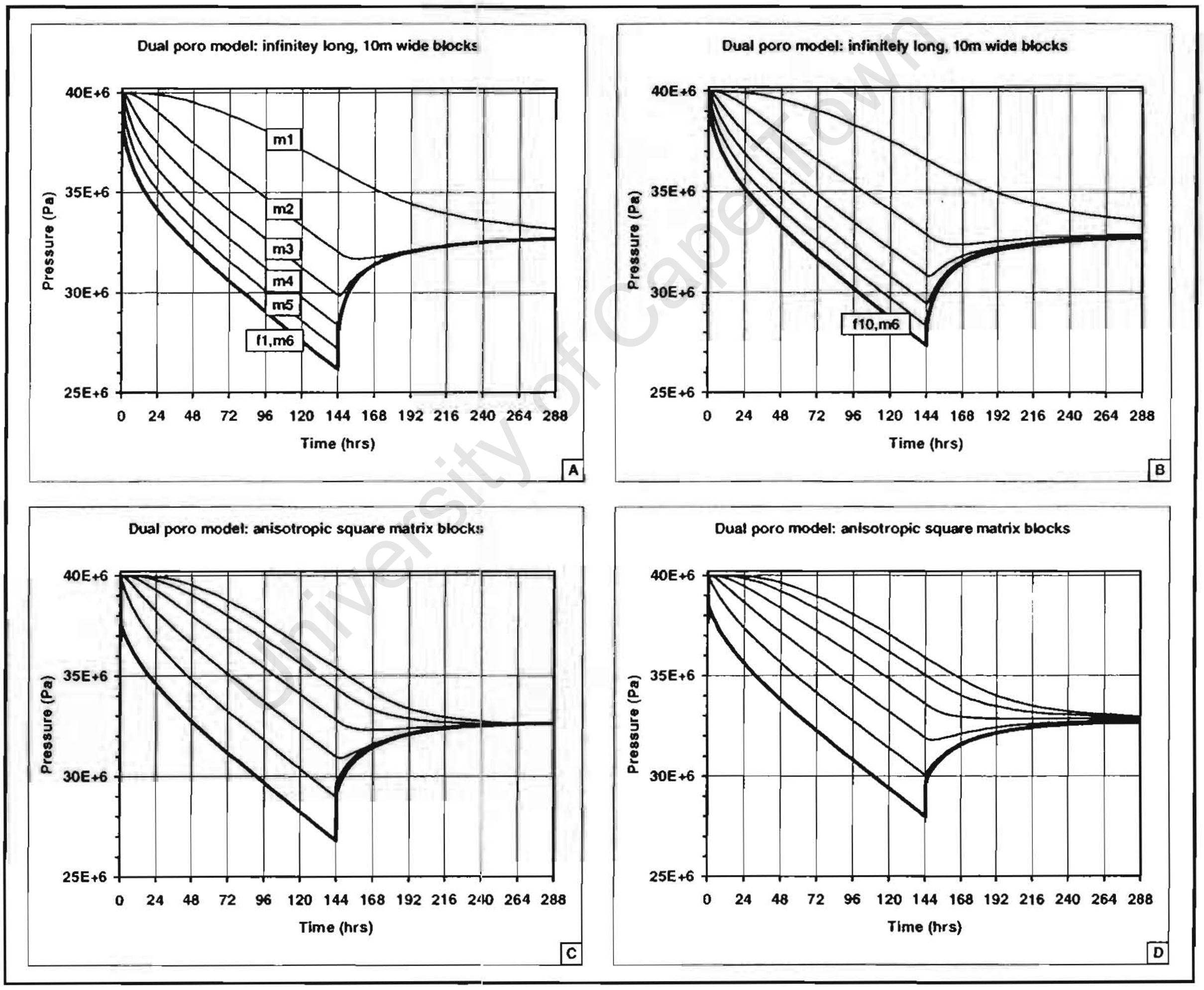

Figure 4.48: *Pressure response in the fracture network and matrix of a dual porosity reservoir. Two pairs of diagrams corresponding to different matrix block shapes, namely, 10m wide ribbon shaped blocks lying parallel to the direction of orientation of the reservoir (diagrams A and B) and 10m*10m square blocks with anisotropic matrix permeability. For each pair, the diagram on the left corresponds to the first (f1) and that on the right to the last (f10) fracture cells and the nodes of their associated matrix cells.*

Summary

In Figure 4.49, the fracture network pressure is shown for the first and last fracture cells (f1 and f10) for each of the matrix block shapes as a function of time. Different responses result from the use of different geometric shapes, not only in terms of the extent of the draw down, but also in the shape of the draw down and build up curves. In the first fracture cell, the order of increasing degree of pressure draw down is as follows:

1) acute angled triangle
2) rectangle oriented parallel to reservoir extension
3) 45 degree triangle
4) rectangle oriented perpendicular to reservoir extension
5) isotropic square (base case)
6) anisotropic square
7) ribbon

In the final fracture cell, the 45 degree triangle shifts to the top of the list. This changing of the ordering is primarily a consequence of the difference in the fracture permeability that alters the pressure gradient across the fracture network.

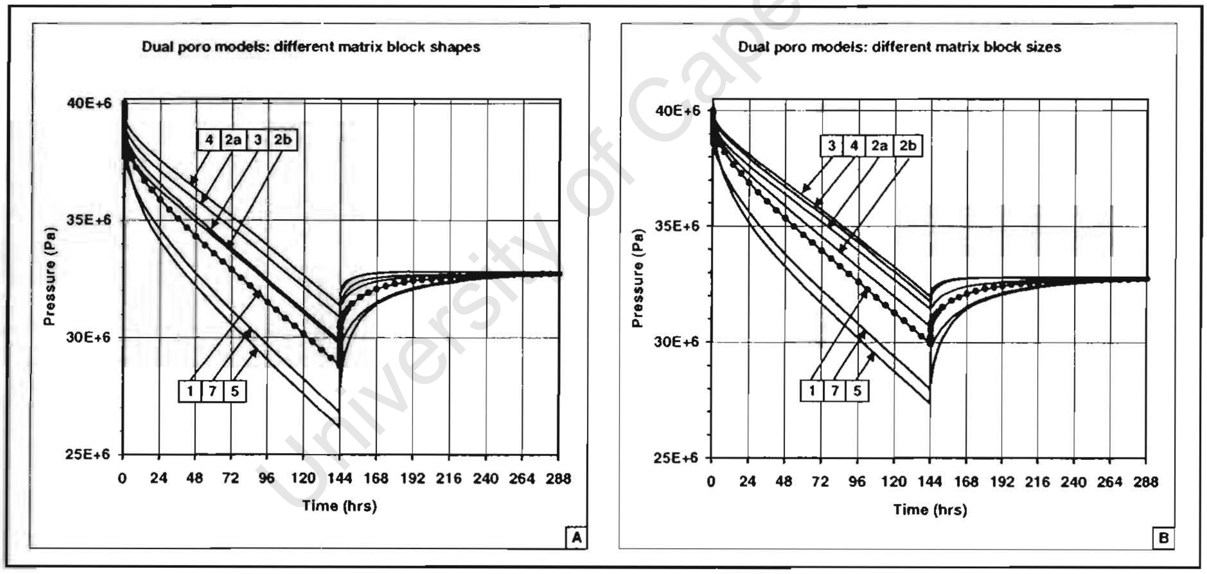

Figure 4.49: *Pressure response in the first (diagram A) and last (diagram B) fracture cells as a function of time through a 6 day draw down period followed by a 6 day build up period from a dual porosity reservoir. Different curves indicate the responses for different matrix block shapes; 1 is a 10m*10m square, 2a is a 20m*5m rectangle oriented parallel to the direction of elongation of the reservoir, 2b is a 5m*20m rectangle oriented perpendicular to the direction of elongation of the reservoir, 3 is a 45 degree right angled triangle, 4 is a 14 degree right angled triangle, 5 is a 10m wide infinitely long strip oriented parallel to the reservoir's direction of elongation, and 7 is a 10m*10m anisotropic ($\varphi = 0.5$) square.*

Conclusions

- The algorithms developed in preceding sections and chapters and implemented in a finite element program have been successfully applied to the modelling of a fractured gas reservoir.
- The results presented in this section have been tested for accuracy through a process of systematic refinement of the primary mesh.
- The finite element code developed for this purpose is able to accommodate, and replicate the effects of variations in all the important components of a fractured reservoir, namely matrix block size, shape, orientation, permeability and anisotropy and fracture porosity, permeability and anisotropy under fairly severe transient but also under pseudo-steady state flowing conditions.
- In a fractured reservoir subjected to changing flowing conditions in the wells, the processes taking place in the fracture network and in the matrix blocks can become complex, and numerical methods developed in this study are most suitable for understanding the behaviour of such a reservoir.
- The shape of the matrix blocks in a fractured reservoir can have a far greater influence on the overall performance of the reservoir than is generally assumed.
- As the matrix permeability of a fractured reservoir is changed from a very low to a very high value, the reservoir performance goes through 5 distinct phases, from single porosity behaviour in which the fracture properties dominate, to dual porosity behaviour dominated by transient effects, to dual porosity behaviour with limited transient effects, to single porosity behaviour in which the permeability of the fractures and the porosity of the matrix dominate, to single porosity behaviour in which the permeability of both the fractures and the matrix and the porosity of the matrix dominate.
- The value of permeability at which the transition from one phase to the next takes place is affected by the size of the matrix blocks, with the transitions taking place at higher values of permeability for the larger sized matrix blocks.

4.4 Reservoir characteristics and model selection criteria

In this section, practical guidelines are given for modelling fractured reservoirs. Different modelling approaches are required for different reservoir characteristics, determined primarily by matrix block size and matrix permeability. From the results presented in Sections 4.2 and 4.3, it is possible to define 'domains', characterised by combinations of matrix permeability and matrix block size, for which different approaches to the modelling process are required (Figure 4.50). Matrix block dimensions are shown to vary over the extremely wide range of 0.01m to 10000m in this illustration. Likewise the matrix permeability spans 11 orders of magnitude, from $10^{-22}m^2$ to $10^{-12}m^2$ (0.0000001mD to 1000mD).

Domain A: ***The dual porosity domain***: Within the elliptical region illustrated in Figure 4.50, the fracture network and the matrix both play important roles in the dynamic behaviour of the reservoir. At any point within this domain, the combination of matrix permeability and block size is such that dual porosity behaviour is likely to occur and must be honoured by the modelling method. This domain can be refined by further division into two sub-domains. Within sub-domain A1, the ratio of matrix permeability to block dimension is such that large pressure gradients exist within the matrix blocks and the modelling process must be capable of honouring transient effects. In reservoirs with properties that fall within sub-domain A2, characterised by smaller matrix blocks and higher matrix permeability than sub-domain A1, pseudo-steady state conditions are expected to be established rapidly, and the rigorous modelling of transient effects is less important.

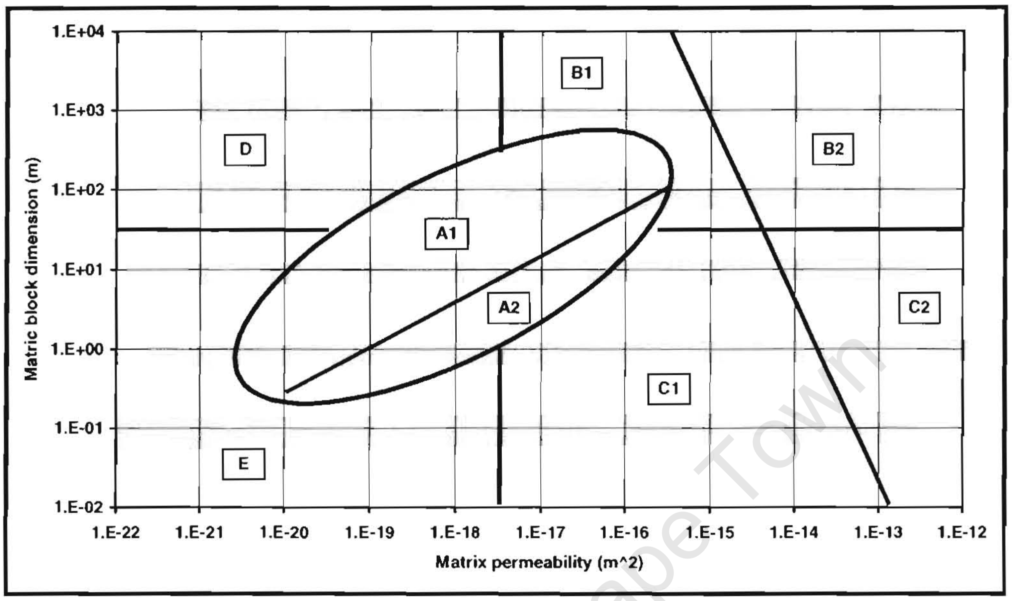

Figure 4.50: *Matrix block size and permeability domains for which different modelling approaches are appropriate.*

Domain B: ***Large matrix block size and high matrix permeability***: In this domain, the relative importance of the fracture network has diminished, due to the sparseness of fractures and the high matrix permeability, to the point where bulk flow through the reservoir may no longer occur exclusively via the fracture network. Significant transport of fluid occurs on a bulk scale through the matrix, and the fractures provide secondary, but very important conduits for the fluid. Such a reservoir can be modelled as a single continuum, to which has been assigned the porosity of the matrix material and a value of permeability which depends on further subdivision of the domain. For reservoirs falling into sub-domain B1, the single porosity continuum should be assigned the permeability of the fracture network. In sub-domain B2, the matrix permeability is comparable with that of the fracture network in magnitude, and the appropriate permeability for the single porosity continuum model is a weighted sum of the matrix and the fracture network permeability values. Fractures can also be treated as an enhancement to the matrix properties, or may be modelled explicitly.

Domain C: ***Small matrix block size and high matrix permeability***: The smaller the block size and the greater the matrix permeability becomes, the quicker the matrix and fracture pressures will equalise. The reservoir can be adequately modelled with a single continuum to which is assigned the permeability of the fracture network if the reservoir characteristics fall within sub-domain C1, or a weighted average of the fracture and matrix permeability values for a reservoir with characteristics falling into sub-domain C2. Likewise, the appropriate porosity is either that of the matrix material or a weighted average of the matrix and the fracture porosity values with the distinction dependent upon the fracture spacing. Generally, the pore volume occupied by the fractures is small relative to that associated with the matrix. However, when the fracture density becomes sufficiently large, the fracture porosity as a percentage of the overall porosity may reach significant values.

Domain D: ***Large matrix block size and low matrix permeability***: As the matrix block size is increased, so the contribution from the matrix material declines and this is accentuated when the matrix permeability has a low value. In this domain, production is almost exclusively controlled by the fracture properties with only a minor contribution attributable to the matrix. However, because this domain is characterised by widely spaced fractures, the overall porosity, (and possibly permeability) of the fracture network is so low that the reservoir is unlikely to be commercially exploitable.

Domain E: ***Small matrix block size and low matrix permeability***: In this domain, the fractures play a dominant role, and without the fracture network, the rock could not be considered a viable reservoir for commercial development. The reservoir can be modelled with a single continuum, to which the properties of the fracture network are assigned. The fracture porosity can be modified to account for contribution from the matrix.

CHAPTER 5

A CASE STUDY: THE LUCY RESERVOIR

The numerical model developed in previous chapters is applied to simulation of a producing fractured gas reservoir. Two aspects in particular have been evaluated: first, the ability to reproduce accurately both field wide and near well bore effects by appropriate refinement of the mesh; and second, the effectiveness of the dual porosity approach.

At the time of writing, the reservoir, referred to for the purposes of this thesis as the 'Lucy' reservoir, is in production and certain information relating to the reservoir is therefore commercially sensitive. The operator and major equity holder of the asset has granted permission, by way of a confidentiality agreement entered into with the author, that the data presented in this thesis may be utilised for academic purposes, but that no information may be presented that would allow the asset to be identified. In compliance with this agreement, no geographical locations are referred to, the names of geological formations are omitted, and company names and any other information that may lead to identification of the asset are not disclosed.

This chapter begins with a discussion of the geological model from which the numerical simulation model was constructed. The geological model is in the form of a three-dimensional description and the process of reducing it to a two-dimensional problem is outlined. This is followed by an account of the historical production from the reservoir in which the production sequences subsequently used as input to the simulator are described. In the third section, construction of the numerical model is described. The results of the numerical simulation are presented in the next section, including a comparison between recorded and simulated pressures from one of the producing wells and a discussion on the changes that were made to the model. Conclusions are drawn in the final section.

5.1 The static reservoir model

The Lucy reservoir comprises a naturally fractured Cretaceous age carbonate rock with very low matrix permeability. In Figure 5.1, the major faults and the wells are superimposed on a contour map of the depth of the structure below sea level. The geometry of the reservoir has been interpreted using seismic data, data obtained from the two production wells indicated in Figure 5.1 as 'well 1' and 'well 2', and an additional appraisal well, and by making use of a regional data base. The operator of the asset provided the geological interpretation.

The reservoir is a steep northerly dipping monoclinal structure with an east-west trending axis dominated by two important faults. The fault referred to as 'fault 2' in Figure 5.1, forming the southern boundary of the reservoir, is a regional event with very large down-throw to the north, and it is the drag on this fault plane that caused the structural trap to form. Fault 1 is a smaller intra-reservoir antithetic fault with limited down-throw to the south. It forms a dislocation within the reservoir that could affect fluid flow. The gas accumulation is bounded in the north by the top structure dipping below the gas-water contact (GWC) and to the east and west by a combination of structural dip closure and minor faulting. The contour map of Figure 5.1 shows some 500m of vertical closure.

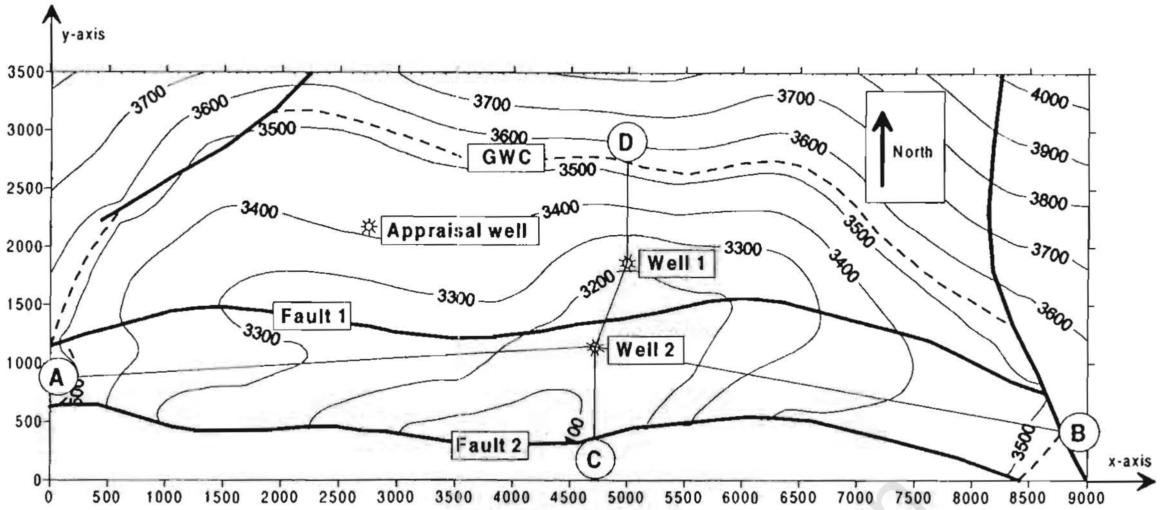

Figure 5.1: *Depth contour map (in meters below sea level) of the top of the Lucy Reservoir structure. Axes are annotated in meters.*

The reservoir interval can be divided in the vertical sense into 8 distinct geologic layers, each with its own distribution of properties. Additionally, there is a separate reservoir located at a shallower depth from which limited production has taken place via well 1. Only the lower reservoir is considered in this study and the contribution from the shallower reservoir to production has been removed. For the purposes of modelling the reservoir as a two-dimensional entity, a distribution for each property has been formed by summing the values of that property over all layers to give

$$\phi_{(f,m)}(x,y) = \sum_{i=1}^{N} \Delta z_i(x,y) * NTG_i(x,y) * \phi_{(f,m)i}(x,y) * Sg_{(f,m)i}(x,y), \text{ and} \qquad (5.1)$$

$$\boldsymbol{k}_{(f,m)}(x,y) = \sum_{i=1}^{N} \Delta z_i(x,y) * NTG_i(x,y) * \boldsymbol{k}_{(f,m),i}(x,y), \qquad (5.2)$$

where $\phi_{(f,m)}(x,y)$ is the porosity distribution of either the fracture network (subscript f) or the matrix material (subscript m), N is the number of vertical layers (in this case, 8), $\Delta z_i(x,y)$ is the gross thickness distribution above the gas-water contact in layer i, $NTG_i(x,y)$ is the net-to-gross ratio distribution in layer i, $\phi_{(f,m),i}(x,y)$ is the porosity distribution of either the fracture network or the matrix material in layer i, $Sg_{(f,m),i}(x,y)$ is the gas saturation distribution of either the fracture network or the matrix material in layer i, $\boldsymbol{k}_{(f,m)}(x,y)$ is the permeability distribution of the fracture network or the matrix material, and $\boldsymbol{k}_{(f,m),i}(x,y)$ is the permeability distribution of the fracture network or the matrix material in layer i.

The result of this summation is a porosity distribution (effectively the net hydrocarbon pore thickness above the gas-water contact) and a permeability distribution (effectively the net permeability thickness product above the gas-water contact) over the entire reservoir section for each of the fracture network and matrix continuums respectively, illustrated as contour maps in Figure 5.2.

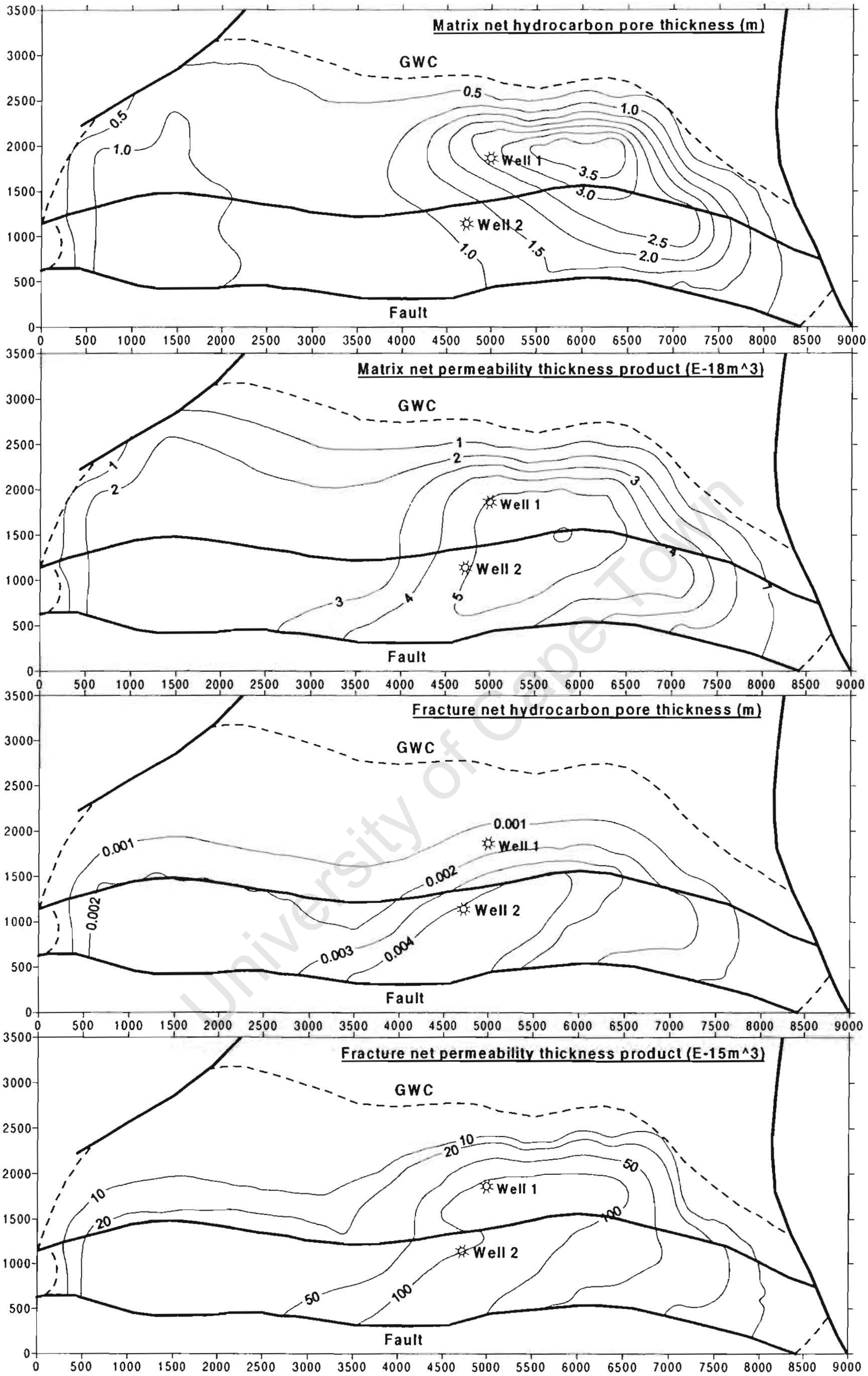

Figure 5.2: *Property distribution contour maps for Lucy Reservoir showing net hydrocarbon pore thickness and the net permeability thickness products above gas-water contact respectively for the matrix material (upper two diagrams) and fracture network (lower diagrams). Axes are in meters.*

The top map of Figure 5.2 shows the net hydrocarbon pore thickness above the gas-water contact for the matrix material. The average porosity of the matrix material throughout the reservoir is approximately 0.04 and the highest value is approximately 0.08. The general trend is that the porosity remains reasonably constant in the south-eastern part of the reservoir and increases in a north-easterly direction in the remainder of the reservoir. The contour map of course reflects both the general porosity trend and variation in net thickness of the reservoir above the gas-water contact. The matrix permeability has been assumed to have a constant value of $0.005*10^{-15}m^2$ throughout. The trend seen in the second map of Figure 5.1 therefore reflects the trend in net reservoir thickness above the gas-water contact. These trends have been established primarily from core and geophysical wireline data collected in the three wells.

Reservoir fracturing was brought about through flexure of the brittle carbonate formation by the tectonic forces that activated the major east-west trending fault belt. The fracture density therefore increases in a southerly direction as the faults are approached. Both the fracture porosity and permeability contour maps shown in the lower two diagrams of Figure 5.2 reflect this trend, overprinted by the net thickness of the reservoir above the gas-water contact. In addition, dynamic information obtained from well 1 suggests that the fracture permeability in the vicinity of this well must be greater than the permeability estimated during the static reservoir modelling process. Hence the fracture porosity and permeability trends differ in this region.

Due to the strongly uni-directional nature of the faulting, the degree of flexure of the reservoir in the north-south direction is far greater than in the east-west direction. For this reason, matrix blocks can be expected to have different dimensions in the two directions. For this work, it has been assumed that the east-west dimensions of all matrix blocks are double their north-south dimensions. The concentration of fractures with a north-south orientation is therefore half of that of fractures with an east-west orientation and consequently, the y-component of the fracture permeability at any point has been assumed to have a value equal to half of that of the x-component permeability. The fracture net permeability thickness product map displayed in Figure 5.2 is that of the x-component permeability.

The interface between the gas and the water has been positively identified in the wells. The line labelled 'gas-water contact' on Figure 5.1 delineates the contact between the gas-water interface and the top of the reservoir. Although the formation extends beyond this limit into the aquifer towards the north, the degree of fracturing diminishes very rapidly in this direction. With relatively spare fractures, if any, in the vicinity of the gas-water contact, fluids would be compelled to move through the matrix material. The very low permeability of the rock matrix, together with the relatively high viscosity of the water, relative to the gas, means that water influx from the north is not likely to be significant. The bounding faults to the south and east, and partly to the west, make the influx of water unlikely, and hence no pressure support from an aquifer has been included in the model. An essential boundary condition equal to zero has consequently been applied along the perimeter of the gas bearing reservoir.

Fluid properties are summarised in Table 5.1. These values have all been derived from accurate laboratory experiments carried out on the produced fluids. Gas 'viscosibility', μb_g, a term used to account for the pressure dependency of viscosity, is defined by

$$\mu_g(P) = \mu_g(P_i)e^{-\mu b_g(P_i - P)}. \tag{5.3}$$

Water compressibility is included to account for expansion of the interstitial water in the pore spaces and is combined with rock compressibility as a term in the expression for total compressibility.

Table 5.1: *Fluid and rock properties for the Lucy Reservoir.*

Parameter	Symbol	Value	Field units	Value	SI units
Gas density (@ P_i)	ρ_g	**21.73**	$lbft^{-3}$	**348.16**	kgm^{-3}
Gas compressibility	c_g	**$86.02*10^{-6}$**	psi^{-1}	**$12.48*10^{-9}$**	Pa^{-1}
Gas viscosity (@ P_i)	μ_g	**0.0415**	cP	**$41.50*10^{-6}$**	Pas
Gas viscosibility	μb_g	**$112.8*10^{-6}$**	psi^{-1}	**$16.36*10^{-9}$**	Pa^{-1}
Water compressibility	c_w	**$3.3*10^{-6}$**	psi^{-1}	**$0.48*10^{-9}$**	Pa^{-1}
Rock compressibility	c_r	**$7.0*10^{-6}$**	psi^{-1}	**$1.02*10^{-9}$**	Pa^{-1}
Initial pressure	P_i	**5674**	psi	**$39.12*10^{6}$**	Pa

5.2 Historical performance

Weekly average historical production rates from the two wells are shown stacked in Figure 5.3. The scale on the lefthand ordinate accurately shows the production expressed in kgs^{-1}, while the scale on the righthand ordinate is an approximation of the equivalent wet gas rate in MMscf/d. Wells produce gas, condensate and, over the period of interest, negligible quantities of water. The flow rates expressed in kgs^{-1} include all fluids flowing from the wells.

The reservoir initially came on stream with well 2 producing at relatively high rates. In week 8, well 1 was brought on stream and well 2 was choked back. Well 1 proved to be the better producer and the bulk of the production was subsequently allocated to this well. Well 2 was shut in for a one week period (week 11) and again for a 5 week period, starting in week 26. During these periods, the choke of well 1 was opened to make up the shortfall. Besides these disturbances, reasonably constant rates were maintained for the two wells up until the end of the period of interest, namely week 49.

Production from the two wells is commingled for export without separation. The offshore platform is visited once and occasionally twice a week, and accurate dead-weight pressure measurements are made at each well head. During the first 27 weeks of production, well head pressure recordings were also made remotely from shore on a continuous basis, but were found to be inaccurate. These measurements were calibrated against the dead weight measurements and adjusted accordingly. Additionally, during the visits, one or both of the wells are production tested, and these results are used for production allocation purposes. The production test involves flowing the well through a test separator for a period of time to obtain accurate flow rates of gas, water and condensate.

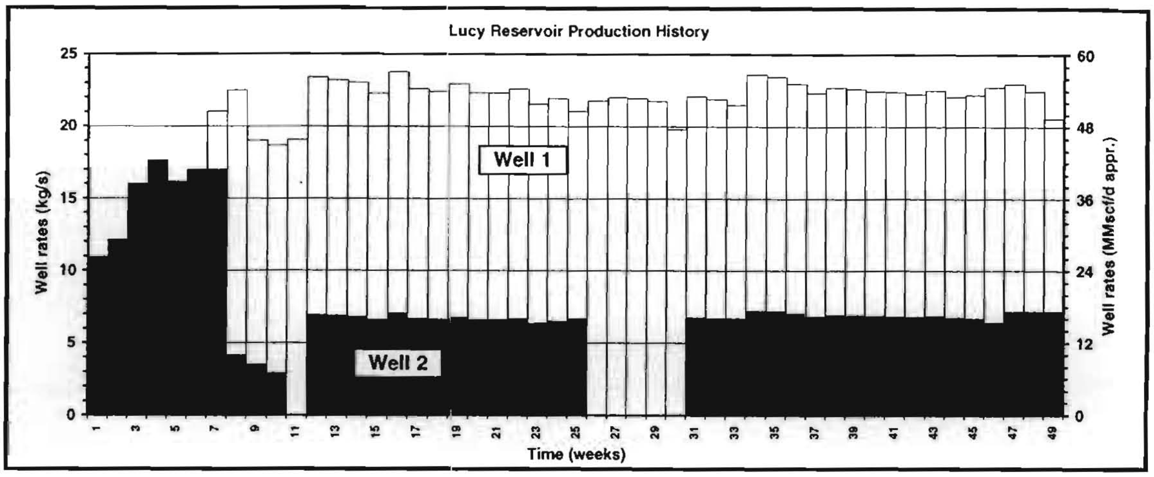

Figure 5.3: *Historical weekly production from the two wells completed in the Lucy Reservoir*

After the sequence depicted in Figure 5.3, a reservoir evaluation test was performed on well 2. This involves flowing the well at a number of different choke settings through the test separator to allow the accurate recording of flow rates. The sequence includes a period during which the well is shut in. Pressure is recorded throughout the test by accurate electronic gauges temporarily installed in the well as close to the formation as possible. The sequence immediately following the end of week 49 incorporating the well test, is illustrated in Figure 5.4.

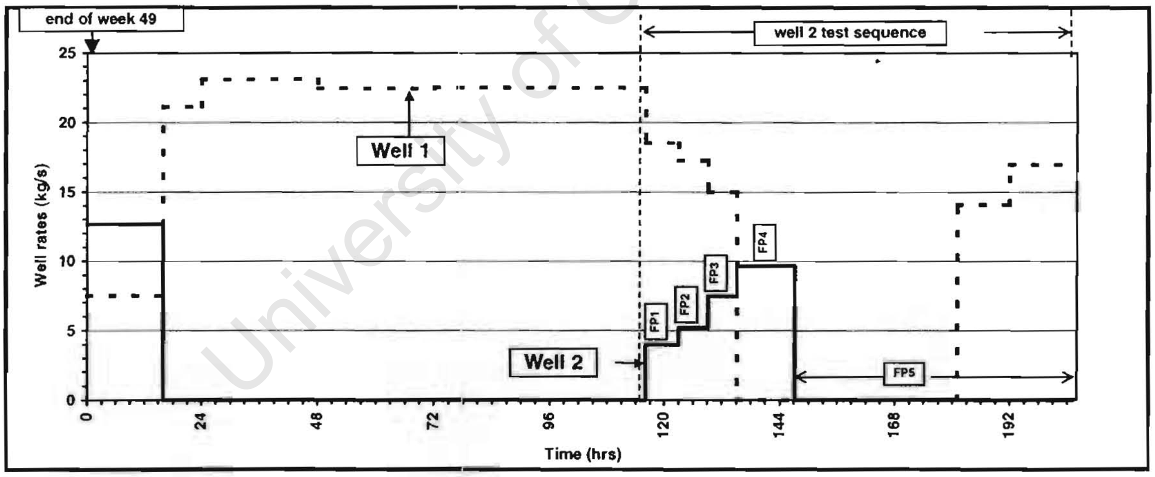

Figure 5.4: *Status of wells before and during the testing of well 2.*

Both wells were initially flowing for a period of 16hrs. Well 2 was then shut in for a period of 100hrs to allow pressure around the well bore to stabilise and to install the pressure gauges. During this time, well 1 was opened up to meet the gas sales contract requirements. Down hole gauges were installed and were operational by a time corresponding to 114hrs in Figure 5.2, marking the start of the test sequence of well 2. During this test, well 1 was kept flowing, initially at changing rates to make up the shortfall in production. Well 1 was then shut in for a period of 46 hours before being brought back on production prior to the end of the well test.

The test sequence of well 2, comprising four flow after flow periods followed by a lengthly shut in, is shown in Table 5.2. The variable status of well 1 during the test of well 2 compromises the analytical interpretation of the well test due to the presence of interference effects.

Table 5.2: *Test sequence for well 2 (refer to Figure 5.4)*

Sequence	Length (hrs)	Flow rate (kgs^{-1})
Flow period 1 (FP1)	6.98	3.97
Flow period 2 (FP2)	6.17	5.23
Flow period 3 (FP3)	6.00	7.48
Flow period 4 (FP4)	12.00	9.65
Flow period 5 (FP5) = build up period	58.06	0.00

5.3 The numerical model

The numerical model has been built with the focus on well 2. The reasons for this are that well 1 was completed in the Lucy reservoir as well as in an overlying reservoir, and although every attempt has been made to remove the limited contribution from the upper reservoir, the well 1 rates are less reliable than those for well 2. Additionally, the reservoir evaluation test carried out on well 2 poses a challenging simulation problem.

The fracture continuum or primary mesh is illustrated in Figure 5.5. In the uppermost diagram, the mesh covering the bulk of the reservoir is shown to be constructed of quadrilateral elements with sides measuring about 500m. The element boundaries have been selected to coincide with important features such as natural boundaries and faults described in Section 5.1, and triangular elements have been used where necessary to conform to the overall shape. In the vicinity of the wells, the mesh becomes progressively more refined. This refinement is limited in the region of well 1, as no attempt is being made to match the bottom hole flowing pressure of this well, and the well is therefore completed in a relatively large element measuring 80m*80m.

Mesh refinement around well 2 is far more gradual, and continues as illustrated in the series of expanded diagrams of Figure 5.5 all the way to the edge of the well bore itself, which is represented by the sides of eight adjoining triangular elements. This allows well flow rates and the bottom hole pressures to be specified directly as boundary conditions, or to be determined directly as output in the normal course of the simulation, as the case may be.

The well has a radius of 31.1cm (12.25in). Away from the well bore, the mesh has been constructed by repeatedly arranging groups of 16 triangles in concentric circles of increasing circumference. The innermost circle of triangular elements extends a distance from the edge of the well bore that is equal to the radius of the well bore itself (15.56cm). Each subsequent circle has a radius equal to double that of the previous circle. This radially symmetric pattern extends to a distance of 160m from the centre of the well, and 160 triangular elements are contained within this radius. Thereafter the symmetry is abandoned as the mesh transforms to fill the reservoir space. A total of 339 elements were needed to describe the reservoir. The simulation was performed using 4 noded quadrilateral and 3 noded triangular elements, resulting in a total of 229 nodes. The mesh was populated with the porosity and permeability distributions illustrated in the upper two diagrams of Figure 5.2.

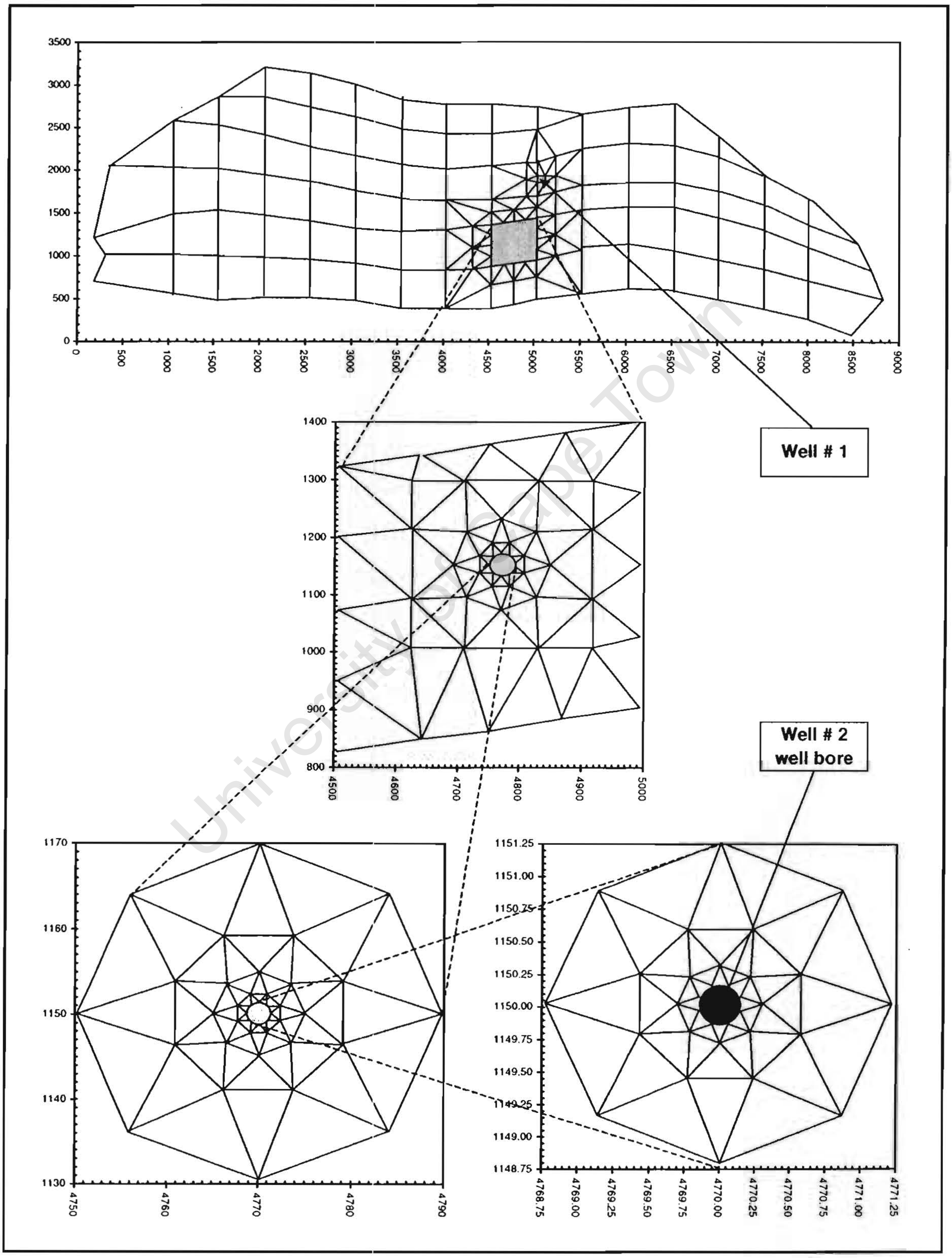

Figure 5.5: *Finite element mesh constructed for simulating the fracture continuum of the Lucy Reservoir. Coordinates are in meters.*

It has been assumed that the matrix blocks are rectangular in shape, with an aspect ratio of 2, and orientated with the long sides parallel to the main fault trends. Matrix block dimensions have been assumed to vary in size according to proximity to the southern bounding fault. Three distinct property sets have been defined (Figure 5.6) and matrix block properties have been assigned to each set (Table 5.3).

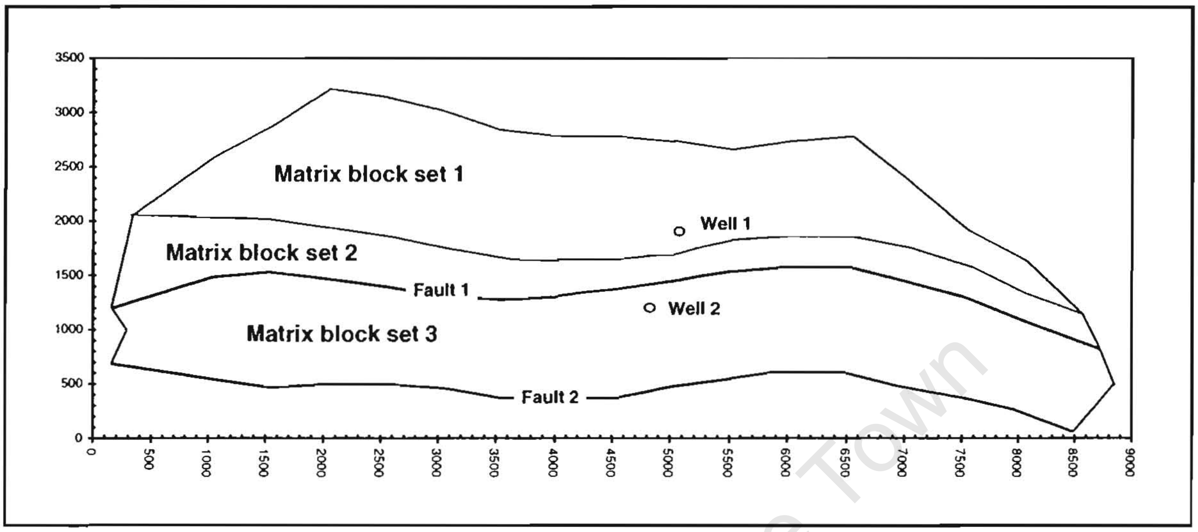

Figure 5.6: *Distribution of matrix block property sets in the Lucy Reservoir. Coordinates are in meters.*

A single string of 5 linear elements has been used to model the representative matrix block associated with each of the primary elements. Nodal spacing has been selected according to the 'equal volume' criterion discussed in Section 4.2.2, tabulated in Table 5.3, and illustrated in Figure 5.7. The secondary meshes have been populated with the porosity and permeability distributions illustrated in the lower two diagrams of Figure 5.2 according to the formulae for converting from two-dimensional to the one-dimensional representation discussed in Section 4.2.1. The string of secondary elements associated with each primary element is in general unique as a result of having to comply with varying matrix properties and matrix block sizes.

Table 5.3: *Dimensions of the matrix blocks and their one-dimensional representations.*

Sequence	Set 1	Set 2	Set 3
Matrix block dimensions (m*m)	40*20	20*10	10*5
Node 1 (m)	0.000	0.000	0.000
Node 2 (m)	3.062	1.531	0.766
Node 3 (m)	5.247	2.624	1.312
Node 4 (m)	7.042	3.521	1.760
Node 5 (m)	8.602	4.301	2.150
Node 6 (m)	10.000	5.000	2.500

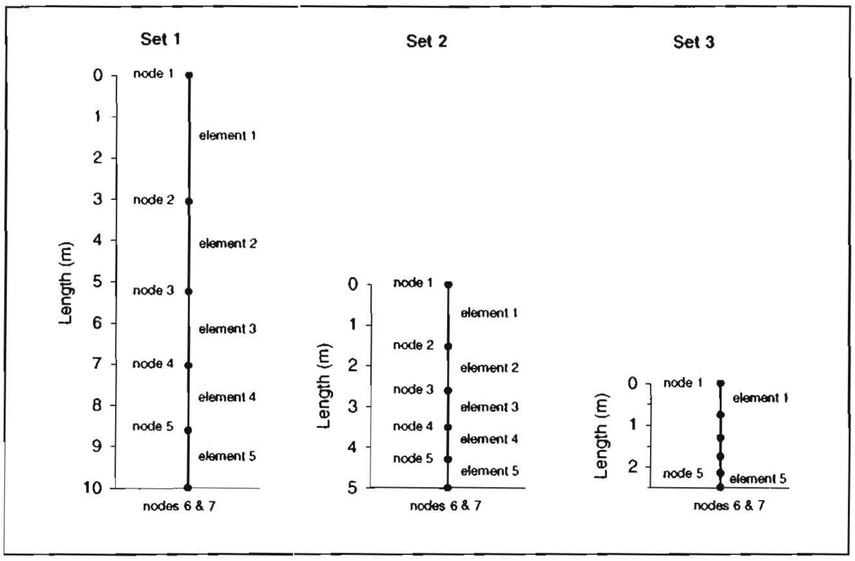

Figure 5.7: *Secondary meshes used for modelling matrix blocks with dimensions 40*20m (set 1), 20*10m (set 2) and 10*5m (set3).*

An extensive investigation involving more than 50 trial simulations was undertaken to determine an optimum set of time stepping parameters. For the simulation of the sequence shown in Figure 5.3, it was found that the maximum time step length that could be accommodated and that would still ensure numerical stability and accurate results was 240s. To provide an additional margin of safety, time steps of 60s were ultimately used. Boundary conditions were specified as weekly average values and therefore time intervals comprising 10080 steps were used. Stringent primary mesh convergence tolerances of 100Pa locally and 1000Pa globally were specified. Secondary mesh time sub-step lengths of 5s were used (12 time sub-steps per time step). The primary mesh was solved using a backward time differencing procedure. A maximum of 7 non-linear iterations was permitted. It was found that with the above group of parameters, convergence to within the specified tolerance levels was always achieved with less than the maximum permissible number of iterations. Simulation of the full sequence illustrated in Figure 5.3 took approximately 60 CPU hours running on a 300MHz Pentium 5 PC.

For the simulation of the reservoir evaluation test sequence shown in Figure 5.4, much smaller time steps were needed to replicate accurately the draw down and build up periods. Each flow period was started afresh with a time interval comprising 100 steps each of length 0.001s. The time step length was thereafter progressively increased by a factor of $\sqrt{2}$ while keeping the number of steps per interval constant at 100, until the step length had reached 6s. Thereafter, the step length was kept constant at 6s and the number of steps per interval increased in increments of 100 until a time interval comprising 600 steps of 6s was reached. Subsequent time stepping was kept at this level until the end of the period was reached. Secondary mesh time sub-stepping was the same as that used in the previous section, while convergence tolerances were halved. The full test sequence illustrated in Figure 5.4 took approximately 15 CPU hours to run on a 166MHz PC.

Control of the simulator was achieved by imposing the appropriate recorded flow rates shown in Figures 5.3 and 5.4. This was achieved for well 1 by specifying internal load conditions for the element in which the well is completed. For well 2, rate control was implemented by specifying concentrated natural boundary conditions at the 8 nodes defining the well bore boundary.

5.4 Simulation results

The well head pressure measurements made during the initial 49 week period have been corrected to down hole conditions using lift performance curves generated for well 2. The difference between well head and bottom hole pressure ranges between 6 and 10MPa depending upon the flowing conditions. These (corrected) recorded pressures are illustrated in Figure 5.8 together with the pressures forecast by the simulator at the 8 nodes defining the well bore margin. There is very good agreement between recorded and simulated pressure values. The greatest difference is in the order of 1MPa and the trends, particularly, are very similar.

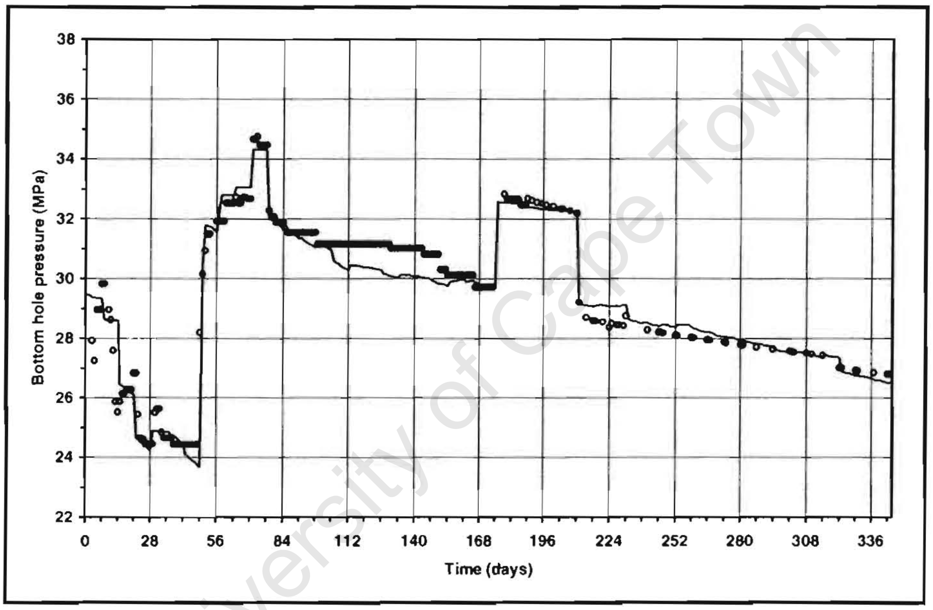

Figure 5.8: *Comparison between recorded (circles) and simulated pressures (continuous line) for well 2 over the period illustrated in Figure 5.3.*

The following changes, in order of decreasing importance, had to be made to the original model in order to achieve this good match.

- In the central part of the field, where the fracture permeability reaches a high value with a maximum of slightly more than $100*10^{-15}m^2$ (Figure 5.2), this value had to be increased significantly to $600*10^{-15}m^2$. This is indicative of the high degree of uncertainty surrounding characterisation of the fracture system. The interference between the two producing wells, evident in the pressure decline recorded at well 2 whilst it is shut in and well 1 is producing (day 175 to 210) suggests that pressure communication between the wells is good, and this requires the presence of a high permeability zone. However, the fracture permeability in the general vicinity of well 2 is likely to be more complex, and this is discussed under the section dealing with the well test.

- The matrix permeability was reduced by a factor of 5. This appears to be a large change for a parameter that is measurable. However, the value used as input to the simulator is, according to equation (5.2), the total permeability-thickness product over the reservoir interval. The need to reduce the value of this parameter may in part be a reflection of the limited vertical extent of the fractures, which results in less matrix being exposed to fractures and therefore a lower value for the thickness over which the permeability-thickness product should be calculated, rather than uncertainty in the value of permeability itself.
- The fracture porosity throughout the reservoir was doubled in value. The requirement to increase the porosity is consistent with the requirement to increase the permeability and suggests a greater fracture width than initially expected.
- The fracture porosity changes with time. This was modelled by increasing the rock compressibility of the fracture continuum to a value approximately three times that shown in Table 5.1, representing marginal closure of fractures as the pressure is reduced.

The draw down is determined primarily by the fracture permeability, and the good agreement between the magnitude of the simulated and recorded pressure values in Figure 5.8, particularly during the first 49 days, suggests that the fracture permeability values are accurate. The magnitude of the pressure during the shut in periods (days 70 to 77 and days 175 to 210) is influenced to a large extent by the porosity of the fracture network, and once again, the good agreement between recorded measurements and simulated results lends confidence to these values. The general rate of decline in pressure over the almost 1 year period is influenced by many factors, although a dominant role is played by the porosity and permeability of the matrix material. Similarity in the trends of the measured and recorded data suggest that these values are accurate. There is some question regarding the accuracy of the recorded pressure values during the period from day 84 to day 168.

In each of the three diagrams presented in Figure 5.9, the pressure profiles in the fracture network are displayed along the traverses A-B and C-D that are shown in Figure 5.1. The three diagrams illustrate the pressure profiles existing at three different times and are discussed individually below.

The uppermost diagram (end of 7th week, or day 49) was selected for display as it is at the end of a period during which well 2 has been flowing at a high rate. The pressure field in the fracture network shows two characteristic features. There is a general decrease in pressure of approximately 2MPa over the entire central portion of the reservoir where the fracture permeability is high. This covers the full extent of traverse C-D and spans the interval from approximately -1000 to +1500m on traverse A-B. This is a consequence of the rapid communication of the pressure facilitated by the high value of fracture permeability. The second feature is the very large degree of draw down (approximately 5MPa) in the immediate vicinity (within 100m) of well 2. The accurate modelling of this requires the use of a very fine local mesh. Well 1 was opened up at the beginning of week 7 and the effect of the limited production from this well is evident as a depression in the pressure profile along C-D, at a distance of approximately +700 to +800m from well 2. The draw down around well 1 is of course not fully replicated in the diagram as the well is completed in an element with dimensions of 80m.

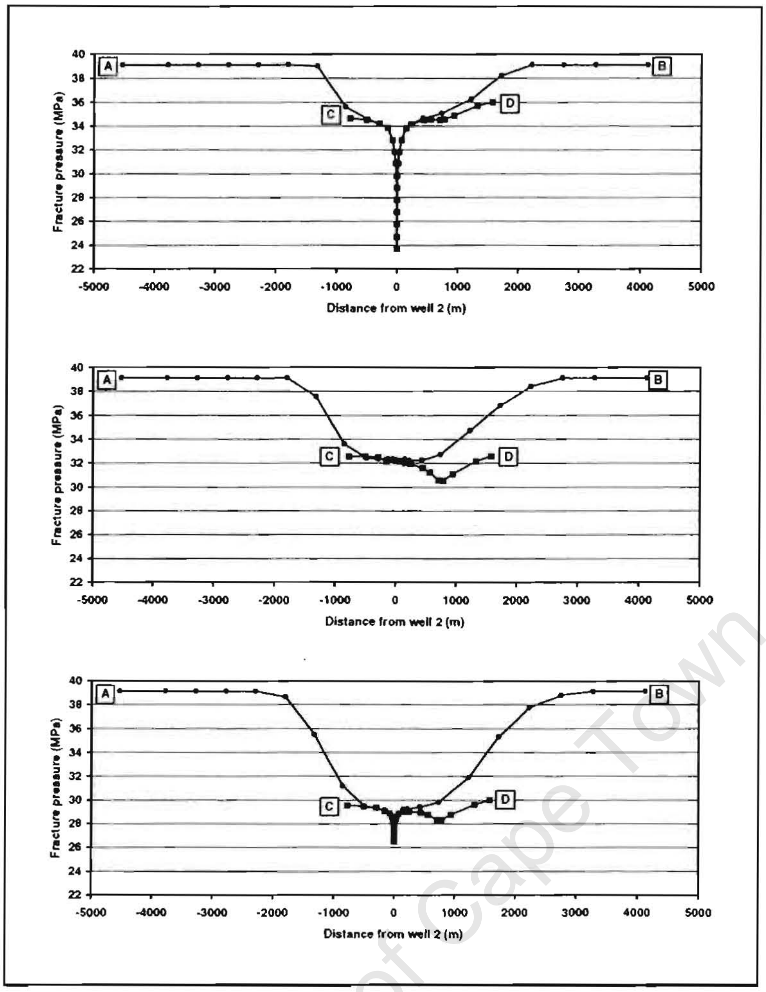

Figure 5.9: *Pressure profiles in the fracture network along the traverses A-B and C-D illustrated in Figure 5.1. The top, centre and bottom diagrams show the status at the end of the 7th week (end of high rate period from well 2), 30th week (end of build up of well 2) and 49th week (end of long, steady flow period) respectively.*

The second diagram shows the status at the end of the 30th week (day 210) which corresponds to the end of a period during which well 2 has been shut in and well 1 has been flowing at very high rates. The deep draw down around well 2 has been eliminated and the draw down around well 1 has become more prominent. The depression in the centre of the field has extended in areal extent. The lowermost diagram shows the status at the end of the modelled sequence (end of the 49th week, or day 343). Both wells have been flowing for a considerable length of time at reasonably constant rates. Limited draw downs are evident around each well. The central depression has increased in magnitude to about 5MPa and pressure decline has extended to distances of -2000 and +3000m from well 2. A large portion of the reservoir still remains at initial pressure.

Two matrix blocks have been selected for further discussion, located at either end of traverse C-D. In the upper diagram of Figure 5.10, the pressure profile existing within the matrix block located at C is illustrated at the three different times discussed in the previous section, namely day 49, day 210 and day 343 respectively.

This matrix block has dimensions of 10m by 5m, and a relatively high value for matrix permeability (approximately $0.8*10^{-18}m^2$ after the history match). At the end of the period of high draw down (curve A), the difference between the pressure at the centre of the block and its edge is approximately 1MPa. After the period of shut in of well 2 (curve B), this has been reduced to about 0.54MPa, and this is maintained to the end of the simulated period (curve C). In the second diagram of Figure 5.10, the pressure profiles in the matrix block located at D are displayed at the same three times. This matrix block has dimensions of 40m by 20m and is characterised by a lower value of permeability than the previous block (approximately $0.2*10^{-18}m^2$ after the history match). The difference between the pressure at the centre of the block and its surface reaches very large values (more than 9MPa). Transient effects dominate and persist throughout the 49 week period. At the end of the 49 week period, the centre of the block is still at initial pressure.

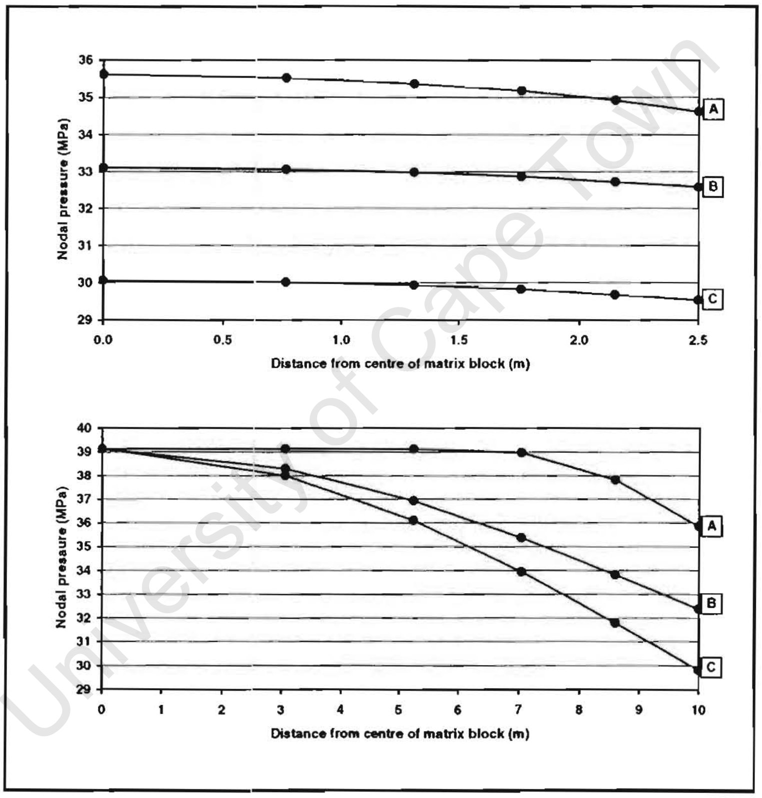

Figure 5.10: *Pressure profiles in two different matrix blocks located at either end of the traverse C-D illustrated in Figure 5.1. The matrix block located at C is illustrated in the upper diagram and the matrix block at position D is illustrated in the lower diagram. In each diagram, the three curves correspond to the status at the end of the 7th week (A), 30th week (B) and 49th week (C).*

A comparison between the recorded and simulated bottom hole pressures for well 2 during the reservoir evaluation test sequence described in Table 5.2 and Figure 5.4 is shown in Figure 5.9. The pressures recorded in the well bore have been adjusted to account for the difference in vertical distance between the depth at which the pressure gauges were located, and the formation. Agreement between the simulated and (corrected) recorded pressure values is fairly poor. The recorded pressures are greatly affected by well bore storage effects, which the numerical model does not have the facility to replicate.

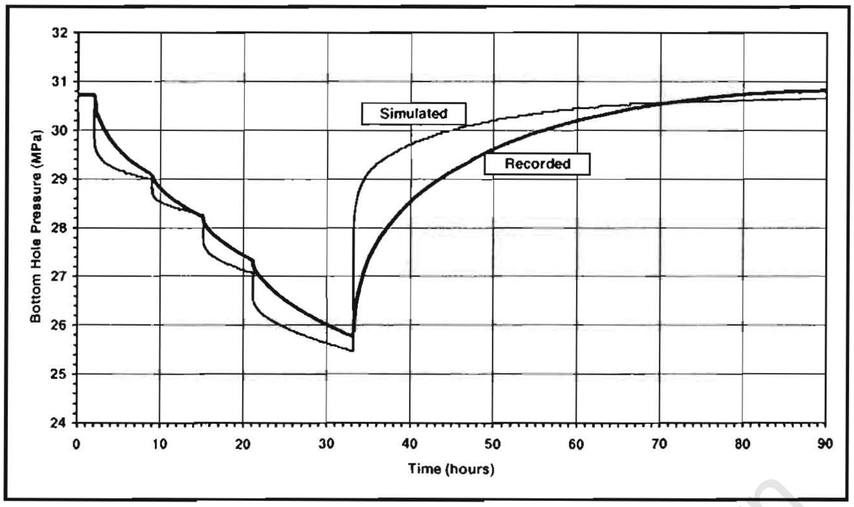

Figure 5.11: *Comparison between recorded (thick line) and simulated (thin line) pressures for well 2 over the well test period illustrated in Figure 5.3. The sequence illustrated here begins at a time corresponding to hour 114 in Figure 5.3.*

It was found that the bottom hole pressure forecast by the simulator is greatly influenced by near well bore phenomena. Matrix blocks in this region are assumed to have dimensions of 10m by 5m. This is larger than the size of many of the primary elements in the refined mesh surrounding the well bore. Although the contribution from a matrix block is nevertheless correctly scaled according to the size of its associated primary element, the concept of a fracture continuum breaks down, and it would be preferable to model fractures explicitly in the near well bore region. In order to achieve the correct degree of draw down observed in Figure 5.11, it was necessary to increase the fracture permeability by a factor of 2 within a radius of 10m of the well. This may be attributable to the precise location of the well bore in the local network of fractures and the number of individual fractures that actually intersect the well bore.

5.5 Conclusions

- The algorithms and modelling techniques developed in preceding chapters and implemented in a finite element program have been successfully applied to the modelling of a producing fractured gas reservoir.
- The Lucy Reservoir has been modelled with a primary finite element mesh that incorporates both the field wide description and very detailed local refinement in the vicinity of a producing well in a single mesh.
- It has been possible to history match successfully approximately one year of production from the Lucy Reservoir.

- The Lucy Reservoir is characterised by high fracture permeability and porosity values in the central thickest region in which the producing wells are located. The fractures are likely to experience a fairly significant degree of closure as the pressure declines. The matrix material has very low values of permeability.
- During the first year of production, large areas of the Lucy Reservoir have not experienced any pressure decline, even within the fracture network. It is likely that the fracture network is poorly connected away from the central region of the reservoir.
- Significant pressure gradients and the resulting transient effects are likely to exist in parts of the reservoir for very long periods of time.
- Matching a reservoir evaluation test with the same mesh used to describe the full field performance has been possible, but is only marginally successful, possibly due to well bore storage and near well bore effects.
- In the vicinity of a well bore, discrete modelling of fractures becomes necessary if the detail of a pressure draw down or build up is to be replicated.
- The process of history matching a dual porosity reservoir is significantly more complex than that of a single porosity reservoir due to the vastly greater number of unknown parameters associated with a fractured reservoir.

CHAPTER 6

CONCLUDING REMARKS

6.1 Opening remarks

This thesis has been concerned with the development, testing and application of a method for modelling and simulating numerically the single phase flow of highly compressible gas through fractured reservoirs. In this chapter the most important results and achievements of this work are listed. The chapter is concluded with a list of topics that remain unresolved and for which additional work would be interesting or beneficial to the industry.

6.2 Motivations and findings

The governing equations derived by various researchers and adopted by the industry for modelling the flow of fluids in reservoirs both with and without fractures have been reviewed and their limitations discussed. In particular controversy over the definition of the potential in Darcy's law as it is applied to single porosity systems has been highlighted. The use of Darcy's law to model fluid flowing through a fracture continuum has been critically reviewed and the factors that influence the value of fracture permeability as it is applied in this context have been investigated, including friction, and viscosity and compressibility of the fluid. Various analytical transfer functions commonly used to model the flow of fluid between the matrix material and the fractures have been discussed by way of a literature survey.

The finite element method has been successfully applied to solve the nonlinear formulation of the set of equations governing the flow of fluid through a porous and permeable medium that arises when the fluid is treated as fully compressible. The nonlinearity of the governing equations has been dealt with successfully through an iterative process applied during each time step. Numerical results for this single porosity model have been verified by comparisons with results obtained using analytical techniques and by successive mesh refinement.

Numerical results presented in this thesis have shown that the geometric shape of a matrix block in a fractured reservoir can have a significant influence on the manner in which the matrix block responds to the pressure in the surrounding fractures, and it is therefore important to capture this information when modelling fractured reservoirs.

Fractured reservoirs are conventionally modelled using the dual porosity approach and it is common to use a pseudo-steady state analytical approximation to deal with the transfer of fluids between a matrix block and its surrounding fractures. It has been demonstrated in this work, by comparison with numerical simulation results, that this approach can lead to poor results when transient conditions prevail, and that such problems require techniques that honour the transient effects. It has been demonstrated that transient flowing conditions from a matrix block can persist for a length of time that is significant with respect to the life of the reservoir if the matrix blocks are large, the matrix permeability is low, and the fluid is highly compressible. Even when the period of transience is short, the use of pseudo-steady state analytical techniques can cause significant errors that persist for a considerable time after transient behaviour has ceased to exist due to the severe distortions that become established during the transient period.

The use of analytical solutions for transient flow of fluid between a single matrix block and the surrounding fracture has been discussed briefly. These solutions are generally only possible under very specific conditions of matrix block geometry, fluid properties and fracture pressure evolution. For full field simulations, during which fracture pressures fluctuate, analytical approximations for transient flow are of limited use.

For the numerical modelling of fractured reservoirs, it has been shown in this work that individual blocks of porous and permeable matrix material that are isolated by the fractures can be reduced to one-dimensional representations while still retaining important information relating to the multi-dimensional geometric shape of the blocks. The nonlinear equations governing the flow of compressible gas through the matrix blocks have been successfully modelled by applying finite element techniques to the one-dimensional representations of individual matrix blocks. The numerical results of these one-dimensional models have been verified by comparison with finely meshed two-dimensional models.

The numerical solution of the transfer of gas between a matrix block and the surrounding fractures using the one-dimensional representations of the matrix block developed in this work permits both transient and pseudo-steady state flow regimes to be honoured. Additionally, essential matrix characteristics that are captured in this approach through correct mesh construction and the use of pseudo-properties are matrix block size and shape, matrix porosity and permeability, and to a limited extent, permeability anisotropy.

The algorithms used to describe the flow of fluid through a porous and permeable formation, through a fracture network continuum, and from isolated blocks of matrix material in a fractured reservoir, have been combined into a unique finite element numerical simulator suitable for forecasting performance of a fractured reservoir without any restrictions being imposed on the compressibility of the fluid. A primary two-dimensional mesh has been used to represent the fracture network. Multiple one-dimensional meshes, each representing a group of matrix blocks, form a secondary mesh system, which is coupled to the primary mesh system. During each time step, the nonlinear flow equations are solved repeatedly until convergence is achieved in both systems independently as well as in the coupled system. This approach allows transient effects that dominate in low permeability matrix blocks to be modelled effectively with finite elements. The development of the algorithms in this manner represents a new approach to the modelling of fractured reservoirs, and permits the full benefit of the finite element method to be realised in the modelling of such reservoirs, namely flexible meshing characteristics and the use of higher order approximations.

A computer program has been developed for the purpose of simulating the performance of two-dimensional petroleum reservoirs by integrating the algorithms for the respective components. The simulator is capable of dealing with fractured or unfractured reservoirs containing fully compressible or slightly compressible fluid. Heterogeneity and anisotropy of the fracture network or in the case of an unfractured reservoir, of the porous and permeable rock matrix, can be accommodated. The simulator can deal with variations in matrix block size, shape, physical properties and anisotropy. As many representative matrix blocks as are required can be accommodated.

The computer algorithms have been used to determine the characteristics of a fractured reservoir. It has been demonstrated that for the purpose of modelling its performance, a fractured reservoir or a portion of such a reservoir can be classified into any of eight different categories, depending on the primary variables, namely matrix permeability and matrix block size. Different modelling approaches are appropriate for each of the categories.

A fractured gas reservoir with very low matrix permeability producing from two wells has been successfully history matched over a one year period of production using the computer program developed in this study.

6.3 Future research

Emanating from the research undertaken in preparation of this thesis are several that have not been resolved in this study and which could be the subject of further research.

- The question of the appropriate form of the potential to be used in Darcy's law is an interesting concept that needs to be investigated in conjunction with thermodynamic principles.
- The manner in which the transfer of fluid is calculated between the string of one-dimensional matrix cells and the corresponding fracture cell can be improved upon. Flow to and from the last element in the string is a source of instability.
- Numerical instability remains a challenge. This is particularly true in the case of the secondary meshes used for modelling the blocks of matrix material. It has been necessary, in some cases, to select very short time steps to control oscillations, which in turn has had a negative impact on the time taken to complete simulation runs.
- The formulation presented in this thesis does not account for pressure gradients that may exist along the length of the edge of a matrix block.
- In the case study, the producing well was modelled explicitly with a refined mesh. A difficulty arises as the scale of the matrix blocks is larger than the radius of the well bore. The fracture permeability in the vicinity of the well is therefore not necessarily equal to the permeability of the fracture continuum and is influenced by the fractures that actually intersect the well. Explicit representation of fractures in the vicinity of the well would be more appropriate. The finite element algorithms and computer code can readily accommodate this change.
- None of the fractured reservoir examples presented in this thesis include more than a single representative matrix block per fracture cell although this can be accommodated with very little

modification. As multiple fracture sets are commonplace, a study of the effect that multiple matrix block sizes have on reservoir performance would be very interesting.

- An example which has not been addressed in this study is a comparison between numerical results and those obtained through applying some of the analytical techniques in use today for the transient analysis of a well test in a fractured reservoir. As the simulator developed in this study specifically deals with transience, such a study would provide useful insight into the numerous parameters that are derived from such an analysis.
- There is considerable scope for optimising time step control as the two mesh systems have different, but linked time stepping and the fracture network is solved implicitly, while the matrix expressions are solved explicitly.
- The FEFRES computer program developed in this work is limited to reservoirs for which the geology of both the fracture network and the matrix blocks can be described in two dimensions. Extending the matrix block description to three dimensions would be trivial. Each block could still be represented in the simulator by a string of one-dimensional elements. The procedures described in section 4.2 could be extended very easily, by, for example, replacing the contour in figure 4.13 with a surface, etc. Extension of the fracture network to three dimensions could be accomplished in two ways. The most general approach would simply be to use three-dimensional elements. This would require a major re-programming effort. A simpler approach would be to build the reservoir model up by stacking a series of two-dimensional meshes. Such an approach would allow most reservoir types to be modelled. If a reservoir were layered, this approach would be most suitable. If a reservoir were massive, then the chances are that a two-dimensional model would be adequate anyhow. The challenge with the stacked layer concept is how to deal with the flow of fluids between layers. It is likely that some finite difference method would be most suitable for this.

APPENDIX A

CONVERSION FACTORS AND NOMENCLATURE

The system of units in common use in the petroleum industry ('oilfield units') does not comply with internationally accepted standards. In this thesis, use has been made of S.I. The factors for converting between the two systems are listed in Table A-1.

Table A-1: *Conversion factors*

Parameter	**Dim.**	***To convert from* (oilfield units)**	***Multiply by***	***to get* (SI units)**
Liquid volume	L^3	Barrels (bbl)	**0.1589873**	cubic meters (m^3)
Gas volume	L^3	Cubic feet (cf)	**0.02831685**	cubic meters (m^3)
Length	L	Feet (ft)	**0.3048**	meters (m)
Length	L	Inches (in)	**0.02540**	meters (m)
Time	T	Days (d)	**86400.0**	seconds (s)
Permeability	L^2	Milli-Darcy (mD)	**$0.986923*10^{-15}$**	square meters (m^2)
Viscosity	$ML^{-1}T^{-1}$	Centi-Poise (cP)	**0.001**	Pascal seconds (Pas)
Pressure	$ML^{-1}T^{-2}$	Pounds/sq inch (psi)	**6894.757**	Pascals (Pa)
Density	ML^{-3}	Pounds/cu ft ($lbft^{-3}$)	**0.01601846**	grams per cc (gcm^{-3})
Mass	M	Pounds	**0.4535924**	kilograms (kg)
Compressibility	$M^{-1}LT^2$	(1/psi)	**$.145038*10^{-3}$**	(1/Pa)
liquid flow rate	L^3T^{-1}	(bbl/d)	**$1.840131*10^{-6}$**	(m^3s^{-1})

Terms commonly in use in the petroleum industry for which the meaning may not be intuitively obvious are explained below:

Build up: The period during which pressure in a wellbore increases after a well has been shut-in.

Bscf: Billion standard cubic feet. An oilfield measure of gas volume at standard conditions.

Draw down: The period during which pressure in a wellbore declines after the well has been opened for flow. Also refers to the amount by which the pressure at any given location and time is below the prevailing average reservoir pressure.

Dual porosity: A descriptive term for a reservoir that contains two distinct but interacting porosity components, such as a fractured reservoir.

Histroy match: The process of adjusting reservoir parameters in order to improve agreement between recorded data and numerical results.

MMscf/d: Million standard cubic feet per day. A measure of gas flow rate at standard conditions.

Pseudo-steady state (PSS): A flow regime which is intermediate between transient and steady state flowing conditions.

Reservoir: A reservoir is a porous and permeable rock formation containing trapped petroleum.

Rock matrix: The porous and permeable rock comprising a petroleum reservoir.

Sand face: The interface between the wellbore and the rock formation.
Shut in: The state of a well for which flow has been arrested by the closing of a choke.
Well bore: The internal space of a well penetrating a petroleum reservoir.
Well bore storage: The period following the closure of a valve located in the well or at surface, during which fluid continues to flow into that part of the well between the sand face and the valve.
Wireline: A description of the process by which data is recorded in a well by instruments attached to the end of a steel cable and lowered into the well.

APPENDIX B

COMPUTER ALGORITHM LOGIC

The logic and sequence of actions required to solve the problem numerically are shown in this section in three flow diagrams and explanatory notes. Each flow diagram is presented in the form of a listing with indentation and numbering indicating hierarchical level. The first diagram (A) shows the overall logic starting at a high level and proceeding as far as the coupling iterations. The other two diagrams are logically embedded within the first but listed separately here. Solution of the secondary mesh via sub-stepping within the coupling iteration is shown in diagram (B) and solution of the primary mesh via nonlinear iterations within the coupling iteration is shown in diagram (C). Greater detail on each item is given in explanatory notes that follow the diagrams.

Diagram A: Program initialisation, time intervalling, time stepping and reporting

```
A.1 Initialise problem
A.2 Repeat for each time interval in this problem
|    A.2.1 Prepare data for this time interval
|    A.2.2 Repeat for each time-step in the current time interval
|    |    A.2.2.1 Prepare data for this time step
|    |    A.2.2.2 Repeat coupling iterations within this time step until convergence is achieved
|    |    |    A.2.2.2.1 Prepare data for this coupling iteration
|    |    |    A.2.2.2.2 Prepare secondary mesh control data
|    |    |    |    B Solve the secondary mesh through time sub-stepping
|    |    |    A.2.2.2.3 Prepare output from secondary mesh for input into primary mesh
|    |    |    A.2.2.2.4 Prepare data for the primary mesh nonlinear iterations
|    |    |    |    C Solve the primary mesh by performing nonlinear iterations
|    |    |    A.2.2.2.5 Prepare output from fracture solution for input into matrix equations
|    |    |    A.2.2.2.6 Check for convergence of coupling iterations
|    |    A.2.2.3 Prepare output from coupling iteration for input into next time step
|    |    A.2.2.4 Perform global material balance calculations for this time step
|    |    A.2.2.5 Increment the time step
|    A.2.3 Report output for this time interval
```

```
|    A.2.4 Increment the time interval
A.3 Output results
```

Diagram B: Solve the secondary mesh through time sub-stepping

```
B.1 Repeat for each primary mesh element
|    B.1.1 Prepare secondary mesh data associated with this primary mesh element
|    B.1.2 Repeat for each time sub-step
|    |    B.1.2.1 Prepare data for this time sub-step
|    |    B.1.2.2 Repeat for each secondary element
|    |    |    B.1.2.2.1 Calculate physical properties for current estimate of pressure
|    |    |    B.1.2.2.2 Form element capacity and stiffness equations
|    |    |    B.1.2.2.3 Build up secondary mesh system equations
|    |    |    B.1.2.2.4 Increment secondary element
|    |    B.1.2.3 Solve secondary mesh system equations
|    |    B.1.2.4 Increment time sub-step
|    B.1.3 Repeat for each secondary element
|    |    B.1.3.1 Calculate flux
|    |    B.1.3.2 Increment secondary element
|    B.1.4 Perform material balance checks
|    B.1.5 Save secondary mesh output flux (loads) for input into primary element
|    B.1.6 Increment primary mesh element
B.2 Continue
```

Diagram C: Solve the primary mesh by performing nonlinear iterations

```
C.1 Prepare data for iterations
C.2 Repeat for each primary element
|    C.2.1 Calculate physical and fluid properties for latest estimate of pressure for this element
|    C.2.2 Form element load vectors incorporating specified ILCs and secondary mesh loads
|    C.2.3 Build up primary mesh system load vector
|    C.2.4 Increment primary element
C.2 Apply specified NBCs by modifying system load vector
C.3 Repeat nonlinear iterations until convergence
|    C.3.1 Repeat for each primary element
|    |    C.3.1.1 Prepare data
|    |    C.3.1.2 Calculate properties for latest estimate of pressure for this element
|    |    C.3.1.3 Form primary element capacity and stiffness matrices
|    |    C.3.1.4 Build up primary mesh system effective stiffness matrix
|    |    C.3.1.5 Increment primary element
|    C.3.2 Apply EBCs by imposing constraint equations on stiffness matrix
|    C.3.3 Forward reduce stiffness matrix
```

```
|     C.3.4 Calculate effective load vector at this step
|     C.3.5 Modify effective load vector for ramped EBCs
|     C.3.6 Reduce effective load vector through back substitution
|     C.3.7 Prepare data for next nonlinear iteration
|     C.3.8 Test for convergence
C.4 Prepare primary mesh output for input into secondary mesh
C.5 Continue
```

Explanatory notes

A.1 Initialise problem

- open input and output files and identify problem type and dimensions
- initialise arrays and matrices and set initial values
- assign values to Gauss point and weight matrices and to transformation matrices
- read primary mesh geometric information, generate infill data

(element types, nodal co-ordinates)

- calculate primary mesh bandwidth and optimise data storage
- read fluid properties and primary mesh physical properties

(fluid: density, compressibility, viscosity, viscosibility, rock: compressibility, porosity and perm. coefficients)

- read and assign initial pressure
- read secondary mesh control data

(no. of distinct matrix block models, distribution of models, no of matrix blocks per type per primary element)

- read secondary mesh geometry and property data

(nodal co-ordinates, porosity and permeability coefficients)

- read secondary mesh control data

(no. of time sub-steps per coupling time step)

- compute initial volumes in place
- report all of above

A.2.1 Prepare data for this time interval

- Read time control data

(no. of steps, step length, convergence criteria)

- Read ILCs, EBCs and NBCs for primary mesh
- prepare ramping of EBCs in primary mesh ($delP_p(t)$)

A.2.2.1 Prepare data for this time step

- assign output from last time step to input for this time step
- update elapsed time and re-set convergence criteria

A.2.2.2.1 Prepare data for this coupling iteration

- update iteration increment

A.2.2.2.2 Prepare secondary mesh control data

- forecast/estimate average pressure in each primary element at end of current time step

(use latest iteration output if it has been done, otherwise linear extrapolation from last 2 time steps)

(use pressure estimated at centroid)

- assign these values to secondary mesh EBCs

A.2.2.2.3 Prepare output from secondary mesh for input into primary mesh

- reconcile secondary mesh pressure, material balance and total fluxes
- generate set of ILCs for primary elements

A.2.2.2.4 Prepare data for the primary mesh nonlinear iterations

- set iteration counters and maximum number of iterations

A.2.2.2.5 Prepare output from fracture solution for input into matrix equations

- generate set of EBCs for each primary element's secondary mesh

A.2.2.3 Prepare output from coupling iteration for input into next time step

- store converged pressure distribution from this step and from previous step
- store loads at end of this time step

A.2.2.4 Perform global material balance calculations for this time step

- reconcile primary and secondary mesh pressures and total fluxes

A.2.3 Report output for this time interval

- report fluxes, pressures, material balance, convergence

A.3 Output results

- report summary

B.1.1 Prepare secondary mesh data associated with this primary mesh element

- identify which representative matrix block is being dealt with
- Initialise system matrices
- if this is start of a new step, update starting pressure distribution from end of last iteration
- if this is merely another coupling iteration, discard pressure distribution from last iteration

(i.e. pressure distribution in secondary mesh is only stored once the coupling iterations have converged)

B.1.2.1 Prepare data for this time sub-step

- Update pressure from end of previous sub-step, if any

B.1.2.2.1 Calculate physical properties for current estimate of pressure

- use latest pressure estimate at beginning of time sub-step at centre of element
- estimate pressure dependant parameters

(fluid density, porosity and viscosity)

- calculate the matrix coefficients

B.1.2.2.2 Form element capacity and stiffness matrices

- compute the components of the $\boldsymbol{C}_s^e(t)$ and $\boldsymbol{K}_s^e(t)$ matrices for the type of element

B.1.2.2.3 Build up secondary mesh system matrices from element matrices

- incrementally build $\boldsymbol{K}_s(t)$ and $\boldsymbol{C}_{lump,s}(t)$

B.1.2.3 Solve secondary mesh system equations

- solve the equations explicitly and modify for EBCs

B.1.3.1 Calculate flux

- first use updated pressure to determine physical parameters in all elements

- calculate fluxes at secondary mesh Gauss points
- interpolate Gauss point fluxes to find fluxes at nodal points

B.1.4 Perform material balance checks

- for each secondary element, use pressure from beginning and end of time step
- determine total volume of gas that should have been expelled to give these pressures
- reconcile with integrated flux over time interval
- determine appropriate flux to use as ILCs in primary mesh

B.1.5 Save secondary mesh output flux (loads) for input into primary element

- store a single ILC value for each primary element

C.1 Prepare data for iterations

- Initiate iteration control

C.2.1 Calculate physical and fluid properties for latest estimates of pressure for this element

- use latest estimates of nodal pressures at beginning and end of this time step, to
- determine corresponding before and after pressures at integration points, then
- use θ to determine appropriate value of pressure at each integration point

(pressure used for determining physical parameters must be consistent with degree of implicitness)

- use these pressures to calculate values of pressure dependent physical parameters

(density, porosity, viscosity)

- synthesise coefficients from physical parameters

C.2.2 Form element load vectors incorporating specified ILCs and secondary mesh loads

- perform numerical quadrature to calculate $F_p^e(t)$
- incorporate specified ILCs and those generated by secondary mesh

C.2.3 Build up primary mesh system load vector

- summation of all element load vectors to get $F_p(t)$

C.2 Apply specified NBCs by modifying system load vector

- modify terms in load vector to accommodate concentrated and distributed NBCs

C.3.1.1 Prepare data

- prepare iteration parameters

C.3.1.2 Calculate properties for latest estimate of pressure for this element

- repetition of C.2.1

C.3.1.3 Form primary element capacity and stiffness matrices

- perform numerical quadrature for this element
- calculate terms of $K_p^e(t)$ and $C_p^e(t)$

C.3.1.4 Build up primary mesh system effective stiffness matrix

- sum element matrix components to build system $K_{ef.p}(t)$ and $CK_p(t)$

C.3.2 Apply EBCs by imposing constraint equations on stiffness matrix

- modify $K_{ef.p}(t)$ and calculate $K_{efP_0.p}(t)$ and $K_{efdP.p}(t)$

C.3.3 Forward reduce stiffness matrix

C.3.4 Calculate effective load vector at this step

- Put together components of $\boldsymbol{F}_{ef.p}(t)$

C.3.5 Modify effective load vector for ramped EBCs

- Modify $\boldsymbol{F}_{ef.p}(t)$ with $\boldsymbol{K}_{efP_0.p}(t)$, $\boldsymbol{K}_{efdP.p}(t)$ and $del\boldsymbol{P}_p(t)$

C.3.6 Reduce effective load vector through back substitution

- Solve for pressure in primary mesh

C.3.7 Prepare data for next nonlinear iteration

- reassign values of latest estimate of pressure

C.4 Prepare primary mesh output for input into secondary mesh

- store latest estimate of pressure distribution at end of this time step

Note that in the above, subscript p indicates primary mesh, s indicates secondary mesh and e indicates element. Where p and s appear without e, they indicate system matrices.

REFERENCES

Amado, L. C. N. and Pedrosa, O. A., 1993. A Finite Volume Approach with Triangular Grids in Reservoir Simulation. SPE Advanced Technology Series, vol. 2, no. 1: p179-185.

Arbogast, T., Keenan, P. T., Wheeler, M. F. and Yotov, I., 1995. Logically Rectangular Mixed Methods for Darcy Flow on General Geometry. SPE paper 29099 presented at the 13th SPE Symposium on Reservoir Simulation, San Antonio, (February 12-15): p51-59.

Asfari, A. and Witherspoon, P. A., 1973. Numerical Simulation of Naturally Fractured Reservoirs. SPE paper 4290 presented at the 3rd Numerical Simulation of Reservoir Performance Symposium of the Society of Petroleum Engineers of AIME, Houston, (January 10-12).

Aziz, K. and Settari, A., 1979. Petroleum Reservoir Simulation. Elsevier Applied Science Publishers, Barking, Essex. ISBN 0-85334-787-5.

Bai, M., Elsworth, D. and Roegiers, J. C., 1993. Multiporosity/Multipermeability Approach to the Simulation of Naturally Fractured Reservoirs. Water resources Research, vol. 29, no. 6 (June): p1621-1633.

Bai, M., Ma, Q. and Roegiers, J. C., 1994. Dual-porosity behaviour of naturally fractured reservoirs. International Journal for Numerical and Analytical Methods in Geomechanics, 18: p359-376.

Bai, M. and Roegiers, J. C., 1994. On the correlation of nonlinear flow and linear transport with application to dual-porosity modelling. Journal of Petroleum Science and Engineering, 11: p63-72.

Barenblatt, G. I., 1960. Basic Concepts of the Single Phase Flow of Fluids Through Fractured Porous Media. Prikladnaia Matematika I Mehanika, Academia Nauk, S.S.S.R., 123 no. 3: p852-64.

Barenblatt, G. I. and Zheltov, J. P., 1960. On the Basic Equations of the Single Phase Flow of Fluids Through Fractured Porous Media. Dokladi Akademii Nauk, S.S.S.R., 123, no.3: p545-48.

Barenblatt, G. I., Zheltov, I. P. and Kochina, I. N., 1960. Basic Concepts in the Theory of Seepage of Homogeneous Liquids in Fissured Rocks (strata). Journal of Applied Mathematical Mechanics, 24(5): p1286-1303.

Bech, N., Jensen, O. K. and Nielson, B., 1991. Modelling of Gravity-Drainage Processes: Analytical and Numerical Solutions. SPE Reservoir Engineering, (February): p129-136.

Beckner, B.L., Chan, H. M. and McDonald, A. E., 1991. Simulating Naturally Fractured Reservoirs Using a Subdomain Method. SPE paper 21241, presented at the 11th Symposium on Reservoir Simulation, Anaheim, California, (February 17-20).

Beckner, B. L., Ishimoto, K., Yamaguchi, S., Firoozabadi, A. and Aziz, K., 1987. Imbibition-Dominated Matrix-Fracture Fluid Transfer in Dual Porosity Simulators. SPE paper 16981 presented at the 62nd Annual Technical Conference and Exhibition of the Society of Petroleum Engineers, Dallas, (September 27-30): p509-523.

Bedford, A. and Drumheller, D. S., 1983. Recent Advances - Theories of Immiscible and Structured Mixtures. Int. J. Eng. Sci., 21: p863-960.

Bhatia, K. S., Advani, S. H. and Lee, J. K., 1989. Finite Element Representation of Two-Phase Fluid Flow through a Naturally Fractured Reservoir. SPE paper 19069 presented at the SPE Gas Technology Symposium, Dallas, (June 7-9): p133-146.

Biot, M. A., 1941. General Theory of Three-Dimensional Consolidation. Journal of Applied Physics, vol. 12, (February): p155-164.

Biot, M. A., 1955. Theory of Elasticity and Consolidation for a Porous Anisotropic Solid. Journal of Applied Physics, vol. 26., no. 2, (February): p182-185.

Biot, M. A., 1956a. Theory of Propagation of Elastic Waves in a Fluid-saturated Porous Solid. J. Acoust. Soc. Am., 28: p168-178.

Biot, M. A., 1956b. Theory of Deformation of a Porous Viscoelastic Anisotropic Solid. Journal of Applied Physics, vol.27, no.5, (May): p459-467.

Bird, R. B., Stewart, W. E. and Lightfoot, E. N., 1960. Transport Phenomena. John Wiley and Sons, New York. ISBN 0 471 07392.

Bossie-Codreanu, D., Bia, P. R and Sabathier, J. C., 1985. The "Checker Model", An Improvement in Modelling Naturally Fractured Reservoirs With a Tridimensional, Triphasic, Black-Oil Numerical Model. Society of Petroleum Engineers Journal, (October): p743-755.

Brooks, A. N. and Hughes, T. J. R., 1982. Streamline Upwind/Petrov-Galerkin Formulations for Convection Dominated Flows with Particular Emphasis on the Incompressible Navier-Stokes Equations. Computer Methods in Applied Mechanics and Engineering, no. 32: p199-259.

Burnett, D. S., 1987. Finite Element Analysis From Concepts to Applications. Addison-Wesley Publishing Company, Menlo Park, California. ISBN0 201 10806 2.

Carey, G. F., Mueller, A., Sepehrnoori, K. and Thrasher, R. L., 1985. Moving Elements for Reservoir Processes. SPE paper 13511 presented at the SPE Reservoir Simulation Symposium, Dallas, (February 10-13): p135-141.

Chase, C. A., 1979. Variational Simulation with Numerical Decoupling and Local Mesh Refinement. SPE paper 7680 presented at the SPE of AIME Fifth Symposium on Reservoir Simulation, Denver, (February 1-2).

Chavent, G. and Jaffre, J., 1986. Mathematical Models and Finite Elements for Reservoir Simulation. Elsevier, Amsterdam. ISBN 0 444 70099 4.

Chavent, G., Jaffre, J., Cohen, G., Dupuy, M. and Dieste, I., 1980. Simulation of Two-Dimensional Waterflooding Using Mixed Finite Elements. SPE paper 10502 presented at the Sixth SPE Symposium on Reservoir Simulation of the SPE of AIME, New Orleans, (January 31): p147-158.

Chen, J., Miller, M. A. and Sepehrnoori, K., 1995. Theoretical Investigation of Countercurrent Imbibition in Fractured Reservoir Matrix Blocks. SPE paper 29141 presented at the 13th SPE Symposium on Reservoir Simulation held in San Antonio, Texas, U.S.A., (February 12-15).

Chen, H. Y., Poston, S. W. and Raghavan, R., 1990. The Well Response in a Naturally Fractured Reservoir: Arbitrary Fracture Conductivity and Unsteady Fluid Transfer. SPE paper 20566 presented at the 65th Annual Technical Conference and Exhibition of the Society of Petroleum Engineers, New Orleans, (September 23-26): p383-398.

Chen, H. Y., Poston, S. W. and Raghavan, R., 1991. An application of the Product-Solution Principle for Instantaneous Source and Green's Function. SPE Formation Evaluation, (June): p161-168.

Cheng, R. T, 1978. Modelling of Hydraulic Systems by Finite-Element Methods. U.S. Geological Survey Report, Menlo Park, California.

Chiang, C. Y., Wheeler, M.F. and Bedient, P. B., 1989. A Modified Method of Characteristics Technique and Mixed Finite Elements Method for Simulation of Groundwater Solute Transport. Water Resources Research, vol. 25, no. 7, (July): p1541-1549.

Coats, K. H., 1989. Implicit Compositional Simulation of Single Porosity and Dual Porosity Reservoirs. SPE paper 18427 presented at the SPE Symposium on Reservoir Simulation in Houston, Texas, U.S.A., (February 6-8).

Collins, R. E., 1961. Flow of Fluid Through Porous Media. Reinhold Publishing Corporation, New York.

Coutinho, A. L. G. A. and Alves, J. L. D., 1996. Parallel Finite Element Simulation of Miscible Displacement in Porous Media. SPE Journal, (December): p487-500.

Craft, B. C. and Hawkins, M., 1991. Applied Petroleum Reservoir Engineering. Prentice-Hill, New Jersey. ISBN 0 13 039884 5.

Crank, J., 1975. The Mathematics of Diffusion. Clarendon, Oxford.

Dake, L. P., 1978. Fundamentals of Reservoir Engineering. Elsevier, The Netherlands. ISBN 0 444 41830X.

Dake, L. P., 1994. The Practice of Reservoir Engineering. Elsevier, Amsterdam. ISBN 0-444-88538-2

Dalen, V., 1979. Simplified Finite-Element Models for Reservoir Simulation. Society of Petroleum Engineers Journal, (October): p333-343.

Darcy, H., 1856. Les fontaines publiques de la ville de Dijon, Dalmont, Paris.

Darlow, B. L., Ewing, R. E. and Wheeler, M. F., 1982. Mixed Finite Element Methods for Miscible Displacement Problems in Porous Media. SPE paper 10501 presented at the sixth SPE Symposium of the SPE of AIME, New Orleans, (January 31-February 3): p137-145.

da Silva, F. V. and Belery, P., 1989. Molecular Diffusion in Naturally Fractured Reservoirs: A Decisive Recovery Mechanism. SPE paper 19672 presented at the 64th Annual Technical Conference and Exhibition of the Society of Petroleum Engineers, San Antonio, (October 8-11): p429-442.

Deb, M. K., Reddy, P. M., Thuren, J. B. and Adams, W. T., 1995. A New Generation Solution Adaptive Reservoir Simulator. SPE paper 30720 presented at the SPE Annual Technical Conference and Exhibition, Dallas, (October 22-25): p175-189.

De Boer, R., 1992. Development of Porous Media Theory - A Brief Historical Review. Transport in Porous Media, 9: p155-164.

de Swaan, A. and Raimirez-Villa, M., 1993. Functions of Flow from Porous Rock Blocks. Journal of Petroleum Science and Engineering, 9: p39-48.

Dhatt, G. and Touzot, G., 1984. The Finite Element Method Displayed. John Wiley and Sons, New York. ISBN 0 471 90110 5.

Diaz-Munio, R. F. and Wellford, L. C., 1981a. A Finite-Element Singular-Perturbation Technique for Convection-Diffusion Problems, Part 1: The One-Dimensional Case. Journal of Applied Mechanics, vol. 48, (June): p265-271.

Diaz-Munio, R. F. and Wellford, L. C., 1981b. A Finite-Element Singular-Perturbation Technique for Convection-Diffusion Problems, Part 2: Two-Dimensional Problems. Journal of Applied Mechanics, vol. 48, (June): p272-275.

Dindoruk, B. and Firoozabadi, A., 1996a. Crossflow in Fractures/Layered Media Incorporating Gravity, Viscous and Phase Behaviour Effects: Part I- Formulation and Features in Layered Media. SPE paper 35457 presented at the 1996 SPE/DOE Tenth Symposium on Improved Oil Recovery, Tulsa, (April 21-24): p569-581.

Dindoruk, B. and Firoozabadi, A., 1996b. Crossflow in Fractures/Layered Media Incorporating Gravity, Viscous and Phase Behaviour Effects: Part II- Features in Fractured Media. SPE paper 35458 presented at the 1996 SPE/DOE Tenth Symposium on Improved Oil Recovery, Tulsa, (April 21-24): p569-581.

Doctors, L. J., 1970. An Application of the Finite Element Technique to Boundary Value Problems of Potential Flow. International Journal for Numerical Methods in Engineering, 2: p243-252.

Douglas Jr., J., Arbogast, T. and Paes, P. J., 1989. Two Models for the Waterflooding of Naturally Fractured Reservoirs. SPE paper 18425 presented at the SPE Symposium on Reservoir Simulation, Houston, (February 6-8), p219-225.

Douglas Jr., J., Paes Leme, P. J., Arbogast, T. and Scmitt, J., 1987. Simulation of Flow in Naturally Fractured Reservoirs. SPE paper 16019 presented at the ninth SPE Symposium on Reservoir Simulation, San Antonio, (February 1-4): p271-279.

Duguid. J. O. and Abel, J. F., 1974. Finite Element Galerkin Method for Analysis of Flow in Fractured Porous Media. Finite Element Methods in Flow Problems, edited by Oden, J. T., Zienkiewicz, O. C., Gallagher, R. H. and Taylor, C. UAH Press, Huntsville, Alabama. Papers presented at the International Symposium on Finite Element Methods in Flow Problems, Swansea, (January): p599-615.

Duguid, J. O. and Lee, P. C. Y., 1977. Flow in Fractured Porous Media. Water Resources Research, vol. 13, no. 3 (June): p558 - 566.

Durlofsky, L. J. and Chien, M. C. H., 1993. Development of a Mixed Finite-Element-Based Compositional Reservoir Simulator. SPE paper 25253 presented at the 12th SPE Symposium on Reservoir Simulation, New Orleans, (February 28 – March 3): p221-231.

Dutra, T. V. and Aziz, K., 1992. A New Double Porosity Reservoir Model for Oil/Water Flow Problems. SPE Reservoir Engineering, (November): p419-425.

Elsworth, D., 1986. A Model to Evaluate the Transient Hydraulic Response of Three-Dimensional Sparsely Fractured Rock Masses. Water Resources Research, vol. 22, no. 13 (December): p1809-1819.

Elsworth, D., 1987. A Boundary Element-Finite Element Procedure for Porous and Fractured Media Flow. Water Resources Research, vol. 23, no. 4 (April): p551-560.

Ewing, R. E. and Heinemann, R. F., 1983. Incorporation of Mixed Finite Element Methods in Compositional Simulation for Reduction of Numerical Dispersion. SPE paper 12267 presented at the Reservoir Simulation Symposium, San Francisco, (November 15-18): p341-347.

Ewing, R. R., Russel, T. F. and Wheeler, M. F., 1983. Simulation of Miscible Displacement Using Mixed Methods and a Modified Method of Characteristics. SPE paper 12241 presented at the Reservoir Simulation Symposium, San Francisco, (November 15-18): p71-79.

Ewing, R.E., Russell, T.F. and Young, L.C., 1989. An Anisotropic Coarse-Grid Dispersion Model of Heterogeneity and Viscous Fingering in Five-Spot Miscible Displacement that matches Experimental and Fine-Grid Simulation. SPE paper 18441 presented at the SPE Symposium on Reservoir Simulation, Houston, (February6-8): p447-465.

Eymard, R. and Sonier, F., 1994. Mathematical and Numerical Properties of Control-Volume, Finite-Element Scheme for Reservoir Simulation. SPE Reservoir Engineering, (November): p283-289.

Farmer, C. L. Heath, D. E. and Moody, R. O., 1991. A Global Optimization Approach to Grid Generation. SPE paper 21236 presented at the 11th SPE Symposium on Reservoir Simulation, Anaheim, USA, (February 17-20): p341-350.

Fillunger, P., 1934. Der Kapillardruck in Talsperren. Die Wasserwirtschaft, 27, H. 13/14.

Forsyth, P. A., 1989. A Control Volume Finite Element Method for Local Mesh Refinement. SPE paper 18415 presented at the SPE Symposium on Reservoir Simulation, Houston, (February 6-8): p85-96.

Fung, L. S. K., 1993. Numerical Simulation of Naturally Fractured Reservoirs. SPE paper 25616 presented at the SPE Middle East Oil Technical Conference and Exhibition, Bahrain, (April 3-6): p203-213.

Fung, L. S. K., Buchanan, L., and Sharma, R., 1994. Hybrid-CVFE Method for Flexible-Grid Reservoir Simulation. SPE Reservoir Engineering, (August): p188-194.

Fung, L. S. K., Hiebert, A. D. and Nghiem, L. X., 1992. Reservoir Simulation with a Control-Volume Finite-Element Method. SPE Reservoir Engineering, (August): p349-357.

Gardner, W., Collier and Farr., 1934. Transactions of the American Geophysical Union, 15: p563.

Gawin, D. and Schrefler, B. A., 1996. Thermo-Hydro-Mechanical Analysis of Partially Saturated Porous Materials. Int. J. Comp. Engng, vol.13, no. 7: p113-143.

Gerke, H. H. and van Genuchten, M. T., 1993. A Dual-Porosity Model for Simulating the Preferential Movement of Water and Solutes in Structured Porous Media. Water Resources Research, vol. 29, no. 2, (February): p305-319.

Gilman, J. R., 1986. An Efficient Finite-Difference Method for Simulating Phase Segregation in the Matrix Blocks in Double-Porosity Reservoirs. SPE Reservoir Engineering, (July): p403-413.

Gilman, J. R. and Kazemi, H., 1983. Improvements in Simulation of Naturally Fractured Reservoirs. Soc. Pet. Eng. J., (August): p695-707.

Gilman, J. R. and Kazemi, H., 1988. Improved Calculations for Viscous and Gravity Displacement in Matrix Blocks in Dual-Porosity Simulators. J. Pet. Technol. (January): p60-90.

Gottardi, G. and Dall'Olia, D., 1992. A control-volume finite-element model for simulating oil-water reservoirs. Journal of Petroleum Science and Engineering, 8: p29-41.

Gottardi, G. and Mesini, E., 1987. A Gas-Oil Reservoir Model by Galerkin's Method. Journal of Petroleum Science and Engineering, vol. 1: p115-125.

Gray, W. G. and Pinder, G. F., 1974. Galerkin Approximation of Time Derivative in the Finite Element Analysis of Groundwater Flow. Water Resources Research, vol. 10, no. 4, (August): p821-828.

Gureghian, A. B., 1975. A Study by the Finite-Element Method of the Influence of Fractures in Confined Aquifers. Society of Petroleum Engineers Journal, (April): p181-191.

Heineman, Z. E. and Brand, C. W., 1988. Gridding Construction for Reservoir Simulation. Paper presented at the First International Forum on Reservoir Simulation, Alpach, Austria, (September).

Heinemann, Z. E., Brand, C., Margit Munka, M. and Chen, Y. M., 1989, 1991. Modelling Reservoir Geometry With Irregular Grids. SPE paper 18412 presented at the Tenth SPE Symposium on Reservoir Simulation, Houston, (February 1989). SPE Reservoir Engineering, (May 1991): p225-232.

Horner, D.R., 1951. Pressure Buildup in Wells. Procedures of The Third World Pet. Congr., Leiden: p503.

Hughes, T. J. R., 1978. A Simple Scheme for Developing 'Upwind' Finite Elements. International Journal Num. Meth. Eng., vol. 12: p1358-1365.

Hughes, T. J. R., Liu, W. K., and Brooks, A., 1979. Finite Element Analysis of Incompressible Viscous Flows by the Penalty Function Formulation. Journal Computational Physics, vol. 30: p1-60.

Huitt, J. L., 1956. Fluid Flow in Simulated Fractures. Am. Inst. Chem. Engineers Jour., 2: p259-264.

Huyakorn, P. S., Lester, B. H. and Faust, C. R., 1983. Finite Element Techniques for Modeling Groundwater Flow in Fractured Aquifers. Water Resources Research, vol. 19, no. 4 (August): p1019-1035.

Huyakorn, P. S., Lester, B. H. and Mercer, J. W., 1983a. An Efficient Finite Element Technique for Modeling Transport in Fractured Porous Media 1. Single Species Transport. Water Resources Research, vol. 19 no. 3 (June): p841-854.

Huyakorn, P. S., Lester, B. H. and Mercer, J. W., 1983b. An Efficient Finite Element Technique for Modeling Transport in Fractured Porous Media 2. Nuclide Decay Chain Transport. Water Resources Research, vol. 19 no. 5 (October): p1286-1296.

Irmay, S., 1965. Modeles Theoriques d'Ecoulement dans les Corps Poreux. Bull RILEM, 29 (December): p37-43.

Ishimoto, K., 1988. Improved Matrix, Fracture Fluid Transfer Function in Dual Porosity Models. SPE paper 17599 presented at the SPE International Meeting on Petroleum Engineering, Tianjin, China, (November 1-4): p495-504.

Javandel, I. and Witherspoon, P. A., 1968. Application of the Finite Element Method to Transient Flow in Porous Media. Society of Petroleum Engineers Journal, (September): p241-252.

Jensen, O. K. and Finlayson, B. A., 1980. Oscillation Limits for Weighted Residual Methods to Convective Diffusion Equations. International Journal for Numerical Methods in Engineering, vol. 15: p1681-1689.

Johnson, C., 1987. Numerical Solution of Partial Differential Equations by the Finite Element Method. Cambridge University Press, Cambridge. ISBN 0 521 345 146.

Jones, T. A., Wooten, S. O. and Kaluza, T. J., 1988. Single-Phase Flow Through Natural Fractures. SPE paper 18175 presented at the 63rd Annual Technical Conference and Exhibition of the Society of Petroleum Engineers, held in Houston, Texas, (October 2-5).

Kaluarachchi, J. J. and Parker, J. C., 1989. An Efficient Finite Element Method for Modelling Multiphase Flow. Water Resources Research, vol. 25, no. 1 (January): p43-54.

Kazemi et al, 1976. Numerical Simulation of Water-Oil Flow in Naturally Fractured Reservoirs. Soc. Pet. Eng. J., (December): p317-326, Trans. AIME, 261.

Kazemi, H. and Gilman, J. R., 1992. Analytical and Numerical Solution of Oil Recovery From Fractured Reservoirs with Empirical Transfer Functions. SPE Reservoir Engineering, (May): p219-227.

Kazemi, H. and Merrill, L. S., 1979. Numerical Simualtion of Water Imbibition in Fractured Cores. Soc. Pet. Eng. J., (June): p175-82.

Kelkar, M. and Gupta, S. P., 1991. A Numerical Study of Viscous Instabilities: Effect of Controlling Parameters and Scaling Considerations. SPE Reservoir Engineering, (February): p121-128.

Kelkar, S. and Zyvoloski, G., 1991. An Efficient, Three-Dimensional, Fully Coupled Hydro-Thermo-Mechanical Simulator: FEHMS. SPE paper number 21242 presented at the 11th SPE Symposium on Reservoir Simulation held in Anaheim California, (February 17-20): p397-404.

Kelly, D. W., Nakazawa, S. and Zienkiewicz, O.C., 1980. A Note on Upwind and Anisotropic Balancing Dissipation in Finite Element Approximations to Convective Diffusion Problems. International Journal for Numerical Methods in Engineering, vol. 15: p1705-1711.

Khataniar, S. and Peters, E. J., 1990. A Finite-element Method for Simulating Unstable Two-phase Flow. Journal of Petroleum Science and Engineering, vol. 4: p169-181.

Khataniar, S. and Peters, E. J., 1991. A Comparison of the Finite Difference and Finite-Element Methods for Simulating Unstable Displacements. Journal of Petroleum Science and Engineering, vol. 5: p205-218.

Kikani, J., 1991. Flux Determination of Finite Conductivity Fractures using Higher Order Interpolation Functions. SPE paper 22658 presented at the 66th Annual Technical Conference and Exhibition of the SPE, Dallas, (October 6-9).

Kocberber, S., 1995. An Automatic, Unstructured Grid-Generation System for Geologically Complex Reservoirs. SPE Computer Applications, (October): p105-111.

Kukreti, A. R., Zaman, M. M., Civan, F. and Rajapaksa, Y., 1988. Finite-Element Analysis of Waterflooding in Irregularly Shaped Reservoirs. Journal of Petroleum Science and Engineering, vol. 1: p277-294.

Lai, W. M., Rubin, D. and Krempl, E., 1993. Introduction to Continuum Mechanics. Pergamon Press, Oxford. ISBN number 0-08-041701-9.

Lamb, H., 1932. Hydrodynamics, 6th edition. Dover Pubications, New York: p581-582.

Langtangen, H. P., 1990. Implicit Finite Element Methods for Two-phase Flow in Oil Reservoirs. International Journal for Numerical Methods in Fluids, vol. 10: p651-681.

Lefebvre, E. J. and Weill, L. M., 1974. Front displacement model in a fractured reservoir. Finite Element Methods in Flow Problems, edited by Oden, J. T., Zienkiewicz, O. C., Gallagher, R. H. and Taylor, C. UAH Press, Huntsville, Alabama. Papers presented at the International Symposium on Finite Element Methods in Flow Problems, Swansea, (January): p653.

Leventhal, S. H., Klein, M. H. and Culham, W. E., 1985. Curvilinear Coordinate Systems for Reservoir Simulation. SPE Journal, (December): p893-901.

Lewis, R. W., Masters, I., Pao, W. K. S. and Ghafouri, H. R., 1998. A Finite Element Double Porosity Model for Heterogeneous Deformable Porous Media. Paper presented at EUROCK (July).

Lewis, R. W., Norris, V. A. and France, P. W., 1975. Finite Element Analysis of a Gas-liquid Interface in a Porous Medium. International Journal for Numerical Methods in Engineering, vol. 9: p433-448.

Lewis, R. W. and Schrefler, B. A., 1987. The Finite Element Method in the Deformation and Consolidation of Porous Media. John Wiley and Sons, Chichester. ISBN 0 471 91210 7.

Lewis, W. L., Schrefler, B. A. and Rahman, N. A., 1998. A Finite Element Analysis of Multiphase Immiscible Flow in Deforming Porous Media for Subsurface Systems. Communications in Numerical Methods in Engineering, vol. 14: p135-149.

Litvak. B. L., 1985. Simulation and Characterization of Naturally Fractured Reservoirs. Paper presented at the Reservoir Characterization Technical Conference, Dallas, (April).

Logan, R. W., Lee, R. L. and Tek, M. R., 1985. Microcomputer Gas Reservoir Simulation Using Finite Element Methods. SPE paper 14449 presented at the 60th Annual Technical Conference and Exhibition of the SPE, Las Vegas, (September 22-25).

Lomize, G. M., 1951. Flow in Fractured Rocks (Russian). Gosenergiocdat, Moscow.

Lough, M. F. Lee, S. H. and Kamath, J., 1996. A New Method to Calculate the Effective Permeability of Grid Blocks Used in the Simulation of Naturally Fractured Reservoirs. SPE paper 36730 presented at the 1996 SPE Annual Technical Conference and Exhibition, Denver (October 6-9): p493-499.

Louis, C., 1969. A Study of Groundwater in Jointed Rocks and its Influence on the Stability of Rock Masses. Rock Mech. Res., Rep. 10, Imperial College, London.

Mathews, C.S. and Russell, D.G., 1967. Pressure Buildup and Flow Tests in Wells, Monograph Vol. 1, Society of Petroleum Engineers of AIME. Dallas, Millet the Printer.

McDonald, A. E., Beckner, B. L., Chan, H. M., Jones, T. A. and Wooten, S. O., 1991. Some Important Considerations in the Simulation of Naturally Fractured Reservoirs. SPE paper 21814 presented at the Rocky Mountain Regional Meting and Low-Permeability Reservoirs Symposium, Denver, (April 15-17): p117-124.

McMichael, C. L. and Thomas, G. W., 1971 and 1973. Reservoir Simulation by Galerkin's Method. SPE paper 3558 presented at the SPE-AIME 46th Annual Fall Meeting, New Orleans, (October 3-6 1971). Society of Petroleum Engineers Journal, (June 1973): p125-138.

Moissis, D. E., Miller, C. A. and Wheeler, M. F., 1989. Simulation of Miscible Viscous Fingering Using a Modified Method of Characteristics: Effects of Gravity and Heterogeneity. SPE paper 18440 presented at the SPE Symposium on Reservoir Simulation, Houston, (February 6-8): p431-446.

Mulder, W. A. and Gmelig Meyling, R. H. J., 1991. Numerical Simualtion of Two-Phase Flow Using Locally Refined Grids in Three-Space Dimensions. SPE paper 21230 presented at the 11th SPE Symposium on Reservoir Simulation, Anaheim USA, (February 17-20): p299-305.

Muralidhar, K., 1989. Study of Flow and Transport in Single Fractures. Proceedings of the Seventh International Conference on Finite Element Methods in Flow Problems, (April 3-7): p710-716.

Muskat, M., 1937. The Flow of Homogeneous Fluids through Porous Media. McGraw-Hill Book Co., New York.

Muskat, M., 1949. The Principles of Oil Production. McGraw-Hill Book Co., New York.

Narasimham, T.N., 1982. Multidimensional Numerical Simulation of Fluid Flow in Fractured Porous Media. Water Resources Research, vol. 18 no. 4: p1235-1247.

Odeh, A., 1965. Unsteady-State Behaviour of Naturally Fractured Reservoirs. Trans. AIME, vol. 234: p60-65.

Oden, J. T., Zienkiewicz, O. C., Gallagher, R. H. and Taylor, C., 1974 (editors for conference proceedings). Finite Elements in Flow Problems. Papers presented at the International Symposium on Finite Element Methods in Flow Problems, Swansea, United Kingdom, (January). UAH press, Huntsville, Alabama.

Onur, M. and Satman, A., 1993. New Type Curves for Analyzing the Transition Time Data From Naturally Fractured Reservoirs. SPE paper 25873 presented at the SPE Rocky Mountain Regional/Low Permeability Reservoir Symposium held in Denver, (April 12-16).

Palagi, C. L. and Aziz, K., 1991 and 1994. Use of Voronoi Grid in Reservoir Simulation. SPE paper 22889 presented at the 66th Annual Technical Conference and Exhibition of the SPE, Dallas, (October 6-9 1991): p77-92. SPE Advanced Technology Series, vol. 2, no.2 (April 1994): p69-77.

Parsons, R., W., 1966. Permeability of Idealised Fractured Rock. Soc. Petroleum Engineers Jour., vol. 6: p126-136.

Peaceman, D. W., 1978. Interpretation of Well-Block Pressures in Numerical Reservoir Simualtion. SPE Journal, (June): p183-194.

Peters, E. J. and Kasap, E., 1986. Simulation of Unstable Miscible Displacement by Finite Element Method. SPE paper 15597 presented at the 61st Annual Technical Conference and Exhibition of the SPE, New Orleans, (October 5-8).

Pollard, P., 1953. Evaluation of acid treatments from pressure build-up analysis. Trans. AIME: p38-43.

Pruess, K and Narasimham, T. N., 1985. A Practical Method for Modelling Fluid and Heat Flow in Fractured Porous Media. Society of Petroleum Engineers Journal (February): p14-26.

Pruess, K. and Wu, Y. S., 1989. A New Semianalytical Method for Numerical Simulation of Fluid and Heat Flow in Fractured Reservoirs. SPE paper 18426 presented at the SPE Symposium on Reservoir Simulation, Houston (February 6-8): p227-238.

Quandalle, P., 1993. Eighth SPE Comparative Solution Project: Gridding Techniques in Reservoir Simulation. SPE paper 25263 presented at the 1983 SPE Symposium on Reservoir Simulation, New Orleans (Feb 28 - March 3).

Reachford, H. H., 1976. A Sampling of Variational Methods. SPE paper 5720 presented at the Fourth Symposium of Numerical Simulation of Reservoir Performance of the SPE of AIME, Los Angeles, (February 19-20).

Riazi, M. R., Whitson, C. H. and da Silva, F., 1994. Modelling of Diffusional Mass Transfer in Naturally Fractured Reservoirs. Journal of Petroleum Science and Engineering, 10: p239-253.

Rossen, W. R. and Kumar, A. T. A., 1992. Single- and Two-Phase Flow in Natural Fractures. SPE paper 24915 presented at the 67th Annual Technical Conference and Exhibition of the Society of Petroleum Engineers, Washington, (October 4-7): p595-603.

Rossen, W. R. and Kumar, A. T. A., 1994. Effect of Fracture Permeabilities on Performance of Naturally Fractured Reservoirs. SPE paper 28700 presented at the SPE International Petroleum Conference and Exhibition of Mexico, Veracruz, (October 10-13): p7-18.

Rossen, R. H. and Shen, E. I. C., 1989. Simulation of Gas/Oil Drainage and Water/Oil Imbibition in Naturally Fracture Reservoirs. SPE Reservoir Engineering, (November): p464-470.

Rozon, B. J., 1989. A Generalized Finite Volume Discretization Method for Reservoir Simulation. SPE paper 18414 presented at the Reservoir Simulation Symposium, Houston, (February 6-8): p71-84.

Russell, T. F., 1982. Finite Elements with Characteristics for Two-Component Incompressible Miscible Displacement. SPE paper 10500 presented at the sixth SPE Symposium on Reservoir Simulation of the SPE of AIME, New Orleans, (January 31-February 3): p123-135.

Russell, T. F., 1989. Stability Analysis and Switching Criteria for adaptive Implicit Methods Based on the CFL Condition. SPE paper 18416 presented at the SPE Symposium on Reservoir Simulation, Houston, (February6-8): p97-107.

Sagar, B., 1978. Galerkin Finite Element Procedure for Analyzing Flow Through Random Media. Water Resources Research, vol. 14, no. 6, (December): p1035-1044.

Saidi, A. M., 1983. Simulation of Naturally Fractured Reservoirs. SPE paper 12270 presented at the Seventh SPE Symposium on Reservoir Simulation held in San Francisco, (November) p15-18.

Santos, R. L. A., Pedrosa, O. A. and Correa, A. C. F., 1992. An Efficient Finite Volume Approach for Modelling Miscible Displacement. SPE paper 23691 presented at the Second Latin American Petroleum Engineering Conference, Caracas (March 8-11): p167-175.

Scheidegger, A. E., 1957. The Physics of Flow through Porous Media. University of Toronto Press.

Schrefler, B. A. and Scotta, R., 2001. A Fully Coupled Dynamic Model for Two-Phase Fluid Flow in Deformable Porous Media. Comput. Methods Appl. Mech. Engrg.: p3223-3246.

Schrefler, B. A. and Xiaoyong, Z., 1993. A Fully Coupled Model for Water Flow and Airflow in Deformable Porous Media. Water Resources Research, vol. 29, no. 1 (January): p155-167.

Shapiro, A. M. and Andersson, J., 1983. Steady State Fluid Response in Fractured Rock: A Boundary Element Solution for a Coupled, Discrete Fracture Continuum Model. Water Resources Research, vol. 19 no. 4 (August): p959-969.

Shaw. D. C., 1993. The Treatment of Wells, Faults, and Other Singularities in a Black-Oil, Finite-Element Reservoir Simulator. SPE paper 25246 presented at the 12th SPE Symposium on Reservoir Simulation, New Orleans, (February 28 – March 3): p127-142.

Sincovec, R. F., 1977. Generalized Collocation Methods for Time-Dependent, Nonlinear Boundary-Value Problems. SPE Journal, (October): p345-352.

Sonier, F., 1993. Full-Field Gas Storage Simualtion Using a Control-Volume Finite-element Model. SPE paper 26655 presented at the 68th Annual Technical Conference and Exhibition of the Society of Petroleum Engineers, Houston, (October 3-6): p515-524.

Sonier, F., Souillard, P. and Blaskovich, F. T., 1986. Numerical Simulation of Naturally Fractured Reservoirs. SPE paper 15627 presented at the 1986 SPE Annual Technical Conference and Exhibition, New Orleans, (October).

Spivak, A., Price, H. S. and Settari, A., 1976 and 1977. Solution of the Equations for Multidimensional, Two-Phase, Immiscible Flow by Variational Methods. SPE paper 5723 presented at the SPE-AIME Fourth Symposium on Numerical Simulation of Reservoir Performance, Los Angeles, (February 19-20 1976). Society of Petroleum Engineers Journal, (February 1977): p27-41.

Sukirman, Y. and Lewis, R. W., 1993. A Finite Element Solution of a Fully Coupled Implicit Formulation for Reservoir Simulation. International Journal for Numerical and Analytical Methods in Geomechanics, vol. 17: p677-698.

Tan, C. T. and Firoozabadi, A., 1995a. Theoretical Analysis of Miscible Displacement in Fractured Porous Media by a One-Dimensional Model: Part 1- Theory. The Journal of Canadian Petroleum Technology, vol. 34, no. 2 (February): p17-27.

Tan, C. T. and Firoozabadi, A., 1995b. Theoretical Analysis of Miscible Displacement in Fractured Porous Media by a One-dimensional Model: Part 2- Features. The Journal of Canadian Petroleum Technology, vol. 34, no. 2 (February): p28-35.

Thomas, L. K. , Dixon, T. N. and Pierson, R. G., 1983. Fractured reservoir simulation. Soc. Pet. Eng. J. (February): p42-54.

Ueda, Y., Murata, S., Watanabe, Y. and Funatsu, K., 1989. Investigation of the Shape Factor used in the Dual-Porosity Reservoir Simulator. SPE paper 19469 presented at the SPE Asia-Pacific Conference, Sydney, (September 13-15): p35-44.

Van Leer, B., 1977. Towards the Ultimate Conservative Difference Scheme. IV. A New Approach to Numerical Convection. Journal of Computational Physics, vol. 23: P276-299.

von Terzaghi, K., 1925. Principles of soil mechanics. Engineering News-Record, 95.

Voronoi, G., 1908. Nouvelles applications des pametres continus a la theorie des formes quadratiques. J. Reine Angew. Math., 134: p198-287.

Warren, J. E. and Root, P. J., 1963. The behaviour of naturally fractured reservoirs. Soc. Pet. Eng. J., 3 (September): p245-255.

Wilson, C. R. and Witherspoon, P. A., 1974. Steady-State Flow in Rigid Networks of Fractures. Water Resour. Res., vol.10, no. 2 (April): p328-335.

Woltman, R., 1794. Beytrage zur hydraulischen Architecteur. Dritter Band, Johann Christian Dietrich, Gottingen.

Wu, Y. S. and Pruess, K., 1988. A Multi-Porosity Method for Simulation of Naturally Fractured Petroleum Reservoirs. SPE Reservoir Engineering, (February): p327-336.

Wu, Y. S., Pruess, K. and Witherspoon, P. A., 1992. Flow and Displacement of Bingham Non-Newtonian Fluids in Porous Media. SPE Reservoir Engineering, (August): p369-376.

Zienkiewicz, O. C., 1966. Solution of anisotropic seepage by finite elements. J. Eng. Mech. Div., Proc. Am. Soc. civ. Eng. 92 EM 1,111.

Zienkiewicz, O. C. and Cheung, Y. K., 1965. Finite Elements in the Solution of Field Problems. The Engineer, vol. 220: p507.

Zienkiewicz, O. C. and Taylor, R. L., 1967. The Finite Element Method, Volume 2, Solid and Fluid Mechanics Dynamics and Non-linearity. McGraw-Hill Book Company, London. ISBN 0 07 084176 6.

Zimmerman, R. W., Somerton, W. H. and King, M. S., 1986. Compressibility of Porous Rocks. Journal of Geophysical Research, vol. 91, no.B12: p12765-12777.

Zimmerman, R., W., 1991. Compressibility of Sandstone. Developments in Petroleum Science, 29. Elsevier, the Netherlands. ISBN 0-444-88325-8.

Zimmerman, R. W. and Bodvarsson, G. S., 1995. Effective Block Size for Imbibition or Absorption in Dual-Porosity Media. Geophysical Research Letters, vol. 22, no. 11 (June): p1461-1464.

Zimmerman, R. W. and Bodvarsson, G. S., 1996. Hydraulic Conductivity of Rock Fractures. Transport in Porous Media 23: p1-30.

Zimmerman, R. W., Bodvarsson, G. S. and Kwicklis, E. M., 1990. Absorption of Water into Porous Blocks of Various Shapes and Sizes. Water Resources Research, vol. 26, no. 11 (November): p2797-2806.

Zimmerman, R. W., Chen, G., Hadgu, T. and Bodsvarsson, G. S., 1993. A Numerical Dual-Porosity Model with Semianalytical Treatment of Fracture/Matrix Flow. Water Resources Research, vol. 29, no. 7 (July): p2127-2137.

Zimmerman, R. W. and Yeo, I. W., 2000. Fluid Flow in Rock Fractures: From the Navier-Stokes Equation to the Cubic Law. Dynamics of Fluids in Fractured Rock, Geophysical Monograph 122 of the AGU: p213-224.